

UNIVERSITY OF CALIFORNIA, SAN DIEGO

Falling, flapping, flying, swimming,...:  
high-*Re* fluid-solid interactions with vortex shedding

A dissertation submitted in partial satisfaction of the  
requirements for the degree Doctor of Philosophy  
in  
Engineering Sciences (Aerospace Engineering)

by

Sébastien Honoré Roland Michelin

Committee in charge:

Professor Stefan G. Llewellyn Smith, Chair  
Professor Eric Lauga  
Professor Paul F. Linden  
Professor William R. Young  
Professor Qiang Zhu

2009

© 2009

Sébastien Honoré Roland Michelin,

All rights reserved.

The dissertation of Sébastien Honoré Roland Michelin is approved, and it is acceptable in quality and form for publication on microfilm:

---

---

---

---

---

Chair

University of California, San Diego

2009

*To S. Olivier and L. Jacquin, whose enthusiasm as teachers and passion for physics and mechanics have convinced me to follow this path.*

## TABLE OF CONTENTS

Signature Page . . . . .		iii
Dedication . . . . .		iv
Table of Contents . . . . .		v
List of Frequently Used Symbols . . . . .		ix
List of Figures . . . . .		x
Acknowledgments . . . . .		xv
Vita, Publications, and Fields of Study . . . . .		xviii
Abstract . . . . .		xx
<b>1 Introduction and thesis outline . . . . .</b>		<b>1</b>
<b>2 A reduced-order model for high-<math>Re</math> fluid-solid interactions . . . . .</b>		<b>6</b>
2.1 Introduction and motivation . . . . .		6
2.2 Numerical simulations of high- $Re$ fluid-solid interactions . . . . .		9
2.2.1 General form of the equations of fluid-solid interaction . . . . .		9
2.2.2 Numerical simulation of fully-coupled fluid-solid interactions and its challenges . . . . .		11
2.2.3 An overview of commonly-used techniques . . . . .		12
2.3 Reduced-order model for sharp-edged solid bodies . . . . .		14
2.3.1 Added mass . . . . .		15
2.3.2 Quasi-steady empirical models . . . . .		17
2.3.3 Vortex shedding in fluid-solid interactions . . . . .		18
2.3.4 Inviscid vortex methods . . . . .		19
2.4 The Brown–Michael point vortex model . . . . .		22
2.4.1 Description . . . . .		22
2.4.2 Irreversible vortex roll-up and shedding criterion . . . . .		23
2.4.3 Equation of motion for a point vortex with unsteady intensity . . . . .		23
2.4.4 Conservation of fluid momentum around the vortex and branch cut . . . . .		24
2.4.5 The Brown–Michael model and conservation of angular momentum . . . . .		27
2.5 Reduced order models of fluid-solid interactions using Brown–Michael vortices . . . . .		29

<b>3</b>	<b>Motion of a rigid sharp-edged solid body shedding vortices . . .</b>	<b>33</b>
3.1	Introduction . . . . .	33
3.2	Equations of motion of a sharp-edged rigid body shedding vortices	35
3.2.1	Geometry . . . . .	35
3.2.2	Complex potential and velocity around the moving solid body	37
3.2.3	Regularity condition and motion of the vortices . . . . .	39
3.2.4	Forces and torques on the solid body . . . . .	40
3.2.5	Coupled equations of motion . . . . .	47
3.3	Small-time behavior and vortex shedding . . . . .	48
3.3.1	Shedding of the first vortices . . . . .	48
3.3.2	Shedding of subsequent vortices . . . . .	50
3.3.3	Favorable and unfavorable shedding conditions . . . . .	52
3.4	Example: stability of the broadside-on fall of a two dimensional flat plate. . . . .	53
3.4.1	Equations of motion . . . . .	54
3.4.2	Fall of a horizontal card . . . . .	58
3.4.3	Comparison with added mass analysis . . . . .	60
3.4.4	Stability of broadside-on fall . . . . .	63
3.5	Conclusions . . . . .	72
<b>4</b>	<b>Passive flapping of flexible flags in axial flow . . . . .</b>	<b>75</b>
4.1	Introduction . . . . .	75
4.2	Model . . . . .	77
4.2.1	Solid model . . . . .	77
4.2.2	Vortex shedding model . . . . .	79
4.2.3	Fluid model . . . . .	80
4.2.4	Numerical method for the flag problem . . . . .	82
4.3	Flapping of a single flag . . . . .	84
4.3.1	Three possible regimes . . . . .	84
4.3.2	Comparison with linear stability results . . . . .	87
4.3.3	Flapping modes . . . . .	87
4.3.4	Hysteresis behavior . . . . .	88
4.3.5	Travelling waves along the flapping flag . . . . .	89
4.4	Flapping of two parallel flags . . . . .	93
4.4.1	Equations of motion of $Q$ flexible plates shedding point vor- tices . . . . .	94
4.4.2	Influence of the distance between plates on their stability .	95
4.4.3	Coupled modes . . . . .	98
4.4.4	Confinement and its effect on the flapping properties . . . .	101
4.5	Conclusions . . . . .	102

5	<b>Linear stability analysis of coupled parallel flexible plates in an axial flow</b> . . . . .	105
5.1	Introduction . . . . .	105
5.2	Aerodynamic coupling of $Q$ flexible plates . . . . .	108
5.2.1	Description of the problem . . . . .	108
5.2.2	Potential flow and wake representation . . . . .	110
5.2.3	Computation of the pressure forcing . . . . .	113
5.2.4	Galerkin decomposition . . . . .	117
5.2.5	Numerical solution . . . . .	118
5.3	Stability of two coupled plates . . . . .	120
5.3.1	Influence of $d$ on the stability of the flat state of rest . . . . .	120
5.3.2	In-phase and out-of-phase modes . . . . .	122
5.3.3	Influence of $d$ on the mode properties . . . . .	126
5.4	Stability of three coupled plates . . . . .	129
5.5	Results for larger $Q$ . . . . .	131
5.5.1	Symmetry argument . . . . .	131
5.5.2	The limit $Q \rightarrow \infty$ . . . . .	134
5.6	Conclusions . . . . .	138
6	<b>Propulsive efficiency of a heaving flexible wing</b> . . . . .	140
6.1	Introduction . . . . .	140
6.2	Description of the model . . . . .	143
6.2.1	Solid model . . . . .	143
6.2.2	Representation of the flow around the wing . . . . .	146
6.2.3	Energy conservation . . . . .	147
6.2.4	Propulsive performance . . . . .	148
6.3	Simulation of the initial value problem and convergence to a periodic state . . . . .	150
6.4	Wing flexibility and propulsive performance . . . . .	152
6.4.1	Optimal flexibility for thrust generation and propulsion efficiency . . . . .	152
6.4.2	Wake structure and thrust production . . . . .	154
6.4.3	Resonance and optimal flexibility for thrust production . . . . .	159
6.5	Influence of flexibility on the flapping amplitude and mode shape . . . . .	161
6.5.1	Resonances between the forcing frequency and the natural frequencies of the system . . . . .	161
6.5.2	Evolution of the flapping mode shape with the flexibility of the profile . . . . .	168
6.6	Conclusions . . . . .	170
7	<b>Conclusions</b> . . . . .	174
7.1	Using a point vortex model to study fluid-solid interactions . . . . .	174
7.2	High- $Re$ fluid-solid interactions . . . . .	177

A	<b>Linear stability analysis of a cantilevered plate in parallel flow</b>	181
B	<b>Numerical solution of Cauchy-type singular integral equations</b>	190
C	<b>Symmetry of the coupled modes of <math>Q</math> flexible plates . . . . .</b>	194
D	<b>Effect of material damping on the performance of a flexible flapping wing . . . . .</b>	196
	4.1 Modification of the solid's equations . . . . .	196
	4.2 Propulsive performance of a heaving visco-elastic wing . . . . .	197
	References . . . . .	200

## LIST OF FREQUENTLY USED SYMBOLS

$z = x + iy$	Position in the complex plane
$F$	Complex potential
$\phi = \text{Re}(F)$	Real potential
$w = u - iv$	Complex velocity $w = dF/dz$
$p$	Pressure field
$u$	Velocity field
$U$	Velocity scale
$L$	Solid characteristic length scale
$\rho$	Fluid density
$\nu$	Fluid kinematic viscosity
$Re = \frac{UL}{\nu}$	Reynolds number
$\mathcal{M}$	Solid mass
$\rho_s$	Solid mass per unit area
$B$	Solid bending rigidity per unit length
$z_n$	Position of point vortex $n$
$\Gamma_n$	Intensity of point vortex $n$
$z_{n,0}$	Position of the generating corner of vortex $n$
$N$	Number of point vortices in the flow
$P$	Number of generating corners on the solid
$Q$	Number of parallel flexible plates or flags
$S$	Number of Galerkin modes used in the expansion

## LIST OF FIGURES

Figure 2.1:	Conservation of momentum around the unsteady point vortex and its corresponding branch cut. . . . .	25
Figure 2.2:	Schematic representation of (a) the complete fluid-solid coupled problem and (b) the reduced-order model using the Brown–Michael point vortex representation. . . . .	31
Figure 3.1:	Motion of a general solid body in the physical $z$ -plane (left) and mapped $\zeta$ -plane (right). The contour $\mathcal{C}$ is mapped onto the solid’s physical boundary $\mathcal{C}$ through the mapping (3.2)	36
Figure 3.2:	Computation of the contour integrals in (3.17): the integration contour is replaced using Cauchy’s theorem by a contour on $\mathcal{C}_\infty$ . . . . .	42
Figure 3.3:	Notation of Figure 3.1 adapted to the case of a falling card	55
Figure 3.4:	(Left) When the plate is released with an initial orientation $\theta_0$ , its initial velocity and acceleration make an angle $\theta_f$ with the vertical axis. (Right) Variations of $\theta_f$ with $\theta_0$ for different values of $Fr$ . . . . .	57
Figure 3.5:	Broadside-on fall of a card ( $\theta_0 = 0$ ) for $Fr = 1$ . (a) Vertical velocity of the plate. (b) Intensity of the right vortex. (c) Vertical distance $d_v$ between the vortex pair and the plate.	59
Figure 3.6:	Scalings of the broadside-on fall with $Fr$ . The vertical velocity (left), vortex intensity (center) and vortex-plate distance (right) are plotted for various $Fr$ against a rescaled time $t\sqrt{Fr}$ . . . . .	61
Figure 3.7:	Fall of a card released with a non-zero angle: successive plate positions (left), plate orientation and horizontal position (center-top), vortex intensities (center bottom) and snapshot of the flow streamlines (right). . . . .	64
Figure 3.8:	Fall of a card released with a non-zero angle, continued . .	65
Figure 3.9:	Influence of $\theta_0$ and $Fr$ on the temporal evolution of $\theta/\theta_0$ . .	66
Figure 3.10:	Influence of $Fr$ on the growth rate and pseudo-period of the unstable fluttering oscillations. . . . .	67
Figure 3.11:	Evolution of (a) the rate of change of the body circulation, the relative vertical velocity of the vortices and the plate’s orientation, and (b) the body circulation, the vertical distance between the vortices and the horizontal plate velocity	68
Figure 3.12:	Stabilizing and destabilizing effects of the force and torque due to added inertia and to the vortices applied by the fluid on the falling card . . . . .	69

Figure 3.13: Evolution of the different contributions to the horizontal momentum associated with the vortices $p_1$ (thick-solid) and $p_2$ (thick-dashed) as defined in (3.69). . . . .	71
Figure 4.1: Vortex shedding behind a flapping flag. The oncoming flow is horizontal and vortices are shed from the trailing edge. The last vortex has unsteady intensity, the other vortices have frozen circulation. . . . .	78
Figure 4.2: Elastic forces and torques applied on a section of the flexible plate between $s$ and $s + ds$ . . . . .	78
Figure 4.3: Instantaneous streamlines for the flow over the flapping flag in the periodic regime for $M^* = 3$ and $U^* = 11.5$ . For reference, the successive positions of the flag in a flapping cycle are plotted as dashed lines. . . . .	85
Figure 4.4: (Left) Frequency spectrum of the solid's energy (solid) and tail orientation (dashed) normalized by their maximum values for clarity, (center) Tail vertical motion phase diagram and (right) evolution of the horizontal force on the flagpole. . . . .	86
Figure 4.5: Critical stability curve of the flag state of rest using the point vortex model (solid) and the linear stability analysis predictions. Comparison with the results obtained with the vortex sheet approach. . . . .	88
Figure 4.6: Flapping mode observed for different values of the inertia ratio. The position of the flag is plotted every $\Delta t = 0.04$ . . . . .	89
Figure 4.7: Hysteresis behavior of the flapping flag: (solid) horizontal force on the flag pole and (dashed) horizontal velocity of imposed flow. . . . .	90
Figure 4.8: Temporal (left) and spatial (right) variations of the phase of the first CEOF in the flapping regime, for (top) the orientation of the flag and (bottom) the local pressure force (dash-dotted) and the elastic force's normal component (dashed). . . . .	92
Figure 4.9: Flow past two identical flexible plates, with leading edge clamped at a cross-stream distance $D$ from each other. . . . .	96
Figure 4.10: Position in the $(M^*, U^*)$ -plane of the critical stability curve of two flexible plates for different values of the relative distance $d$ . The results for an isolated plate are also given for reference. . . . .	97
Figure 4.11: Streamlines of the flow past two plates with $M^* = 0.5$ and $U^* = 8$ , (a) in the in-phase flapping mode with $d = 0.15$ and (b) in the out-of-phase flapping mode with $d = 0.7$ . . . . .	99
Figure 4.12: Evolution and scalings of the flapping characteristics with the relative distance $d$ in the in-phase flapping mode of two plates with $M^* = 5$ and $U^* = 11$ . . . . .	102

Figure 5.1:	(Top) Sketch of the in-phase and out-of-phase modes observed experimentally for two flexible plates. (Bottom) Sketch of the in-phase, out-of-phase and symmetric modes observed experimentally for three flexible plates. . . . .	108
Figure 5.2:	Horizontal flow over $Q$ parallel plates. Continuity of pressure is enforced upstream and downstream along the direction of each plate. . . . .	110
Figure 5.3:	(a) Critical stability curve of a single cantilevered flexible plate using the double wake (DW) representation (solid) and the vortex sheet (VS) wake model (dashed). (b) Maximum growth rate observed with the DW representation. . . . .	112
Figure 5.4:	Critical stability curve of the state of rest of two plates in the $(M^*, U^*)$ -plane for increasing plate separation. The thick solid line is the stability curve for one flag only using the same approach (equivalent to $d = \infty$ ). . . . .	121
Figure 5.5:	(a) Growth rate and (b) nature of the most unstable mode for increasing $d$ . In (b), the stability region of the state of rest is shown in black, while grey (resp. white) regions correspond to an out-of-phase (resp. in-phase) dominant mode. . . . .	123
Figure 5.6:	Evolution of the dominant mode properties for $M^* = 2$ (left) and $M^* = 4$ (right). (Top) Regime observed, (center) growth rate of the most unstable mode and (bottom) frequency of the dominant mode. . . . .	124
Figure 5.7:	Dominant mode for $M^* = 4$ and $U^* = 13$ for (left) $d = 0.1$ and (right) $d = 0.2$ . The position of each plate is plotted every quarter-period. . . . .	125
Figure 5.8:	Variations of (a) the frequency and (b) the growth rate of the four in-phase (thick lines) and out-of-phase (thin lines) least stable modes for $M^* = 4$ and $U^* = 13$ . . . . .	127
Figure 5.9:	Same as figure 5.8 for $M^* = 2$ and $U^* = 10$ . . . . .	127
Figure 5.10:	Evolution of the envelope of the least stable in-phase and out-of-phase modes with increasing $d$ for $M^* = 4$ and $U^* = 13$ . The envelope is computed as the maximum vertical deflection achieved for $0 \leq x \leq 1$ . . . . .	130
Figure 5.11:	Dominant mode properties for three plates. (Top) Nature of the dominant mode: stable (black), symmetric (dark gray), out-of-phase (light gray) and in-phase mode (white). (Center) Maximum growth rate. (Bottom) Frequency. . . . .	132
Figure 5.12:	Frequency (left) and growth rate (right) of the four least stable in-phase, out-of-phase and symmetric modes for three plates with $M^* = 3$ and $U^* = 13$ . . . . .	133

Figure 5.13: Evolution of the critical stability curve with an increasing number of plates for $d = 0.2$ (left) and $d = 0.5$ (right). The limit $Q \rightarrow \infty$ described in section 5.5.2 is plotted as a thick black line. . . . .	136
Figure 5.14: Evolution in the $(M^*, U^*)$ -plane of the dominant mode properties for an infinite number of equally-spaced plates positioned at a distance $d = 0.2$ (left) and $d = 0.5$ (right) from each other. . . . .	137
Figure 6.1: Heaving flexible wing in a steady axial flow. The heaving motion of amplitude $A$ is imposed at the leading edge and vortices are shed from the trailing edge. . . . .	144
Figure 6.2: Frequency spectrum and time evolution of the trailing-edge absolute vertical displacement for $\mu = 2$ , $\varepsilon = 0.05$ and $\bar{f} = 5/2\pi$ above and below the fluttering instability threshold. . . . .	151
Figure 6.3: Evolution of the normalized mean thrust, normalized power input and propulsive efficiency with $\eta$ for a flapping wing of mass ratio $\mu = 0.2$ and various flapping amplitude and frequency. . . . .	153
Figure 6.4: Streamlines of the flow over the flapping wing and vortex wake structure for $\mu = 0.2$ , $\varepsilon = 0.1$ and $\bar{f} = 5/2\pi$ (top) in the rigid case, (center) at the maximum of thrust production and (bottom) at the drag-thrust transition. . . . .	155
Figure 6.5: Characteristics of the reversed Von-Kármán street behind the flapping wing. $\Gamma_w$ is the amplitude of the wake vortices, $a$ the wavelength and $b$ the width of the vortex street. . . . .	157
Figure 6.6: Induced wake vortices velocity $\mathcal{V}$ behind the flapping wing for $\mu = 0.2$ , $\varepsilon = 0.1$ and $\bar{f} = 5/2\pi$ and comparison to the theoretical prediction for an infinite reversed Von Kármán vortex street (Lamb, 1932). . . . .	158
Figure 6.7: Mean thrust $\langle \mathcal{T} \rangle$ produced by the flapping wing for $\mu = 0.2$ , $\varepsilon = 0.1$ and $\bar{f} = 5/2\pi$ , and comparison to the theoretical prediction of Von Kármán. . . . .	160
Figure 6.8: Evolution of the normalized mean thrust $\langle \mathcal{T} \rangle$ , trailing-edge flapping amplitude $\mathcal{D}$ , vortex wake intensity $\Gamma_w$ and induced velocity $\mathcal{V}$ with the rigidity $\eta$ , for $\mu = 0.2$ , $\varepsilon = 0.1$ and $\bar{f} = 5/2\pi$ . . . . .	161
Figure 6.9: Evolution of the normalized trailing-edge flapping amplitude $\mathcal{D}$ with $\sqrt{\eta/\mu}$ for $\varepsilon = 0.05$ , $\bar{f} = 5/2\pi$ and for $\mu = 0.2$ and $\mu = 2$ . . . . .	163
Figure 6.10: Influence of the forcing amplitude $\varepsilon$ on the position of the resonances in the trailing-edge flapping amplitude for $\mu = 0.2$ , $\varepsilon = 0.1$ and $\bar{f} = 5/2\pi$ . . . . .	164

Figure 6.11: (a) Comparison between the absolute flapping amplitude $\mathcal{D}$ and relative flapping amplitude $\mathcal{D}^*$ at the trailing edge, for $\mu = 0.2$ . (b) Phase difference between the leading-edge and trailing-edge motions. . . . .	165
Figure 6.12: Position of the resonances in the $(\eta, \bar{f})$ -plane and structure of the corresponding mode for $\varepsilon = 0.01$ and (a) $\mu = 0.2$ or (b) $\mu = 2$ , and comparison to the prediction of the linear stability analysis of Appendix A . . . . .	167
Figure 6.13: Evolution of the mode shape with $\eta$ for $\mu = 0.2$ , $\varepsilon = 0.1$ and $\bar{f} = 5/2\pi$ . . . . .	169
Figure A.1: Critical stability curve obtained with the VS linear stability analysis method for a single flexible plate clamped at its leading edge and placed in a uniform axial flow. . . . .	189
Figure D.1: Evolution of (a) the mean thrust, (b) flapping efficiency and (c) trailing edge absolute flapping amplitude with wing rigidity for increasing values of the material damping coefficient. . . . .	198

## ACKNOWLEDGMENTS

Many people have helped me during my time at UCSD and I would like to acknowledge their support here. First and foremost, I would like to thank my fiancée Marissa, for her support and understanding from the time I applied to graduate school to this day. Together, we shared the daily succession of satisfaction and frustration of our graduate student lives, and she is always here to listen to me, encourage me and remind me what is most important in life. Without her help, I probably would not be here today.

I would also like to thank my parents, Béatrice and Patrick, and my brothers, Laurent and Stéphane, for their continuous encouragement and affection throughout the years even after I moved to the other side of the world.

I would like to thank my research advisor, Stefan Llewellyn Smith, for his support and advice from our first meeting at Ecole Normale Supérieure in Paris throughout the four years of my PhD. He offered his guidance and encouragement when I needed them the most, while at the same time teaching me to be an independent scientist. I would also like to extend my gratitude to Eric Lauga for many helpful conversations over the last couple of years, for his valuable feedback on my work and his insight on the international academic world and for making me discover low-Reynolds number locomotion.

I am also grateful to my other doctoral committee members for accepting to follow the progression of my work and offer precious comments and advice on the direction of my research. I would like to thank Paul Linden from whom I learned a lot about environmental flows and the peer-reviewed scientific publishing process, Bill Young for several helpful discussions on conservation laws in point vortex models and Qiang Zhu for his valuable expertise on solid dynamics and fish swimming. I would like to extend my gratitude to Glenn Ierley whose availability and helpful suggestions on spectral methods were much appreciated.

I would like to thank Laurent Jacquin and Patrick Huerre for their encour-

agement and guidance, while at Ecole polytechnique and, later on, when applying for graduate school, as well as Marie-Solange Tissier and Ecole des Mines de Paris for their mentoring and support.

I would finally like to thank all my friends, here in San Diego and back in France, for their support and all that we have shared.

I would like to acknowledge the generous support of Joan and Irwin Jacobs through the Jacobs Graduate Fellowship. The research presented in this dissertation was also supported by the National Science Foundation (award CTS-0133978) and the Human Frontier Science Program (Research Grant RGY 0073/2005).

Chapter 2 and Chapter 3, in part, have been published in *Theoretical and Computational Fluid Dynamics*, “An unsteady point vortex method for coupled fluid-solid problems” by S. Michelin and S. G. Llewellyn Smith, 2009, **23**, 127–153, (Springer), doi:10.1007/S00162-009-0096-7. The dissertation author was the primary investigator and author of this material.

Some material drawn from Chapter 3 and Chapter 4 has been accepted for publication in *Theoretical and Computational Fluid Dynamics*, “Falling cards and flapping flags: understanding fluid-solid interactions using an unsteady point vortex method” by S. Michelin and S. G. Llewellyn Smith, 2009 (Springer), doi: 10.1007/S00162-009-0117-6. The dissertation author was the primary investigator and author of this material.

Chapter 4, in part, has been published in the *Journal of Fluid Mechanics*, “Vortex shedding model of a flapping flag” by S. Michelin, S. G. Llewellyn Smith and B. J. Glover, 2008, **617**, 1–10 (Cambridge University Press), doi: 10.1017/S0022112008004321. The dissertation author was the primary investigator and author of this material.

Chapter 5, in part, has been accepted for publication in the *Journal of Fluids and Structures*, “Linear stability analysis of coupled parallel flexible plates in an axial flow” by S. Michelin and S. G. Llewellyn Smith (Elsevier Science), doi:10.1016/j.jfluidstructs.2009.06.002. The dissertation author was the primary

investigator and author of this material.

Chapter 6, in part, has been published in *Physics of Fluids*, “Resonance and propulsive efficiency of a heaving flexible membrane” by S. Michelin and S. G. Llewellyn Smith, 2009, **21** (7), 071902, (American Institute of Physics), doi: 10.1063/1.3177356. The dissertation author was the primary investigator and author of this material.

## VITA

2002	Diplôme d'ingénieur, Ecole polytechnique, France
2003–2004	Research Scholar, Scripps Institution of Oceanography, University of California, San Diego
2005	Corps des Mines, Ecole des Mines de Paris, France
2005–2009	Research Assistant, Dept. of Mechanical and Aerospace Engineering, University of California, San Diego.
2009	Ph.D., Engineering Sciences Dept. of Mechanical and Aerospace Engineering, University of California, San Diego.

## PUBLICATIONS

- S. Michelin** and E. Lauga (2009). The long-time dynamics of two hydrodynamically coupled swimming cells. *Bull. Math. Biol.*, submitted.
- S. Michelin** and S.G. Llewellyn Smith (2009). Linear stability analysis of coupled parallel flexible plates in an axial flow, doi:10.1016/j.jfluidstructs.2009.06.002. *J. Fluids Struct.* (in press).
- S. Michelin** and S.G. Llewellyn Smith (2009). Falling cards and flapping flags: understanding fluid-solid interactions using an unsteady point vortex method, doi:10.1007/S00162-009-0117-6. *Theor. Comput. Fluid Dyn.* (in press).
- S. Michelin** and S.G. Llewellyn Smith (2009). Resonance and propulsive efficiency of a heaving flexible membrane, doi:10.1063/1.3177356. *Phys. Fluids*, **21**, 071902.
- S. Michelin** and S.G. Llewellyn Smith (2009). An unsteady point vortex method for coupled fluid solid problems, doi:10.1007/S00162-009-0096-7. *Theor. Comput. Fluid Dyn.*, **23**, 127–153.
- S. Michelin**, S.G. Llewellyn Smith, and B.J. Glover (2008). Vortex shedding model of a flapping flag, doi:10.1017/S0022112008004321. *J. Fluid Mech.*, **617**, 1–10.
- S.G. Llewellyn Smith, **S. Michelin**, and D.G. Crowdy (2008). The dipolar field of rotating bodies, doi:10.1017/S0022112008001857. *J. Fluid Mech.*, **607**, 109–118.
- D. Sipp, D. Fabre, **S. Michelin**, and L. Jacquin (2005). Stability of a vortex with a heavy core, doi:10.1017/S0022112004003143. *J. Fluid Mech.*, **526**, 67–76.

## SELECTED PRESENTATIONS

S. Michelin and S. G. Llewellyn Smith, 2009: Flapping of flexible membranes in high- $Re$  flows and application to locomotion, *Fluid & Elasticity 2009*, Carry-le-Rouet, France

S. Michelin and S. G. Llewellyn Smith, 2008: A vortex shedding model of a flapping membrane, *61st Annual Meeting of the American Physical Society - Division of Fluid Dynamics*, San Antonio, Texas.

S. Michelin and S.G. Llewellyn Smith, 2008: Falling, flapping, flying, swimming,...: understanding fluid-solid interactions using an unsteady point vortex model, *IUTAM Symposium: 150 years of vortex dynamics*, Copenhagen, Denmark.

S. Michelin and S.G. Llewellyn Smith, 2007: Flying, swimming, falling,...: fluid-solid interactions with vortex shedding, *60th Annual Meeting of the American Physical Society - Division of Fluid Dynamics*, Salt Lake City, Utah.

S. Michelin and S.G. Llewellyn Smith, 2007: Application of point vortices model to Maxwell's problem, *3rd European SCAT Workshop and Summerschool, "Vortices and Vortex Sheets: theorics, numerics and applications"*, Porquerolles, France.

S. Michelin and S.G. Llewellyn Smith, 2006: Vortex shedding model and Maxwell's problem, *59th Annual Meeting of the American Physical Society - Division of Fluid Dynamics*, Tampa, Florida.

## FIELDS OF STUDY

Major Field: Fluid mechanics

**Fluid-solid interactions:**

Professor Stefan G. Llewellyn Smith

**Vortex dynamics and complex analysis:**

Professor Stefan G. Llewellyn Smith

**Hydrodynamic interaction between low- $Re$  swimmers:**

Professor Eric Lauga

## ABSTRACT OF THE DISSERTATION

Falling, flapping, flying, swimming,...:  
high- $Re$  fluid-solid interactions with vortex shedding

by

Sébastien Honoré Roland Michelin

Doctor of Philosophy in Engineering Sciences (Aerospace Engineering)

University of California, San Diego, 2009

Professor Stefan G. Llewellyn Smith, Chair

The coupling between the motion of a solid body and the dynamics of the surrounding flow is essential to the understanding of a large number of engineering and physical problems, from the stability of a slender structure exposed to the wind to the locomotion of insects, birds and fishes. Because of the strong coupling on a moving boundary of the equations for the solid and fluid, the simulation of such problems is computationally challenging and expensive. This justifies the development of simplified models for the fluid-solid interactions to study their physical properties and behavior.

This dissertation proposes a reduced-order model for the interaction of a sharp-edged solid body with a strongly unsteady high Reynolds number flow. In such a case, viscous forces in the fluid are often negligible compared to the fluid inertia or the pressure forces, and the thin boundary layers separate from the solid at the edges, leading to the shedding of large and persistent vortices in the

solid's wake. A general two-dimensional framework is presented based on complex potential flow theory. The formation of the solid's vortical wake is accounted for by the shedding of point vortices with unsteady intensity from the solid's sharp edges, and the fluid-solid problem is reformulated exclusively as a solid-vortex interaction problem.

In the case of a rigid solid body, the coupled problem is shown to reduce to a set of non-linear ordinary differential equations. This model is used to study the effect of vortex shedding on the stability of falling objects.

The solid-vortex model is then generalized to study the fluttering instability and non-linear flapping dynamics of flexible plates or flags. The fluttering instability and resulting flapping motion result from the competing effects of the fluid forcing and of the solid's flexural rigidity and inertia. Finally, the solid-vortex model is applied to the study of the fundamental effect of bending rigidity on the flapping performance of flapping appendages such as insect wings or fish fins.

# 1

## Introduction and thesis outline

In comparison with the vast literature available on the dynamics of solids in vacuum or the motion of fluids in infinite or fixed-wall domains, research at the interface of these two subjects on the coupled dynamics of fluids and solids is rather recent. Such problems are concerned with the coupled motion of a solid and the surrounding fluid or the coupled motion of an enclosed flow and its boundaries. As will be pointed out in the next Chapter, the understanding of such situations can be particularly difficult when the dynamics are strongly coupled — when it is not possible for example to neglect the motion of the solid boundary when solving for the fluid flow, or when the fluid effect on the solid’s motion cannot be understood without solving in detail for the fluid motion.

Such coupled situations are nonetheless present in almost every engineering domain. Only a few examples are listed below. The instability resulting from the interaction between the wind forcing and the structural response of the Tacoma Narrows bridge that eventually led to its collapse is a dramatic famous example of the importance of fluid-solid interactions in the design of slender structures like bridges. Winds also interact with vegetation and influence the development of plants and their individual or collective behavior (de Langre, 2008). The dynamics of flexible pipes conveying fluids is another classical example of a strongly

coupled fluid-structure interaction problem that can lead to divergence or flutter instabilities of the whole system also known respectively as the “garden-hose” and “fire-hose” instabilities (Paidoussis, 1998). In blood circulation, the elasticity of the arterial walls is an important element in the regulation of the pulsatile blood flows throughout the whole organism, and a weakening of these elastic properties can be responsible for the formation of aneurysms (see for example Lasheras, 2007). Fluid-solid interactions are also an essential element of locomotion in fluids for biological species such as birds, insects, fishes and bacteria (Childress, 1981; Triantafyllou et al., 2000; Wang, 2005), but also for man-made applications such as aircrafts and helicopters.

The coupling between the fluid and solid motions, though always present, can have a more or less important effect on the resulting dynamics of the solid, depending on the relative order of magnitudes of the fluid and solid properties. For example, if  $T_{el}$ ,  $T_{solid}$  and  $T_{fluid}$  represent respectively the characteristic time-scales associated with the solid’s internal dynamics (e.g. periods of elastic waves on the body surface), the solid’s motion (e.g. the flapping period of an insect wing) and the fluid’s motion (e.g. a typical time-scale of the flow far from the body or relaxation time of the flow dynamics due to a change in the position of the boundaries), then different regimes can be identified (de Langre, 2001). If  $T_{el} \ll \{T_{fluid}, T_{solid}\}$ , then the effect of flexibility can probably be neglected to a good approximation, as the deformation waves along the solid body propagates almost instantaneously compared to the outside flow time scale. The solid can then be treated as rigid. If  $T_{fluid} \gg T_{solid}$ , then the rate of change in the flow at infinity can be neglected compared to the rate of change induced by the solid’s motion. On the other hand, if  $T_{fluid} \ll T_{solid}$ , then the fluid flow adapts almost instantaneously to the displacement of the solid boundary and quasi-steady approximations for the fluid forces using drag coefficients might be used instead of solving for the full fluid dynamics.

In strongly coupled fluid-solid interactions, the fluid and solid responses

occur on similar time scales. Then steady results for the fluid forces on the solid derived in steady or quasi-steady settings are in general no longer valid. This dissertation focuses on such configurations, in which the motions of the solid and of the surrounding fluid are strongly coupled. The theoretical analysis of such configurations is challenging because of the unsteadiness of the coupled motions and the nonlinearities of the problem due to the large displacement of the solid boundaries. The computational simulation of such fluid-solid interactions is also difficult, partly for the same reasons.

This dissertation presents the study of several fluid-solid interaction problems using a reduced-order model for the flow dynamics. Such an approach falls between the full numerical simulation and the empirical application of steady results such as lift and drag coefficients to unsteady cases. It avoids the computational cost and complexity of the former while providing a more rigorous approach to the fluid dynamics than the latter. Using particular properties of the flow field, when viscous effects are limited to the formation of strong vortices from the solid's edges, we study the motion of both rigid and flexible bodies. Our interest lies both in the stability of the fluid-solid system and the nonlinear dynamics resulting from potential instabilities.

The dissertation is organized as follows. In Chapter 2, an overview of high- $Re$  fluid-solid interaction problems is presented, together with computational challenges related to the strong coupling of the fluid and solid motions. Some numerical techniques that have been developed for these strongly coupled problems are also briefly introduced. Examples of reduced-order models for such problems are presented. Such models are particularly useful to obtain qualitative and quantitative information on the main physical phenomena involved, but the assumptions of each model must be carefully studied with respect to the particular regime considered. Here, we focus on two-dimensional fluid-solid interaction for which the flow is characterized by the shedding of vortex structures from sharp edges on the solid body. An inviscid model is presented based on a representation of the wake

of the solid using point vortices with unsteady intensity.

Chapter 3 then applies this reduced-order model to the motion of a rigid body. Taking advantage of the time-independent solid geometry and using the unsteady point vortex model, the fluid-solid problem is reduced to a set of nonlinear ordinary differential equations (ODE) for the solid and the vortices. This framework is then used to study the experimentally-observed destabilizing effect of vorticity shedding on the broadside-on fall of a thin card.

The remainder of the dissertation is concerned with deformable elastic objects. The fluid-solid interaction becomes more complex as the number of degrees of freedom in the body motion becomes large or infinite. One now needs to solve not only for the center of mass position and general orientation of the body, but also for its internal dynamics. Chapters 4 through 6 consider flexible structures with internal bending rigidity and infinitely small thickness (referred to as plates, sheets or flags), and placed in parallel flows (or equivalently, pulled at a constant velocity through a fluid at rest). In Chapter 4, the flag is clamped at its leading edge and can move passively under the combined actions of the flow and of its internal elasticity. The fluttering instability leading to the flapping mechanism of flexible flags is investigated, as well as the characteristics of the flapping motion. The case of one flag is presented in detail, and some insight on the coupled dynamics of two parallel plates is presented, particularly the nature of the observed coupled modes. The flow is described using the point vortex approach presented in Chapter 2. The nonlinear description of the solid dynamics allows us to consider large displacements of the sheets, not only their linear stability.

Chapter 5 then proposes a theoretical investigation of the linear stability of plate assemblies. The focus lies on small-amplitude motions and on the linear stability of an array of  $Q$  parallel plates clamped at their leading edge in a parallel flow. The nature of the coupled modes and the influence on the overall stability of the relative distance is investigated in detail for two and three plates and some general results are drawn in the case of  $Q$  plates.

In Chapter 6, the effect of solid flexibility on the propulsive performance of a flapping apparatus is investigated, by generalizing the model of Chapter 4 to the case of a heaving flexible sheet. The sheet is here a representation of a two-dimensional section of an insect wing. At the leading edge, the motion and orientation is imposed by the operator (the insect), and the remainder of the wing reacts passively to this forcing, under the influence of its inertia, of its rigidity and of the flow forcing.

Finally, Chapter 7 summarizes the main conclusions of the present dissertation on both the point vortex method and the particular fluid-solid problems considered throughout this work. The applicability and limits of the point vortex model are discussed as well as possible extensions of this model to other problems where its significantly-reduced computational cost and low order representation of the solid's wake makes it attractive.

## 2

# A reduced-order model for high- $Re$ fluid-solid interactions

## 2.1 Introduction and motivation

Complex interaction phenomena can arise from the coupled motions of a solid body and a surrounding fluid, such as the trajectories of falling tree leaves and paper cards (Willmarth et al., 1964; Smith, 1971; Field et al., 1997; Belmonte et al., 1998; Mahadevan et al., 1999; Andersen et al., 2005b) or the wind-induced flapping of flags (Zhang et al., 2000; Watanabe et al., 2002b; Balint and Lucey, 2005; Shelley et al., 2005; Eloy et al., 2008).

In both cases, the motion of the solid is significantly modified by the presence of a surrounding flow, and its motion can only be understood by solving for the fluid and solid dynamics together. For example, solving the equation for the falling paper card without including any fluid effect would lead to the classical result of Newtonian mechanics that the card falls along a straight vertical line without any rotation and with velocity increasing linearly in time. This behavior would be strictly independent of the mass of the card. We know from our daily experience of falling tree leaves that this prediction is incorrect and the effect of the fluid must be taken into account. For a falling sphere, the presence of the fluid could be included to a good approximation, and without solving for the fluid motion explicitly, by including a linear or quadratic drag force. Such a model

based solely on viscous drag forces could be adapted to the geometry of a card by changing the drag coefficient. However, it is unable to reproduce such complex trajectories as tumbling and fluttering regimes. In particular, for a thin solid, a more detailed description of the unsteady fluid motion and of its coupling to the solid's is necessary. This very simple physical situation, sometimes referred to as Maxwell's problem (Maxwell, 1854), illustrates the complexity of representing properly fluid-solid interactions. In Chapter 3, we revisit this problem using the particular reduced-order method presented at the end of this Chapter.

The Reynolds number, defined as  $Re = UL/\nu$ , with  $U$  the characteristic flow velocity,  $L$  the typical dimension of the solid body and  $\nu$  the kinematic viscosity of the fluid, is a measure of the relative importance of inertial and viscous forces in the flow. In both the falling card and flapping flag problems,  $Re$  is large enough for viscous effects to be confined in thin boundary layers close to the surface of the solid.

High- $Re$  fluid-solid interactions are essential for aerial and aquatic biological locomotion: birds, insects and fishes flap their wings and fins to create around them a flow able to generate the thrust and lift forces necessary to their motion in their environment (Triantafyllou et al., 2000; Wang, 2005). Understanding the physical mechanisms involved in such locomotion schemes is an ongoing challenge from both a biophysical and an engineering point of view. If the dynamics of a gliding bird can resemble the fixed-wing aerodynamics and lift generation at the core of aircraft design, most other bird flight maneuvers such as take-off and landing, and flapping flight techniques used by insects belong to a completely different range of physics, as they are fundamentally unsteady (Childress, 1981). In the same way, fishes use strongly unsteady stroke patterns to create their swimming motion, and differ significantly from man-made underwater vehicles whose propulsion and maneuvering are based, like an aircraft's, on the physics of steady flows over profiled elements (rudders and propeller blades). As engineers have recently dedicated a lot of research efforts on the development of new and more energy-

efficient propulsion schemes, biomimetic designs seem particularly attractive and require a better understanding of the physics involved in such locomotion modes. The interest for insect flight mechanisms has also been greatly enhanced in the recent years by the development of unmanned micro-aerial vehicles, whose significantly reduced weight compared to a traditional aircraft makes them more suitable for unsteady flapping flight.

Much remains to be understood on the dynamics of a single fish or insect in an otherwise uniform flow, but also on hydrodynamical mechanisms leading to potential reduction in the energy consumption. Some fish species have been observed to take advantage of the vortex street created by the flow over obstacle or other fishes to maintain a stationary position at lower energy cost (Liao et al., 2003a,b). Recent experimental (Beal et al., 2006) and numerical studies (Eldredge and Pisani, 2008) have shown that a fish can swim passively upstream in the vortex street created by a cylinder.

Several other experimental studies have emphasized the possibility of generating locomotion from passive fluid-solid interactions. In an experiment by Vandenberghe et al. (2004, 2006), a purely vertical heaving motion of a horizontal plate was observed to generate a transverse motion. This symmetry breaking was investigated numerically by Alben and Shelley (2005). Childress et al. (2006) considered a passive artificial paper bug able to hover in an oscillating air column. We understand here by passive locomotion a situation in which the motion of the solid body (or the propulsive force) in a particular direction results from the interaction with the fluid – a forcing can be applied by an operator but in another direction (e.g. vertical heaving motion generating a horizontal velocity).

The present dissertation focuses on such high- $Re$  fluid-solid problems, where viscous effects are limited to thin boundary layers around the solid and most of the fluid action on the solid is the result of pressure forces created by the highly unsteady flow. Several particular applications will be discussed: the fall of a rigid paper card (Chapter 3), the stability and flapping of elastic solids

exposed to parallel flows (Chapters 4 and 5) and propulsion using a flexible wing (Chapter 6). The last topic is closely related to the biological locomotion schemes used by insects or fishes. The different techniques and approaches presented in this dissertation are however not limited to these particular situations, and could be applied to other fluid-solid interaction problems.

## 2.2 Numerical simulations of high-*Re* fluid-solid interactions

The complexity of the flows involved in the examples of fluid-solid interactions presented above excludes a purely theoretical approach. The numerical simulation of the coupled problem provides valuable insight on the structure of the flow, the different forces applied on the solid and many more physical quantities that are not always accessible from experiments. Several challenges however arise from the coupling of the solid's and fluid's dynamics and we present them in this section, as well as some example of computational techniques used to overcome these difficulties.

### 2.2.1 General form of the equations of fluid-solid interaction

In all of the previously mentioned applications, the fluid motion can be described satisfyingly by the incompressible Navier–Stokes equations for a Newtonian fluid, which can be written, once non-dimensionalized using the fluid density  $\rho$ , the typical flow velocity  $U$  and length scale  $L$  as

$$\frac{\partial \mathbf{u}}{\partial t} + (\mathbf{u} \cdot \nabla) \mathbf{u} = \nabla \cdot \boldsymbol{\sigma}, \quad \text{with } \boldsymbol{\sigma} = -p\mathbf{I} + \frac{1}{Re} (\nabla \mathbf{u} + \nabla \mathbf{u}^T), \quad (2.1)$$

$$\nabla \cdot \mathbf{u} = 0. \quad (2.2)$$

Here,  $\mathbf{u}$  and  $p$  are respectively the velocity and pressure field in the flow, and  $\boldsymbol{\sigma}$  is the stress tensor. On the solid boundary  $\mathcal{S}$ , the flow velocity satisfies the no-slip

boundary condition

$$\mathbf{u}(\mathbf{x}) = \mathbf{u}_S(\mathbf{x}) \quad \forall \mathbf{x} \in \mathcal{S}. \quad (2.3)$$

In the inviscid limit ( $Re = \infty$ ), the viscous contribution to the stress tensor disappears and the no-slip boundary conditions must be replaced by the continuity of normal velocity on the solid's surface

$$\mathbf{u}(\mathbf{x}) \cdot \mathbf{n} = \mathbf{u}_S(\mathbf{x}) \cdot \mathbf{n}(\mathbf{x}) \quad \forall \mathbf{x} \in \mathcal{S}, \quad (2.4)$$

with  $\mathbf{n}$  the local normal to the solid boundary. The equations of motion for the fluid simplify then into the Euler equations

$$\frac{\partial \mathbf{u}}{\partial t} + (\mathbf{u} \cdot \nabla) \mathbf{u} = -\nabla p, \quad \nabla \cdot \mathbf{u} = 0. \quad (2.5)$$

The solid's dynamics is described using Newton's law, which can be written as

$$\frac{d\mathbf{p}_S}{dt} = \int_{\mathcal{S}} (\boldsymbol{\sigma} \cdot \mathbf{n}) dS + \mathbf{f}, \quad (2.6)$$

$$\frac{d\mathbf{L}_S}{dt} = \int_{\mathcal{S}} \mathbf{x} \times (\boldsymbol{\sigma} \cdot \mathbf{n}) dS + \boldsymbol{\mathcal{T}}, \quad (2.7)$$

with  $\mathbf{p}_S$  and  $\mathbf{L}_S$  the total linear and angular momentum of the solid,  $\mathbf{n}$  the unit normal pointing into the fluid and  $\mathbf{f}$  and  $\boldsymbol{\mathcal{T}}$  external force and torque on the solid (e.g. gravity (Chapter 3) or forcing by the operator (Chapter 6)). These equations are valid for both rigid and flexible solid bodies. In the case of a flexible solid, additional information on the internal dynamics must be given to fully describe the solid's deformation (see for example Chapter 4).

In the case of a rigid body,  $\mathbf{p}_S$  and  $\mathbf{L}_S$  are linear functions of the center of mass velocity  $\mathbf{U}$  and rotation rate  $\boldsymbol{\Omega}$  of the solid body

$$\begin{pmatrix} \mathbf{p}_S \\ \mathbf{L}_S \end{pmatrix} = \mathbf{M} \cdot \begin{pmatrix} \mathbf{U} \\ \boldsymbol{\Omega} \end{pmatrix}, \quad (2.8)$$

with  $\mathbf{M}$  the inertia matrix. The boundary condition (2.3) then becomes

$$\mathbf{u}(\mathbf{x}) = \mathbf{U} + \boldsymbol{\Omega} \times (\mathbf{x} - \mathbf{x}_C) \quad \forall \mathbf{x} \in \mathcal{S}, \quad (2.9)$$

with  $\mathbf{x}_C$  the position of the solid's center of mass.

### 2.2.2 Numerical simulation of fully-coupled fluid-solid interactions and its challenges

In the case of a rigid body, the motion of the solid is described by a set of Ordinary Differential Equations (ODE) for the solid's position and orientation (2.6)–(2.7). The fluid motion is on the other hand described by a system of Partial Differential Equations (PDE) for the fluid velocity and pressure (2.1)–(2.2). This difference in the nature of the equations generally requires the use of parallel coupled solvers for the fluid and solid dynamics. The main difficulty in the simulation of fully-coupled fluid-solid interactions – where the motions of the fluid and solid are not prescribed but are the result of their coupled dynamics – resides in the positioning of the grid used for the fluid solver and the numerical implementation of the coupling between the fluid and solid solvers. This coupling appears through the kinematic boundary condition (2.3) or (2.4) and the forcing by the fluid on the right-hand side of the solid's equation. Both couplings occur on the solid's boundary, whose position is itself the result of the coupled dynamics. The situation is even more complex in the case of a flexible body that can deform under the action of the flow, as the solid's shape is also the result of the coupled dynamics of the fluid and solid.

The form of the coupling makes the use of explicit schemes attractive because implicit schemes require solving iteratively for the solid's position and the pressure and velocity fields in the fluid simultaneously. However, the coupling of the solid and fluid dynamics introduces some new stability constraints on the time-step used that were not present for example in the computation of the flow past a solid body whose motion is prescribed. The time-step required for stability of the coupled simulation is much smaller than the time-step required for high-accuracy, making the use of efficient implicit formulations an attractive alternative (see for example Alben, 2008b).

### 2.2.3 An overview of commonly-used techniques

Two approaches are commonly used to overcome these difficulties: coupled fluid-solid solvers and immersed boundary methods. These two general techniques differ mostly in the choice of the grid for the fluid domain.

In the first approach, the solid and fluid motions are treated by two coupled solvers. This approach is well illustrated by the work of Connell and Yue (2007) on a Fluid-Structure Direct Simulation (FSDS) method to solve for the motion of a flapping flag. The fluid dynamics is solved by discretizing the Navier–Stokes and continuity equations (2.1)–(2.2) onto a grid fitted to the deformable solid body. The position of the solid body is obtained by discretizing the equations for an elastic and infinitesimally thin membrane. The use of two separate solvers requires to solve iteratively for the velocity and pressure fields in the flow together with iterative solving for the position of the solid, and every update in the solid’s position requires also to update the grid used for the fluid. Stability issues due to added mass in that iterative process must be treated carefully (see for example Connell and Yue, 2007). However, having two independent solvers also allows for independent development and validations (see Connell, 2006, for more details).

In the case of a rigid body, there is no need to redefine the grid for the fluid domain at each modification of the solid’s geometry. Instead, the equations for the flow velocity and pressure can be solved in a co-moving frame in which the solid boundary is fixed. The formulation is particularly simplified in the two-dimensional case of a cylindrical body with elliptic cross-section (see for example Huang, 2001; Wang, 2000a,b; Pesavento and Wang, 2004; Andersen et al., 2005b; Alben, 2008b), but the approach is, in theory, applicable to any body shape.

In the second approach, the Eulerian form of the fluid equations (2.1)–(2.2) is solved on a fixed grid, defined independently from the position of the solid body, whose motion is solved in a Lagrangian fashion (Peskin, 1972; Mittal and Iac-

carino, 2005). These methods are referred to as Immersed Boundary Methods. The continuous form of equations (2.1)–(2.2) is solved on this grid and the effect of the solid body is introduced in the form of a distribution of point forces that transmits to the fluid the internal stresses in the solid, thereby enforcing implicitly the no-slip boundary condition (2.3). This method was initially introduced by Peskin (1972, 1977) in the study of blood flow through a deformable heart valve and was recently used in the study of falling bodies (Mittal et al., 2004) and of filaments flapping in soap-films (Zhu and Peskin, 2002, 2003). The Eulerian–Lagrangian formulation is particularly well-suited for problems with moving boundaries as it avoids having to recreate a mesh every time the geometry or position of the solid boundary is modified (Mittal and Iaccarino, 2005). Defining a fixed grid independent of the geometry of the domain boundary also permits the use of Cartesian grids and efficient computational methods (e.g. spectral methods). Immersed boundary methods are also well-adapted to problems with an elastic body as the internal forces in the solid can be stated explicitly. A purely rigid solid requires more attention as stability problems arise (the characteristic time-scale of the restoring force tends to zero).

An alternative approach to deal with rigid body problems has been proposed using a volume penalization method (Angot et al., 1999). The Eulerian–Lagrangian approach remains the same and the grid used for the fluid flow is fixed and does not depend on the body position. The additional forcing in the fluid equations is distributed not only on the surface of the fluid-solid boundary but in the whole solid body. The physical idea behind the volume penalization method is to represent the solid body as a porous medium, with a permeability that tends to zero. This approach was recently coupled to the equations of motion of a solid body to study the fall of a card and a particular insect flapping scheme (Kolomenskiy and Schneider, 2008; Kolomenskiy et al., 2008).

One of the main limitations of such Eulerian–Lagrangian formulations resides in their computational cost as  $Re$  is increased in order to resolve properly

the boundary layers whose thickness decreases with  $Re$  (e.g. like  $Re^{-1/2}$  for laminar boundary layers). The grid should be thin enough to have several points in the boundary layer, but since the grid is generated independently from the body position, this generally requires a larger number of points than when using a structured grid fitted to the body shape. A trade-off is then necessary between the cost of re-meshing the fluid domain after each change in the body shape and the cost associated with an increased number of grid points.

### **2.3 Reduced-order model for sharp-edged solid bodies**

Although a number of methods are available to compute the coupled motion of a solid body and the surrounding flow, the computational cost of such techniques is generally high, even for two-dimensional problems. This justifies a parallel effort to obtain reduced-order models of such interaction problems. Such models are not intended to replace full numerical simulations but instead reproduce the main physical features at a reduced computational cost. Hence a first physical assessment of the problem's physics can be obtained. Such reduced-order models can also be used as a surrogate for numerical simulations where the computation cost of such simulation is prohibitive (e.g. optimization problems). The point vortex method presented in this dissertation is such a model. Before describing its physical basis and mathematical formulation, a brief review of other reduced order models is presented. These fall into two different categories, depending on whether they provide an empirical formulation for the fluid forces or a simplified representation of the fluid flow from which fluid forces can be computed exactly. The former includes models for the fluid drag in terms of a constant drag coefficient. The latter includes models such as added-mass theory or the point vortex method presented in this dissertation: a simplified representation of the flow is adopted (e.g. purely irrotational flow or irrotational flow with vortex shedding satisfying

the regularity condition) from which the forces on the solid body are computed exactly.

### 2.3.1 Added mass

In the limit of zero viscosity, if the flow is started from rest, it remains irrotational at all time, and the velocity field  $\mathbf{u}$  can be obtained from a flow potential  $\phi$  that satisfies the following Laplace problem:

$$\begin{aligned}\nabla^2\phi &= 0 \quad \text{in the fluid domain,} \\ \frac{\partial\phi}{\partial n} &= \mathbf{u}_S \cdot \mathbf{n} \quad \text{on the body,} \\ \nabla\phi &\rightarrow \mathbf{U}_\infty \quad \text{at infinity.}\end{aligned}\tag{2.10}$$

In the case of a rigid solid body moving in a fluid at rest at infinity, the fluid-solid problem can be described using the inviscid theory developed by Kirchhoff (see Lamb, 1932, Chapter VI). The system (2.10) is linear in the boundary condition on the solid body. Using the boundary condition (2.9) for a rigid solid body, and defining the generalized velocity vector  $\mathbf{V}^T = (\mathbf{U}^{*T}, \boldsymbol{\Omega}^T)$ , where  $\mathbf{U}^*$  is the velocity vector of the center of mass referred instantaneously in the frame  $(\mathbf{e}_1, \mathbf{e}_2, \mathbf{e}_3)$  moving with the body, the flow potential is obtained as

$$\phi = \sum_{i=1}^6 V_i \phi_i,\tag{2.11}$$

with  $\phi_i$  satisfying the following problem:

$$\nabla^2\phi_i = 0 \quad \text{in the fluid domain}\tag{2.12}$$

$$\nabla\phi_i \rightarrow 0 \quad \text{at infinity}\tag{2.13}$$

$$\nabla\phi_i \cdot \mathbf{n} = \begin{cases} \mathbf{e}_i \cdot \mathbf{n} & (1 \leq i \leq 3) \\ \mathbf{e}_{i-3} \cdot (\mathbf{x} \times \mathbf{n}) & (4 \leq i \leq 6) \end{cases} \quad \text{on the solid body,}\tag{2.14}$$

Then the kinetic energy of the fluid may be expressed as

$$T = \frac{1}{2} \mathcal{M}_{ij} V_i V_j\tag{2.15}$$

with  $\mathcal{M}$  the symmetric added-mass tensor whose coefficients are determined from

$$\mathcal{M}_{ij} = \rho \int_S \phi_i \frac{\partial \phi_j}{\partial n} ds. \quad (2.16)$$

The total kinetic energy of the {fluid + solid} system is conserved, and one observes that the effect of the fluid is a non-isotropic added inertia. The force and torque on the solid body have components that can be obtained (in the same frame  $(\mathbf{e}_1, \mathbf{e}_2, \mathbf{e}_3)$  rigidly attached to the body) from Kirchhoff's theory (Lamb, 1932) as

$$F_j = -\mathcal{M}_{ij} \dot{U}_i - \varepsilon_{jkl} \mathcal{M}_{li} U_i \Omega_k, \quad (2.17)$$

$$T_j = -\mathcal{M}_{j+3,i} \dot{U}_i - \varepsilon_{jkl} \mathcal{M}_{l+3,i} U_i \Omega_k - \varepsilon_{jkl} \mathcal{M}_{li} U_k U_i, \quad (2.18)$$

with  $1 \leq i \leq 6$  and  $1 \leq j, k, l \leq 3$ .

A simple physical interpretation is provided by the example of a plate impulsively accelerated from rest. For an acceleration parallel to the plate, the motion can occur without any fluid displacement (the plate has zero thickness), and there is no resistance from the fluid (viscosity is absent here). On the other hand, if the plate is moved in the normal direction, a resistive force appears because some fluid needs to be moved from one side of the plate to the other to allow the displacement, thereby increasing the inertia of the system. The added mass coefficients therefore depend on the geometry of the solid. More examples of the computation of added mass coefficients can be found in Newman (1977). Note that, contrary to the physical inertia tensor of a solid, the added mass tensor can have non-diagonal terms coupling translation and rotation. As a result, for some non-symmetric bodies, a purely linear acceleration can generate a force orthogonal to the acceleration or a torque. The non-diagonal terms of  $\mathcal{M}$  are also associated with properties of the potential far from the body. A discussion of the vanishing of such dipolar terms in two-dimensional problems was presented in Llewellyn Smith et al. (2008).

The physical argument for added mass theory remains valid for a flexible body: an acceleration of the solid will encounter fluid resistance equivalent to an

added inertia as fluid needs to be pushed around the moving body. However, in the case of a flexible body, no such elegant formulation exists as the number of degrees of freedom in the solid deformation is not necessarily finite, and added mass depends on the instantaneous shape of the solid.

### 2.3.2 Quasi-steady empirical models

In some other special circumstances, the forces on a solid can be determined from the solid's motion without solving for the whole flow, for example, in some steady flow situations. The best-known such result is the Kutta-Joukowski lift theorem, that states that the lift on a two-dimensional airfoil moving horizontally at a velocity  $U$  in a fluid of density  $\rho$  with a circulation around the airfoil equal to  $\Gamma$  (this circulation is in general the result of the shedding of a starting vortex from the trailing edge of the airfoil, that has moved away from the wing) is equal to  $\rho U \Gamma$  (see for example Saffman, 1992).

Quasi-steady empirical models have been proposed to include additional fluid effects other than added inertia to better fit the description of a particular problem. For example, Tanabe and Kaneko (1994) proposed an empirical model for a falling card in which fluid forces are the superposition of three different contributions: added mass, viscous drag (with non isotropic drag coefficients to account for the different aspect ratios of the body considered) and a lift force similar to the result of the Kutta-Joukowski theorem. This theorem requires the knowledge of the circulation around the body, and Tanabe and Kaneko (1994) assume that  $\Gamma$  takes the steady state value obtained for a plate. However, such a result is only valid in steady flows and at small angle of attack, two assumptions that are clearly violated in the case of a falling card and this strongly limits the validity of such an approach (Mahadevan et al., 1995; Tanabe and Kaneko, 1995).

More recently, a similar model was proposed for a falling ellipse that allows the circulation to depend on more than just the angle of attack and the translation velocity, but also includes a contribution from the rotation and a cor-

rection to take into account stall effects at high angle of attack (Pesavento and Wang, 2004; Andersen et al., 2005a). The model relies on the determination of 6 non-dimensional coefficients that are expected to depend on the Reynolds number and can be computed to fit the result of direct numerical simulations. Such a model is an improvement compared to the added mass approach and the work of Tanabe and Kaneko (1994), but it still fails to include unsteady effects of the shedding of vorticity. Such effects are expected to be important in a large number of situations including the ones considered in this dissertation like the falling card problem or insect flapping flight.

### 2.3.3 Vortex shedding in fluid-solid interactions

In section 2.1, several applications of fluid-solid interactions with relatively high Reynolds number were presented. In all these applications, the flow is characterized by the presence of regions of concentrated vorticity (vortices). The vorticity is the result of the solid body's motion in the flow and is created in the boundary layers whose thickness is a decreasing function of  $Re$ . These boundary layers separate into free shear layers and roll up on themselves to produce these vortical structures. The separation and vortex shedding are even more pronounced when the solid body has a sharp edge (e.g. the trailing edge of a flapping wing). These vortices are essential elements of numerous fluid-solid interaction problems. The shedding of staggered rows of vortices in classical or reversed Von-Kármán streets is associated with the production of drag or thrust by a flapping body. Insects and fishes heavily rely on the formation of a vortex wake to create the lift and thrust forces necessary for their motion. The unsteady nature of this vortex shedding must be taken into account when describing the dynamics of the flow around the solid body.

Such features are not incorporated in an added mass approach where the flow is purely potential, and this omission can lead to significant modifications in the behavior of the solid body as will be discussed in more details in section

3.4.3. The unsteady effect of vortex shedding is in general also not included into the quasi-steady models discussed in section 2.3.2. The purpose of the inviscid vortex methods is to account for the shedding of vorticity from the solid in a more accurate manner, while still retaining a simplified representation of the flow by neglecting viscous forces.

### 2.3.4 Inviscid vortex methods

In the applications considered here, the viscous drag is in general much smaller than the pressure contributions to the fluid forces. Furthermore, it was previously reported on some test cases using direct numerical simulation, that above intermediate values of the Reynolds number ( $Re \sim 200\text{--}1000$ ) and for laminar flows, the fluid forces depend only weakly on  $Re$  (Wang, 2000a). A first approximation to the flow problem therefore consists in neglecting viscosity by considering an inviscid flow representation. However, even if it has a negligible effect on the fluid forces, viscosity is the critical element leading to the shedding of vorticity from the sharp edges of a solid body by separation of the thin boundary layers, as mentioned in the previous section. To be physically accurate, an inviscid representation should retain this information.

The distinction must be emphasized here between a purely inviscid approach (added mass) and an inviscid vortex method: in the former, all effects of viscosity are neglected. In the latter, the viscous contributions to the fluid forces on the solid are neglected and the slip boundary condition is applied (2.4), but the vortex shedding effect of viscosity is maintained by introducing manually vorticity singularities in the flow. The amount of vorticity as well as its initial location is however not arbitrary: the point vortices or vortex sheets must be started from the sharp edge of the solid body responsible for the shedding of vorticity. The presence of a sharp edge in potential flow leads to a velocity singularity in the flow velocity there. The intensity of the shed vorticity is determined by satisfying the regularity condition on the flow field at the shedding edge (also known as Kutta

condition), thereby guaranteeing that the flow is parallel to the corner’s tangent, as is the case for boundary layer separation in the real problem.

We focus here on two dimensional problems. These are in general a good approximation when the solid is close to cylindrical with a span much larger than the size of its cross-section (e.g. dragonfly wing). However, some purely three-dimensional effects will not be included in this theory, such as the wing-tip vortices responsible, for example, for an aircraft’s wake vortices. The exact effect of these wing-tip vortices on the performance of insect flapping flight is still debated. The two-dimensional assumption allows the use of the powerful tools of complex potential theory.

In inviscid vortex methods, the shedding of vorticity can be continuous or discrete. In the former case, at each time step of the simulation a new element of vorticity is created that is later on advected with the flow with a constant circulation. This method was introduced initially by Clements (1973). An equivalent formulation was proposed more recently for the flow past a rigid plate (Jones, 2003) and generalized to a flexible membrane or elastic sheet (Shukla and Eldredge, 2007; Alben and Shelley, 2008; Alben, 2009). The solid’s wake is then represented as a vortex sheet whose position is advected using the Birkhoff–Rott equation (see for example Saffman, 1992) and circulation acts as a Lagrangian tracer on the vortex sheet. The intensity of vorticity added to the sheet is determined by the regularity condition at the shedding edge.

The point vortex method used in this dissertation belongs to the discrete case and is described in more details in section 2.4. Instead of creating a new element of vorticity at each time step, the intensity of the last shed vortex is modified so as to satisfy continuously the regularity condition at the shedding edge. These point vortices with unsteady intensity (also known as Brown–Michael vortices (Brown and Michael, 1954)) are advected by the flow using a modified equation to enforce the conservation of momentum around the vortex and associated branch cut (see Rott, 1956, and section 2.4.4). The intensity of the vortices

varies monotonically in time to represent the irreversible nature of vortex roll-up (Graham, 1977; Cortelezzi and Leonard, 1993; Keller, 1998). This shedding criterion is presented in more details in section 2.4.2. This representation was used to study a purely translating flow past a semi-infinite plate (Cortelezzi and Leonard, 1993; Cortelezzi, 1995) and the control of vortex shedding past a finite plate under an imposed normal flow using suction behind the plate (Cortelezzi, 1996; Cortelezzi et al., 1997). Cortelezzi et al. (1997) also compared the behavior of this discrete shedding method to a continuous shedding representation.

These two approaches present the advantage that no arbitrary choice is made for the time of shedding, the intensity of the shed vorticity or the initial position of the vortices. Intermediate methods have been proposed in which vortices with steady intensity are shed but not at each time step in order to reduce the computational cost (see for example Mason, 2003; Xiong and Kelly, 2008). The main disadvantages of such a method are that the regularity condition is satisfied only at the time-steps when a new vortex is shed, and the initial position of the new vortex is not determined in a unique way, but instead seems somewhat arbitrary.

The main advantage of the point vortex approach over the continuous vortex sheet method resides in its simplicity. The point vortex model does not require solving an integro-differential equation for the motion of the free vortex sheet. The numerical solution of such an equation requires the discretization of the sheet into a set of vorticity elements (Smith, 1968; Pullin, 1978). A smoothing kernel must be introduced to avoid numerical issues linked to ill-posedness of the free vortex sheet equation (Krasny, 1986a,b). The vortex sheet started from the sharp corner of a solid body will roll-up on itself in an infinitely tight spiral (Pullin, 1978). In numerical simulations, the last vortex element inside the spiral deserves particular treatment. Smith (1968) and Pullin (1978) explicitly state that this last vortex and the corresponding branch cut must be force-free which is equivalent to the Brown–Michael model. It is therefore of interest to understand how a purely Brown–Michael vortex model behaves when coupled with the solid motion.

## 2.4 The Brown–Michael point vortex model

### 2.4.1 Description

We consider the motion of a cylindrical solid body of sharp-edged cross-section and infinite span in a fluid. The flow around the solid is assumed two-dimensional, incompressible, inviscid and initially at rest. According to Kelvin’s circulation theorem, it remains irrotational at all time and potential flow theory is used to describe the flow. In the absence of vortex shedding, the presence of sharp edges on the solid body generates an algebraic velocity singularity there. To satisfy the regularity condition at each of the sharp corners, vorticity is introduced in the flow in the form of point vortices with unsteady and monotonically increasing intensity (in magnitude). In the following, we simply refer to these vortices as unsteady point vortices. This method was previously used to study the vortex shedding past a finite or semi-infinite plate with prescribed orthogonal translation (Cortelezzi and Leonard, 1993; Cortelezzi, 1996; Cortelezzi et al., 1997) – the purpose of the present work is to generalize the method to arbitrary motions of a general body, including rotation, and to formulate the fully coupled problem.

The point vortex, whose intensity is adjusted at each time to cancel exactly the singularity in the velocity field at the generating sharp corner, is a low-order representation of the roll-up of the vortex sheet shed in a real flow from the solid corner by the separation of the boundary layers. In this model, the vorticity is considered to be concentrated at one point, and the vorticity of the remainder of the sheet is neglected. The reader is referred to Cortelezzi (1993) for more details. In complex potential flow theory, the point vortex must be connected to the generating corner by a branch cut for the point vortex logarithmic complex potential to be single-valued. The complex velocity is continuous across the branch cut as is the streamfunction (imaginary part of the complex potential). However, the real part of the complex potential is discontinuous and the jump is equal to  $\pm\Gamma_n$  with  $\Gamma_n$  the intensity of the corresponding point vortex.

### 2.4.2 Irreversible vortex roll-up and shedding criterion

Through the regularity condition, the intensity of the unsteady point vortex is adjusted in time, representing the infinite roll-up of a vortex sheet and the transfer of vorticity from the shedding edge to the vortex core. It is not physically possible to unroll such a vortex sheet since this would correspond to a negative diffusion inside the core. To include this physical argument in the point vortex model, we require that the intensity of the point vortices does not decrease in magnitude. If the intensity of a point vortex reaches an extremum, this vortex will keep a steady intensity later on and a new unsteady vortex is started from the same generating corner to enforce the regularity condition at all time. Graham (1977) first discussed this shedding criterion, as well as other possible shedding criteria for point vortices in the flow around a sharp wedge. At any time in the flow past a solid body with  $P$  generating corners,  $P$  vortices are being shed with unsteady intensity  $\Gamma_1(t), \dots, \Gamma_P(t)$  to satisfy the regularity of the flow at each of these corners. There may be other vortices present in the flow, which were shed in the past, and whose intensities  $\Gamma_{P+1}, \dots, \Gamma_N$  have been frozen.

### 2.4.3 Equation of motion for a point vortex with unsteady intensity

Several models have been proposed for the motion of point vortices in the presence of solid bodies. In Kirchhoff's equation, the velocity of the point vortex is that of the desingularized background flow and Newton's second law is satisfied everywhere in the fluid except at the position of the vortex itself (Lamb, 1932). However, for an unsteady point vortex, this approach results in an unbalanced force on the branch cut (Rott, 1956). To satisfy the conservation of momentum around both the vortex and the branch cut, this equation needs to be modified. Denoting  $\dot{z}_n$  the velocity of the point vortex  $n$  with position and intensity  $(z_n, \Gamma_n)$ ,

shed from the corner of (time-varying) position  $z_{n,0}$ , we have

$$\dot{z}_n + (z_n - z_{n,0}) \frac{\dot{\Gamma}_n}{\Gamma_n} = \overline{\tilde{w}_n}, \quad (2.19)$$

with  $\tilde{w}_n$  the desingularized complex velocity of the fluid at the position of the vortex. Equation (2.19) is usually referred to as the Brown–Michael equation (Brown and Michael, 1954), although it was in fact first introduced by Edwards (1954) in the study of the steady three-dimensional vortex sheet shed by a delta wing. In this steady three-dimensional setting, the third dimension plays the role of the time-dependence in (2.19). The Brown–Michael equation was then proposed by Cheng (1954) and Rott (1956) for unsteady two-dimensional flows and point vortices with unsteady intensity. A derivation of (2.19), based on a conservation of fluid momentum argument is presented below.

#### 2.4.4 Conservation of fluid momentum around the vortex and branch cut

In this section we provide a conservation of momentum argument for the Brown–Michael equation (2.19) based on complex analysis. This is essentially a formalization of the physical arguments of Brown and Michael (1954) written in the language of the present work (see also Saffman, 1992). For a general contour  $\mathcal{C}$  enclosing only fluid and moving with a (spatially-dependent) velocity  $\mathbf{u}_c$ , Newton’s second law for the fluid inside  $\mathcal{C}$  is given by

$$\dot{\mathbf{M}} = - \int_{\mathcal{C}} p \mathbf{n} \, dl - \int_{\mathcal{C}} \rho \mathbf{u} [(\mathbf{u} - \mathbf{u}_c) \cdot \mathbf{n}] \, dl, \quad (2.20)$$

where the left-hand side is the rate of change of the momentum in  $\mathcal{C}$  and the terms on the right-hand side are respectively the force applied by the outside fluid on the contour and the flux of momentum through  $\mathcal{C}$ . Using complex notation,  $w = u - iv$ , and Bernoulli’s equation

$$p = p_0(t) - \rho(\dot{F} + \bar{\dot{F}} + w\bar{w})/2, \quad (2.21)$$

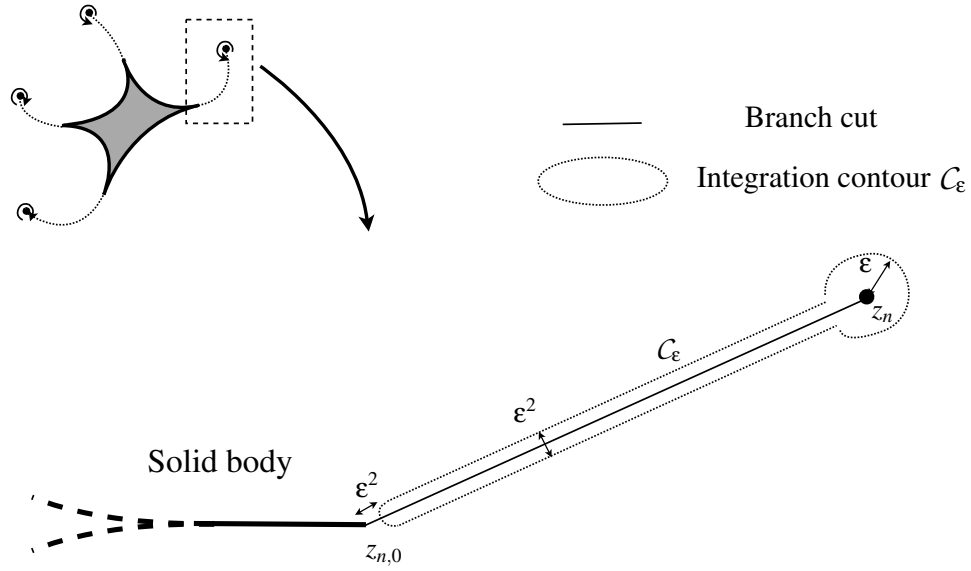


**Figure 2.1:** Conservation of momentum around the unsteady point vortex and its corresponding branch cut.

(2.20) becomes

$$\dot{M} = -\frac{i\rho}{2} \int_C (\dot{F} + \dot{\bar{F}}) dz + \overline{\frac{i\rho}{2} \int_C w (w - w_c) dz} + \frac{i\rho}{2} \bar{w}_c \int_C w d\bar{z}. \quad (2.22)$$

When shedding an unsteady vortex from corner  $n$ , the logarithmic form of the complex potential leads to a branch cut between  $z_{n,0}$  and  $z_n$ . We choose here to define it as the straight line connecting these two points (but its specific location is arbitrary). We now consider a contour  $\mathcal{C}_\varepsilon$  enclosing the vortex and the branch cut as shown on Figure 2.1. As  $\varepsilon$  goes to zero,  $\mathcal{C}_\varepsilon$  encloses only the vortex and the branch cut.

The chosen contour crosses the branch cut. This is not problematic as we are not carrying out an inverse Fourier transform or other integral that requires avoiding branch cuts. On the contrary, we are integrating a function whose real part is discontinuous, and this is why, physically, there is a net force. In (2.22), the last two integrals only involve  $w$ , a single-valued function analytic everywhere

except at the vortex position. The intensity of the vortex is chosen to satisfy the regularity condition so that  $w$  is bounded at the generating corner  $z_{n,0}$ . The existence of the branch cut only affects the first integral. The integrand  $\text{Re}(F)$  is discontinuous across the branch cut, but this discontinuity is finite and equal to  $\pm\Gamma_n$ .

Note that Graham (1980) uses a contour enclosing all the vortices and branch cuts as well as the solid. This contour can be used to derive an expression for the force on a solid from the expansion of the potential at infinity of the same form as the one considered in this paper, but uses the Brown–Michael equation (2.19) to obtain this result. In particular only one contour is used, which cannot lead to separate equations for each unsteady vortex.

A careful calculation shows that

$$\int_{\mathcal{C}_\varepsilon} \text{Re}[-i \log(z - z_n)] dz = -2\pi(z_n - z_{n,0}) + O(\varepsilon). \quad (2.23)$$

The complex potential and velocity can be decomposed as

$$F = \frac{\Gamma_n}{2i\pi} \log(z - z_n) + \tilde{F}_n(z), \quad w = \frac{\Gamma_n}{2i\pi(z - z_n)} + \tilde{w}_n(z), \quad (2.24)$$

with  $\tilde{F}_n$  and  $\tilde{w}_n$  single-valued and analytic on and inside  $\mathcal{C}_\varepsilon$  except at the vortex position  $z_n$ . Near the vortex, the velocity of the contour is  $w_c = \dot{z}_n$ . Using these results, the integrals in (2.22) can be evaluated exactly and when  $\varepsilon \rightarrow 0$ , we obtain

$$\dot{M} \rightarrow i\rho \left[ \dot{\Gamma}_n(z_n - z_{n,0}) + \Gamma_n(\dot{z}_n - \dot{\tilde{w}}_n) \right].$$

However, when  $\varepsilon \rightarrow 0$ , the surface enclosed in  $\mathcal{C}_\varepsilon$  goes to zero and the velocity is bounded along the branch cut. Near the vortex, the flow is purely azimuthal so when the contour is shrinking down, the linear momentum enclosed in  $\mathcal{C}_\varepsilon$  goes to zero, leading to the Brown–Michael equation (2.19).

The derivation detailed here shows that the Brown–Michael equation leads to Newton’s second law being satisfied in the fluid around the vortex and around the branch cut. Any choice of contour  $\mathcal{C}$  enclosing only part of the branch

cut would have led to a similar equation

$$\dot{z}_n + (z_n - z^*) \frac{\dot{\Gamma}_n}{\Gamma_n} = \overline{\dot{w}_n},$$

with  $z^*$  the position of the crossing point of  $\mathcal{C}$  with the branch cut. Kirchhoff's equation corresponds to  $z^* = z_n$  and only conserves the fluid momentum around the vortex. However, only the choice  $z^* = z_{n,0}$  corresponding to the Brown–Michael equation (2.19) guarantees the conservation of momentum in an integrated sense around the whole branch cut. If  $z^* \neq z_{n,0}$ , there exists an unbalanced force on the remainder of the branch cut between  $z_{n,0}$  and  $z^*$ . Nothing in this argument depends on the shape of the body.

### 2.4.5 The Brown–Michael model and conservation of angular momentum

Following the same approach as in section 2.4.4, we consider a contour  $\mathcal{C}$  moving with a spatially-dependent velocity  $\mathbf{u}_c$  and enclosing a finite surface  $\mathcal{A}$  containing only fluid. The conservation of angular momentum for the fluid inside  $\mathcal{C}$  can be written as

$$\dot{\Sigma} = - \int_{\mathcal{C}} p(\mathbf{r} \times \mathbf{n}) dl - \int_{\mathcal{C}} \rho(\mathbf{r} \times \mathbf{u}) [(\mathbf{u} - \mathbf{u}_c) \cdot \mathbf{n}] dl, \quad (2.25)$$

where  $\Sigma$  is the total angular momentum inside  $\mathcal{C}$

$$\Sigma = \iint_{\mathcal{A}} \rho(\mathbf{r} \times \mathbf{u}) dS, \quad (2.26)$$

and  $\mathbf{r}$  is the position vector measured with respect to a fixed point in the inertial reference frame. Note that  $\Sigma$  is well-defined even if  $\mathcal{C}$  encloses a point vortex: close to the vortex, the flow is purely azimuthal and behaves like  $1/r'$  with  $r'$  the distance to the vortex core, and  $\Sigma$  converges there. Using Bernoulli's equation (2.21), (2.25) can be rewritten in complex notation, defining  $\Sigma = \Sigma \mathbf{e}_3$  with  $\mathbf{e}_3$  the unit vector in the third dimension,

$$\dot{\Sigma} = -\frac{\rho}{2} \text{Re} \left[ \int_{\mathcal{C}} (F_t + \bar{F}_t) \bar{z} dz + \int_{\mathcal{C}} z w^2 dz - w_c \int_{\mathcal{C}} (wz - \bar{w}\bar{z}) dz \right]. \quad (2.27)$$

We now apply this result to the contour  $\mathcal{C}_\varepsilon$  defined in the previous section (Figure 2.1). The complex velocity is continuous across the branch cut as is the imaginary part of  $F$ .  $\text{Re}(F)$  is discontinuous across the branch cut and the discontinuity is equal to  $\pm\Gamma_n$ . Near the corner, the flow has been regularized through the regularity condition that determines  $\Gamma_n$  and both  $w$  and  $F$  have finite values there. Therefore, all the contour integrals converge near the corner as  $\varepsilon$  goes to zero (Figure 2.1). For small  $\varepsilon$ , the second and third integrals' contributions around the branch cut are  $O(\varepsilon)$  as  $w$  is continuous across the branch cut.

Computing the  $O(1)$  contributions of all three integrals in (2.27), leads as  $\varepsilon \rightarrow 0$  to

$$\dot{\Sigma} = -\frac{\rho}{2}\text{Re}\left[\dot{\Gamma}_n(|z_{n,0}|^2 - |z_n|^2) + 2\Gamma_n z_n(\tilde{w}_n - \dot{z}_n)\right]. \quad (2.28)$$

with  $\tilde{w}_n$  the desingularized flow velocity at the vortex position, as defined in (2.24). As  $\varepsilon$  tends to zero, the area enclosed in  $\mathcal{C}_\varepsilon$  also tends to zero. The angular momentum per unit area is finite even near a point vortex. Therefore, the left-hand side of (2.28) tends to zero with  $\varepsilon$ . If the point vortex satisfies the Brown–Michael equation (2.19), the right-hand side of (2.28) does not vanish with  $\varepsilon \rightarrow 0$ , but instead creates a residual unbalanced torque on the branch cut equal to

$$\mathcal{T}_b = -\frac{\rho\dot{\Gamma}_n}{2}|z_n - z_{n,0}|^2. \quad (2.29)$$

We notice that this unbalanced torque is proportional to the vortex shedding rate. Angular momentum is therefore conserved in the case of vortices with steady intensity, and only the vortices being currently shed introduce this additional torque.  $\mathcal{T}_b$  is also proportional to the square of the distance between the vortex and its generating corner. The physical interpretation of this additional term is therefore the following: physically, vorticity is shed from the generating corner where the boundary layer separates into a free shear layer. The present discrete shedding model, instead of introducing a new element of vorticity close to the shedding corner, modifies the intensity of the last shed vortex to satisfy the regularity condition. This instantaneous transfer of vorticity from the generating corner to the

vortex core induces an instantaneous change of the flow angular momentum that is reflected in this unbalanced torque on the branch cut.

The fact that the Brown–Michael vortex model cannot satisfy at the same time conservation of both linear and angular momenta in an integral sense around the vortex and branch cut is, however, not a surprise, and is inherent to any discrete representation of the continuous physical vorticity shedding. Introducing a point vortex in the flow provides three additional degrees of freedom for the system: the vortex position (2) and its intensity (1). The regularity condition guarantees the finiteness of the flow velocity at the shedding corner and gives one constraint on the vortex system. The conservation of both linear and angular momenta would provide three additional constraints for a total of four constraints for three degrees of freedom. It is therefore not possible to satisfy these four constraints at the same time and one needs to make a choice on the conservation laws and flow constraints to be enforced. The Brown–Michael model enforces the regularity condition and conservation of linear momentum. In that regard, it is an improvement compared to a Kirchhoff vortex model that satisfies neither momentum conservation laws. Other vortex shedding models have been discussed in the literature to overcome the non-conservation of angular momentum (Howe, 1996), but it is necessary to point out that any model that removes any unphysical torque, cannot satisfy both the regularity condition and the conservation of linear momentum.

## **2.5 Reduced order models of fluid-solid interactions using Brown–Michael vortices**

In Chapters 3, 4 and 6, the previously described vortex model will be coupled to the equations of motion for the generating solid body to obtain a reduced-order representation of the fluid-solid interaction problems of interest. Formally, the flow is entirely determined by the knowledge of the position and velocity of the

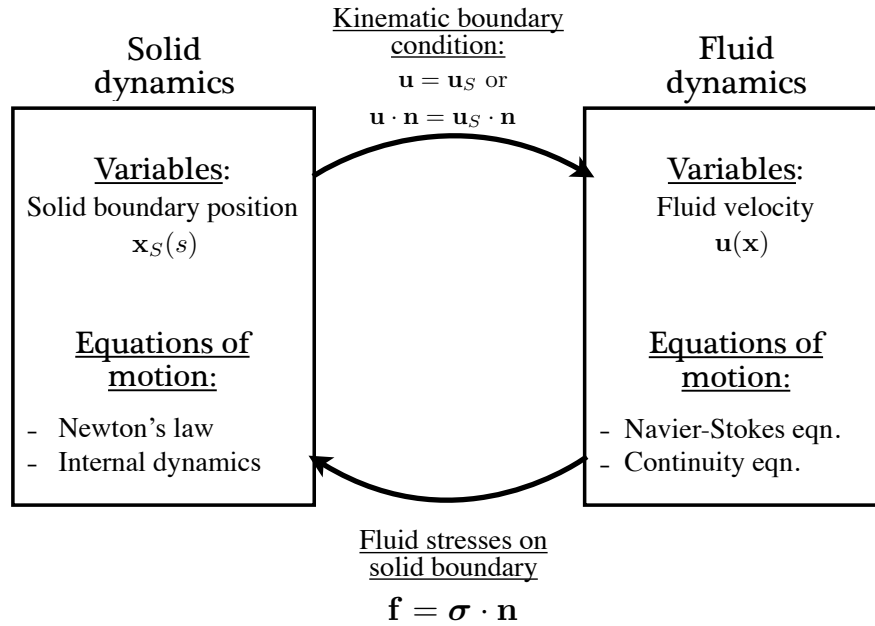
solid boundary, of the vortices' intensity and position and of the total circulation at infinity. The flow problem can be formulated as follow for the complex potential  $F = \phi + i\psi$  with  $\phi$  the velocity potential and  $\psi$  the streamfunction:

$$\begin{cases} F \text{ is analytic in the fluid domain except at } z = z_n \\ \tilde{F}_n = F - \frac{\Gamma}{2\pi i} \log(z - z_n) \text{ is analytic in } z = z_n \\ \text{Im} \left( \frac{\partial F}{\partial s} \right) = \text{Im} \left( w_S \frac{\partial z_S}{\partial s} \right) \quad \text{on the solid body} \\ \text{Re} \left( \int_{\mathcal{C}_\infty} dF \right) = \Gamma_\infty, \end{cases} \quad (2.30)$$

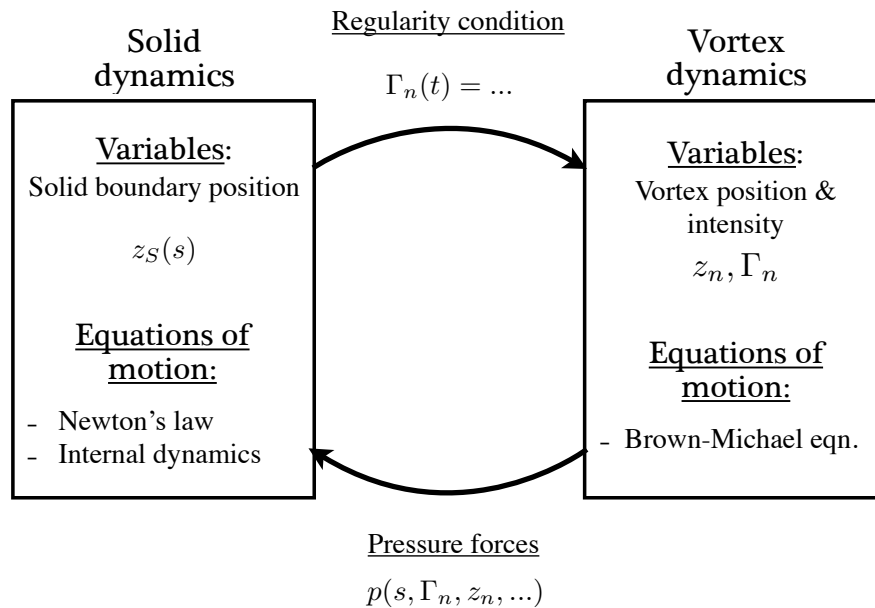
with  $z_n$  and  $\Gamma_n$  the position of the point vortices. The solid boundary is defined as a closed non-intersecting curve in the complex plane  $z_S(s)$  with  $0 \leq s \leq L$  and  $z_S(0) = z_S(L)$ .  $w_S = \overline{\partial z_S / \partial t}$  is the complex velocity of the boundary (we use here the same classical convention  $w = u - iv$  as for the fluid velocity).  $\mathcal{C}_\infty$  is a circle of radius  $R \rightarrow \infty$  encircling the body and all the vortices present in the flow and  $\Gamma_\infty$  is the circulation at infinity.

Through Kelvin's theorem,  $\Gamma_\infty$  is a constant of the problem and in the remainder of this dissertation, unless indicated otherwise, the system is started from rest so that  $\Gamma_\infty = 0$ . The solution of (2.30) for the complex velocity  $w = dF/dz$  is unique. Note also that the unsteady nature of  $\Gamma_n$  is irrelevant in solving for  $F$ . From  $F$  and  $w$ , the pressure is obtained from Bernoulli's theorem (2.21). From the pressure field, all the forces and torques applied by the fluid on the solid can be computed and used on the right-hand side of the solid body dynamics. The coupling of the fluid and solid dynamics (Figure 2.2a) is replaced by a coupled solid-vortex problem (Figure 2.2b).

In the coupled fluid-solid formulation, the coupling occurs through the kinematic boundary conditions (2.3) or (2.4) and the stress applied by the fluid on the solid boundary  $\mathbf{f} = \boldsymbol{\sigma} \cdot \mathbf{n}$  (with  $\boldsymbol{\sigma}$  given in (2.1) and  $\mathbf{n}$  the outward-pointing normal on the solid boundary). In the coupled vortex-solid approach, the coupling occurs through the regularity condition at each shedding corner that determines the intensity of the unsteady point vortices and the pressure forces on the solid boundary that are implicit functions of the vortices' properties  $(z_n, \Gamma_n)$ .



(a) Fluid-solid coupled problem



(b) Vortex-solid coupled problem

**Figure 2.2:** Schematic representation of (a) the complete fluid-solid coupled problem and (b) the reduced-order model using the Brown–Michael point vortex representation.

The treatment of the solid dynamics as well as the computation of the complex potential differs depending on the problem considered and the type of solid (rigid or flexible, finite area or infinitesimally thin). In the case of a rigid solid body, a general framework for the coupled solid–vortex problem is presented in Chapter 3 using conformal mapping theory. Although it is in theory generalizable to deformable solids using time-dependent conformal maps, in the case of flexible sheets (Chapters 4 and 6) a simpler treatment of the potential flow is possible by representing the deformable thin solid as a vortex sheet attached to the solid.

In the case of a rigid solid body or a deformable body with a discrete set of degrees of freedom (e.g. three-link swimmer), the solid–vortex problem illustrated on Figure 2.2(b) can be written in terms solely of ordinary differential equations, allowing a particularly efficient solution using any ODE solver such as Matlab’s `ode45`. For a continuously deformable body, the solid dynamics requires the solution of a partial differential equation coupled to the ODE for the vortices’ properties. In both cases, the computational cost is significantly lower than for a direct numerical simulation of an equivalent flow (the computations can typically be performed in less than a few minutes on a personal laptop computer).

Chapter 2 and Chapter 3, in part, have been published in *Theoretical and Computational Fluid Dynamics*, “An unsteady point vortex method for coupled fluid-solid problems” by S. Michelin and S. G. Llewellyn Smith, 2009, **23**, 127–153 (Springer), doi:10.1007/S00162-009-0096-7. The dissertation author was the primary investigator and author of this material.

# 3

## Motion of a rigid sharp-edged body shedding vortices

### 3.1 Introduction

In Chapter 2, we presented a general inviscid model to study the coupled dynamics of a solid body with sharp edges and laminar high- $Re$  flows in the two-dimensional limit. A potential flow representation is used and point vortices with unsteady intensity are shed from the generating sharp corners. Using the linearity of Laplace's equation, the complex potential and velocity field are obtained by linear superposition. Assuming the system is started from rest, the circulation at infinity must be equal to zero. Hence the solution for the flow velocity is unique and entirely determined by giving the position and intensity of each point vortex, and the position and velocity of the solid body.

In this Chapter, we focus on the particular case of a two-dimensional rigid body. The position of any point in the solid body is determined by only three variables, the position of the body's center of mass and an orientation angle. Formally, the number of unknowns in the system is finite and equal to  $3N + 3$  with  $N$  the number of vortices present in the flow. Taking advantage of this finite numbers of degrees of freedom, the purpose of this Chapter is to obtain the equations of motion for the fluid and the solid body as a finite set of ordinary differential equations.

By definition, the geometry of a rigid body is time-independent and the position of its boundary is simply obtained by rotation and translation of a time-independent contour (e.g. the reference position of the solid body). In two-dimensional potential flow problems, conformal mappings can be a powerful technique: if one is able to find a function  $\zeta = f(z)$  mapping any point outside the solid boundary in the physical plane  $\mathcal{C}$  onto a domain of same connectivity  $\mathcal{C}$  in the mapped  $\zeta$ -plane such that  $f$  is analytic and univalent outside of  $\mathcal{C}$ , then the complex potential in the physical plane  $F(z)$  and in the mapped plane  $\tilde{F}(\zeta)$  are simply related by

$$F(z) = \tilde{F}(f(z)).$$

If the body is simply connected, then Riemann's mapping theorem ensures that  $f$  always exists such that the outside of  $\mathcal{C}$  in the physical plane can be mapped onto the outside of the unit circle (see for example Nehari, 1952). The geometry of the solid body can then be easily obtained using the conformal mapping

$$z = z_0(t) + be^{i\alpha(t)} f^{-1}(\zeta), \quad (3.1)$$

with  $z \in \mathcal{C}$  and  $\zeta \in \mathcal{C}$ ,  $z_0$  the position of a reference point fixed relative to the solid body and  $\alpha(t)$  an orientation angle. Equation (3.1) isolates the time-dependence of the solid boundary position into a translation and a rotation of a fixed contour defined by  $f^{-1}(\zeta)$ .

In this Chapter, a general sharp-edged solid body is considered. Point vortices with unsteady intensity are shed from the sharp edges to enforce the regularity of the flow at the generating corner, following the model presented in section 2.4. The intensity of a point vortex is a monotonic function of time: when a vortex reaches a maximum intensity, its intensity becomes frozen and a new vortex is started from the corresponding corner (see section 2.4.2).

The Chapter is organized as follows. In section 3.2, the equations of

motion are obtained for the coupled motion of a general sharp-edged solid body and Brown–Michael point vortices as a set of nonlinear ODEs. The forces applied on the solid by the fluid are analyzed in terms of added inertia and transfer of linear and angular momenta to the vortices. The small-time behavior of these equations is analyzed further in section 3.3. This framework is then applied to the particular case of a falling card in a fluid initially at rest in section 3.4. The stability of the broadside-on fall position is investigated and the present vortex shedding model is compared to the results obtained with added inertia only. The shedding of vorticity, and more particularly the transfer of horizontal momentum to the vortex wake, are shown to be responsible for the destabilization of the broadside-on position, consistently with experimental observations. Finally, some conclusions on the general method for rigid bodies with arbitrary shapes as well as on the falling card problem are drawn in section 3.5.

## 3.2 Equations of motion of a sharp-edged rigid body shedding vortices

The motion of the solid body is studied in the inertial laboratory frame using a fixed system of axes.  $z = x + iy$  and  $w = u - iv$  are the complex variables describing respectively the position and velocity in the physical space. Conformal mapping is used to describe the solid geometry and compute the flow around the body. We write  $\zeta$  for the position in the mapped plane.

### 3.2.1 Geometry

The geometry and motion of the solid body are described by mapping its physical boundary  $\mathcal{C}$  from the circle  $\mathcal{C}$  of radius  $a$  centered at the origin in the mapped plane through the transformation

$$z = c + e^{i\theta}g(\zeta), \tag{3.2}$$

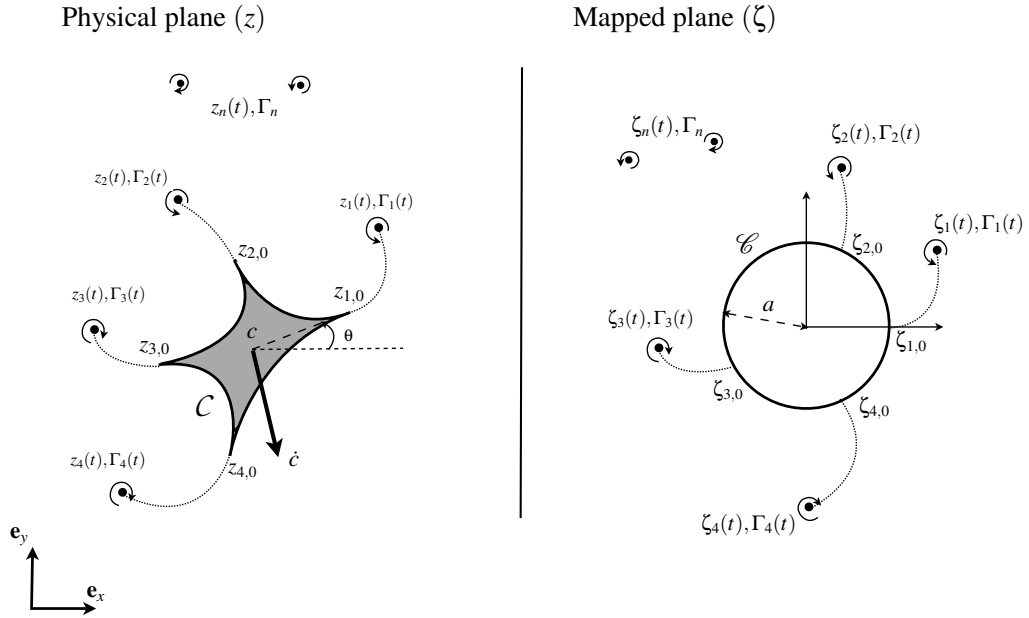


**Figure 3.1:** Notation used for the motion of a general solid body. (Left) In the physical plane, the position is noted by  $z = x + iy$  and the physical contour of the solid body is  $\mathcal{C}$ . The position of the center of mass is  $c$  and the orientation  $\theta$  is measured as the angle between a reference direction in the solid and the horizontal axis. (Right) The problem is considered in the mapped plane, where positions are noted by  $\zeta$ . The contour  $\mathcal{C}$  is mapped onto  $\mathcal{C}$  in the physical space through the mapping (3.2).

where  $c$  is the position of the centroid in physical space and  $\theta$  denotes the rotation of the solid body compared to a reference configuration (note that the definitions of  $c$ ,  $\theta$  and  $g$  are interdependent). In the following, we will consider only homogeneous bodies so  $c$  is also the position of the center of mass. This notation is summarized on Figure 3.1. The function  $g$  maps the outside of  $\mathcal{C}$  in the mapped plane onto the outside of the solid body  $\mathcal{C}$  in the physical plane. We assume that this mapping is univalent on and outside of  $\mathcal{C}$  (each point outside the solid  $\mathcal{C}$  corresponds to one and only one point outside  $\mathcal{C}$  in the mapped plane). We focus on mappings  $g$  of the form

$$g(\zeta) = \sum_{j=-1}^M \frac{G_j}{\zeta^j}, \quad (3.3)$$

satisfying the following properties:

- $g'$  has no zero outside of  $\mathcal{C}$ , and a finite number  $P$  of zeros on  $\mathcal{C}$  itself, at  $\zeta_{p,0} = ae^{i\phi_p}$  with  $0 \leq \phi_p \leq 2\pi$  for  $1 \leq p \leq P$ . We further assume that  $g''(\zeta_{p,0})$  is non-zero and finite: these points correspond to corners of the solid boundary  $\mathcal{C}$  in the physical plane, where both edges of the sharp corner have the same tangential direction.
- $G_{-1} = 1$ , so that  $g(\zeta) \sim \zeta$  at infinity.
- $c$  is the position of the centroid of the body, therefore (see for example Llewellyn Smith et al. (2008))

$$\sum_{k,l=-1,k+l \geq -1}^M \frac{l G_k G_l \bar{G}_{k+l}}{a^{2(k+l)}} = 0. \quad (3.4)$$

Only the first of the above conditions is restrictive as the second and third can always be achieved by redefining the parameter  $a$  and the variables  $\theta$  and  $c$ . Although we restrict ourselves to solid bodies with flat corners (zero angle), this form of mapping allows to describe a wide variety of solid body shapes with sharp edges.

The area and moment of inertia with respect to the center of mass of this body can be computed as

$$\mathcal{S} = \frac{1}{2} \text{Im} \left[ \int_{\mathcal{C}} \overline{g(\zeta)} g'(\zeta) d\zeta \right] = \pi \left( a^2 - \sum_{k=1}^M \frac{k |G_k|^2}{a^{2k}} \right), \quad (3.5)$$

$$I = \frac{\mathcal{M}}{4\mathcal{S}} \text{Im} \left[ \int_{\mathcal{C}} (\overline{g(\zeta)^2} - g(\zeta)^2) g(\zeta) g'(\zeta) d\zeta \right]. \quad (3.6)$$

with  $\mathcal{M}$  the mass of the solid body. We assume here that the solid is homogeneous. A complicated expression for  $I$  can be obtained explicitly in terms of the coefficients  $G_k$ .

### 3.2.2 Complex potential and velocity around the moving solid body

The solid body is shedding vortices from its  $P$  sharp edges during its motion. At time  $t$ , we denote by  $\zeta_n$  the positions of the vortices in the mapped

plane, by  $z_n$  their corresponding positions in the physical plane and by  $\Gamma_n$  their intensities, with  $1 \leq n \leq N$ . By convention, vortex  $p$  is being shed from corner  $p$  corresponding to  $\zeta_{p,0} = ae^{i\phi_p}$  in the mapped plane ( $1 \leq p \leq P$ ). The  $(N - P)$  other vortices have a frozen intensity and have been shed and released in the past (see section 2.4.2). Therefore,  $\Gamma_{P+1}, \Gamma_{P+2}, \dots, \Gamma_N$  are independent of time while the first  $p$  vortices have unsteady intensity  $\Gamma_1(t), \dots, \Gamma_P(t)$ . This convention requires renumbering the vortices when a new vortex is started:  $N$  is incremented and the vortex that was just frozen becomes vortex  $N$ . We assume that there is no flow and no net circulation at infinity (this is the case for example when the system is started from rest according to Kelvin's circulation theorem).

The complex potential can then be obtained as a linear superposition of the contribution of the motion of the body and of the different vortices:

$$F = F_b + \sum_{n=1}^N \Gamma_n F_n. \quad (3.7)$$

The potential  $F_b$  is harmonic outside the solid body and the corresponding velocity decays like  $z^{-2}$  at infinity. On the solid boundary  $\mathcal{C}$ , it satisfies (see for example Crowdy et al. (2007)):

$$\operatorname{Re}[-iF_b] = \operatorname{Re} \left[ -i\dot{c}(z - c) - \frac{\omega}{2}|z - c|^2 \right], \quad (3.8)$$

with  $\omega = \dot{\theta}$ , the angular velocity of the solid. This can be easily related to the Schwarz problem on the unit disk and can be solved using the Poisson formula, defining  $U = -\dot{c}e^{i\theta}$ ,

$$F_b = U(\zeta - g(\zeta)) + \frac{a^2}{\zeta} \bar{U} - i\omega r(\zeta), \quad r(\zeta) = \sum_{l=1}^{M+1} \frac{R_l}{\zeta^l} \text{ and } R_l = \sum_{k=-1}^{M-l} \frac{\bar{G}_k G_{l+k}}{a^{2k}}, \quad (3.9)$$

with  $0 \leq l \leq M + 1$ . Note that the velocity potential  $r(\zeta)$  due to the rotation has a dipolar component at infinity unless  $R_1 = \sum G_l \bar{G}_{l+1}/a^{2l} = 0$  as investigated in Llewellyn Smith et al. (2008).

The potential due to each point vortex satisfying the no-flow boundary condition on the solid and the zero-circulation condition at infinity can be obtained

in the mapped plane using the circle theorem as:

$$F_n = \frac{1}{2\pi i} \log \left[ \frac{\zeta - \zeta_n}{\zeta - \frac{a^2}{\zeta_n}} \right]. \quad (3.10)$$

This definition differs from the one in Milne-Thomson (1968) because the circulation at infinity must be zero here.

Finally, the complex potential  $F = \phi + i\psi$  is obtained by linear superposition, as is the complex velocity  $w = u - iv = dF/dz$ :

$$F = U(\zeta - g(\zeta)) + \frac{a^2}{\zeta} \bar{U} - i\omega r(\zeta) + \sum_{n=1}^N \frac{\Gamma_n}{2\pi i} \log \left( \frac{\zeta - \zeta_n}{\zeta - \frac{a^2}{\zeta_n}} \right), \quad (3.11)$$

$$w = \dot{c} + \frac{e^{-i\theta}}{g'(\zeta)} \left[ U - \frac{a^2}{\zeta^2} \bar{U} - i\omega r'(\zeta) + \sum_{n=1}^N \frac{\Gamma_n}{2\pi i} \left( \frac{1}{\zeta - \zeta_n} - \frac{\bar{\zeta}_n}{\zeta \bar{\zeta}_n - a^2} \right) \right]. \quad (3.12)$$

From (3.8), the potential  $r(\zeta)$  satisfies  $\text{Re}(r(ae^{i\phi})) = g(ae^{i\phi})\overline{g(ae^{i\phi})}/2$  for  $0 \leq \phi \leq 2\pi$ . Differentiating this relation twice with respect to  $\phi$ , and applying it at  $\zeta_{p,0}$ , remembering that  $g'(\zeta_{p,0}) = 0$ , leads to the following relations:

$$\text{Im}(\zeta_{p,0} r'_p) = 0, \quad \text{Re}[\zeta_{p,0} r'_p + \zeta_{p,0}^2 (r''_p - g''_p \bar{g}_p)] = 0, \quad (3.13)$$

where we defined for convenience of notation  $g_p = g(\zeta_{p,0})$  and similarly,  $g''_p$ ,  $r'_p$  and  $r''_p$  are the values of the corresponding functions of  $\zeta$  when evaluated at  $\zeta_{p,0}$ .

### 3.2.3 Regularity condition and motion of the vortices

The regularity condition at the shedding edges  $z_{p,0}$  imposes that  $w$  is finite there. In (3.12), the term between brackets must vanish at  $\zeta_{p,0}$  to cancel the singularity introduced by  $g'$  vanishing at these points. Using  $\zeta_{p,0} = a^2/\bar{\zeta}_{p,0}$ , we obtain

$$2\text{Im}(U\zeta_{p,0}) - \omega\zeta_{p,0}r'_p + \sum_{n=1}^N \frac{\Gamma_n}{2\pi} \left( 1 + 2\text{Re} \left[ \frac{\zeta_{p,0}}{\zeta_n - \zeta_{p,0}} \right] \right) = 0, \quad 1 \leq p \leq P. \quad (3.14)$$

Note from (3.13) that all terms in (3.14) are real.

Rewriting the complex potential in (3.11) as  $F = \tilde{F}_n + \frac{\Gamma_n}{2\pi i} \log(\zeta - \zeta_n)$ , the regularized velocity (2.19) is

$$\tilde{w}_n = \frac{e^{-i\theta}}{g'(\zeta_n)} \left[ \frac{d\tilde{F}_n}{d\zeta}(\zeta_n) - \frac{\Gamma_n}{4i\pi} \frac{g''(\zeta_n)}{g'(\zeta_n)} \right], \quad (3.15)$$

where the last term is known as the Routh correction (Lin, 1941; Clements, 1973). Using (3.2), (3.12) and (3.15), the equation of motion for the vortices (2.19) becomes, in the mapped plane,

$$g'(\zeta_n)\dot{\zeta}_n + (g(\zeta_n) - g(\zeta_{n,0})) \frac{\dot{\Gamma}_n}{\Gamma_n} = -i\omega g(\zeta_n) + \frac{1}{g'(\zeta_n)} \left[ \bar{U} - \frac{a^2}{\bar{\zeta}_n^2} U + i\omega \overline{r'(\zeta_n)} \right] \quad (3.16)$$

$$- \sum_{j \neq n} \frac{\Gamma_j}{2\pi i} \left( \frac{1}{\bar{\zeta}_n - \bar{\zeta}_j} - \frac{\zeta_j}{\zeta_j \bar{\zeta}_n - a^2} \right) + \frac{\Gamma_n}{2\pi i} \left( \frac{\zeta_n}{\zeta_n \bar{\zeta}_n - a^2} + \frac{\overline{g''(\zeta_n)}}{2g'(\zeta_n)} \right).$$

### 3.2.4 Forces and torques on the solid body

In this section, explicit expressions are derived for the total force and torque on the body, which are defined as the integral of the pressure forces and torques over the body surface. This definition ensures that the transfer of energy from the fluid to the solid (work of the total force and torque) is the opposite of the transfer of energy from the solid to the fluid (integral along the body of the pressure multiplied by the normal velocity, as identified in the energy conservation equation obtained from Euler's equations). At this point, one can naturally wonder whether the total energy of the system is conserved in such a formulation. However, it is very difficult to define the energy of the system here since the kinetic energy of a fluid with point vortices is infinite. Although the integral of the fluid kinetic energy converges far from the body and vortices due to the absence of net flow or circulation there, each point vortex introduces a logarithmic singularity in the kinetic energy of the flow. We do not attempt here to suggest or prove that the regular part of the kinetic energy should be a conserved quantity. Instead, we focus on the conservation of linear and angular momenta as both quantities are finite, even for a flow with point vortices.

## Force

The force on a solid body shedding vortices can be obtained from the results of Sedov (1965) in terms of complex integrals over the body:

$$f = f_x + if_y = i\rho \sum_{n=1}^N z_{n,0} \dot{\Gamma}_n + \overline{\frac{i\rho}{2} \int_C w^2 dz} + \frac{d}{dt} \left[ i\rho \int_C z w dz \right] + \rho S \ddot{c} \quad (3.17)$$

with  $c$  the position of the solid's centroid and  $z_{n,0}$  the position of corner  $n$  in the physical plane. The integrands in (3.17) are analytic functions of  $z$  except at the positions of the different vortices. According to Cauchy's theorem, the integration contour can be stretched to infinity without changing the value of the integrals provided that the contribution around each vortex is removed:  $\int_C = \int_{C_\infty} - \sum \int_{C_n}$  with  $C_n$  an infinitesimally small circle around the  $n$ -th vortex and  $C_\infty$  a circle of radius  $R \gg 1$  encircling the solid body and all the vortices at all time (see Figure 3.2). On  $C_\infty$ , the complex potential and complex velocity can be expanded as

$$F = F_0 + \frac{a_1}{z} + \frac{a_2}{z^2} + O(R^{-3}), \quad w = -\frac{a_1}{z^2} - \frac{2a_2}{z^3} + O(R^{-4}) \quad (3.18)$$

and (3.18) defines the variables  $a_1$  and  $a_2$ , while near the  $n$ -th vortex,

$$w = \frac{\Gamma_n}{2\pi i(z - z_n)} + \tilde{w}_n + O(z - z_n). \quad (3.19)$$

Using (3.18) and (3.19) as well as (2.19), the force on the solid body (3.17) simplifies to

$$f = 2\pi\rho \frac{da_1}{dt} + \rho S \frac{d^2 c}{dt^2}. \quad (3.20)$$

The expression for  $a_1$  can be obtained from (3.2) and (3.11). At infinity,

$$\zeta = ze^{-i\theta} - (ce^{-i\theta} + G_0) - G_1 \frac{e^{i\theta}}{z} + O(R^{-2}), \quad (3.21)$$

and after expanding (3.11) for  $\zeta \rightarrow \infty$ , we obtain

$$a_1 = \left[ a^2 \bar{U} - G_1 U - i\omega R_1 + \sum_{n=1}^N \frac{i\Gamma_n}{2\pi} \left( \zeta_n - \frac{a^2}{\zeta_n} \right) \right] e^{i\theta}, \quad (3.22)$$

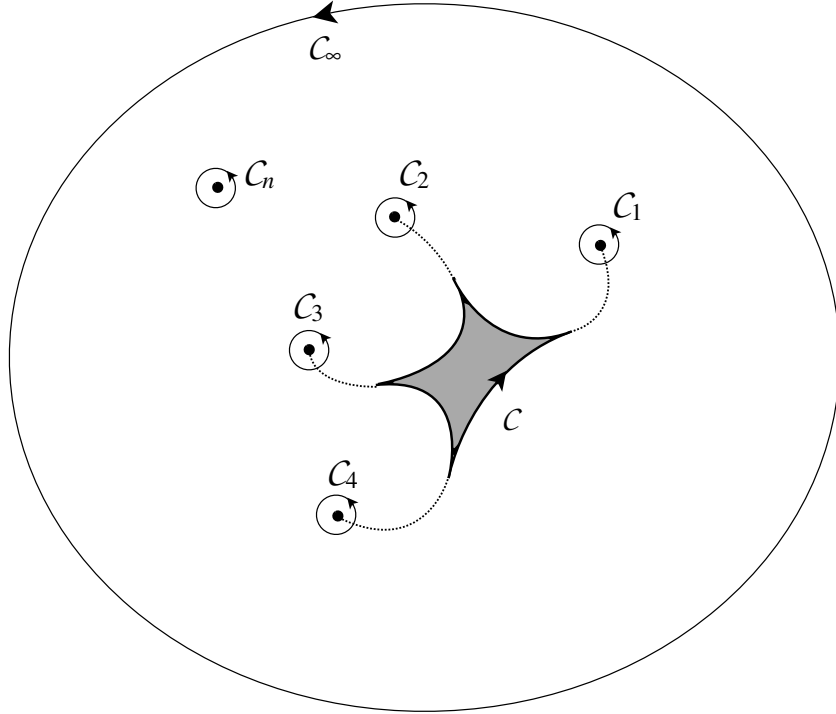


**Figure 3.2:** Details of the contours used in the computation of the integrals in (3.17) with analytic integrand outside the body except at the position of the vortices. From Cauchy's theorem, the contour integral on  $\mathcal{C}$  can be replaced by a contour integral on a circle  $\mathcal{C}_\infty$  with radius going to infinity, if the contribution from each of the infinitesimally small circular contours  $\mathcal{C}_n$  encircling each vortex (steady or unsteady) is removed.

so that the force (3.20) becomes

$$f = \rho e^{i\theta} \left[ (2\pi a^2 - S) \dot{U} - 2\pi G_1 \dot{U} - 2\pi i R_1 \dot{\omega} + i\omega (2\pi a^2 - S) \bar{U} \right. \\ \left. - 2\pi i \omega G_1 U + 2\pi R_1 \omega^2 + i \frac{d}{dt} \sum_{n=1}^N \Gamma_n \left( \zeta_n - \frac{a^2}{\bar{\zeta}_n} \right) - \omega \sum_{n=1}^N \Gamma_n \left( \zeta_n - \frac{a^2}{\bar{\zeta}_n} \right) \right]. \quad (3.23)$$

### Barycentric torque on the solid body

The computation by Sedov (1965) of the torque applied by the fluid on the body about a fixed point can be extended easily to the case of a point moving in the laboratory frame. If this point is taken to be the centroid of the solid body (or equivalently its center of mass since we will consider here only homogeneous

bodies), the torque simplifies further to:

$$\begin{aligned} \mathcal{T}^* = \frac{\rho}{2} \sum_{n=1}^N |z_{n,0} - c|^2 \dot{\Gamma}_n + \frac{\rho}{2} \operatorname{Re} \left[ 2\dot{c} \int_{\mathcal{C}} (z - c) w dz - \int_{\mathcal{C}} (z - c) w^2 dz \right. \\ \left. + \frac{d}{dt} \int_{\mathcal{C}} |z - c|^2 w dz \right]. \end{aligned} \quad (3.24)$$

The integrands are analytic functions of  $z$  except for the last integral

$$A = \int_{\mathcal{C}} |z - c|^2 w dz. \quad (3.25)$$

However, on the mapped circle  $\mathcal{C}$ , we have  $\bar{\zeta} = a^2/\zeta$  and therefore, on the contour of the solid body  $\mathcal{C}$ ,

$$|z - c|^2 = g(\zeta) \overline{g(\zeta)} = \left( \sum_{k=-1}^M G_k \zeta^{-k} \right) \left( \sum_{j=-1}^M \frac{\bar{G}_j \zeta^j}{a^{2j}} \right) = R_0 + \sum_{l=1}^{M+1} \left( \frac{R_l}{\zeta^l} + \frac{\bar{R}_l \zeta^l}{a^{2l}} \right), \quad (3.26)$$

with the definition of  $R_l$  in (3.9) for  $0 \leq l \leq M + 1$ . Using the previous equation as well as (3.12), one obtains:

$$\begin{aligned} A = \int_{\mathcal{C}} \left[ R_0 + \sum_{l=1}^{M+1} \left( \frac{R_l}{\zeta^l} + \frac{\bar{R}_l \zeta^l}{a^{2l}} \right) \right] \cdot \left[ U \sum_{k=1}^M \frac{k G_k}{\zeta^{k+1}} - \bar{U} \frac{a^2}{\zeta^2} + i\omega \sum_{l=1}^M \frac{l R_l}{\zeta^{l+1}} \right. \\ \left. + \sum_{n=1}^N \frac{\Gamma_n}{2\pi i} \left( \frac{1}{\zeta - \zeta_n} - \frac{\bar{\zeta}_n}{\zeta \bar{\zeta}_n - a^2} \right) \right] d\zeta. \end{aligned} \quad (3.27)$$

Using Cauchy's theorem, the previous integral can be computed as

$$\begin{aligned} A = - \sum_{n=1}^N \Gamma_n \left[ R_0 + \sum_{l=1}^{M+1} \left( \frac{R_l}{\zeta_n^l} + \frac{\bar{R}_l}{\bar{\zeta}_n^l} \right) \right] - 2\pi\omega \sum_{l=1}^{M+1} \frac{l |R_l|^2}{a^{2l}} \\ + 2\pi i \left( -\bar{R}_1 \bar{U} + U \sum_{l=1}^M \frac{l G_l \bar{R}_l}{a^{2l}} \right), \end{aligned} \quad (3.28)$$

and from the centroid condition (3.4), we also have

$$\sum_{l=1}^M \frac{l G_l \bar{R}_l}{a^{2l}} = R_1. \quad (3.29)$$

Hence, finally,

$$A = - \sum_{n=1}^N \Gamma_n [R_0 + 2\operatorname{Re}(r(\zeta_n))] - 2\pi\omega \sum_{l=1}^{M+1} \frac{l |R_l|^2}{a^{2l}} - 4\pi \operatorname{Im}(R_1 U). \quad (3.30)$$

Note that  $A$  is real.

Considering the other integrals in (3.24), the integrands are analytic except at the position of the different vortices, and we can therefore apply the same technique used for the force in the previous section by stretching the integration contour to infinity and removing the contribution of the infinitesimally small contours around each vortex. Doing so, we obtain for the torque:

$$\mathcal{T}^* = \frac{\rho}{2} \sum_{n=1}^N |z_{n,0} - c|^2 \dot{\Gamma}_n + \rho \operatorname{Re} \left[ \sum_{n=1}^N \Gamma_n (\tilde{w}_n - \dot{c})(z_n - c) - 2\pi i a_1 \dot{c} \right] + \frac{\rho \dot{A}}{2}, \quad (3.31)$$

with  $a_1$  and  $A$  respectively defined in (3.22) and (3.30). Using (2.19), and  $g(\zeta_n) = (z_n - c)e^{-i\theta}$ ,  $\mathcal{T}^*$  can be rewritten

$$\mathcal{T}^* = \frac{\rho}{2} \sum_{n=1}^N \left[ \dot{\Gamma}_n |g(\zeta_n) - g(\zeta_{n,0})|^2 + \frac{d}{dt} (\Gamma_n |g(\zeta_n)|^2) \right] - 2\pi \rho \operatorname{Im} [U a_1 e^{-i\theta}] + \frac{\rho \dot{A}}{2}. \quad (3.32)$$

Using (3.22) and (3.30), the barycentric torque is finally obtained as

$$\begin{aligned} \mathcal{T}^* = & \frac{\rho}{2} \sum_{n=1}^N \left\{ \dot{\Gamma}_n |g(\zeta_n) - g(\zeta_{n,0})|^2 + \frac{d}{dt} \left[ \Gamma_n \left( |g(\zeta_n)|^2 - R_0 - 2\operatorname{Re}(r(\zeta_n)) \right) \right] \right. \\ & \left. - 2\Gamma_n \operatorname{Re} \left[ U \left( \zeta_n - \frac{a^2}{\bar{\zeta}_n} \right) \right] \right\} + 2\pi \rho \operatorname{Im} [G_1 U^2] + 2\pi \rho \omega \operatorname{Re} [R_1 U] \\ & - \pi \rho \dot{\omega} \sum_{l=1}^{M+1} \frac{l |R_l|^2}{a^{2l}} - 2\pi \rho \operatorname{Im} [R_1 \dot{U}]. \end{aligned} \quad (3.33)$$

### Conservation of total momentum and comparison with the case of steady vortices

It is enlightening to compare the expressions (3.20) and (3.32) for the motion of a solid body shedding unsteady point vortices to the situation where the solid body does not shed vorticity but moves in a flow with pre-existing point vortices of steady intensity. Ramodanov (2000) derived the equations of motion of a cylinder and a single point vortex with steady intensity. It was also shown that the equations of motion of a two-dimensional solid body and  $N$  point vortices with steady intensity are Hamiltonian (Shashikanth et al., 2002; Shashikanth, 2005; Borisov et al., 2007b; Kanso and Oskouei, 2008).

From Kanso and Oskouei (2008), the force  $\mathbf{f}_s$  and barycentric torque  $\mathcal{T}_s^*$  on the solid body in the case of an inviscid flow with point vortices of steady intensity are obtained as

$$\mathbf{f}_s = -\frac{d\mathbf{p}_{fluid}}{dt}, \quad (3.34)$$

$$\mathcal{T}_s^* \mathbf{e}_3 = \frac{\rho}{2} \frac{d}{dt} \left( \sum_{k=1}^N \Gamma_k \|\mathbf{x}_k - \mathbf{c}\|^2 \right) \mathbf{e}_3 - \dot{\mathbf{c}} \times \mathbf{p}_{fluid} + \frac{\rho}{2} \frac{d}{dt} \int_C \|\mathbf{x} - \mathbf{c}\|^2 (\mathbf{n} \times \mathbf{u}) ds \quad (3.35)$$

with  $\mathbf{x}_k$  the position vector of vortex  $k$  and  $\mathbf{p}_{fluid}$  the fluid linear momentum

$$\mathbf{p}_{fluid} = \rho \int_C \mathbf{x} \times (\mathbf{n} \times \mathbf{u}) ds + \rho \sum_{k=1}^N \Gamma_k \mathbf{x}_k \times \mathbf{e}_3. \quad (3.36)$$

In (3.20),  $2\pi a_1 = i \int_{C_\infty} z w dz$  and using the identity (see for example Sedov, 1965)

$$\int_C z d\psi = \frac{dSc}{dt}, \quad (3.37)$$

the expression (3.20) derived for the force in the case of shedding of vortices with unsteady intensity can be rewritten  $f = -\dot{p}_{fluid}$  with  $p_{fluid} = -i\rho \int_C z d\phi - i\rho \sum \Gamma_k z_k$  with  $\phi$  the real part of the complex potential. This is equivalent (in complex notation) to the expression (3.34) obtained from the Hamiltonian system used in Kanso and Oskouei (2008). As in the derivation by Graham (1980) who obtained a result similar to (3.20) for a fixed solid, the form of the equation of motion for the point vortices (2.19) is essential as it allows one to cancel exactly any unbalanced force on the branch cut introduced by the shedding of a point vortex with unsteady intensity (see section 2.4.4). The momentum is conserved in the fluid in an integral sense around the vortex and the branch cut, which explains the similarity with the result of the Hamiltonian theory in Kanso and Oskouei (2008).

Following a similar approach and transferring (3.35) to complex notation, we observe that the three last terms on the right-hand side of (3.32) correspond to the three terms on the right-hand side of (3.35) in the same order. The shedding of unsteady point vortices introduces an additional term  $\mathcal{T}_v$  in the barycentric

torque applied on the solid, proportional to the product of the rate of change of each vortex intensity and of the square of the distance between that vortex and the generating corner.

A careful application of the conservation of angular momentum in an integral sense around the vortex and branch cut shows that, because of the form of (2.19), an unbalanced torque (2.29) remains on the branch cut equal to the opposite of the additional term  $\mathcal{T}_v$  (see section 2.4.5). Our analysis is therefore consistent with other studies on complex potential flows, in the sense that linear momentum is conserved, and the rate of change of the total angular momentum is equal to the opposite of the torque applied by the fluid on the branch cut.

The existence of this additional term is inherent to the vortex model chosen here as discussed in section 2.4.5. Because of the limited number of degrees of freedom available for the position of the point vortex (its intensity is fixed by the regularity condition), it is not possible to satisfy at the same time the conservation of linear and angular momentum around the vortex and branch cut.

### Added inertia contributions and momentum transfer to the vortices

In (3.23) and (3.33), the terms not involving  $\Gamma_n$  can be identified to added mass terms (see section 2.3.1). For the general shape considered here, the added-mass coefficients can be recovered from (3.23) and (3.33). Considering the reference directions 1 and 2 of added mass theory to coincide with the horizontal and vertical axes when  $\theta = 0$ , then the  $3 \times 3$  symmetric added-mass tensor  $\mathcal{M}_{ij}$  with  $i, j = 1, 2, 6$  is obtained as (see for example Newman (1977))

$$\mathcal{M} = \rho \begin{bmatrix} 2\pi [a^2 + \text{Re}(G_1)] - S & -2\pi \text{Im}(G_1) & -2\pi \text{Im}(R_1) \\ -2\pi \text{Im}(G_1) & 2\pi [a^2 - \text{Re}(G_1)] - S & 2\pi \text{Re}(R_1) \\ -2\pi \text{Im}(R_1) & 2\pi \text{Re}(R_1) & \pi \sum \frac{|R_l|^2}{a^{2l}} \end{bmatrix}. \quad (3.38)$$

The terms proportional to  $\Gamma_n$  or  $\dot{\Gamma}_n$  are additional forces and torques resulting from the shedding of vorticity. Using the results of section 3.2.4, they

can be divided into two kinds: those arising from the transfer of angular momentum and linear momentum from the solid to the fluid as explained in Shashikanth et al. (2002) and an additional torque, corresponding to an additional transfer of angular momentum because of the vortex representation chosen here.

### 3.2.5 Coupled equations of motion

We assume here that an external force  $\mathcal{F}(t)$  and torque  $\mathcal{T}(t)$  are applied on the solid body. The system of equations for the coupled vortex–solid problem is:

$$\begin{aligned} \mathcal{M}\ddot{c} = & \mathcal{F}(t) + \rho e^{i\theta} \left[ (2\pi a^2 - S)\dot{\bar{U}} - 2\pi G_1 \dot{U} - 2\pi i R_1 \dot{\omega} + i\omega(2\pi a^2 - S)\bar{U} \right. \\ & - 2\pi i \omega G_1 U + 2\pi R_1 \omega^2 + i \frac{d}{dt} \sum_{n=1}^N \Gamma_n \left( \zeta_n - \frac{a^2}{\bar{\zeta}_n} \right) \\ & \left. - \omega \sum_{n=1}^N \Gamma_n \left( \zeta_n - \frac{a^2}{\bar{\zeta}_n} \right) \right], \end{aligned} \quad (3.39)$$

$$\begin{aligned} I\dot{\omega} = & \mathcal{T}(t) + 2\pi\rho \text{Im}[G_1 U^2] + 2\pi\rho\omega \text{Re}[R_1 U] - \pi\rho\dot{\omega} \sum_{l=1}^{M+1} \frac{l|R_l|^2}{a^{2l}} - 2\pi\rho \text{Im}[R_1 \dot{U}] \\ & + \frac{\rho}{2} \sum_{n=1}^N \left\{ \dot{\Gamma}_n |g(\zeta_n) - g(\zeta_{n,0})|^2 - 2\Gamma_n \text{Re} \left[ U \left( \zeta_n - \frac{a^2}{\bar{\zeta}_n} \right) \right] \right. \\ & \left. + \frac{d}{dt} \left[ \Gamma_n \left( |g(\zeta_n)|^2 - R_0 - 2\text{Re}(r(\zeta_n)) \right) \right] \right\}, \end{aligned} \quad (3.40)$$

$$\begin{aligned} g'(\zeta_n)\dot{\zeta}_n + (g(\zeta_n) - g(\zeta_{n,0})) \frac{\dot{\Gamma}_n}{\Gamma_n} = & -i\omega g(\zeta_n) + \frac{1}{g'(\zeta_n)} \left[ \bar{U} - \frac{a^2}{\bar{\zeta}_n^2} U + i\omega \overline{r'(\zeta_n)} \right. \\ & \left. - \sum_{j \neq n} \frac{\Gamma_j}{2\pi i} \left( \frac{1}{\bar{\zeta}_n - \bar{\zeta}_j} - \frac{\zeta_j}{\zeta_j \bar{\zeta}_n - a^2} \right) + \frac{\Gamma_n}{2\pi i} \left( \frac{\zeta_n}{\zeta_n \bar{\zeta}_n - a^2} + \frac{\overline{g''(\zeta_n)}}{2g'(\zeta_n)} \right) \right], \end{aligned} \quad (3.41)$$

$$2\text{Im}(U\zeta_{p,0}) - \omega\zeta_{p,0}r'_p + \sum_{n=1}^N \frac{\Gamma_n}{2\pi} \left( 1 + 2\text{Re} \left[ \frac{\zeta_{p,0}}{\zeta_n - \zeta_{p,0}} \right] \right) = 0, \quad 1 \leq p \leq P \quad (3.42)$$

with  $U = -\dot{c}e^{i\theta}$ . At time  $t$ , the number of real unknowns is  $2N + P + 3$  [position and orientation of the solid body (3 unknowns), position of the vortices ( $2N$  unknowns)]

and intensity of the vortices being presently shed from each corner ( $P$  unknowns), the other intensities having been frozen to a known value]. The system (3.39)–(3.42) is a system of  $2N + P + 3$  equations [2 from Newton’s second law (3.39), 1 from the conservation of angular momentum (3.40),  $2N$  for the position of the vortices (3.41) and  $P$  from the regularity condition at each corner (3.42)].

### 3.3 Small-time behavior and vortex shedding

The system is started from rest at  $t = 0$  and evolves from this rest position because of an external force (e.g. gravity) or torque. The motion of the sharp edges induces the shedding of vortices from each corner. When a new vortex is started from a generating corner, the right-hand side of the equation of motion (3.41) for this vortex is singular as the vortex and its image conjugate are at the same point. We show in the following that the distance between the generating corner and the vortex in the mapped plane varies like a fractional power of time, consistent with the singular behavior at  $t = 0$ . The following section uses the same approach as in Cortelezzi and Leonard (1993) and Cortelezzi (1995), whose results are thereby extended to arbitrary body shapes and motions. We focus on the vortex shedding and, as in Cortelezzi and Leonard (1993), assume first that the solid motion is known. The initial behavior of the solid body can then be obtained from the small-time analysis of (3.39)–(3.40).

#### 3.3.1 Shedding of the first vortices

We first consider the case of the first vortex shed from each of the  $P$  generating corners when the motion of the solid is started. We assume that initially  $U \sim U_0 t^\alpha$  and  $\omega \sim \omega_0 t^\beta$ .

Defining the reduced variable  $\eta_p$  such that  $\zeta_p = \zeta_{p,0}(1 + \eta_p)$  and keeping

only the dominant terms in (3.41) and (3.42), we obtain for  $1 \leq p \leq P$

$$2\text{Im}(U\zeta_{p,0}) - \omega\zeta_{p,0}r'_p + \frac{\Gamma_p}{\pi}\text{Re}\left(\frac{1}{\eta_p}\right) = 0, \quad (3.43)$$

$$g''_p\eta_p\dot{\eta}_p + \frac{g''_p\eta_p^2}{2}\frac{\dot{\Gamma}_p}{\Gamma_p} = \frac{1}{a^4g''_p\bar{\eta}_p}\left[-2i\text{Im}(U\zeta_{p,0}) + i\omega\overline{\zeta_{p,0}r'_p} - \frac{i\Gamma_p}{2\pi}\left(\frac{1}{\eta_p + \bar{\eta}_p} + \frac{1}{2\bar{\eta}_p}\right)\right], \quad (3.44)$$

as the contribution of vortices  $j \neq p$  to the regularity condition at corner  $p$  and to the induced velocity on vortex  $p$  are negligible. Remembering that  $\zeta_{p,0}r'_p$  is real (see equation (3.13)), we can define the real quantity  $F_p(t) = 2\text{Im}(U\zeta_{p,0}) - \omega\zeta_{p,0}r'_p \sim F_{p0}t^\mu$ , with  $\mu = \min(\alpha, \beta)$  and obtain

$$\Gamma_p = -\frac{2\pi\eta_p\bar{\eta}_p}{\eta_p + \bar{\eta}_p}F_p(t) \quad (3.45)$$

$$\eta_p\dot{\eta}_p + \frac{\eta_p^2}{2}\frac{\dot{\Gamma}_p}{\Gamma_p} = -\frac{iF_p(t)}{a^4|g''_p|^2\bar{\eta}_p}\left(1 - \frac{\eta_p(3\bar{\eta}_p + \eta_p)}{2(\eta_p + \bar{\eta}_p)^2}\right). \quad (3.46)$$

If we decompose the complex number  $\eta_p$  into its polar representation, we obtain a system of equations identical to the one derived by Cortelezzi (1995) for the shedding of Brown–Michael point vortices from a semi-infinite plate with imposed motion. This is intuitively reasonable, as the initial shedding is expected to be driven by the local behavior of the flow, so the present approach generalizes previous results to arbitrary bodies with both translation and rotation. Using the same method as in Cortelezzi (1995), we obtain that, initially,

$$\begin{aligned} z_p - z_{p,0} &= \frac{\zeta_{p,0}^2 g''_p e^{i\theta}}{2} \eta_p^2, & \eta_p &= e^{-i\frac{\pi}{4}\text{sgn}(F_{p0})} \left[ \frac{|F_{p0}|}{a^4(2\mu + 1)|g''_p|^2\sqrt{2}} \right]^{1/3} t^{(\mu+1)/3}, \\ \Gamma_p &= -\text{sgn}(F_{p0})\pi \left[ \frac{2F_{p0}^4}{(2\mu + 1)a^4|g''_p|^2} \right]^{1/3} t^{(4\mu+1)/3}. \end{aligned} \quad (3.47)$$

Here,  $\eta_p^2$  is purely imaginary and  $g''_p\zeta_{p,0}^2e^{i\theta}$  is the orientation of the local tangent. Hence, the first vortices are shed orthogonally to the shedding corner.

We have shown that if  $U$  and  $\omega$  initially have power-law behaviors,  $t^\alpha$  and  $t^\beta$ , the circulation of the vortices behaves like  $t^{(4\mu+1)/3}$  and the distance to

the shedding corner like  $t^{2(\mu+1)/3}$ , where  $\mu = \min(\alpha, \beta)$ . Taking this information into account, we observe that in (3.39) and (3.40) the added mass terms initially dominate the contribution of the vortices. Under prescribed external forces and torques, the initial motion of the solid body is driven by added inertia. The influence of vortex shedding only becomes important later on. This is particularly convenient for the solution of this problem as it allows one to solve for the initial solid motion using added mass theory and then use the result for  $U$  and  $\omega$  to determine the initial behavior of the vortices.

### 3.3.2 Shedding of subsequent vortices

When a vortex reaches a maximum intensity at  $t = t_s$ , its intensity is frozen and a new vortex is started from the corresponding shedding corner to satisfy the regularity condition there. The vortices are also reindexed so as to keep the first  $P$  vortices be the ones with unsteady intensity. The equation of motion for the new vortex needs to be solved analytically at small time as the right-hand side of (3.41) displays an initial singularity as for the first vortices. Without loss of generality, we assume that the new vortex is shed from corner 1. This new vortex is labelled 1 while the vortex that was just frozen becomes vortex  $N$ . Because  $\dot{\Gamma}_N = 0$  and is continuous at  $t = t_s$ , the velocity of all vortices  $2 \leq j \leq N$  are continuous as well as their intensity and so is the velocity and rotation rate of the solid body.

As before, we define  $\eta$  so that  $\zeta_1 = \zeta_{1,0}(1 + \eta)$ . Substitution in (3.42) leads to:

$$2\text{Im}(U\zeta_{1,0}) - \omega\zeta_{1,0}r'_1 + \frac{\Gamma_1}{\pi}\text{Re}\left(\frac{1}{\eta}\right) + \sum_{n=2}^N \frac{\Gamma_n}{2\pi} \left[1 + 2\text{Re}\left(\frac{\zeta_{1,0}}{\zeta_n - \zeta_{1,0}}\right)\right] = 0. \quad (3.48)$$

We assume that  $\eta \sim \tau^\delta$ ,  $\Gamma_1 \sim \tau^\gamma$  (with  $\tau = t - t_s$  and  $t_s$  the time of shedding) and that  $\text{Re}(\eta)$  is not initially negligible compared to  $|\eta|$ ; by dominant balance in the previous equation, enforcing the regularity condition at  $t = t_s^\pm$ , we obtain  $\gamma = \delta + 2$ . Then, the effect of the new vortex in the right-hand side of (3.41) is

negligible and by dominant balance  $\delta = 1/2$  and  $\gamma = 5/2$ . The equation of motion (3.41) simplifies, keeping only the dominant terms and using (3.42),

$$\begin{aligned} \zeta_{1,0}^2 g_1'' \left( \eta \dot{\eta} + \frac{5\eta^2}{4\tau} \right) &= -i\omega g_1 + \frac{1}{g_1'' \zeta_{1,0}^2} \left[ 2U\zeta_{1,0} + i\omega \overline{r_1'' \zeta_{1,0}^2} \right. \\ &\quad \left. + \sum_{n=2}^N \frac{i\Gamma_n}{2\pi} \left( \frac{\zeta_k^2 \bar{\zeta}_{1,0}^2}{(\zeta_j \zeta_{1,0} - a^2)^2} - \frac{\bar{\zeta}_{1,0}^2}{(\bar{\zeta}_{1,0} - \bar{\zeta}_n)^2} \right) \right], \end{aligned} \quad (3.49)$$

where all quantities other than  $\eta$  are evaluated at  $\tau = 0$ . The right-hand side of the previous equation is  $O(1)$ , and corrections to that approximation would only add terms of order  $O(\tau)$  that are initially negligible. Using (3.13), (3.14) and  $\zeta_{1,0} \bar{\zeta}_{1,0} = a^2$ ,

$$\begin{aligned} a^4 |g_1''|^2 \left( \eta \dot{\eta} + \frac{5\eta^2}{4\tau} \right) &= 2\text{Re}(U\zeta_{1,0}) + i\omega \overline{(\zeta_{1,0} r_1' - \bar{g}_1 g_1'' \zeta_{1,0}^2 + r_1'' \zeta_{1,0}^2)} \\ &\quad - \sum_2^N \frac{\Gamma_n}{\pi} \text{Im} \left( \frac{\zeta_{1,0} \zeta_n}{(\zeta_n - \zeta_{1,0})^2} \right). \end{aligned} \quad (3.50)$$

This can be integrated for  $\eta$  to give

$$\begin{aligned} \eta^2 &= C\tau, \quad \text{with} \\ C &= \frac{4}{7a^4 |g_1''|^2} \left[ 2\text{Re}(U\zeta_{1,0}) + i\omega \overline{(\zeta_{1,0} r_1' - \bar{g}_1 g_1'' \zeta_{1,0}^2 + r_1'' \zeta_{1,0}^2)} \right. \\ &\quad \left. - \sum_2^N \frac{\Gamma_n}{\pi} \text{Im} \left( \frac{\zeta_{1,0} \zeta_n}{(\zeta_n - \zeta_{1,0})^2} \right) \right]. \end{aligned} \quad (3.51)$$

From (3.13), we observe that  $C$ , and therefore  $\eta^2$ , are purely real. In physical space,

$$z_1 - z_{1,0} = \frac{C}{2} e^{i\theta} g_1'' \zeta_{1,0}^2 \tau, \quad (3.52)$$

and the vortex is shed parallel to the local tangent at the shedding corner whose direction is given by  $e^{i\theta} g_1'' \zeta_{1,0}^2$ . This result extends to arbitrary motions and shapes the result obtained by Cortelezzi and Leonard (1993) for a semi-infinite plate in pure translation. It is consistent with the physical analysis of Graham (1977): at the time of shedding, the vortices already present cancel the normal background flow through the regularity condition and the flow is therefore dominated by the

tangential component at the corner, which carries the newly shed vortex parallel to the tangential direction. Note that we restrict ourselves here to the case of flat corners (zero angle). In the case of a finite angle, the direction of shedding depends on the direction of the flow at the corner (Graham, 1977).

### 3.3.3 Favorable and unfavorable shedding conditions

If  $C > 0$ ,  $\eta$  is purely real and the vortex goes out of the solid body. However, if  $C < 0$ ,  $\eta$  is purely imaginary and this violates the initial assumption of this analysis that  $\text{Re}(\eta)$  is not negligible compared to  $\text{Im}(\eta)$ . Carrying out the small-time analysis to the next order shows that  $\zeta_1$  is located on the circle  $\mathcal{C}$ . Hence, in the physical plane, the vortex is pushed by the flow onto the solid boundary  $\mathcal{C}$ . This is problematic as the vortex and its image would be at the same position and this introduces a singularity in the equations. The case  $C < 0$  is of the same nature as the limitations to the vortex sheet method presented in Jones (2003) and Jones and Shelley (2005). In those works, it is observed that the integration fails if a newly shed Lagrangian element of the vortex sheet is forced to remain on the solid boundary by the outside flow. Our numerical simulations with prescribed motions confirm the observations by Jones (2003) that this problem occurs mainly at low angles of attack when  $\text{Re}(U\zeta_{1,0})$  is negative, but that it can also occur at high angles of attack, when the solid body is forced to interact with its own wake. Cortelezzi and Leonard (1993) considered the occurrence of such an event to be the result of a numerical error. This does not contradict our analysis as the situations considered numerically by Cortelezzi and Leonard (1993) involved the motion of a plate normal to itself with no reversal of the direction of motion, so that vortices are always carried away from the plate. In that case,  $C < 0$  does not occur.

We refer to the case  $C > 0$  (resp.  $C < 0$ ) as favorable (resp. unfavorable) shedding conditions. The case  $C < 0$  is the main limitation of the present method. It is expected that a purely inviscid approach cannot resolve this issue, as

physically, in such a situation of shedding at low angle of attack, the new vortex is expected to remain trapped near the shedding edge and interact with the boundary layer, a situation that is not described well by an inviscid model. However, because of the discrete shedding mechanism used here, the occurrence of  $C < 0$  is only problematic when a new vortex is being shed.

### 3.4 Example: stability of the broadside-on fall of a two dimensional flat plate.

In this section, we use the method outlined previously for a general solid body to study the particular case of a falling two-dimensional flat plate. This problem, known as Maxwell’s problem (Maxwell, 1854), has been extensively studied experimentally for objects such as falling disks (Willmarth et al., 1964; Field et al., 1997) and long falling plates (Smith, 1971; Belmonte et al., 1998; Belmonte and Moses, 1999; Andersen et al., 2005b). The similar problem of the oscillatory motion of a rising buoyant cylinder was also investigated recently (Fernandes et al., 2005, 2007). Depending on  $Re$  and the relative inertia of the fluid and solid, different regimes have been observed. Defining  $Re$  based on the solid’s chord or width, the typical terminal velocity and the fluid viscosity, it was observed that, below a critical  $Re_c$  (typically  $Re_c \sim 200$ ), the fall in the broadside-on (horizontal) position is stable. Initial non-zero angles lead to viscously dampened fluttering oscillations (Willmarth et al., 1964). At higher  $Re$ , the dampened regime is not observed. From a non-horizontal initial orientation, three regimes are typically observed: periodic fluttering, periodic tumbling or chaotic (Smith, 1971; Field et al., 1997). More recently two-dimensional numerical simulations were performed for a falling ellipse using moving fitted grids (Huang, 2001; Andersen et al., 2005b). Using the inviscid approach described in the present paper, we study as an example the effect of vortex shedding on the stability of the broadside-on fall. The experimental and numerical results at large  $Re$  predict a destabilization of the broadside-on fall

(Willmarth et al., 1964; Smith, 1971; Field et al., 1997).

A homogeneous plate of half-length  $l$ , mass  $\mathcal{M}$  and negligible thickness is released from rest at  $t = 0$  with an initial angle to the horizontal  $\theta_0$  ( $-\pi/2 \leq \theta_0 \leq \pi/2$ ), and falls under the effect of gravity so that  $\mathcal{F}(t) = -i\mathcal{M}g$  and  $\mathcal{T}(t) = 0$ . Its moment of inertia is  $I = \mathcal{M}l^2/3$ . The center of mass of the plate is initially at the origin of a fixed system of axes in the inertial laboratory frame. In the following, all quantities are non-dimensionalized using the half-length  $l$  of the plate, the density of the fluid  $\rho$  and gravity  $g$  as reference scales. Two non-dimensional parameters characterize the problem:  $\theta_0$ , the initial release angle, and the ratio of solid and fluid inertia identified as the Froude number in Jones and Shelley (2005):  $Fr = \mathcal{M}/2\rho l^2$ .

### 3.4.1 Equations of motion

#### Coupled equations for the vortex-plate system

The plate of unit half-length is obtained using the particular mapping:

$$g(\zeta) = \zeta + \frac{a^2}{\zeta} \quad (3.53)$$

with  $a = 1/2$ . In the framework of the present paper, all the coefficients  $G_j$  are zero except for  $G_{-1} = 1$  and  $G_1 = a^2 = 1/4$ . From (3.9), we obtain that all  $R_j$  are equal to zero except for  $R_0 = 2a^2 = 1/2$  and  $R_2 = a^4 = 1/16$ . The solid body has two sharp corners,  $\phi_1 = 0$  and  $\phi_2 = \pi$ , corresponding to  $\zeta_{1,0} = a$  and  $\zeta_{2,0} = -a$ , where  $g_1'' = 2/a = 4$  and  $g_2'' = -2/a = -4$  (see Figure 3.3). The complex potential (3.11) and velocity (3.12) simplify to

$$F = -\frac{2ia^2\text{Im}(U)}{\zeta} - \frac{i\omega a^4}{\zeta^2} + \sum_{n=1}^N \frac{\Gamma_n}{2\pi i} \log \left( \frac{\zeta - \zeta_n}{\zeta - \frac{a^2}{\zeta_n}} \right), \quad (3.54)$$

$$w = \dot{c} + \frac{\zeta^2 e^{-i\theta}}{\zeta^2 - a^2} \left[ U - \frac{a^2 \bar{U}}{\zeta^2} + \frac{2i\omega a^4}{\zeta^3} + \sum_{n=1}^N \frac{\Gamma_n}{2\pi i} \left( \frac{1}{\zeta - \zeta_n} - \frac{\bar{\zeta}_n}{\zeta \bar{\zeta}_n - a^2} \right) \right] \quad (3.55)$$

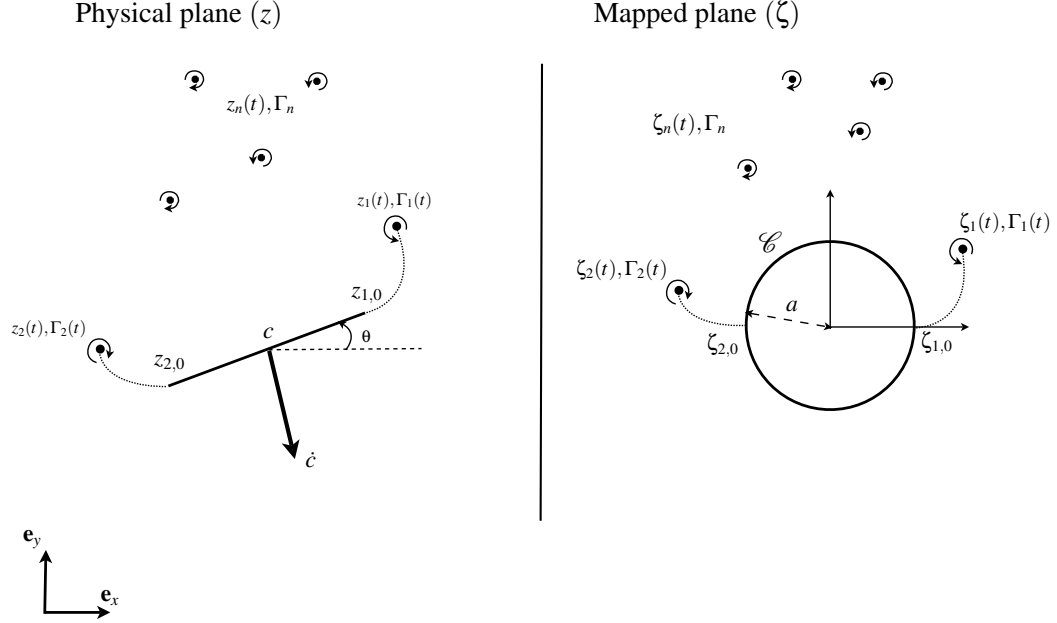


**Figure 3.3:** Notation of Figure 3.1 adapted for the particular case of a falling card. The position of the plate's center of mass is noted  $c$  and the orientation  $\theta$  is the angle between the plate and the horizontal axis. In the mapped plane, the two shedding corners  $\zeta_{1,0}$  and  $\zeta_{2,0}$  are the intersections of the circle  $\mathcal{C}$  with the horizontal axis.

where, as before,  $\dot{c} = -\bar{U}e^{i\theta}$ . The plate is infinitely thin so  $S = 0$  and there is no buoyancy effect. The only force externally applied on the plate is gravity. In non-dimensional form, the system of coupled equations for the motion of the vortices and the plate is obtained from (3.39)–(3.42).

$$2Fr(\ddot{c} + i) = e^{i\theta} \left[ -i\pi\text{Im}(\dot{U}) + \pi\omega\text{Im}(U) + i\frac{d}{dt} \sum_{n=1}^N \Gamma_n \left( \zeta_n - \frac{a^2}{\bar{\zeta}_n} \right) - \omega \sum_{n=1}^N \Gamma_n \left( \zeta_n - \frac{a^2}{\bar{\zeta}_n} \right) \right], \quad (3.56)$$

$$\left( \frac{2Fr}{3} + \frac{\pi}{8} \right) \dot{\omega} = \pi\text{Im}[U]\text{Re}[U] + \frac{1}{2} \sum_{n=1}^N \left\{ \dot{\Gamma}_n \frac{|\zeta_n - \zeta_{n,0}|^4}{|\zeta_n|^2} - 2\Gamma_n \text{Re} \left[ U \left( \zeta_n - \frac{a^2}{\bar{\zeta}_n} \right) \right] + \frac{d}{dt} \left[ \Gamma_n (\zeta_n \bar{\zeta}_n - a^2) \left( 1 + \frac{a^2}{\zeta_n^2} + \frac{a^2}{\bar{\zeta}_n^2} - \frac{a^2}{\zeta_n \bar{\zeta}_n} \right) \right] \right\}, \quad (3.57)$$

$$\begin{aligned} \left(1 - \frac{a^2}{\zeta_n^2}\right) \dot{\zeta}_n + \frac{(\zeta_n - \zeta_{n,0})^2 \dot{\Gamma}_n}{\zeta_n \Gamma_n} = -i\omega \left(\zeta_n + \frac{a^2}{\zeta_n}\right) + \frac{\bar{\zeta}_n^2}{\bar{\zeta}_n^2 - a^2} \left[\bar{U} - \frac{a^2}{\bar{\zeta}_n^2} U - \right. \\ \left. - \frac{2i\omega a^4}{\bar{\zeta}_n^3} - \sum_{j \neq n} \frac{\Gamma_j}{2\pi i} \left(\frac{1}{\bar{\zeta}_n - \bar{\zeta}_j} - \frac{\zeta_j}{\zeta_j \bar{\zeta}_n - a^2}\right) \right. \\ \left. + \frac{\Gamma_n}{2\pi i} \left(\frac{\zeta_n}{\zeta_n \bar{\zeta}_n - a^2} + \frac{a^2}{\bar{\zeta}_n(\bar{\zeta}_n^2 - a^2)}\right) \right], \end{aligned} \quad (3.58)$$

$$\pm \text{Im}(U) + \omega a + \sum_{n=1}^N \frac{\Gamma_n}{4\pi a} \left(1 \pm 2\text{Re} \left[\frac{a}{\zeta_n \mp a}\right]\right) = 0. \quad (3.59)$$

The system (3.56)–(3.59) is a complete system of ordinary differential equations for the plate's position  $c$  and orientation  $\theta$ , the vortices positions  $z_n$  (or equivalently  $\zeta_n$  in the mapped plane) and the two unknown intensities  $\Gamma_1$  and  $\Gamma_2$ .

The limit case  $Fr = 0$  deserves some additional comment. In that case, the left-hand side of (3.56) vanishes while the left-hand side of (3.57) does not. However, on the right-hand side of (3.56) added-mass terms depend on  $\ddot{c}$  through  $\dot{U}$  and therefore (3.56) does not degenerate into an algebraic equation. Furthermore, in the case  $Fr = 0$ , the forcing gravity term disappears, and the solution of (3.56)–(3.59) is trivial: the body does not move and no vortex is shed.

### Small-time behavior

We have shown in section 3.3.1 that initially, the effects of vortex shedding are negligible compared to added-inertia. Retaining only added-inertia terms, by dominant balance in (3.56) and (3.57), we obtain that  $\dot{c}$  and therefore  $U$  are initially linear functions of time while  $\omega \sim t^3$ . The small-time behavior of the falling card is obtained from (3.56) and (3.57) defining  $c = x_c + iy_c$ :

$$\dot{\omega} = O(t^2), \quad \ddot{x}_c = -\frac{\pi \sin 2\theta_0}{2(\pi + 2Fr)} + O(t), \quad \ddot{y}_c = -1 + \frac{\pi \cos^2 \theta_0}{\pi + 2Fr} + O(t) \quad (3.60)$$

which is equivalent to the results of Jones and Shelley (2005), since in both the point vortex and the vortex sheet methods, the initial behavior of the falling card is dominated by added mass effects. The initial acceleration of the plate makes an angle  $\theta_f$  with the vertical ( $\tan \theta_f = \ddot{x}/\ddot{y}$ ) which depends on both  $\theta_0$  and  $Fr$

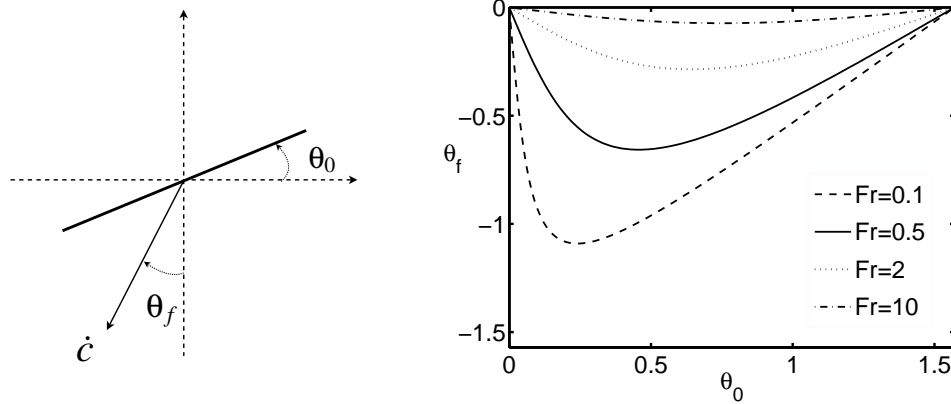


**Figure 3.4:** (Left) When the plate is released with an initial orientation  $\theta_0$ , its initial velocity and acceleration make an angle  $\theta_f$  with the vertical axis. Note that  $\theta_f < 0$  if  $\theta_0 > 0$ . (Right) Variations of  $\theta_f$  with  $\theta_0$  for different values of  $Fr$ . The case  $\theta_0 < 0$  is obtained by symmetry.

(see Figure 3.4). For all  $Fr$ , the plate falls vertically if  $\theta_0 = 0$  (broadside-on) or  $\theta_0 = \pm\pi/2$  (edge-on). For large  $Fr$  (heavy plate), the plate's initial fall is almost vertical ( $|\theta_f| \ll 1$ ) as the inertia of the fluid is negligible compared to the solid's. For small  $Fr$  (light plate), the plate tends to slide initially parallel to itself ( $\theta_f \sim \theta_0 - \pi/2$ ) in order to reduce the relative flow normal to the plate that induces the largest added inertia.

Then, we obtain from (3.60) and  $U = -\dot{c}e^{i\theta}$  that initially

$$U \sim U_0 t, \quad \text{with } U_0 = \left( \frac{\pi \sin \theta_0}{\pi + 2Fr} - \frac{2iFr e^{i\theta_0}}{\pi + 2Fr} \right) t. \quad (3.61)$$

From the results of section 3.3.1, the initial motion of the two vortices is obtained as

$$z_1 - (c + e^{i\theta_0}) = z_2 - (c - e^{i\theta_0}) = \frac{ie^{i\theta_0} t^{4/3}}{2} \left[ \frac{2Fr \cos \theta_0}{3\sqrt{2}(\pi + 2Fr)} \right]^{2/3}, \quad (3.62)$$

$$\Gamma_1 = -\Gamma_2 = 4\pi t^{5/3} \left[ \frac{Fr^4 \cos^4 \theta_0}{6(\pi + 2Fr)^4} \right]^{1/3}.$$

The trajectories of the vortices relative to the plate are initially symmetric as their initial motion is driven by the normal component of the local flow, that is identical for each of the shedding corners.

## Numerical solution

The system of ODEs (3.56)–(3.59) is solved using the variable time-step Matlab ODE solver `ode45`. The integration is done analytically using (3.60) and (3.62) over the first time step  $\Delta t$  (typically  $10^{-5}$ ) because the solver can not handle directly the singular initial behavior of (3.58). The event tracking function is used to detect when  $\dot{\Gamma}_1$  or  $\dot{\Gamma}_2$  vanishes at which point the integration is stopped, the corresponding vortex intensity becomes frozen, the vortices are reindexed accordingly and a new vortex is started. As for the first vortices, the system is integrated by hand for the first time step, using the results of section 3.3.2 whose main result (3.51) becomes, in the particular case studied here,

$$\zeta_1 \sim \zeta_{1,0}(1 + \eta), \quad \text{with } \eta^2 = \frac{4\tau}{7} \left[ 2\text{Re}(U) - \sum_{n=2}^N \frac{\Gamma_n}{\pi} \text{Im} \left( \frac{\zeta_n}{(\zeta_n - \zeta_{1,0})^2} \right) \right]. \quad (3.63)$$

As discussed in 3.3.3,  $\eta^2$  is purely real, and depending on its sign, leads to favorable or unfavorable shedding conditions. In the former case, a new vortex is started successfully and the integration is carried on further using the ODE solver. In the latter case, the integration stops since the shedding of the new vortex cannot be handled using an inviscid vortex method.

### 3.4.2 Fall of a horizontal card

When the card is released initially with  $\theta_0 = 0$ , the problem is symmetric with respect to the vertical axis, and this symmetry remains at all time. The card falls vertically with  $\theta = 0$  (broadside-on). One vortex is shed from each corner with opposite intensities and symmetric positions with respect to the vertical axis. The intensity of these vortices never reaches an extremum so no new vortex is shed. We denote by  $d_v = \text{Im}(z_1 - c) = \text{Im}(z_2 - c)$  the vertical distance between the plate and the vortex pair.

Both fluid effects (added inertia and vortex shedding) tend to slow down the plate (see Figure 3.5a) as they both correspond to a transfer of negative vertical

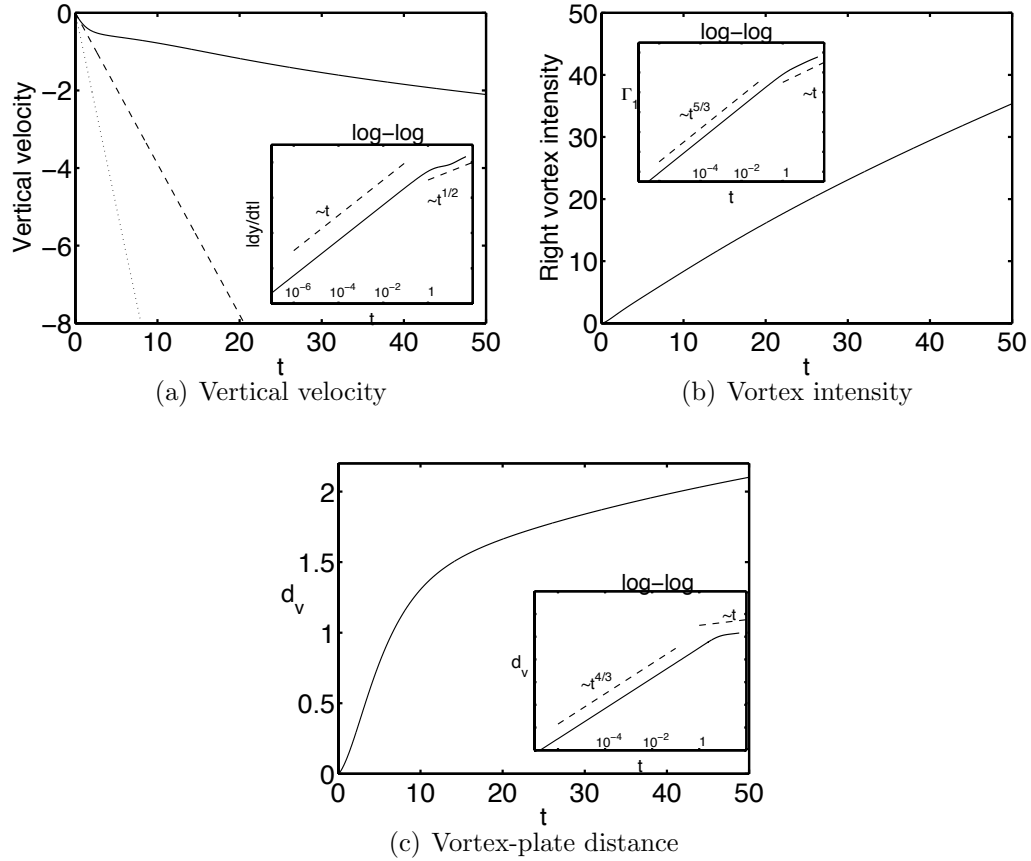


**Figure 3.5:** Broadside-on fall of a card ( $\theta_0 = 0$ ) for  $Fr = 1$ . (a) Vertical velocity of the plate: (solid) full vortex shedding model, (dashed) added inertia only and (dotted) fall in vacuum. (b) Intensity of the right vortex. (c) Vertical distance  $d_v$  between the vortex pair and the plate. In each plot, the insert gives a logarithmic plot of the corresponding quantity obtained with the full vortex shedding model to identify scalings.

momentum to the fluid. Figure 3.5 allows us to identify different phases in the broadside-on fall. During the first phase ( $t < 1$  for  $Fr = 1$ ), the motion of the plate is dominated by added inertia and gravity. The distance  $d_v$  and intensity  $\Gamma_1$  follow the scaling laws obtained in (3.62). After a transition phase ( $1 < t < 15$ ), during which the vortex shedding influence becomes important and the plate acceleration quickly decreases, a long-time regime is achieved in which the fluid forces almost balance gravity. Although the plate dynamics does not seem to follow an exact power-law, its vertical velocity behaves almost like  $\sqrt{t}$ . The vortex wake intensity grows linearly in time and its distance to the plate varies like  $t^{1/4}$ . This distance varies much slower than the plate vertical position, so the vortex pair seems trapped in the wake of the falling card.

As in Jones and Shelley (2005), when redefining the time scale such that  $t' = t\sqrt{Fr}$  and rescaling the other quantities accordingly, the time evolution of the different quantities for different values of  $Fr$  collapse onto similar evolution curves (see Figure 3.6). With this new reference time-scale, the evolution of the system is almost independent of  $Fr$ . Note that the agreement is best at low  $Fr$  (typically  $Fr < 1$ ).

### 3.4.3 Comparison with added mass analysis

Before studying the behavior of a falling card released with a non-zero angle, we present a brief summary of the solid motion obtained by representing the fluid effects with added inertia only. This also will be useful in the remaining sections to emphasize the effect of vortex shedding. In this section only, the fluid forces and torques are entirely given by the added inertia contribution. Viscosity and vorticity are both neglected. The equations of motion can be obtained from added-mass theory (Newman, 1977) or directly from (3.56)–(3.57) by removing the

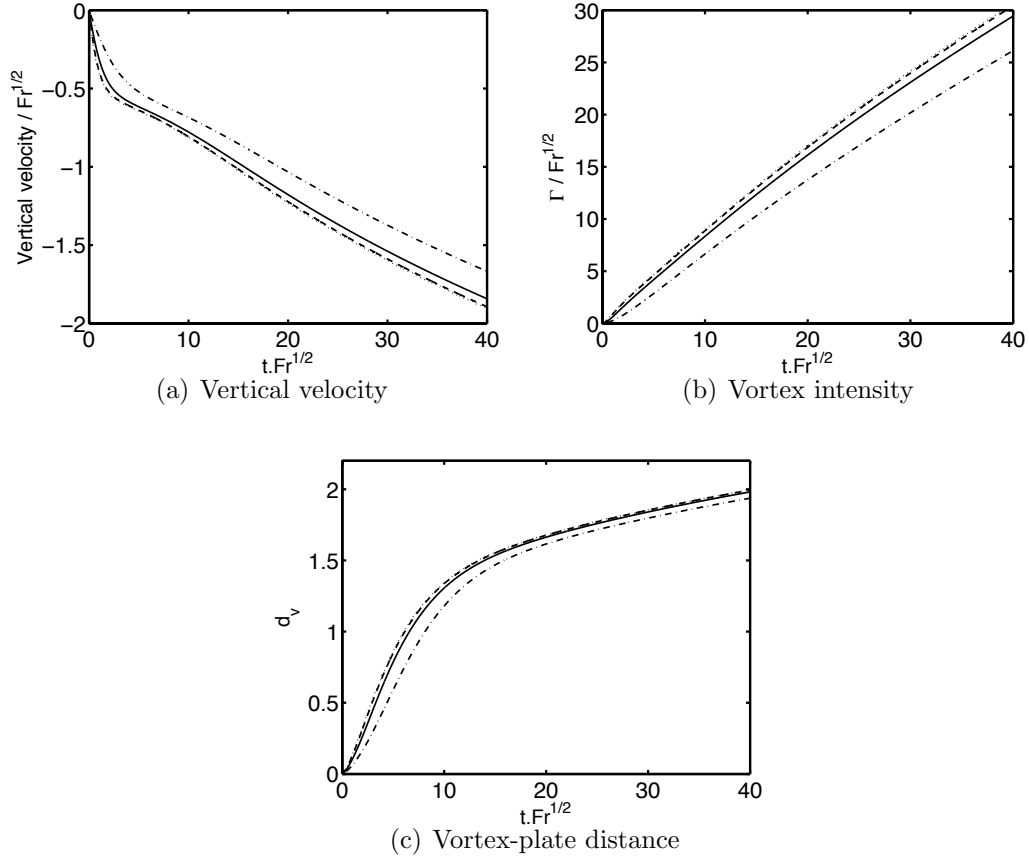


**Figure 3.6:** Scalings of the broadside-on fall with  $Fr$ : (left) the vertical velocity of the plate, (center) the intensity of the vortices and (right) the vertical distance between the vortices and the plate are plotted for  $Fr = 0.05$  (dotted),  $Fr = 0.2$  (dashed),  $Fr = 1$  (solid) and  $Fr = 4$  (dash-dotted), against a rescaled time  $t\sqrt{Fr}$ . The different quantities (velocity, circulation) are rescaled accordingly.

contribution of the vortices:

$$\begin{aligned}
 \left(\frac{2Fr}{\pi} + \sin^2 \theta\right) \ddot{x}_c - \frac{1}{2} \sin 2\theta \ddot{y}_c &= \dot{\theta} (\dot{y}_c \cos 2\theta - \dot{x}_c \sin 2\theta), \\
 -\frac{1}{2} \sin 2\theta \ddot{x}_c + \left(\frac{2Fr}{\pi} + \cos^2 \theta\right) \ddot{y}_c &= -\frac{2Fr}{\pi} + \dot{\theta} (\dot{y}_c \sin 2\theta + \dot{x}_c \cos 2\theta), \\
 \left(\frac{1}{8} + \frac{2Fr}{3\pi}\right) \ddot{\theta} &= \left(\frac{\dot{x}_c^2 - \dot{y}_c^2}{2}\right) \sin 2\theta - \dot{x}_c \dot{y}_c \cos 2\theta.
 \end{aligned} \tag{3.64}$$

From (3.64) or its equivalent in a system of axes attached to the plate, an equation for the orientation  $\theta$  only can be obtained (Mahadevan, 1996)

$$\left(\frac{1}{8Fr} + \frac{2}{3\pi}\right)\ddot{\theta} + \frac{t^2 \sin 2\theta}{(\pi + 2Fr)} = 0, \quad \text{with } \dot{\theta}(0) = 0 \text{ and } \theta(0) = \theta_0 \quad (3.65)$$

and the motion of the plate's center of mass is recovered from  $\theta$  using

$$\dot{x}_c = -\frac{\pi t \sin 2\theta}{2(\pi + 2Fr)}, \quad \dot{y}_c = -\frac{t}{\pi + 2Fr} (2Fr + \pi \sin^2 \theta). \quad (3.66)$$

The solution of (3.65) has an oscillatory behavior with decreasing amplitude as confirmed by the WKB solution valid for small initial angle  $\theta_0$  and  $t \gg 1$ :

$$\theta(t) \sim \frac{C_0}{\sqrt{t}} \cos \left( t^2 \sqrt{\frac{12\pi Fr}{(\pi + 2Fr)(3\pi + 16Fr)}} + \phi_0 \right), \quad (3.67)$$

with  $C_0$  and  $\phi_0$ , two constants obtained by matching with the initial behavior. Exploring the parameter space  $(\theta_0, Fr)$  shows that, in two dimensions, added inertia only produces a fluttering behavior with algebraically decreasing amplitude and linearly increasing frequency. This is consistent with other theoretical studies that showed that  $\theta = 0$  is a stable position and  $\theta = \pm\pi/2$  an unstable position (Kozlov, 1989; Mahadevan, 1996). Adding asymmetric viscous drag can generate other regimes like tumbling (Kozlov, 1990; Mahadevan, 1996). See also Borisov et al. (2007a) for a more complete review of the asymptotic behavior of a falling solid body in an ideal fluid with no shed vorticity.

For large  $Fr$  (heavy plate), the solid inertia is dominant and the motion tends to a pure translation (oscillation in  $\theta$  with zero frequency). For small  $Fr$ , the forcing on the solid occurs over a very long time scale  $Fr^{-1/2}$  and the motion of the plate is negligible unless  $t \gg 1$ . The oscillation frequency grows the fastest when both the solid and fluid inertia are comparable, emphasizing the fluid-solid interaction nature of the fluttering motion.

These results show that an infinite- $Re$  model based exclusively on added-inertia (therefore neglecting both viscosity and vorticity shedding) fails to explain

the destabilization of the broadside-on fall observed in high- $Re$  experiments. The shedding of vorticity from the plate edges is therefore essential to understand the behavior of the falling plate when viscosity is neglected.

### 3.4.4 Stability of broadside-on fall

We now consider the case of a card released with a small non-zero initial angle  $\theta_0$  using the vortex shedding model. A wide range of the parameter space  $(\theta_0, Fr)$  was explored, leading to the following result: a card initially released with a small non-zero initial angle undergoes fluttering oscillations with growing amplitude (see Figures 3.7 and 3.8). The broadside-on fall position is therefore unstable<sup>1</sup>; this is consistent with the results obtained using the full vortex sheet representation (Jones and Shelley, 2005).

We are interested in the development of the instability and how it is influenced by the two non-dimensional parameters  $Fr$  and  $\theta_0$ . Figures 3.7 and 3.8 show the behavior of the falling card for  $\theta_0 = \pi/1024$  and increasing values of  $Fr$ . In all three experiments, new vortices are shed according to the shedding criterion described in the previous sections (three or four in the cases presented in Figures 3.7 and 3.8). The wake is dominated by a pair of strong counter-rotating vortices, whose primary effect is to slow down the falling card. The asymmetry introduced by the fluttering motion of the plate is clearly visible on the plot of the streamlines. The plate undergoes a fluttering motion with growing amplitude as can be seen in the variation of its orientation and horizontal position.

### Scaling of the instability development

During this growing fluttering motion, the orientation angle is observed to oscillate within an exponential envelope (Figure 3.9). We can define the growth

---

<sup>1</sup>We understand here by instability that for any small value of the initial angle (initial values  $\theta_0$  as low as  $\pi/2^{15}$  were tested), the plate is observed to move away from the broadside-on equilibrium. We do not attempt to provide a mathematical proof of the instability of the time-dependent solution of equations (3.56)–(3.59).

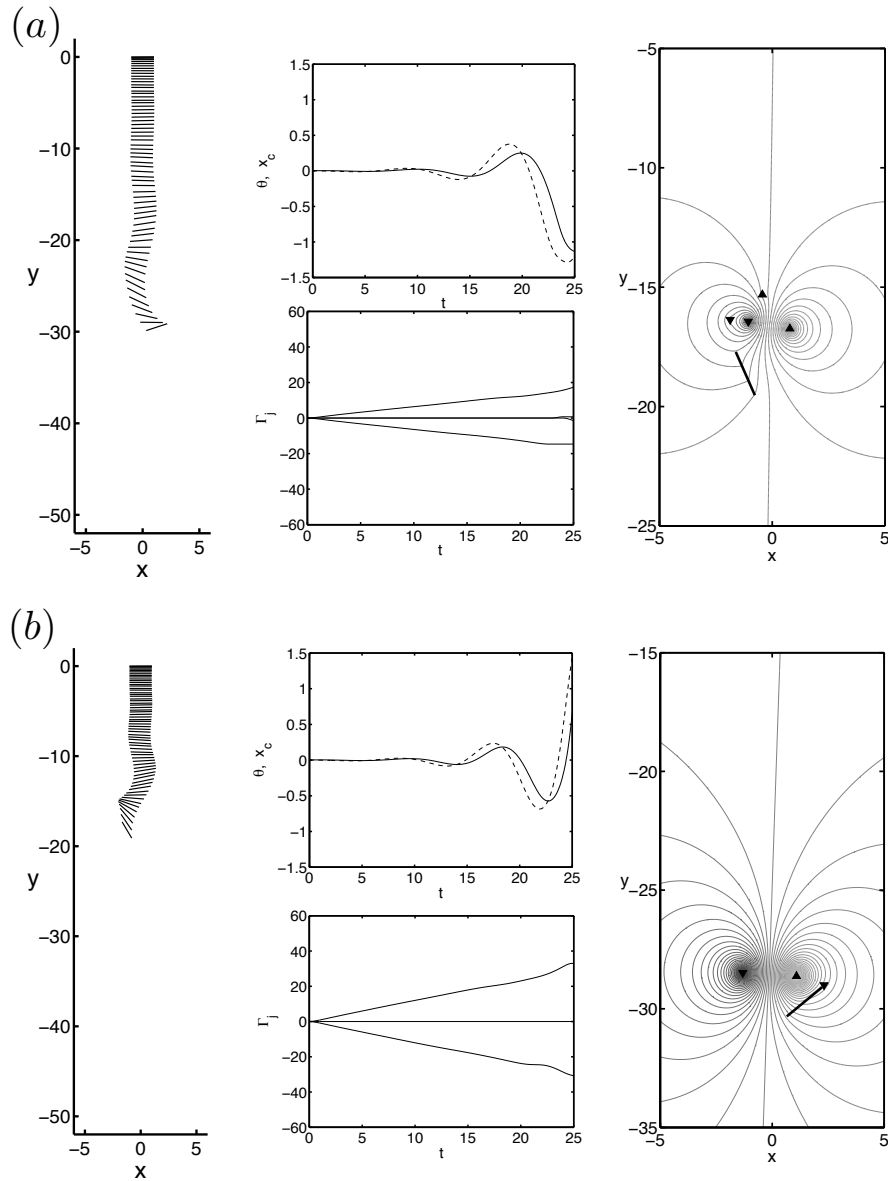


**Figure 3.7:** Fall of a card released with an initial angle  $\theta_0 = \pi/1024$  and (a)  $Fr = 0.75$  and (b)  $Fr = 1.5$  for  $0 \leq t \leq 25$ . (Left) The plate position is plotted every  $\Delta t = 0.4$ . (Center-top) Evolution of the plate orientation (solid) and of the horizontal position of its center of mass (dashed). (Center-bottom) Intensity of the successively shed vortices. (Right) Streamlines of the flow around the falling plate and positions of the vortices at  $t = 25$ . Positive (resp. negative) vortices are represented with upward- (resp. downward-) pointing triangles. To show the difference in velocity magnitude between the different cases, the spacing between two streamlines corresponds to a difference in the streamfunction of 0.5 for all values of  $Fr$ .

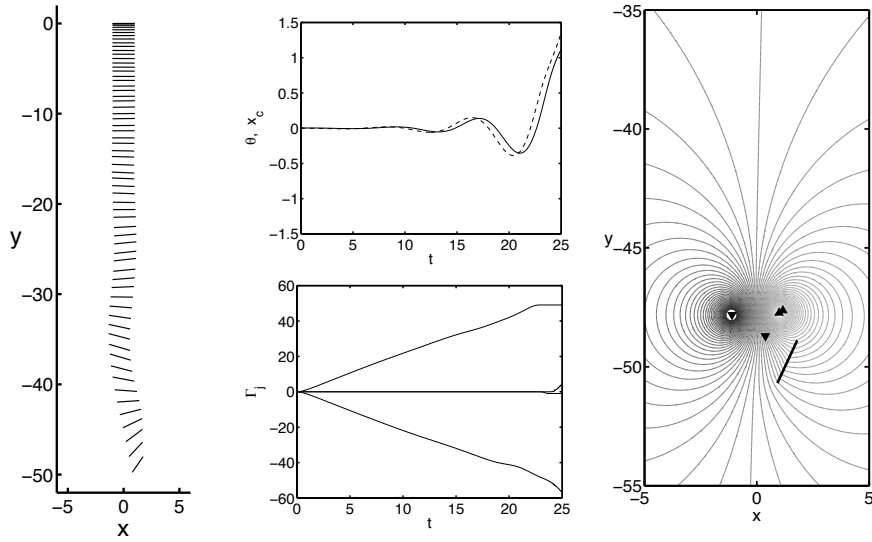


**Figure 3.8:** Fall of a card released with an initial angle  $\theta_0 = \pi/1024$  and  $Fr = 3$  (same as in Figure 3.7).

rate  $\sigma$  of the instability characterizing the exponential envelope and a pseudoperiod  $\tau$  for the oscillations. Figure 3.9 shows the influence of  $Fr$  and  $\theta_0$  on the evolution of  $\theta$ . We observe that the variations of  $\theta/\theta_0$  are independent of  $\theta_0$  during the growth regime. The influence of  $\theta_0$  becomes important when  $\theta$  reaches  $O(1)$  values and the exponential growth saturates. The Froude number  $Fr$  is observed to influence the pseudoperiod of the oscillations. However, the growth rate of the instability (that determines the shape of the exponential envelope on Figure 3.9a) seems independent of  $Fr$ .

This qualitative analysis is confirmed by the quantitative results of Figure 3.10. Focusing on the successive extrema of the orientation  $\theta_m$ , we observe that for all  $Fr$ ,  $|\theta_m| \sim \theta_0 e^{\sigma t}$  with  $\sigma = 0.23$  (Figure 3.10a). The pseudoperiod  $\tau$  of the oscillations is obtained using the successive occurrences of  $\theta = 0$  and is plotted on Figure 3.10(b) against  $Fr$ , showing a slow decrease of the pseudo-period with  $Fr$ , and  $\tau \sim Fr^{-0.12}$ . This very weak dependance in  $Fr$  is consistent with the observations of Jones and Shelley (2005), when the different variables are rescaled

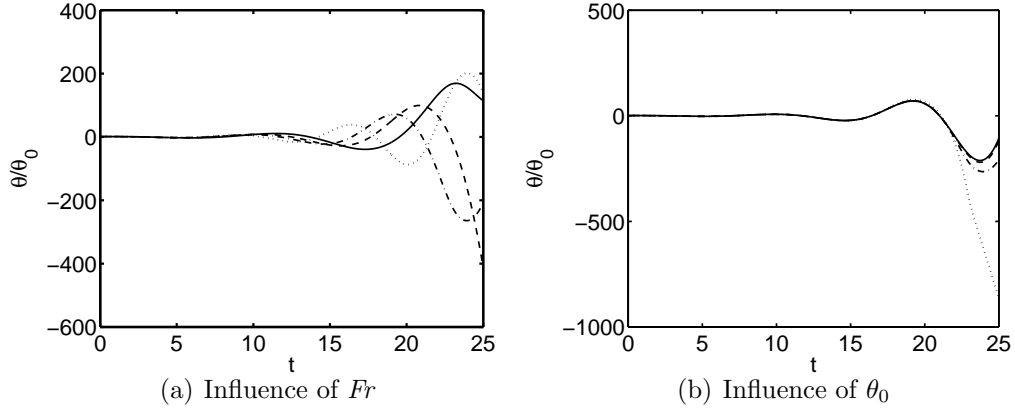


**Figure 3.9:** Evolution of  $\theta/\theta_0$  in time. (Left) Influence of  $Fr$ :  $\theta/\theta_0$  is plotted for  $\theta_0 = \pi/1024$  and  $Fr = 0.2$  (solid),  $Fr = 0.5$  (dashed),  $Fr = 1$  (dash-dotted) and  $Fr = 5$  (dotted). (Right) Influence of  $\theta_0$ :  $\theta/\theta_0$  is plotted for  $Fr = 1$  and  $\theta_0 = \pi/4096$  (solid),  $\theta_0 = \pi/2048$  (dashed),  $\theta_0 = \pi/1024$  (dash-dotted) and  $\theta_0 = \pi/512$  (dotted).

appropriately to match the notation in Jones and Shelley (2005).

### Characteristics of the growing-amplitude fluttering regime

During this phase, the vertical motion is at leading order identical to the broadside-on solution obtained for  $\theta_0 = 0$ . The horizontal position experiences oscillations with the same characteristics  $\sigma$  and  $\tau$  as the  $\theta$ -oscillations. The oscillations of  $\theta$  and  $x_c$  are however not in phase: the maximum horizontal deviation is reached slightly before the maximum orientation angle (Figures 3.7 and 3.8).

During this fluttering regime, the vortex wake is dominated by a pair of counter-rotating vortices as in the case  $\theta = 0$ . The asymmetry of the wake is characterized by a net circulation around the solid body of  $\Gamma_b = -(\Gamma_1 + \Gamma_2)$  and a difference between the vertical positions of the two vortices of  $\delta_v = \text{Im}(z_1 - z_2)$ . For small  $\theta_0$ ,  $\Gamma_b$  and  $\delta_v$  remain small during the initial fluttering regime.

The dominant motion is vertical, and for non-zero  $\theta$ , the angle of attack at one edge (leading edge) is slightly smaller than at the other (trailing edge). The vorticity shedding rate is expected to be slightly larger at the leading edge, and the corresponding vortex remains closer to the shedding edge because of the Brown-

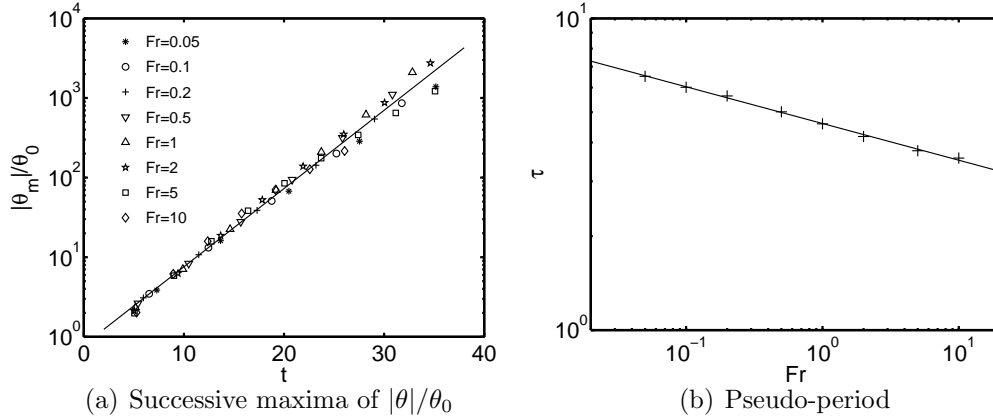


**Figure 3.10:** Influence of  $Fr$  on the development of the instability for  $\theta_0 = \pi/8092$ . (Left) Successive maxima of  $|\theta|/\theta_0$ . The solid line corresponds to the best exponential fit. The corresponding growth rate is about 0.23. (Right) Pseudo-period  $\tau$  of the growing oscillations. The solid line shows the best power-law fit corresponding to  $\tau \sim Fr^{-0.12}$ .

Michael corrective term in (2.19) that tends to pull the vortex back to its shedding corner. This corrective term represents the faster roll-up of a more intense vortex sheet on itself, keeping the center of vorticity closer from the shedding corner. An asymmetry in the vertical velocities of the vortices is therefore introduced and the leading edge vortex moves downward faster with the plate than the other vortex. For  $\theta > 0$ , the left vortex (negative) grows faster than the right vortex and  $\dot{\Gamma}_b > 0$  and  $\dot{\delta}_v > 0$ . We indeed observe that  $\theta$ ,  $\dot{\Gamma}_b$  and  $\dot{\delta}_v$  are approximately in phase throughout the oscillation (Figure 3.11a). Because of the small phase difference between the horizontal and angular motions, the two vortices have about the same vertical position ( $\delta_v \sim 0$ ) and opposite intensities ( $\Gamma_b \sim 0$ ) when the plate horizontal velocity changes sign (Figure 3.11b).

### Destabilization and transfer of momentum to the vortices

A physical interpretation of this destabilization is obtained by considering the fluid effect on the solid body. In this section, we will successively consider the transfer of momentum (linear or angular) and of kinetic energy to the solid body.

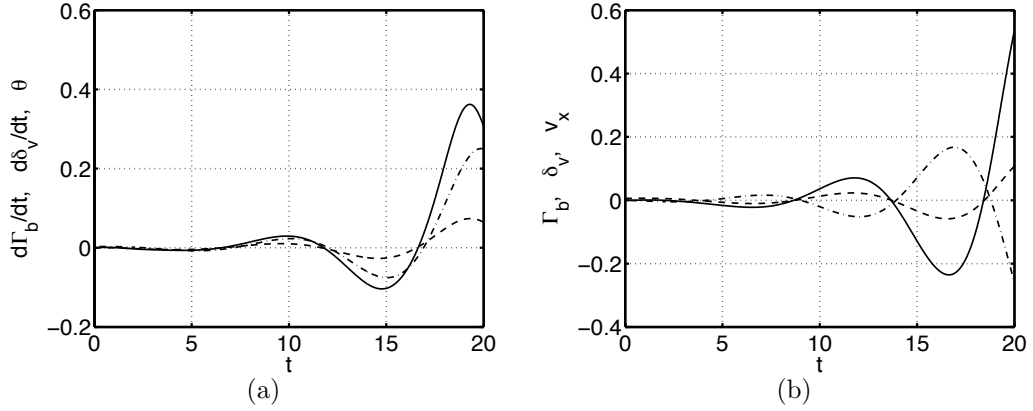


**Figure 3.11:** (a) Evolution of the rate of change of the circulation around the body  $\dot{\Gamma}_b$  (solid), the relative vertical velocity of the vortices  $\dot{\delta}_v$  (dashed) and the orientation of the plate  $\theta$  (dash-dotted) in the fluttering regime for  $Fr = 0.75$  and  $\theta_0 = \pi/1024$ . (b) Evolution of the circulation around the body  $\Gamma_b$  (solid), the relative vertical distance between the vortices  $\delta_v$  (dashed) and the horizontal plate velocity  $v_x$  (dash-dotted) in the fluttering regime for  $Fr = 0.75$  and  $\theta_0 = \pi/1024$ .

Since the body is rigid, these two quantities are easily related. As discussed in section 3.2.4, the fluid effects can be decomposed in two parts: added inertia and transfer of linear and angular momentum to the vortices.

The equations of motion of the plate can be rewritten as

$$2Fr \ddot{c} = -2i Fr + f^a + f^v, \quad \frac{2Fr}{3} \ddot{\theta} = \mathcal{T}^a + \mathcal{T}^v, \quad (3.68)$$

where the first term on the right-hand side of Newton's second law is the gravity forcing and  $a$  and  $v$  superscripts refer to forces and torques due to added inertia and transfer of momentum to the vortices respectively. The vertical motion is at leading order identical to the broadside-on case, so we focus on the horizontal and angular motions of the plate.

The effects of vortex shedding and added inertia on the horizontal and angular motions of the plate are analysed in Figure 3.12 by plotting the rate of work of the different contributions as well as their integrated effect in time (that is, the change of solid kinetic energy due to the corresponding force or torque). A positive rate of work will be destabilizing: the forcing acts in the same direction

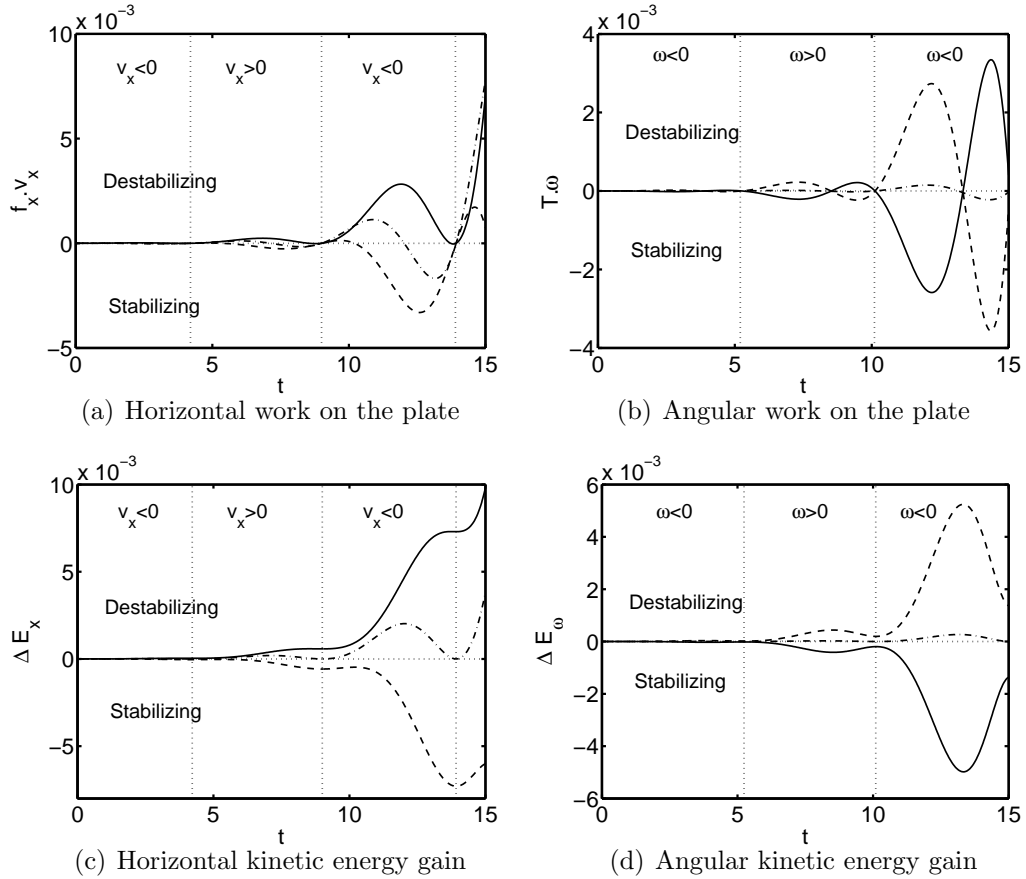


**Figure 3.12:** Stabilizing and destabilizing effects of the fluid on the falling card for  $Fr = 0.75$  and  $\theta_0 = \pi/1024$ . (Top) Rate of work of the vortex contribution (solid), the added inertia contribution (dashed) and the total (dash-dotted) horizontal force (a) and torque (b) on the falling card. (Bottom) Horizontal (c) and rotational (d) kinetic energy gain of the plate due to the vortices (solid) and the added inertia contribution (dashed). The horizontal and rotational solid kinetic energy is also plotted (dash-dotted). The sign of the horizontal velocity  $v_x = \text{Re}(\dot{c})$  and angular velocity  $\omega$  is indicated for reference.

as the motion. Figure 3.12(a)–(c) shows that added inertia tends to dampen the horizontal side-to-side motion of the card, while the transfer of momentum to the vortices has a destabilizing effect and creates a net energy gain. In the angular motion, the effects of added inertia and of the vortices give opposite contributions to the rotational work  $\mathcal{T}\omega$  on the plate, the former being slightly larger than the latter (Figure 3.12b-d).

The transfer of horizontal momentum to the vortices is therefore at the origin of the destabilization of the broadside-on fall and arises from the asymmetry of the wake. We now propose a physical analysis of the origin of this destabilizing horizontal momentum transfer. For a small enough initial angle, the fall of the card is a perturbation of the symmetric case studied in section 3.4.2, with a pair of counter-rotating vortices, with intensity and position in the mapped plane  $(\Gamma_0, \zeta_0)$  and  $(-\Gamma_0, -\bar{\zeta}_0)$ . The vertical physical distance between the plate and the vortex pair, defined in section 3.4.2, is then  $d_0^{(v)} = \zeta_0 + a^2/\zeta_0$ .

From section 3.2.4 and Kanso and Oskouei (2008), the horizontal linear momentum of the vortices is obtained at leading order as

$$p_x^{(v)} \sim \overbrace{\Gamma_0 \delta_v - \Gamma_b d_0^{(v)}}^{p_1} - \overbrace{4\theta \Gamma_0 \operatorname{Re} \left( \frac{a^2}{\zeta_0} \right)}^{p_2}. \quad (3.69)$$

The two terms on the right-hand side have the following interpretations:

- $p_1$  is the horizontal momentum due to the asymmetry of the wake: if  $\delta_v > 0$ , the intrinsic velocity of the vortex pair is tilted to the right and the wake carries positive horizontal momentum. In the same way, if  $\Gamma_1 > |\Gamma_2|$  ( $\Gamma_b < 0$ ) the asymmetry in the intensity of the vortices deflects the wake slightly to the right, and corresponds to a positive horizontal vortex momentum. As  $\delta_v$  and  $\Gamma_b$  vary in phase (see Figure 3.11b), the first two terms in (3.69) have opposite effects.  $p_1$  is observed to vary in a very good approximation like  $-v_x$ , with  $v_x$  the horizontal velocity of the plate's center of mass (Figure 3.13). The

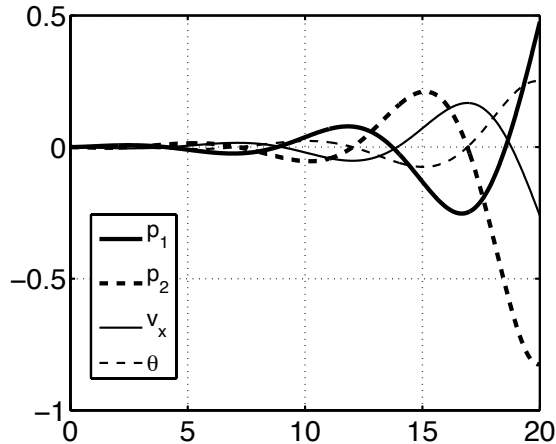


**Figure 3.13:** Evolution for  $\theta_0 = \pi/1024$  and  $Fr = 0.75$  of the different contributions to the horizontal momentum associated with the vortices  $p_1$  (thick-solid) and  $p_2$  (thick-dashed) as defined in (3.69). The plate’s horizontal velocity  $v_x$  (thin solid) and orientation  $\theta$  (thin-dashed) are also plotted for comparison.

corresponding force  $-\dot{p}_1$  therefore behaves like a (negative) correction to the plate’s inertia (not to be mistaken to the added inertia discussed in section 3.4.3). In particular, it tends to accelerate the plate’s horizontal motion at the beginning of each half-period when  $|v_x|$  starts increasing.

- $p_2$  is the horizontal momentum associated with the image vorticity and is due to the non-horizontal orientation of the plate:  $\Gamma_0 \text{Re}(a^2/\zeta_0)$  corresponds to the vortex momentum normal to the plate associated with the image vorticity and is monotonically increasing in time. To a very good approximation,  $p_2$  varies in phase with  $-\theta$  (Figure 3.13): for  $\theta < 0$  and a symmetric vortex pair, the vortices would be deflected to the right, thereby inducing a positive horizontal vortex momentum. The corresponding force on the plate  $-\dot{p}_2$  hence behaves like  $\omega$ . As the horizontal and angular motions are almost in phase (with the latter being slightly in advance on the former), the vortex force associated with the rotation of the plate around its vortex wake is acting in the same direction as the plate’s velocity throughout most of the

oscillation.

In a summary, during the fluttering oscillations of the plate, the relative motions of the plate and of the vortices, and particularly the resulting deflection of vortex momentum associated with the image vorticity (similar to the behavior of point vortices close to a wall), generates a destabilizing force that cannot be damped by added inertia effects. This destabilization is transmitted to the rotational motion of the plate through added inertia.

### 3.5 Conclusions

A general framework for the study of the two-dimensional coupled motion of a sharp-edged solid body in a high- $Re$  flow has been presented using potential flow theory and a representation of the vortical wake in terms of point vortices with unsteady intensity determined to satisfy the regularity of the flow velocity on the solid body. The Brown–Michael vortex model, used previously to study vortex shedding past a fixed semi-infinite or finite plate, has been extended to arbitrary body shapes and coupled to the solid dynamics to provide a reduced-order description of the fluid-solid problem in terms of ordinary differential equations only. The forces and torques on the solid body have been analysed in terms of transfer of linear and angular momentum to the vortices. This physically-based model significantly reduces the computational cost and complexity of the simulation of the fluid-solid problem compared to direct numerical simulations and also compared to a continuous vortex sheet approach. In addition, the numerical and physical difficulties of the vortex sheet model, due to the necessary smoothing of the Cauchy kernel to regularize the free vortex sheet velocity and to the treatment of the last Lagrangian vortex element, are not present here. The point vortex approach described here also provides a powerful tool for understanding the structure of the vortical wake and its influence on the solid body.

The method was then used in the simple geometry of a flat plate to

study the fall of a rigid card in a fluid initially at rest. The different forces and torques applied by the fluid on the card were analysed. The broadside-on fall, where the plate falls in its horizontal position, was found to be unstable and, for small initial angles, a fluttering regime with growing amplitude was observed. This is in agreement with numerous experimental and numerical studies at high  $Re$  present in the literature. Using the reduced-order representation of the vortex wake provided by the point vortex model, it was shown that the destabilization is caused by the deflection of linear momentum associated with the vortices by the plate's fluttering motion around them. The net effect is an amplification of the horizontal motion which then amplifies the rotation amplitude of the fluttering motion through the coupling of rotation and translation by added inertia. In comparison, a representation of the fluid effects exclusively in terms of added inertia was found unable to predict such a behavior. This example shows the physical validity of the proposed model as well as the interest of a low-order representation to understand the destabilization mechanism.

Further integration of the coupled equations of motion showed different possible regimes, including the flip of the card once the  $\theta$  oscillations reach a finite amplitude, and the transition to rotating patterns that can be identified with the tumbling regimes observed experimentally. This is an improvement compared to the vortex sheet approach, in which the shedding failure occurred always before the flip of the card. The integration eventually breaks down at an unfavorable shedding event, limiting our ability to study the influence of  $\theta_0$  and  $Fr$  on the long-time regime.

The unsteady point vortex method is therefore limited, as is the vortex sheet method, by its inability to represent vortices that are not shed away from the solid body. Failure events were identified when a new vortex is being shed under unfavorable conditions, where the outside flow tends to push the newly shed vortex back onto the shedding corner. This situation occurs mostly in leading-edge shedding conditions at small angle of attack, and this limitation is inherent

to the inviscid nature of the flow representation chosen here. Several solutions could be considered to overcome this shedding failure including the shedding of multiple vortices at the same time, or the absence of shedding of a new vortex: under such conditions, the flow velocity is singular at the shedding edge, where the bound vorticity doesn't vanish, hence representing the attached vortex. The shedding of a vortex from that corner would then be restarted at a later time when the conditions are favorable. However, the inviscid nature of these representations might pose a problem as viscous effects and interaction of the leading-edge vortex with the boundary layers on the solid body are expected to play an important role.

Despite this limitation, the point vortex method presented here is a powerful tool in a large variety of situations where leading-edge shedding is not present or is neglected. Its computational simplicity makes it suitable for a large number of situations where the cost of direct numerical simulation is prohibitive (e.g. optimization problems). The point vortex method was also recently used to study the coupling between flexible bodies and high  $Re$  flows (Michelin et al., 2008) as presented in Chapter 4.

Chapter 2 and Chapter 3, in part, have been published in *Theoretical and Computational Fluid Dynamics*, “An unsteady point vortex method for coupled fluid-solid problems” by S. Michelin and S. G. Llewellyn Smith, 2009, **23**, 127–153 (Springer), doi:10.1007/S00162-009-0096-7. The dissertation author was the primary investigator and author of this material.

Some material drawn from Chapter 3 and Chapter 4 has been accepted for publication in *Theoretical and Computational Fluid Dynamics*, “Falling cards and flapping flags: understanding fluid-solid interactions using an unsteady point vortex method” by S. Michelin and S. G. Llewellyn Smith, 2009 (Springer), doi: 10.1007/S00162-009-0117-6. The dissertation author was the primary investigator and author of this material.

# 4

## Passive flapping of flexible flags in axial flow

### 4.1 Introduction

A fluttering instability can develop from the interaction of the internal dynamics of an elastic structure and an axial flow. The flapping of wind-forced flags is a canonical example of such an interaction problem, which is also of interest in various other engineering (Watanabe et al., 1991, 2002a,b) and medical applications (Huang, 1995; Balint and Lucey, 2005). This instability arises from the competition between the destabilizing effect of the aerodynamic pressure and the stabilizing effect of the (small) bending rigidity of the structure.

The fluttering flag instability has been the focus of a large number of experimental studies including soap-film (Zhang et al., 2000), water-tunnel (Shelley et al., 2005) and wind-tunnel experiments (Eloy et al., 2008). Recently, full numerical simulations of the coupled fluid and solid dynamics have been carried out using immersed-boundary methods (Zhu and Peskin, 2002) and coupled fluid–solid solvers (Connell and Yue, 2007). The latter study identified three possible behaviors for the flag: stable and flat, periodic flapping, and chaotic. These experimental and numerical studies considered two-dimensional configurations in the limit where the width of the flag is large enough for deformations in the third dimensions to be neglected. Another domain of active research is the opposite limit

of small aspect ratio and the fluttering of thin ribbons or strips (e.g. Datta and Gottenberg, 1975; Yadykin et al., 2001; Lemaitre et al., 2005).

To understand the onset of the instability, several papers have focused on the linear stability of the flat position (see the review by Paidoussis, 2004). The two-dimensional linear stability of infinite flexible plates under axial flow was first studied by Rayleigh (1878). More recently, Kornecki et al. (1976) carried out a linear stability study of the two-dimensional problem, modelling the wake behind a finite-length clamped plate as a distribution of vorticity (see Eloy et al., 2008, with increased numerical resolution), and Argentina and Mahadevan (2005) proposed a similar approach and investigated the effect of the drag-induced tension. Eloy et al. (2007) carried out a linear stability analysis including three-dimensional effects (see also Shayo, 1980; Lucey and Carpenter, 1993).

In all these studies, only one elastic sheet or plate was considered. Recently, experiments (Zhang et al., 2000; Jia et al., 2007) and numerical studies (Farnell et al., 2004) have also focused on the modification of the stability and flapping properties in the case of two parallel filaments. Depending on their relative distance, the two filaments appear to lock either in-phase or out-of-phase. Jia and Yin (2008) studied the case of two flapping filaments with one filament positioned downstream from the other. Ristroph and Zhang (2008) identified an anomalous drafting mechanism in a similar two-flag experiment: the upstream flag experiences a reduction of drag because of the presence of a second flag directly downstream.

The purpose of the present work is to propose a reduced-order model for the flow over two-dimensional flags that is able to obtain the long-time behavior and finite-amplitude flapping. It also reproduces the main characteristics of the problem as observed in full numerical simulations and experiments while significantly reducing the computational complexity. A potential flow representation is used for the two-dimensional flow past an infinitely thin inextensible elastic strip of finite length. The wake is represented by discrete point vortices, unlike the

vortex sheet representation described in Alben and Shelley (2008). Here, the intensity of the last point vortex shed is adjusted in time to satisfy the regularity of the flow velocity at the trailing edge (Brown–Michael vortex) and a new vortex is shed when the previous one reaches a maximum intensity (Cortelezzi and Leonard, 1993; Michelin and Llewellyn Smith, 2009c).

In section 4.2, the model used here is described in the case of a single flag. The fluttering instability is investigated in section 4.3, as well as the characteristics of the periodic flapping regime and their evolution as the flow velocity is increased. The propagating waves (kinematic and dynamic) along the flags are also studied. Section 4.4 focuses on the two-flag problem. After a brief presentation on the generalization of the model to two plates or flags, the coupled flapping modes are studied, as well as the modifications of the stability properties with the relative distance.

## 4.2 Model

A two-dimensional model of a flapping flag of infinite span is considered. The flag is inextensible and clamped at its fixed end;  $L$ ,  $B$  and  $\rho_s$  are respectively its length, bending rigidity per unit length and mass per unit area. The surrounding fluid density is  $\rho$ , and a uniform horizontal flow at infinity  $U_\infty$  is prescribed. In the following, all quantities are non-dimensionalized using  $L$ ,  $U_\infty$  and  $\rho$  as reference values. Positions and velocities are defined with respect to a fixed system of axes with origin at the clamped end of the flag.

### 4.2.1 Solid model

A finite-displacement inextensible Euler–Bernoulli beam model is considered. The position of the flag is  $\zeta(s, t)$  ( $0 \leq s \leq 1$  is the arclength), and  $\theta(s, t)$  is the angle between the local tangent and the horizontal axis (see Figure 4.1). We note the elastic torque  $M(s, t)$ , the tension  $T(s, t)$  and the normal elastic force

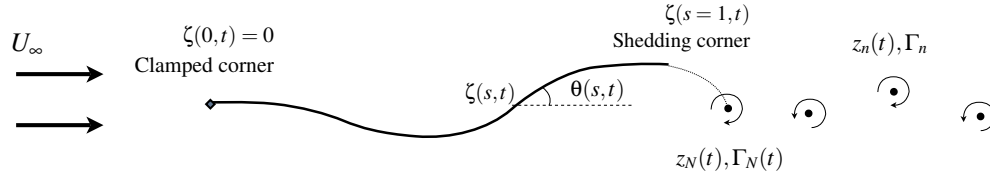


**Figure 4.1:** Vortex shedding behind a flapping flag. The oncoming flow is horizontal and vortices are shed from the trailing edge. The last vortex has unsteady intensity, the other vortices have frozen circulation.

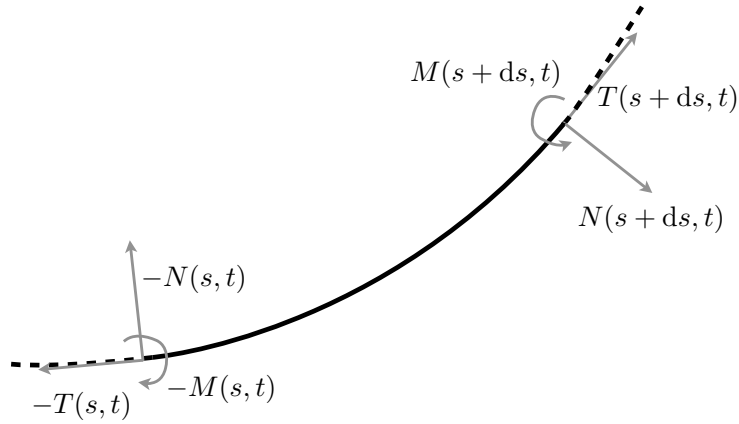


**Figure 4.2:** Elastic forces and torques applied on a section of the flexible plate between  $s$  and  $s + ds$

$N(s, t)$  in the flag. By convention, these quantities represent the forces (or torque) applied by the downstream part of the flag ( $s \leq s' \leq 1$ ) to the upstream section ( $0 \leq s' \leq s$ ). The Euler–Bernoulli assumption for a slender beam states that the elastic torque is related to the curvature by

$$M(s, t) = \eta \theta_s, \quad (4.1)$$

with  $\eta$  the non-dimensional rigidity. The equation of motion of the flexible plate is obtained by considering a section of the plate between  $s$  and  $s + ds$  (Figure 4.2). For infinitesimally thin plates, the rotational inertia of the section scales like  $(ds)^2$

and can be neglected. The torque balance on the segment then leads to

$$N(s, t) + \frac{\partial M}{\partial s} = 0. \quad (4.2)$$

Using (4.2), Newton's second law for the plate's segment becomes, together with the inextensibility condition,

$$\mu \ddot{\zeta} = [e^{i\theta} (T - i\eta\theta_{ss})]_s - i[p]^\pm e^{i\theta}, \quad \zeta_s = e^{i\theta} \quad (4.3)$$

where a subscript  $s$  stands for  $\partial/\partial s$  and dotted variables for  $\partial/\partial t$ , with clamped-free boundary conditions:

$$\zeta(0, t) = \theta(0, t) = 0, \quad \theta_s(1, t) = \theta_{ss}(1, t) = T(1, t) = 0. \quad (4.4)$$

This model is equivalent to the one used in Alben and Shelley (2008). Here  $\mu = \rho_s/\rho L$  and  $\eta = B/\rho U_\infty^2 L^3$  are respectively the non-dimensional flag density and bending rigidity, while  $\sqrt{\eta}$  is also the time-scale ratio of the response to the pressure forcing and the bending stiffness. For comparison purposes with the linear stability results of Eloy et al. (2008), we will also use in the following the alternative non-dimensional parameters

$$M^* = \frac{1}{\mu} = \frac{\rho L}{\rho_s}, \quad U^* = \sqrt{\frac{\mu}{\eta}} = U_\infty L \sqrt{\frac{\rho_s}{B}}. \quad (4.5)$$

Here  $U^*$  is the free-stream velocity non-dimensionalized by the flag rigidity and inertia.

## 4.2.2 Vortex shedding model

The vortex shedding model presented in Chapter 2 is used here to represent the wake of the flexible flags. The flow around the flag is assumed to be irrotational. To satisfy the regularity condition for the flow at the trailing edge, point vortices are introduced following the method suggested by Cortelezzi and Leonard (1993) and Cortelezzi (1996) for the prescribed flow over fixed semi-infinite and finite plates, and applied in Michelin and Llewellyn Smith (2009c) to the coupled

motion of a falling card and the surrounding fluid. In this approach, one point vortex with unsteady intensity is released from each shedding corner. At each time step, the intensity is adjusted so as to satisfy the regularity condition: the flow velocity  $w$  must remain finite at the trailing edge. These vortices, with position  $z_n$  and intensity  $\Gamma_n$ , are also known as Brown–Michael point vortices (Brown and Michael, 1954; Rott, 1956), and obey the modified equation of motion (see Chapter 2 and (2.19))

$$\dot{z}_n + (z_n - \zeta(1, t)) \frac{\dot{\Gamma}_n}{\Gamma_n} = \overline{\tilde{w}_n}, \quad (4.6)$$

where the overbar denotes the complex conjugate. The second term accounts for the conservation of fluid momentum around the vortex and associated branch cut, and  $\tilde{w}_n$  is the desingularized flow velocity at the vortex position (Saffman, 1992).

When a vortex reaches maximum intensity, the intensity of this vortex is frozen and a new vortex is started from the shedding corner (see section 2.4.2). Because the angle of attack is always small in this problem, vortex shedding is neglected at the leading edge and vortices are shed from the trailing edge only. Therefore at any time, the vortex wake consists of  $N - 1$  vortices  $(z_j(t), \Gamma_j)$  with steady intensity and one unsteady point vortex  $(z_N(t), \Gamma_N(t))$ .

### 4.2.3 Fluid model

The flow is assumed inviscid and the flag is infinitesimally thin. On both sides of the flag, the normal velocity of the flow must be equal to that of the flag. However, the presence of the flag introduces a discontinuity in the tangential velocity, and the influence of the flag on the flow is that of an attached vortex sheet. The potential flow around the deformable flag can therefore be solved by representing the infinitely thin flag as a bound vorticity distribution  $\kappa(s, t)$  (Jones, 2003; Shukla and Eldredge, 2007; Alben and Shelley, 2008; Alben, 2009). The complex flow velocity is the superposition of a uniform flow at infinity, and the contribution of the vorticity distribution (bound vortex sheet for the flag and point

vortices for the wake):

$$w = 1 + \frac{1}{2\pi i} \left[ \int_0^1 \frac{\kappa ds}{z - \zeta(s, t)} + \sum_{j=1}^N \frac{\Gamma_j}{z - z_j} \right]. \quad (4.7)$$

Using the Plemelj formula and following Shukla and Eldredge (2007), the normal flow boundary condition on the flag  $\text{Im}[e^{-i\theta}(\bar{w} - \dot{\zeta})] = 0$  becomes a Fredholm singular integral equation for  $\kappa$ . Assuming the system is started from rest, the total circulation at infinity must vanish at all time (Kelvin's circulation theorem). Together with the regularity condition  $w(\zeta(1, t), t) \neq \infty$ , these two conditions can be rewritten as a system of equations for  $\kappa$  and the intensity  $\Gamma_N$  of the last shed vortex (the others are known and frozen):

$$\frac{1}{2\pi} \int_0^1 \text{Re} \left[ \frac{e^{i\theta(s_0)}}{\dot{\zeta}(s_0) - \zeta(s)} \right] \kappa ds = \text{Im} \left[ e^{i\theta(s_0)} \left( 1 + \frac{1}{2\pi i} \sum_{j=1}^N \frac{\Gamma_j}{\zeta(s_0) - z_j} - \dot{\zeta} \right) \right], \quad (4.8)$$

$$\int_0^1 \kappa ds + \sum_{j=1}^N \Gamma_j = 0, \quad \kappa(1, t) = 0, \quad (4.9)$$

where the integral on the left-hand side of (4.8) is understood as the principal value. Note that because of the Cauchy-like form of the kernel in (4.8), the first condition in (4.9) is necessary for the problem for  $\kappa$  to be well-posed (Tuck, 1980).

The desingularized velocity  $\tilde{w}_n$  in (4.6) is

$$\tilde{w}_n = 1 + \frac{1}{2\pi i} \left[ \int_0^1 \frac{\kappa ds}{z_n - \zeta(s, t)} + \sum_{j \neq n} \frac{\Gamma_j}{z_n - z_j} \right]. \quad (4.10)$$

The initial position of the vortex at the corner of the solid induces a singularity in (4.10). A small-time expansion of the vortex position can be performed following Cortelezzi and Leonard (1993) and Michelin and Llewellyn Smith (2009c) and the resulting analytic small-time solution is used for the first time step of each new vortex. This small-time solution was presented in section 3.3 for the case of a rigid body; the formalism is however unchanged when considering a flexible body, as we are interested in the early stages of vortex shedding, on time scales much smaller than the characteristic time of deformation of the solid body and for distances

between the vortex and the trailing edge much smaller than the typical curvature radius of the flag.

From Bernoulli's theorem, the pressure jump across the flag is (writing  $\phi = \text{Re}(F)$  for the real flow potential)

$$\begin{aligned} [p]^\pm(s_0) &= -\frac{\partial}{\partial t} (\phi^+ - \phi^-) - \frac{1}{2} \text{Re} \left[ \overline{(w^+ - w^-)} (w^+ + w^-) \right] \\ &= -\frac{D_s[\phi]^\pm}{D_s t} - \text{Re} \left[ \left( \frac{w^+ + w^-}{2} - \dot{\zeta} \right) \overline{(w^+ - w^-)} \right], \end{aligned} \quad (4.11)$$

with  $w^+$  (resp.  $w^-$ ) the flow velocity on the upper (resp. lower) side of the flag, and  $D_s/D_s t$  the material derivative on the flag following the flag's motion. Then, by definition of  $\kappa$ ,  $w^+ - w^- = -\kappa e^{-i\theta}$ , and by integrating the tangential component from the leading edge (where  $\phi^+ = \phi^-$  since no vorticity is shed) to  $s_0$ , we obtain

$$[\phi]^\pm(s_0) = -\int_0^{s_0} \kappa(s, t) ds. \quad (4.12)$$

The pressure jump is then finally obtained as

$$[p]^\pm(s_0) = \int_0^{s_0} \dot{\kappa} ds + \kappa(s_0) w_p(s_0), \quad (4.13)$$

with  $w_p$  the average of the relative tangential fluid velocities on either sides of the flag (Jones, 2003; Alben and Shelley, 2008)

$$w_p(s_0) = \text{Re} \left[ e^{i\theta(s_0)} \left( \frac{1}{2\pi i} \int_0^1 \frac{\kappa(s) ds}{\zeta(s_0) - \zeta(s)} + 1 - \sum_{j=1}^N \frac{i\Gamma_j}{2\pi(\zeta(s_0) - z_j)} - \dot{\zeta}(s_0) \right) \right]. \quad (4.14)$$

#### 4.2.4 Numerical method for the flag problem

A system of equations for  $\theta$  and  $T$  alone can be obtained by combining both equations in (4.3):

$$T_{ss} - \theta_s^2 T = -[p]^\pm \theta_s - 2\eta \theta_s \theta_{sss} - \eta \theta_{ss}^2 - \mu \theta^2, \quad (4.15)$$

$$\mu \ddot{\theta} = -[p]^\pm_s - \eta \theta_{ssss} + (T + \eta \theta_s^2) \theta_{ss} + 2T_s \theta_s. \quad (4.16)$$

Determining the flag position as  $\zeta(s, t) = \int_0^s e^{i\theta} ds'$  automatically satisfies the inextensibility condition. Then the boundary conditions are obtained from (4.4) and Newton's second law applied to the whole flag as

$$\theta(0, t) = \theta_s(1, t) = \theta_{ss}(1, t) = T(1, t) = 0, \quad (4.17)$$

$$\mu \int_0^1 \int_0^s e^{i\theta} \left( i\ddot{\theta} - \dot{\theta}^2 \right) ds' ds = T(0) - i\eta\theta_{ss}(0) - i \int_0^1 [p]^\pm e^{i\theta} ds. \quad (4.18)$$

The flag orientation  $\theta$  is decomposed using the Chebyshev polynomials of the first kind

$$\theta = \sum_{j=1}^J c_j(t) T_j(2s - 1), \quad (4.19)$$

and equations (4.6), (4.8), (4.9), (4.13), (4.15) and (4.16) are used to integrate  $c_j(t)$  and  $(z_n, \Gamma_n)$  in time using a second-order-accurate finite-difference scheme. The fourth-order derivative in space in (4.16) is treated semi-implicitly and all non-linear terms in (4.15)–(4.16) are evaluated explicitly. Chebyshev spectral methods are particularly well-adapted to handle the square-root singular behavior of the general solution of (4.8) near  $s = 0$  and  $s = 1$ , and combine easily with the numerical methods used to solve this integral equation (see appendix B). In the simulations presented here,  $J = 50$  polynomials were used in the expansion (4.19). Test runs were performed with a higher number of polynomials without any significant change in the accuracy of the results.

From (4.6), (4.10) and the time derivative of (4.8),  $\dot{\Gamma}_N$ ,  $\dot{z}_n$ ,  $\dot{\kappa}$  and therefore  $[p]^\pm$  are linear functions of the flag acceleration  $\ddot{\theta}$  (and therefore  $\ddot{c}_j$ ). At each time step, using (4.6), (4.8), (4.9) and (4.13), the contribution to  $\dot{\Gamma}_N$ ,  $\dot{z}_n$  and  $[p]^\pm$  arising from  $\ddot{c}_j$  is computed in the form of a linear operator acting on  $\ddot{c}_j$ , separately from the remaining part of these quantities that can be evaluated explicitly. In (4.15)–(4.16), the contribution of  $\ddot{c}_j$  to the pressure can then be isolated and put on the left hand side (acting in the same way as an added inertia term) to compute the solid's acceleration directly. The computational cost is thereby greatly reduced in comparison with other methods (for example Alben and Shelley, 2008), since no

iteration of the fluid-solid solver is necessary here. The second-order accuracy of the solver was checked using (4.3) and the conservation of the flag energy:

$$\dot{E} = W_p, \quad \text{with } E = \int_0^1 \left[ \frac{1}{2} \mu |\dot{\zeta}|^2 + \frac{1}{2} \eta \theta_s^2 \right] ds, \quad W_p = - \int_0^1 [p]^\pm \text{Im} \left[ \dot{\zeta} e^{-i\theta} \right] ds, \quad (4.20)$$

where  $E$  is the total mechanical energy of the flag and  $W_p$  is the rate of work of pressure forces.

### 4.3 Flapping of a single flag

The flag is initially at rest ( $\theta(s, t < 0) = 0$ ) and at  $t = 0$  the horizontal flow at infinity is ramped up continuously to its steady state value. A small transient vertical perturbation is added to move the system from this trivial equilibrium (perturbations of the form  $v = \epsilon t^\alpha e^{-\beta t}$  were used; different values of  $\alpha$  and  $\beta$  were tested with no significant impact on the long-time behavior). In each run, the rigidity and inertia of the flag are fixed, and the flow at infinity can be varied inducing a change of the non-dimensional velocity  $U^*$  defined in (4.5).

#### 4.3.1 Three possible regimes

For a given inertia ratio  $M^*$ , three regimes were observed. For small  $U^*$  (low wind speed), the initial perturbation creates a small motion of the flag that quickly decays, and the flag returns to its rest position.

When  $U^*$  is increased above a critical value  $U_c^*$  ( $U_c^* = 9.6$  for  $M^* = 3$ ), this rest position becomes unstable. For intermediate values of  $U^*$  ( $9.6 \leq U^* \leq 12$  for  $M^* = 3$ ), a periodic flapping develops, after a transient regime, in which the energy of the flag oscillates with an exponentially growing envelope. One point vortex is shed during each half-stroke and the intensity of the point vortices have alternating signs. Downstream from the flag (about one flag length's away), these point vortices arrange themselves in a weak von Kármán street and are advected with  $U_\infty$  close to the horizontal axis (Figure 4.3). This is in good agreement with

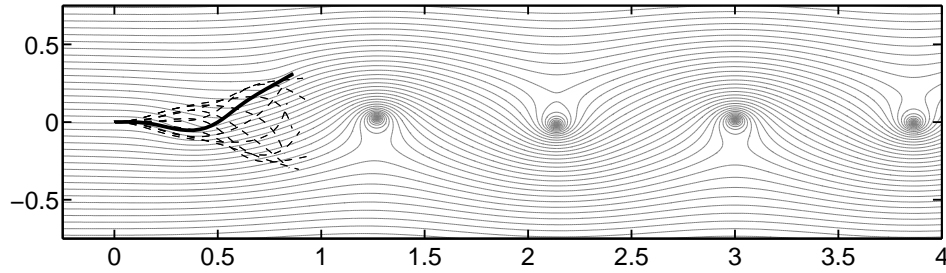


**Figure 4.3:** Instantaneous streamlines for the flow over the flapping flag in the periodic regime for  $M^* = 3$  and  $U^* = 11.5$ . The grey lines are the streamlines. For reference, the successive positions of the flag in a flapping cycle are plotted as dashed lines.

the positioning of the centers of vorticity in the vortex sheet approach (Alben and Shelley, 2008). This situation differs significantly from thrust-generating flapping, where the vortices are advected faster due to their reversed von Kármán arrangement (see Chapter 6).

The motion of the flag in this flapping regime is highly periodic. The power spectra of the flag total energy (4.20) and tail orientation  $\theta(1, t)$  display sharp peaks (see the left-hand column of Figure 4.4a-b). Note that the orientation spectrum contains only odd harmonics ( $\omega_0, 3\omega_0 \dots$ ) while the energy is a quadratic function of the kinematic variables and its spectrum only contains the even harmonics ( $2\omega_0, 4\omega_0, \dots$ ). We also observe that the non-dimensional fundamental flapping frequency is not modified by the variation of  $U^*$ . This is in agreement with experimental results showing a linear increase of the dimensional flapping frequency with the imposed flow velocity (Shelley et al., 2005). In the phase plot of the flag tail position, the outgrowing spiral corresponds to the instability development from the initial rest position, and convergence to a limit-cycle is clearly seen for  $U^* \leq 12$  (center column of Figure 4.4). The decreasing number of oscillations (or spiral turns) shows an increase of the instability growth rate with  $U^* - U_c^*$ . The horizontal force applied by the flag on its attachment pole at  $s = 0$  also shows strong periodicity (right-hand column of Figure 4.4a-b).

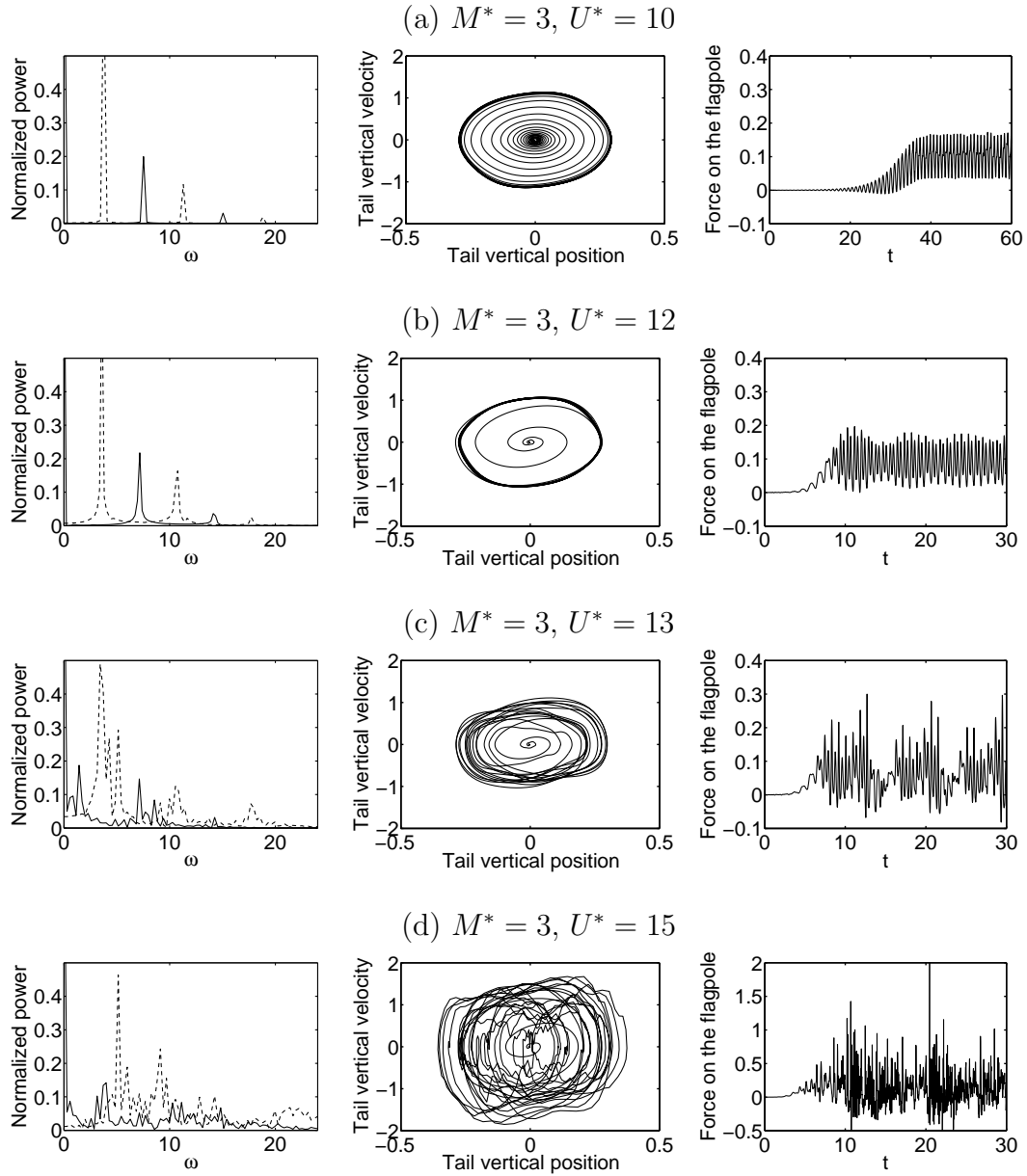


**Figure 4.4:** (Left) Frequency spectrum of the solid energy  $E$  (solid) and of the tail orientation  $\theta(1, t)$  (dashed) normalized by their maximum values for clarity, (center) Tail vertical velocity vs. tail vertical displacement phase plot and (right) Time variations of the horizontal force on the flagpole, plotted for  $M^* = 3$  and  $U^* = 10, 12, 13$  and  $15$  (top to bottom).

When the flow velocity is increased further, the periodicity breaks down. The tail trajectory in the phase diagram shows a weaker limit-cycle behavior at  $U^* = 13$  and periodicity is lost at  $U^* = 15$  (see center column of Figure 4.4). A transition from a discrete energy spectrum (Figure 4.4a-b) to a broad-band spectrum (Figure 4.4c-d) is observed. This strong unsteadiness, also observed for the force on the flagpole, leads to snapping events (large acceleration of the flag tail) inducing peak values of the force on the flagpole of up to ten times its mean value in the flapping regime (see right-hand column of Figure 4.4d). A discussion of the chaotic nature of the flag motion when the flow velocity is increased was proposed in the work by Connell and Yue (2007).

### 4.3.2 Comparison with linear stability results

For a given  $M^*$ , the critical velocity  $U_c^*$  is computed as the minimum value of  $U^*$  above which the state of rest of the flag becomes unstable. The corresponding critical curve is plotted in Figure 4.5 in both the  $(M^*, U^*)$  and  $(\mu, \eta)$  planes for comparison with previous studies. We also plot for reference the results from the linear stability analysis (Kornecki et al., 1976), which have been presented and confirmed experimentally in Eloy et al. (2008). A summary of the method used for the linear stability calculation is presented in appendix A.

We observe that the present point vortex method matches very well the stability region predicted by the linear analysis, particularly the existence of several branches corresponding to different mode structures, and does significantly better than the vortex sheet model which underpredicts the critical velocity  $U_c^*$ .

### 4.3.3 Flapping modes

As experimentally observed by Eloy et al. (2008) and predicted by the linear stability analysis, each branch of Figure 4.5 corresponds to a different mode structure: the first branch ( $M^* < 1$ ) corresponds to mode 2 (one neck), while the second ( $1 < M^* < 7$ ) and third ( $8 < M^* < 15$ ) correspond respectively to

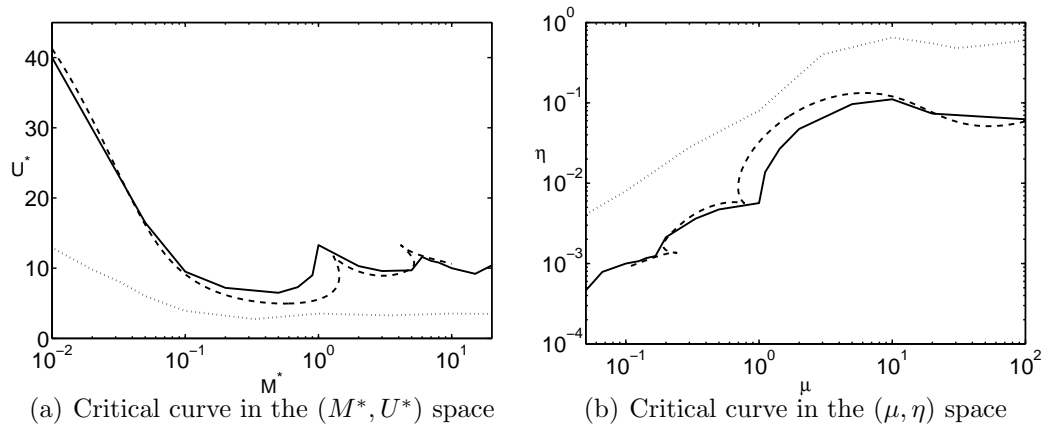


**Figure 4.5:** Critical curve for the stability of the flag state of rest using the present point vortex model (solid) and linear stability analysis presented in Eloy et al. (2008) following the method of Kornecki et al. (1976) (dashed) (see appendix A). The same critical curve obtained using the vortex sheet approach (Alben and Shelley, 2008) is plotted (dotted) for comparison.

mode 3 (two necks) and mode 4 (three necks). This mode structure is observed in the large-amplitude flapping results of our model (see Figure 4.6). Increasing  $M^*$  further, a mode 5 (four necks) can also be observed in our simulations (Figure 4.6d). The flapping mode structure seems to be determined by the most linearly unstable mode. Several other forms of initial perturbations have been tested to try to trigger a different mode (in particular transient periodic forcing at the desired frequency) without any change in the resulting dominant mode structure in the permanent regime.

#### 4.3.4 Hysteresis behavior

Experimental studies on flapping flags have pointed out the hysteresis behavior of the flag when the velocity of the flow at infinity is varied (Zhang et al., 2000; Shelley et al., 2005; Eloy et al., 2008). Starting from rest, the flag remains straight until the critical velocity  $U_{c1}^*$  is reached, at which point a periodic flapping of large amplitude develops. However, if the flow velocity is subsequently reduced, large scale flapping is maintained until  $U^* = U_{c2}^*$ , with  $U_{c2}^* < U_{c1}^*$ .

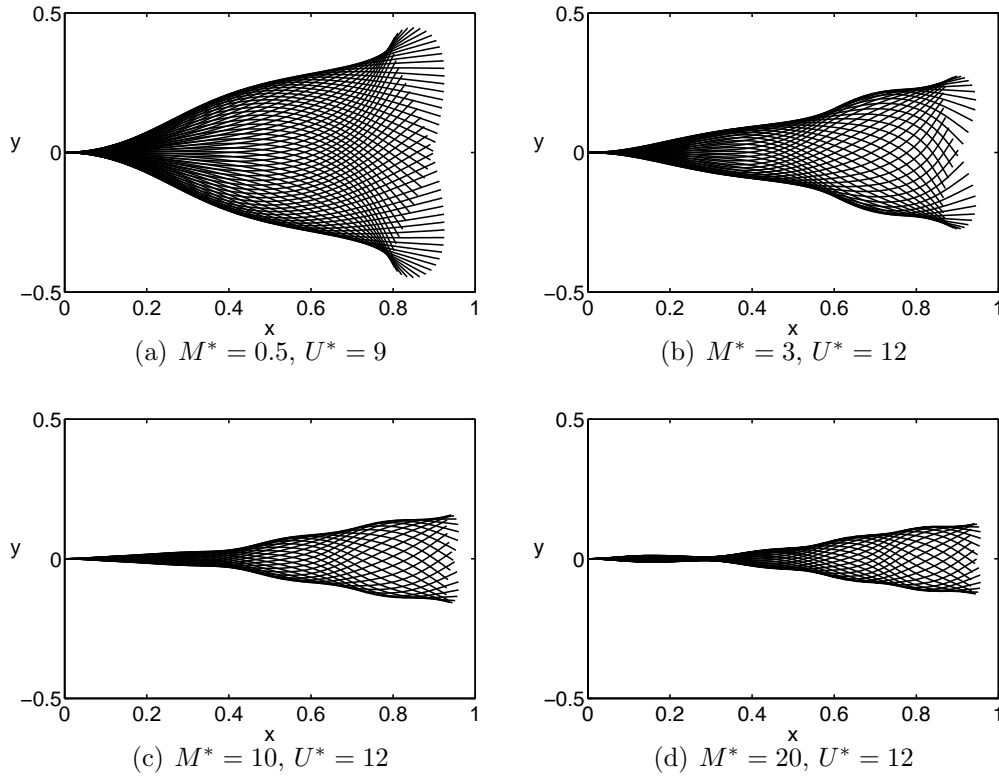


**Figure 4.6:** Flapping mode observed for different values of the inertia ratio. The position of the flag is plotted every  $\Delta t = 0.04$ .

Such behavior is observed here (Figure 4.7). The width of the hysteresis cycle ( $\sim 4.5\%$ ) is comparable to that observed in Alben and Shelley (2008), but much smaller than that observed in the experiments ( $\sim 20\%$  for Eloy et al. (2008)). Alben and Shelley (2008) suggested that dissipative effects of viscosity or structural damping can be at the origin of these discrepancies.

### 4.3.5 Travelling waves along the flapping flag

This section focuses on the flapping regime that develops at intermediate velocity  $U^*$  and studies the propagation of waves along the flag in that regime.

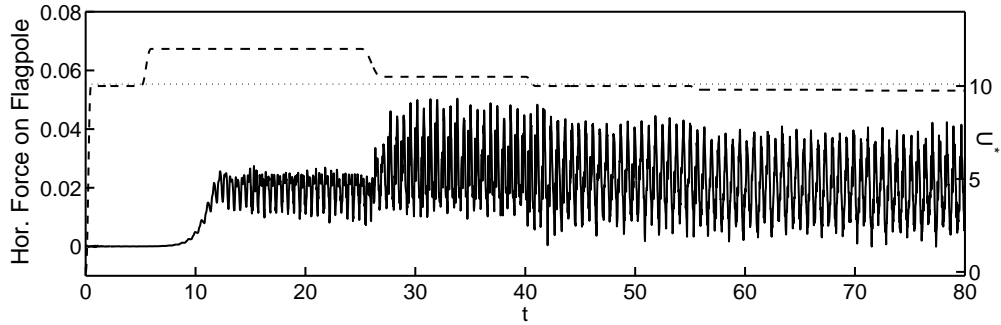


**Figure 4.7:** Hysteresis behavior at  $M^* = 10$ : (solid) horizontal force on the flagpole and (dashed) horizontal velocity of imposed flow. The critical velocity  $U_{c1}^* = 10.1$  is plotted for reference (dotted). Initially, when  $U^* < U_{c1}^*$  the initial perturbation is damped exponentially. Flapping develops when  $U^*$  is increased above the critical value. When  $U^*$  is then gradually reduced, it is possible to maintain a flapping state until  $U^* = U_{c2}^* = 9.6 < U_{c1}^*$ . If  $U^*$  is further decreased, the flapping amplitude decreases exponentially (not shown).

### Complex Empirical Orthogonal Functions and propagating waves

Empirical Orthogonal Functions (EOFs) (also known as Proper Orthogonal Decomposition) are used to decompose a signal  $f(s, t)$  into a superposition of normal modes  $f(s, t) = \sum a_n(t)b_n(s)$ . The modes' spatial and temporal structures are such that, when truncated at any order, the root mean square of the residue is minimized (Wallace and Dickinson, 1972). The Complex Empirical Orthogonal Function (CEOF) decomposition is well-suited to identify moving patterns. The EOF decomposition is applied to the complex function  $F = f + if^H$  where  $f^H$  is the Hilbert transform of  $f$  (see Barnett, 1983, for more details). We have

$$f(s, t) = \text{Re} \left[ \sum_n A_n(t) \bar{B}_n(s) \right] = \sum_n a_n(t) b_n(s) \cos(\psi_n(t) - \varphi_n(s)), \quad (4.21)$$

where  $A_n = a_n e^{i\psi_n}$  and  $B_n = b_n e^{i\varphi_n}$  can be obtained from the Singular Value Decomposition of the discrete representation of  $F$ . The advantage of this method becomes apparent when this decomposition is applied to the flag problem: for example, for  $M^* = 10$  and  $U^* = 11$ ,  $\theta$  can be represented by its first CEOF with a root-mean-square error of less than 1%. The spatial amplitude  $b$  gives the shape of

the mode considered, and the temporal amplitude  $a$  gives the temporal fluctuations of the mode amplitude. In the highly periodic regimes considered here,  $a$  is very close to a constant.

We are most interested in the phase functions  $\psi(t)$  and  $\varphi(s)$  whose variations are shown in Figure 4.8 for the first mode of the orientation, pressure force and normal elastic force in the periodic flapping regime. The temporal phase  $\psi$  is a linear function with a slope equal to the fundamental frequency  $\omega_0$  of the mode and the spatial phase  $\varphi$  has a linear trend away from the clamped corner, suggesting the propagation of waves along the flag. A phase speed in  $s$  can be defined from (4.21) as  $c^{(s)} = \dot{\psi}/\varphi_s$ . Because the flag deformation is not small, a wave traveling along the flag with a velocity  $c^{(s)}$  travels along the horizontal axis at reduced phase velocity  $c^{(x)}$ . Then  $c^{(x)}$  is of the same sign as  $c^{(s)}$  and  $|c^{(x)}| < |c^{(s)}|$ .

### **Kinematic and dynamic waves along the flag**

For the orientation angle  $\theta$ ,  $c^{(s)} > 0$  and the corresponding  $c^{(x)}$  is close to  $U_\infty$ : the deformation wave is created and advected by the outside flow. We refer to this wave as the *direct kinematic wave*, as all the kinematic fields (orientation, position and velocity) follow the same pattern. A horizontal wave-speed not greater than  $U_\infty$  in this passive drag-producing configuration is consistent with the work of Lighthill (1960), where thrust production is associated with deformation waves travelling faster than  $U_\infty$ . Triantafyllou (1992) also showed that a linear deformation wave traveling along an infinite flag extracts energy from the flow if its phase velocity is smaller than the outside flow velocity. In the permanent flapping regime, the mean energy transfer from the flow to the flag is equal to zero, and this is qualitatively consistent with the phase velocity being equal to the outside flow velocity.

However, we observe that the pressure and normal elastic forces in the flag have the form of a wave travelling upstream from the trailing edge where vorticity shedding prescribes the pressure jump as (4.13) simplifies at the trailing edge to

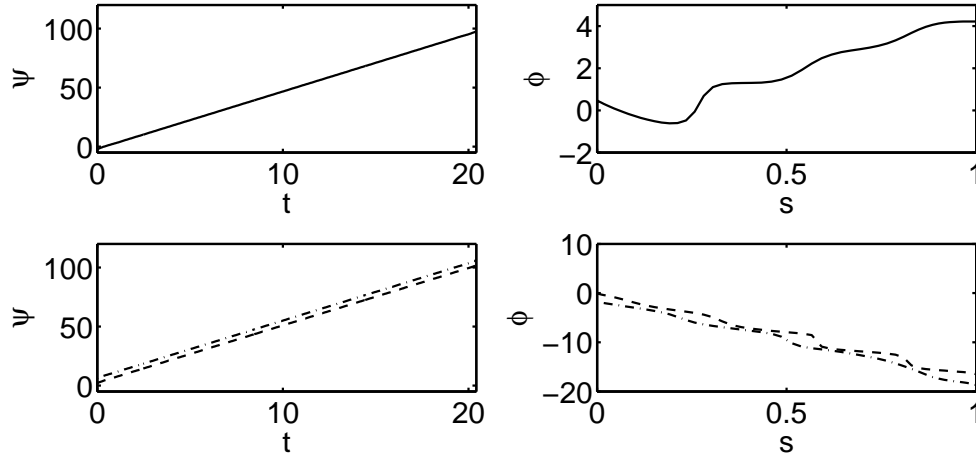


**Figure 4.8:** Temporal (left) and spatial (right) variations of the phase of the first CEOF in the flapping regime at  $M^* = 10$  and  $U^* = 11$ , for (top) the orientation of the flag  $\theta(s, t)$  and (bottom) the local pressure force (dash-dotted) and the normal component of the elastic forces in the flag (dashed). The range of  $t$  used covers about 16 periods of the flapping regime.  $\psi > 0$ , therefore monotonic variations of  $\varphi$  and  $\varphi_s > 0$  (resp.  $\varphi_s < 0$ ) indicate a wave travelling to the right (resp. left).

$[p]^\pm = -\dot{\Gamma}_N$  (Figure 4.8). This pressure disturbance is carried upstream along the flag by its internal elasticity. Note that this *reverse dynamic wave* travels slower than the direct kinematic wave propagates downstream. A similar behavior was observed for the tension in the flag.

### Limitations of the analysis

It is however difficult to go beyond the qualitative analysis of the propagating waves presented above. The phase velocity is a locally defined quantity as  $\varphi$  is not a linear function of  $s$ . In particular, in regions where the flapping amplitude is small (necks), the phase varies rapidly with  $s$ , leading to smaller values of the phase velocity.

The main obstacle to a quantitative comparison of the phase velocities for various  $M^*$  and  $U^*$  resides in the large amplitude of deformation of the flag during the flapping motion: the phase velocity computed here is a velocity *along*

*the flag* (which is itself moving in time) and not simply along the horizontal axis. Furthermore, the propagating waves imply that a given point on the flag does not have a fixed horizontal position as in the limit of infinitesimally small deformations (see Chapter 5). Instead, each point far enough from the leading edge displays a vertical figure of 8 trajectory whose horizontal extent is non-negligible.

However, the physical concept behind the analysis is observed over the whole spectrum of  $M^*$  and  $U^*$  considered: kinematic quantities such as  $\theta(s, t)$  and  $\text{Im}(\zeta(s, t))$  correspond to a direct wave traveling along the flag at a velocity close to  $U_\infty$ , and we therefore suspect this wave is carried by the outside flow. In the mean time, dynamic quantities such as the pressure jump and elastic forces correspond to reverse dynamic waves whose phase velocity, averaged over the flag's length, varies between  $1/3$  and  $2/3$  of the outside flow velocity.

## 4.4 Flapping of two parallel flags

The approach presented in section 4.2 can be generalized easily to the case of  $Q$  identical flexible plates (or flags), whose leading edges are clamped at an equal distance  $D$  from each other. An additional non-dimensional parameter, the relative distance between the plates,  $d$ , is introduced:

$$d = \frac{D}{L}. \quad (4.22)$$

In this section, we are interested in the influence of  $d$  on the stability of the flat state of rest of the plates and on the nature and properties of the coupled modes. We first present briefly the equations of the problem for general  $Q$  before focusing on the case  $Q = 2$ .

#### 4.4.1 Equations of motion of $Q$ flexible plates shedding point vortices

In the following, we note  $\zeta^{(q)}(s, t)$  and  $\theta^{(q)}(s, t)$  the position and orientation of plate  $q$ . The inextensibility condition for plate ( $q$ ) leads to

$$\zeta^{(q)}(s, t) = (q - 1)d + \int_0^s e^{i\theta^{(q)}(s, t)} ds. \quad (4.23)$$

The position and intensity of the vortices shed from plate  $q$  are noted  $z_n^{(q)}$  and  $\Gamma_n^{(q)}$  with  $1 \leq n \leq N_q$  and  $N_q$ , the total number of vortices shed from the trailing edge of plate  $q$ . The equation of motion of the vortices is directly obtained from (4.6) as

$$\dot{z}_n^{(q)} + (z_n^{(q)} - \zeta^{(q)}(1, t)) \frac{\dot{\Gamma}_n^{(q)}}{\Gamma_n^{(q)}} = \overline{\dot{w}_n^{(q)}}, \quad 1 \leq n \leq N_q, \quad 1 \leq q \leq Q. \quad (4.24)$$

The effect of plate  $q$  on the flow is represented by a bound-vorticity distribution  $\kappa^{(q)}(s, t)$ . The flow field is obtained as the superposition of the flow at infinity and the contribution from the attached vorticity from each plate and from all the vortices present in the flow:

$$w(z, t) = 1 + \frac{1}{2\pi i} \sum_{q=1}^Q \left[ \int_0^1 \frac{\kappa^{(q)}(s, t) ds}{z - \zeta^{(q)}(s, t)} + \sum_{n=1}^{N_q} \frac{\Gamma_n^{(q)}}{z - z_n^{(q)}} \right]. \quad (4.25)$$

A system of integral equations for  $\kappa^{(q)}$  is obtained from the continuity of normal velocity on each plate. The conservation of circulation must be enforced for each plate, considering a material contour initially enclosing plate  $q$  *only*. Together with the regularity condition at the trailing edge of each plate, this leads to

$$\begin{aligned} & \frac{1}{2\pi} \sum_{k=1}^Q \int_0^1 \operatorname{Re} \left[ \frac{e^{i\theta^{(q)}(s_0)}}{\zeta^{(q)}(s_0) - \zeta^{(k)}(s)} \right] \kappa^{(k)}(s) ds \\ & = \operatorname{Im} \left[ e^{i\theta^{(q)}(s_0)} \left( 1 + \frac{1}{2\pi i} \sum_{k=1}^Q \sum_{j=1}^{N_k} \frac{\Gamma_j^{(k)}}{\zeta^{(k)}(s_0) - z_j^{(k)}} - \dot{\zeta}^{(q)} \right) \right], \end{aligned} \quad (4.26)$$

$$\int_0^1 \kappa^{(q)} ds + \sum_{j=1}^{N_q} \Gamma_j^{(q)} = 0, \quad \kappa^{(q)}(1, t) = 0, \quad \text{for } 1 \leq q \leq Q. \quad (4.27)$$

The pressure force applied on plate ( $q$ ) is (4.13)

$$[p^{(q)}]^\pm(s_0) = \int_0^{s_0} \dot{\kappa}^{(q)}(s) ds + \kappa^{(q)}(s_0) w_p^{(q)}(s_0), \quad \text{with} \quad (4.28)$$

$$w_p^{(q)}(s_0) = \text{Re} \left\{ e^{i\theta^{(q)}(s_0)} \left[ 1 - \frac{\dot{\zeta}^{(q)}(s_0)}{\zeta^{(q)}(s_0)} + \frac{1}{2\pi i} \sum_{k=1}^Q \left( \int_0^1 \frac{\kappa^{(k)}(s) ds}{\zeta^{(q)}(s_0) - \zeta^{(k)}(s)} \right. \right. \right. \\ \left. \left. \left. + \sum_{j=1}^{N_k} \frac{\Gamma_j^{(k)}}{\zeta^{(q)}(s_0) - z_j^{(k)}} \right) \right] \right\}.$$

Finally, the equation of motion for each plate is obtained as in (4.15)-(4.16) as a system of equations for  $\theta^{(q)}$  and  $T^{(q)}$  the tension in plate ( $q$ ) (the position of each plate being recovered using (4.23))

$$T_{ss}^{(q)} - \theta_s^{(q)2} T^{(q)} = -[p^{(q)}]^\pm \theta_s^{(q)} - 2\eta \theta_s^{(q)} \theta_{sss}^{(q)} - \eta \theta_{ss}^{(q)2} - \mu \dot{\theta}^{(q)2}, \quad (4.29)$$

$$\mu \ddot{\theta}^{(q)} = -[p^{(q)}]^\pm - \eta \theta_{ssss}^{(q)} + (T^{(q)} + \eta \theta_s^{(q)2}) \theta_{ss}^{(q)} + 2T_s^{(q)} \theta_s^{(q)}, \quad (4.30)$$

$$\theta^{(q)}(0, t) = \theta_s^{(q)}(1, t) = \theta_{ss}^{(q)}(1, t) = T^{(q)}(1, t) = 0 \quad (4.31)$$

$$\mu \int_0^1 \int_0^s e^{i\theta^{(q)}} \left( i \ddot{\theta}^{(q)} - \dot{\theta}^{(q)2} \right) ds' ds = T^{(q)}(0) - i \eta \theta_{ss}^{(q)}(0) - i \int_0^1 [p^{(q)}]^\pm e^{i\theta^{(q)}} ds. \quad (4.32)$$

Equations (4.23)-(4.32) are integrated in time using the same method as outlined for a single flag in section 4.2.4. The general method to solve the system of integral equations (4.26)-(4.27) is discussed in more details in appendix B.

In the following, we present results for the case of  $Q = 2$  coupled flexible plates (see Figure 4.9).

#### 4.4.2 Influence of the distance between plates on their stability

In this section, the stability of two parallel identical flexible plates is investigated. The flow is started from rest and ramped up to its unit long time value at  $t = 0$ . A perturbation is introduced to the system in the form of either (i) a small transient vertical component in the imposed flow as in section 4.3 or

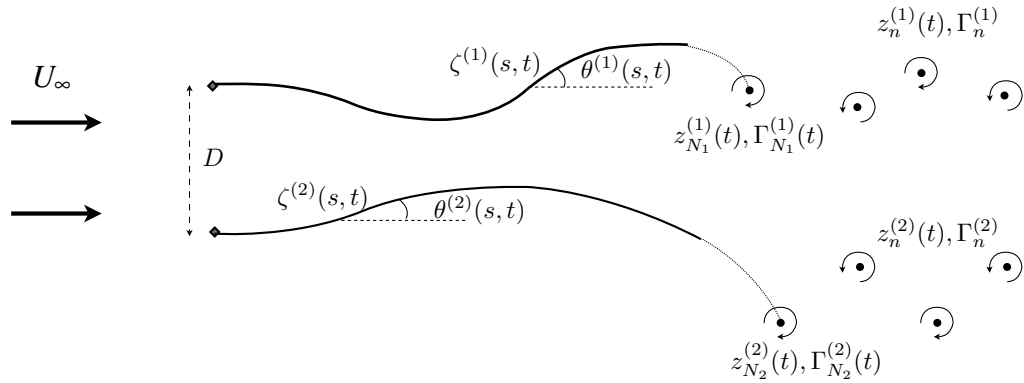


**Figure 4.9:** Flow past two identical flexible plates, with leading edge clamped at a cross-stream distance  $D$  from each other.

(ii) a small transient vertical displacement of the leading edge of plate 1. The latter option ensures the breaking of the symmetry between the two plates. No significant difference in the stability threshold or long-term flapping behavior was observed using the two methods.

The stability of the flat state of rest of a single flexible plate in an unbounded domain using the present unsteady point vortex method was presented in section 4.3 and in Michelin et al. (2008). Guo and Paidoussis (2000b) showed that the presence of boundaries influences the stability characteristics of the flag in the linear regime and a linear stability analysis of the case of several plates is presented in Chapter 5. We are interested here in the modification of the critical stability curve with the distance between the two flags. For a particular value of  $M^*$  and  $d$ , the critical value  $U_c(M^*, d)$  is determined as the minimum  $U^*$  for which the plates do not return to their initial state of rest after a small transient perturbation was applied.

Figure 4.10 shows the stability curve in the  $(M^*, U^*)$  plane for several values of  $d$ . The stability of one single plate is also reported and corresponds to the case  $d = \infty$ . As a general result, the stability region is reduced and the state of rest is destabilized by the proximity of a second plate. One can also observe that

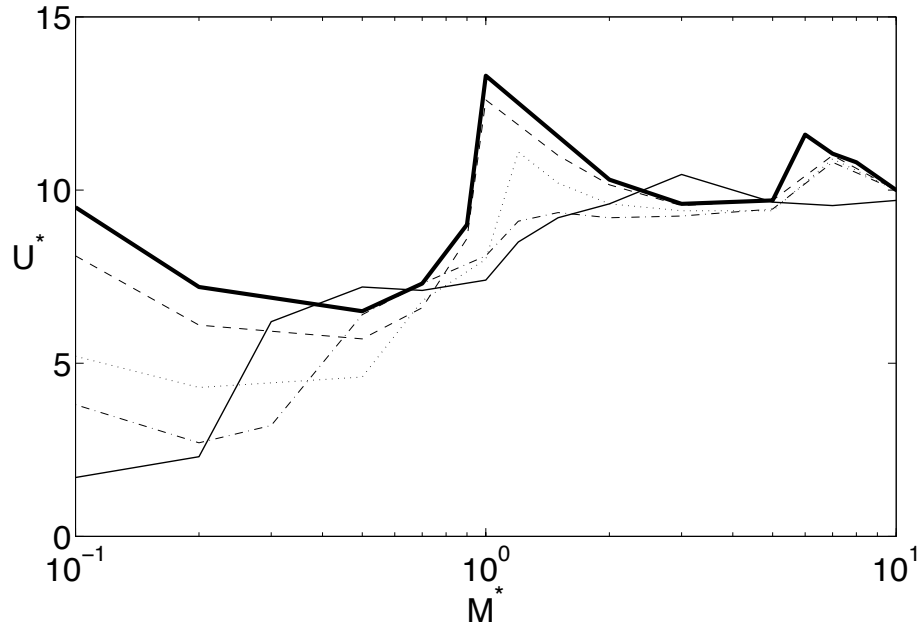


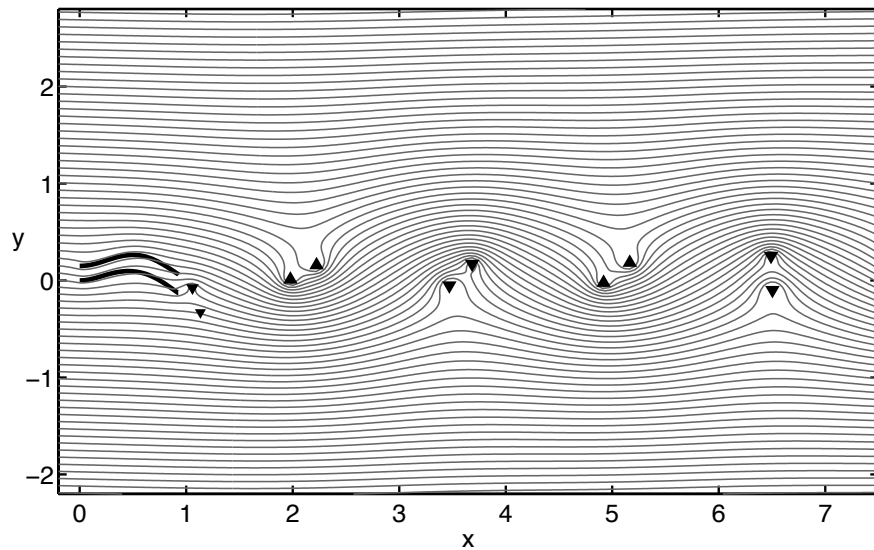
**Figure 4.10:** Position in the  $(M^*, U^*)$ -plane of the critical stability curve of two flexible plates for  $d = 0.1$  (thin solid),  $d = 0.2$  (dash-dotted),  $d = 0.4$  (dotted) and  $d = 1$  (dashed). The stability curve obtained for one isolated plate ( $d = \infty$ ) is also given for reference (thick solid). Below the critical curve, the two plates come back to their flat state of rest after being perturbed. Above the critical curve, the state of rest is unstable and flapping can develop.

heavier or shorter flags (small  $M^*$ ) are more affected by the proximity of the second plate. This can seem at first counter-intuitive as one might expect the closing gap between the plates to have more influence for flags with low inertia. However, for a single plate, a small  $M^*$  also corresponds to dominant modes with larger spatial structure (typically one-neck modes) while a larger  $M^*$  corresponds to dominant modes with shorter wave-length (see for example Michelin et al., 2008; Eloy et al., 2008). If one considers that the relevant length ratio for the perturbation of a particular mode is  $D/\lambda$  rather than  $D/L$  (with  $\lambda$  the mode's characteristic length scale), then modes with long wavelengths should be more influenced than modes with shorter wavelengths.

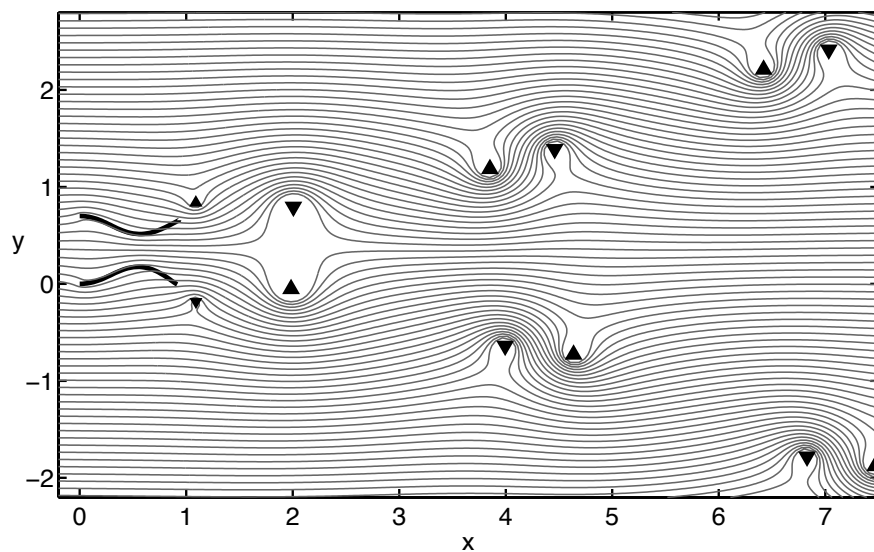
### 4.4.3 Coupled modes

The coupled motion of two identical flapping elastic sheets has recently been the focus of soap-film (Zhang et al., 2000; Jia et al., 2007) and wind-tunnel experiments (Schouveiler and Eloy, 2009). In both cases, it was observed that the motion of two sheets positioned at a short enough distance locked into one of the two following regimes: in-phase and out-of-phase. These two modes were also observed in recent numerical simulations (Farnell et al., 2004; Zhu and Peskin, 2003) and preliminary results on the motion of two flexible plates using the point vortex method presented in this dissertation confirmed the existence of in-phase and out-of-phase coupled modes (Michelin and Llewellyn Smith, 2009a).

- *in-phase mode*: in this mode, the two plates display very similar motions (see Figure 4.11a and Figure 6a of Jia et al. (2007)). During each half-period, one vortex is shed from each plate’s trailing edge and the two vortices have the same sign and intensity. For small enough  $d$ , their motion can be represented as an advection by the outside flow and other vortices, combined with a mutual rotation around their center of vorticity. In that regard, the wake of two plates positioned at a short distance and flapping in phase is very similar to that of one single flag. Because of the presence of the fluid flow between the plates, the equivalent elastic plate has modified characteristics (non-dimensional inertia and rigidity) compared to those of the individual plates. These modifications are however expected to depend not only on the plates’ separation but also on the shape of the flapping mode.
- *out-of-phase mode*: in the out-of-phase mode, the displacements of the two plates are symmetric with respect to the horizontal axis. During each half-period, one vortex is shed from each plate’s trailing edge but this time, the two vortices have opposite intensities. The resulting wake pattern is quite different from that of the in-phase mode: the vortices shed during the same half-period form a vortex pair, which is advected faster or slower than the



(a) In-phase flapping



(b) Out-of-phase flapping

**Figure 4.11:** Streamlines of the flow past two plates with  $M^* = 0.5$  and  $U^* = 8$ , (a) in the in-phase flapping mode with  $d = 0.15$  and (b) in the out-of-phase flapping mode with  $d = 0.7$ . The position of the vortices is also indicated with upward- (resp. downward-) pointing triangles corresponding to positive (resp. negative) intensity.

background flow, depending on its orientation. Within one period of flapping, two vortex pairs are formed, one of them catching up on the other because of this disposition. As a result, the two vortices shed from the same trailing edge get closer and the vortex pair system can rearrange itself into two vortex pairs consisting of vortices shed from the same plate. The resulting self-advection of these vortex pairs induces a  $V$ -shape wake (see Figure 4.11b and Figures 6b–d of Jia et al. (2007)).

For given solid and flow characteristics, the soap-film results of Zhang et al. (2000) showed that at large distance  $d$ , the filaments tend to lock in an out-of-phase regime, and as  $d$  was decreased, a transition was observed toward in-phase modes. Jia et al. (2007) repeated the experiment and also varied the filaments' length, observing that this transition from out-of-phase to in-phase flapping is not necessarily present. Instead, in the case of long filaments, the out-of-phase mode was observed for both large and small  $d$ .

A similar phenomenon is observed here using the point vortex representation for the wake: for some values of  $M^*$  and  $U^*$ , the transition from out-of-phase to in-phase flapping is indeed observed with decreasing  $d$  (see Figure 4.11). However, the existence of the transition seems to be determined not only by the relative distance  $d$ , but also by the mass ratio  $M^*$  and non-dimensional flow velocity  $U^*$ . For example, for  $M^* = 5$  and  $U^* = 11$ , we observed a persistence of the in-phase flapping even at large distances (two or three times the plate's length). This is also confirmed by looking at the nature of the dominant mode predicted by the linear stability analysis (see Michelin and Llewellyn Smith, 2009b, and Chapter 5).

Our ability to produce a map of the regimes observed in the  $(M^*, U^*, d)$ -space is however strongly limited by the impossibility for this model to represent the contact between two plates. For small plate separation  $d$ , a contact between the plates becomes very likely, particularly during the transient regime just after the perturbation (when the two plates' motions are not locked yet) or in an out-of-phase mode. Contact of the two filaments was indeed observed in soap-film

experiments (see Figure 4 in Zhang et al., 2000).

#### 4.4.4 Confinement and its effect on the flapping properties

Beyond the influence of the presence of a second flapping structure in the vicinity of the first one, a question of interest lies in the modification of the flapping regime (e.g. amplitude) and the resulting drag on the attachment of the plate with varying plate separation. Figure 4.12 presents the evolution with  $d$  of the flapping characteristics for the in-phase flapping mode observed for  $M^* = 5$  and  $U^* = 11$ . The proximity of the two plates induces an increase in the flapping amplitude, scaling as  $d^{-1/2}$ . No significant modification of the flapping frequency is observed. Therefore, the velocity of the plates' trailing edges also increases for decreasing  $d$ , and the scaling is the same. The total energy of each plate (4.20) therefore scales like  $d^{-1}$ . An increase of the flapping velocity and amplitude induces stronger vortices shed by the plate, resulting in an increase in the momentum carried by the vortices and therefore the average drag on each of the plate.

This result points out the influence of confinement on the passive response of flexible structures to an imposed parallel flow. The increased amplitude of flapping with smaller  $d$  is consistent with the physical idea that the proximity of the two plates induces a mutual destabilization. In parallel plate assemblies as used in cooling systems for example, this increased instability or flapping motion amplitude is to be controlled to avoid damage on the structure (Miller, 1960; Kim and Davis, 1995). From another point of view, one can also see that the mechanical energy stored in each plate is greater than that of a single flag flapping in the same flow. If one is interested in the design of energy harvesting systems, assuming the existence of a technology to harvest the bending energy of a flexible plate or membrane (see Allen and Smits, 2001, for other examples of energy harvesting systems based on this idea), then the use of assemblies of flexible plates rather than uncorrelated structures would be beneficial as more energy is extracted by the plates from the flow.

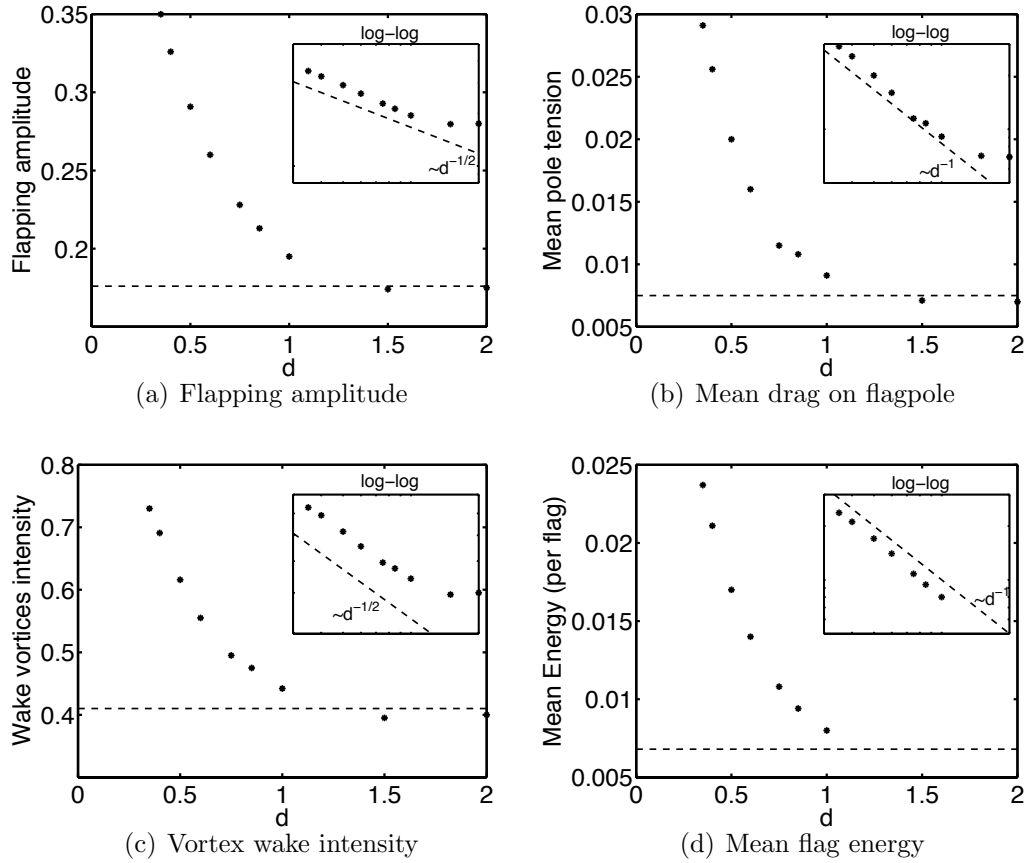


**Figure 4.12:** Evolution and scalings of the flapping characteristics with the relative distance  $d$  in the in-phase flapping mode of two plates with  $M^* = 5$  and  $U^* = 11$ .

## 4.5 Conclusions

We have shown that the unsteady point vortex model is able to reproduce both qualitatively and quantitatively the physical characteristics of the flapping of a flexible flag. The use of point vortices rather than full vortex sheets removes several computational issues due to the kernel singularities in the advection of free vortex sheets, and significantly reduces the computational complexity and cost.

The stability of the flag's state of rest and the structure of the flapping modes were studied and found to be in very good agreement with the analysis of Kornecki et al. (1976), which has been successfully compared by Eloy et al. (2008)

to experimental results. An analysis of the flapping regime showed the existence of direct kinematic waves (orientation, position and velocity) travelling with the same direction and velocity as the imposed flow, and the existence of reversed dynamic waves (pressure jump and elastic force) travelling in the opposite direction and carrying upstream along the flag the pressure change induced by the vortex shedding at the trailing edge. The study of these wave dynamics, in particular the variations of their phase velocity with the flag characteristics, is however limited by the strongly nonlinear deformation of the flag.

The model was also extended to the coupled motion of two flexible plates. We showed that the proximity of another plate had a destabilizing effect on the flat state of rest, but that the loss in stability was strongly dependent upon the relative inertia of the fluid and solid. In the fully-developed regime, two coupled modes were observed, in-phase and out-of-phase, but a map of the observed regime in the  $(M^*, U^*, d)$ -plane could not be obtained because of the possibility for the plates touching, a situation observed experimentally but impossible to represent in our model. Finally, a scaling of the flapping mode characteristics with the relative distance  $d$  was obtained. This analysis of the stability of multiple coupled plates is complemented by the linear stability analysis presented in Chapter 5.

In the present geometry, the flexible flag is clamped at its leading edge parallel to the flow in an infinite domain of fluid. Several other situations of interest should be studied to extend the present work in particular the effect of the presence of a solid wall on the flag stability (see the linear stability analysis of Guo and Païdoussis, 2000b). The present model can also be extended to study flapping structures tethered to massive substrates: the plate is in that situation clamped orthogonally to the imposed flow onto a solid wall. The present model would then account for the shedding of vorticity from this structure as it reconfigures under the influence of the wind flow. A very similar geometry was recently considered in a soap-film experiment (Alben et al., 2002, 2004). Alben et al. (2004) also proposed a theoretical computation of the equilibrium shape. This problem is of interest

to understand the reduction of the drag coefficient on botanical structures using shape reconfiguration (Vogel, 1989; Harder et al., 2004).

Chapter 4, in part, has been published in the *Journal of Fluid Mechanics*, “Vortex shedding model of a flapping flag” by S. Michelin, S. G. Llewellyn Smith and B. J. Glover, 2008, **617**, 1–10 (Cambridge University Press), doi: 10.1017/S0022112008004321. The dissertation author was the primary investigator and author of this material.

Some material drawn from Chapter 3 and Chapter 4 has been accepted for publication in *Theoretical and Computational Fluid Dynamics*, “Falling cards and flapping flags: understanding fluid-solid interactions using an unsteady point vortex method” by S. Michelin and S. G. Llewellyn Smith, 2009 (Springer), doi: 10.1007/S00162-009-0117-6. The dissertation author was the primary investigator and author of this material.

# 5

## Linear stability analysis of coupled parallel flexible plates in an axial flow

### 5.1 Introduction

In Chapter 4, we studied the dynamics of a single flag or flexible plate, and of two coupled plates in a parallel flow using a point vortex representation of the vortex wake and an elastic Euler–Bernoulli model for the plates. We considered large displacements of the plate and not only its linear stability analysis. Although the numerical simulation of the fully-developed regime allows for the study of various properties of the regime (flapping amplitude, drag,...), the impossibility of simulating a contact between the plates using this approach significantly limited our ability to identify the nature of the coupled modes (in-phase or out-of-phase). In this Chapter, we focus instead on the linear stability analysis of the problem of multiple coupled parallel flexible plates in an axial flow. Although we won't be able to study directly the properties of the fully-developed regime using this approach, the properties of the linear modes, and in particular those of the dominant (or most unstable) mode, are of interest as they influence the structure of the nonlinear regime (see section 4.3.3).

The flapping motion, also observed experimentally (Zhang et al., 2000; Shelley et al., 2005; Eloy et al., 2008) and in full numerical simulations (Connell and

Yue, 2007; Zhu and Peskin, 2002) is the result of the destabilization of the plate's straight position by fluttering under the competing effects of aerodynamic pressure forcing, solid inertia and solid flexural rigidity. In that regard, the nature of the instability is similar to that of flow-conveying pipes (Paidoussis, 1998). Beyond the fundamental interest of this instability and the resulting flapping motions, this mechanism is at the origin of the flapping of flags in the wind and is also of interest for engineering (Watanabe et al., 2002b) and biomedical applications (Huang, 1995; Balint and Lucey, 2005). Hydroelastic instabilities of parallel-plate assemblies are also important in the study of industrial cooling systems, as found in some nuclear reactors (Miller, 1960; Kim and Davis, 1995; Guo and Paidoussis, 2000a).

Since the first two-dimensional stability analysis by Rayleigh (1878), several models have been proposed to understand the instability threshold in the case of a single elastic plate. Shelley et al. (2005) considered the one-dimensional linear stability of a flag of infinite span and length under parallel flow forcing. Lemaitre et al. (2005) used a slender-body approximation to study the linear stability of long elastic ribbons. Kornecki et al. (1976) studied the linear stability of a finite-length cantilevered plate of infinite span, using a representation of the vortical wake as a vortex sheet (Theodorsen, 1935; Bisplinghoff et al., 1955), and Argentina and Mahadevan (2005) used a similar approach to study the influence of in-plane tension and finite span on the stability threshold. Guo and Paidoussis (2000b) considered the stability of a finite-length two-dimensional plate in a channel with various boundary conditions, using a simpler representation of the wake. Eloy et al. (2007) used the same approach to investigate the influence of three-dimensional effects on the stability of a finite-length cantilevered plate.

In the case of multiple parallel elastic plates, the imposed flow acts both as a forcing and a coupling mechanism between the motion of the plates. When the distance between the plates is of the order of or less than their length, it is expected that their dynamics will be strongly coupled. Zhang et al. (2000)

generalized their soap-film experiment to two parallel filaments and showed that the filaments' dynamics became coupled and that, depending on their relative distance, in-phase and out-of-phase modes could be observed (Figure 5.1). This observation was confirmed by Jia et al. (2007) who also considered filaments of various lengths. Depending on the length of the filaments, they observed either a transition from out-of-phase to in-phase flapping when bringing the filaments close together, or a persistence of the out-of-phase mode even at small separation. These results suggest that the nature of the observed regime is strongly dependent on more than just the relative distance between the different plates or filaments. Numerical simulations (Zhu and Peskin, 2003; Farnell et al., 2004; Huang et al., 2007; Michelin and Llewellyn Smith, 2009a) have also reported the existence of these two classes of regimes. Tang and Païdoussis (2009) presented a numerical study of the stability criteria for the in-phase and out-of-phase modes. More recently, Schouveiler and Eloy (2009) considered three and more coupled plates in a wind-tunnel experiment and observed various mode structures (Figure 5.1). In particular, in the symmetric mode, the middle plate was observed to remain still. Guo and Païdoussis (2000a) studied the linear stability of an infinite number of parallel plates of finite aspect ratio, clamped on their side edges and free at the leading and trailing edges. They however focused only on one particular type of modes (the out-of-phase mode, where the motions of two consecutive plates are always opposite), using the resulting symmetries to significantly reduce the complexity of the system.

The purpose of the present study is to propose a linear stability analysis of  $Q$  coupled flexible plates of infinite span, clamped at their leading edge in a uniform imposed flow. We investigate the existence and nature of coupled modes, that were previously observed experimentally and numerically (Zhang et al., 2000; Zhu and Peskin, 2003; Jia et al., 2007), as well as the influence of the plates' separation on the stability of the trivial state of rest and the structure of the linearly dominant flapping modes. In section 5.2, the double-wake method used in

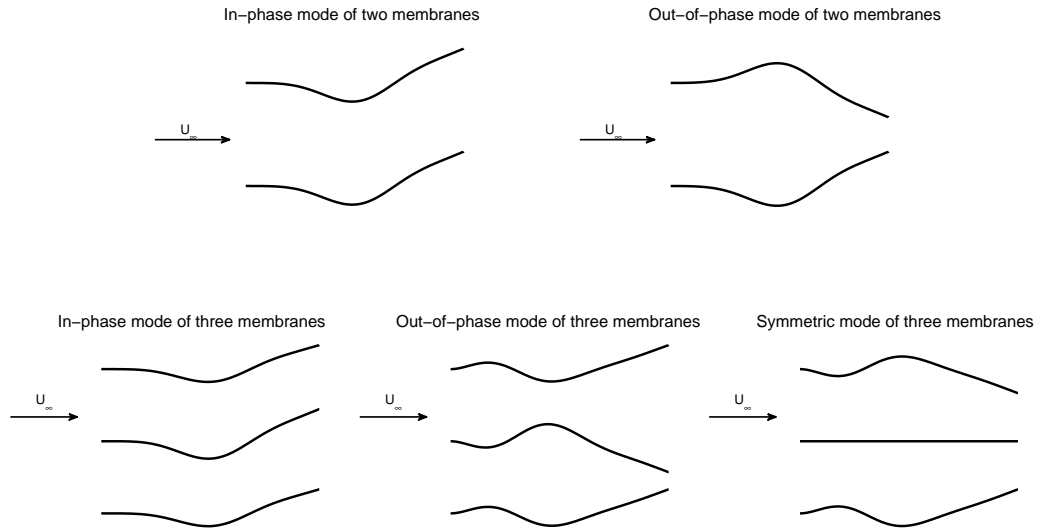


**Figure 5.1:** (Top) Sketch of the in-phase and out-of-phase modes observed experimentally for two flexible plates (Zhang et al., 2000; Jia et al., 2007). (Bottom) Sketch of the in-phase, out-of-phase and symmetric modes observed experimentally for three flexible plates (Schouveiler and Eloy, 2009).

Guo and Paidoussis (2000b) and Eloy et al. (2007) for a single plate is extended to the case of an arbitrary number of equidistant parallel plates. In sections 5.3 and 5.4, results on the linear stability of respectively two and three plates and the structure of the most unstable modes are discussed. Section 5.5 proposes an overview of expected results at larger  $Q$  as well as a discussion of the influence of  $Q$  on the critical stability curve for a fixed distance between the plates, and the nature of the corresponding dominant modes. Finally, conclusions are drawn in section 5.6.

## 5.2 Aerodynamic coupling of $Q$ flexible plates

### 5.2.1 Description of the problem

We are interested here in the linear stability of  $Q$  horizontal identical flexible and inextensible plates, placed in a parallel imposed flow along the horizontal

direction. The plates' span is assumed to be infinite so that the flow and plates' displacements can be considered two-dimensional. The plates are clamped at their leading edge and are equally spaced along the vertical axis at a distance  $D$  from each other: the leading edge of plate  $j$  ( $1 \leq j \leq Q$ ) is located at  $(0, (j-1)D)$ . All plates have length  $L$  in the streamwise direction, mass per unit area  $\rho_s$  and flexural rigidity  $B = Eh^3/[12(1-\nu^2)]$  (per unit length in the third dimension). Here,  $E$  and  $\nu$  are respectively the Young modulus and Poisson ratio of the plates, and  $h$  is the plate's thickness ( $h \ll L$ ). The velocity and density of the imposed flow are  $\rho$  and  $U_\infty$ . The problem is characterized by three non-dimensional parameters  $(M^*, U^*, d)$  defined as:

$$M^* = \frac{\rho L}{\rho_s}, \quad U^* = U_\infty L \sqrt{\frac{\rho_s}{B}}, \quad d = \frac{D}{L}. \quad (5.1)$$

In the following, all quantities are non-dimensionalized using  $\rho$ ,  $U_\infty$  and  $L$  as reference values: positions are non-dimensionalized by  $L$ , time is non-dimensionalized by  $L/U_\infty$ , velocity by  $U_\infty$  and pressure by  $\rho U_\infty^2$ . We are interested in the linear stability of the state of rest for which all the plates are horizontal and parallel to the incoming flow.

Assuming that the displacement of each plate from its state of rest is small, the geometry of plate  $j$  is described by the vertical displacement  $y^{(j)}(x, t)$  of the point located at a distance  $x$  along plate  $j$  in the state of rest. We are interested in the stability of infinitesimal perturbations, therefore  $|y^{(j)}| \ll 1$ . We assume that the plate is inextensible: any plate element must conserve its length at all time. Therefore, if  $\xi^{(j)}(x, t)$  is the horizontal displacement of the point located at a distance  $x$  along plate  $j$  in the state of rest, the inextensibility of the plate can be expressed as

$$\left(1 + \frac{\partial \xi^{(j)}}{\partial x}\right)^2 + \left(\frac{\partial y^{(j)}}{\partial x}\right)^2 = 1. \quad (5.2)$$

This relation implies that if  $y^{(j)}$  is of order  $\varepsilon$  (with  $\varepsilon \ll 1$ ), then the horizontal displacement  $\xi^{(j)}(x, t)$  is of order  $\varepsilon^2$ , and we neglect this horizontal displacement here. Assuming that the dynamics is governed by the Euler–Bernoulli equation

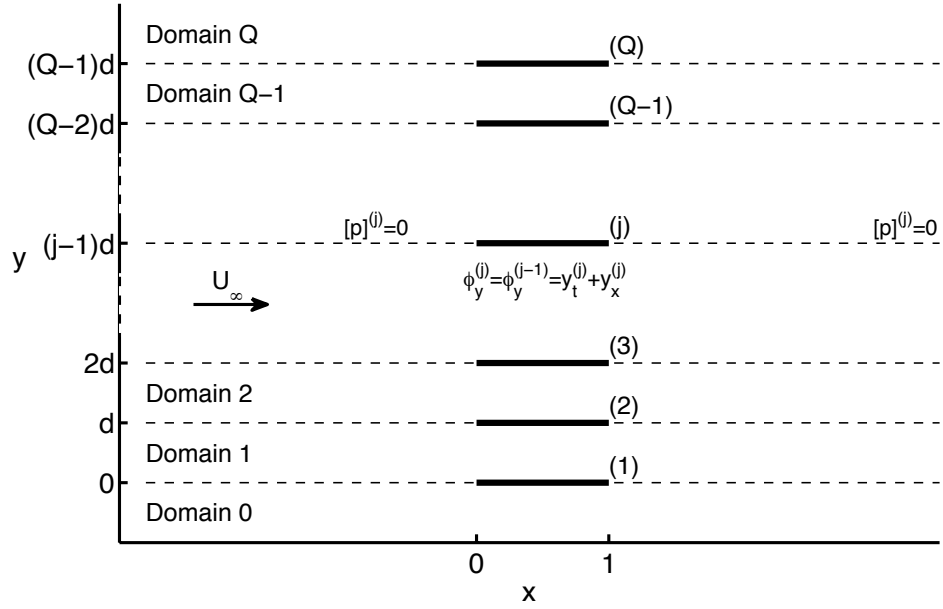


**Figure 5.2:** Horizontal flow over  $Q$  parallel plates. The plate index ( $j$ ) is indicated as well as the  $Q + 1$  domains into which the fluid is partitioned. On each plate, continuity of normal velocity is enforced. Continuity of pressure is enforced upstream and downstream of each plate.

with clamped-free boundary conditions, and keeping only the dominant terms, the equation of motion of plate  $j$  is obtained as:

$$\frac{\partial^2 y^{(j)}}{\partial t^2} = -\frac{1}{U^{*2}} \frac{\partial^4 y^{(j)}}{\partial x^4} - M^* [p]^{(j)}(x), \quad (5.3)$$

$$y^{(j)}(0, t) = y_x^{(j)}(0, t) = y_{xx}^{(j)}(1, t) = y_{xxx}^{(j)}(1, t) = 0,$$

where  $[p]^{(j)}$  is the pressure difference between the upper and lower sides of plate  $j$ .

### 5.2.2 Potential flow and wake representation

The fluid domain is divided into  $Q + 1$  domains (see Figure 5.2):

- Domain 0:  $y < 0$ ,
- Domain  $j$  ( $1 \leq j \leq Q - 1$ ):  $(j - 1)d < y < jd$ ,

– Domain  $Q$ :  $y > Qd$ .

We assume that the flow is potential in all domains, and the flow potential is continuously differentiable in each domain. In (5.3), we have  $[p]^{(j)}(x) = p^{(j)}(x, (j-1)d^+) - p^{(j-1)}(x, (j-1)d^-)$ .

From Bernoulli equation, the pressure in domain  $j$  is given by

$$p^{(j)}(x, y) = -\frac{\partial \Phi^{(j)}}{\partial t} - \frac{1}{2} |\nabla \Phi^{(j)}|^2, \quad (5.4)$$

where  $\Phi^{(j)}$  is the total flow potential, which can be decomposed as

$$\Phi^{(j)}(x, y) = x + \phi^{(j)}(x, y), \quad (5.5)$$

with  $\phi^{(j)}$  the perturbation of the potential due to the motion of the plates away from their state of rest ( $|\nabla \phi^{(j)}| \ll 1$ ). Keeping only the linear terms, the pressure forcing on each plate becomes:

$$[p]^{(j)}(x) = -\left(\frac{\partial}{\partial t} + \frac{\partial}{\partial x}\right) (\phi^{(j)} - \phi^{(j-1)}) \quad (5.6)$$

evaluated at  $y = (j-1)d$ .

The major difficulty in such situations is the representation of the wake. In the case of one single flapping plate, several models have been proposed. Using Theodorsen's theory (Theodorsen, 1935; Bisplinghoff et al., 1955), Kornecki et al. (1976) represented the wake of a single flexible plate as a distribution of vorticity along the horizontal axis advected at leading order by the imposed flow. The intensity of the vorticity shed at each time was such that the regularity condition is enforced at the trailing edge. In the following, we refer to this method as the Vortex Sheet (VS) method. Computations with better accuracy *using the same method and assumptions* were reported recently (Eloy et al., 2008). A summary of the method is presented in Appendix A. This elegant method is, however, difficult to generalize to two plates or one plate close to a wall, as it is based on the possibility of isolating the contribution of the frequency to the circulatory pressure with the so-called Theodorsen's function (Bisplinghoff et al., 1955). An

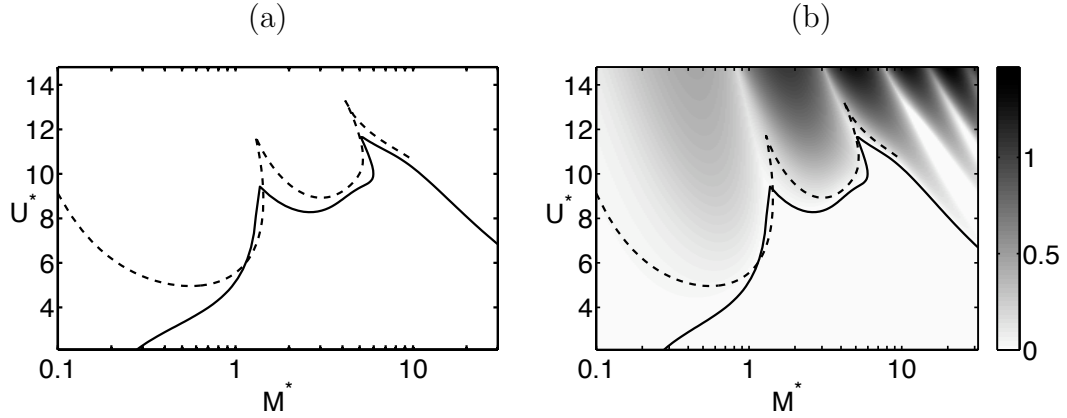


**Figure 5.3:** (a) Critical stability curve of a single cantilevered flexible plate of infinite span using the double wake (DW) representation (solid) and using the vortex sheet (VS) wake model (dashed). (b) Stability curves of (a) superimposed on the maximum growth rate observed with the double wake representation.

alternative approach has been proposed, representing the presence of the wake by the continuity of the pressure across the horizontal axis downstream from the plate ( $[p]^{(j)}(x) = 0$  for  $x > 1$ ): Guo and Païdoussis (2000b) and Eloy et al. (2007) used this method to study respectively the two-dimensional stability of a plate with infinite span in an inviscid channel flow and the three-dimensional stability of a finite-span plate in an unbounded flow. In this method, the pressure distribution is solved in Fourier space and the absence of singularities at both edges is assumed, thereby introducing an “upstream wake” to deal with the leading edge singularity. In the following, we shall therefore refer to this method as the Double Wake (DW) approach.

Although this double-wake assumption is not based on any physical argument, it was observed that in the case of a single plate, it leads to a good prediction of the critical velocity for fluttering instability (Eloy et al., 2007; Watanabe et al., 2002b), particularly for lighter plates ( $M^* \geq 1$ ) as can be seen on Figure 5.3. Both methods (VS and DW) predict the existence of different branches in the stability curve, each branch corresponding to different mode structures being most unstable. The first branch corresponds to a mode 2 (one-neck mode), the second branch

to a mode 3 (two-neck mode), and so on. Figure 5.3(b) shows the superposition of the stability curves obtained with each method, and the maximum growth rate observed using the DW representation. This provides some insight on the behavior at small  $M^*$ . The VS model predicts a stable flat state while the DW predicts unstable behavior. However, the associated growth rates (obtained with the DW method) are very small in the region of disagreement between the two theories.

The difference between the two approaches resides solely on the treatment of the wake. At high values of  $M^*$ , the dominant modes have shorter wavelengths and it is therefore expected that their dynamics are less influenced by the wake and more by the local displacement of the plate. Conversely, the first branch has a characteristic spatial scale of the order of the length of the plate, and is strongly influenced by the description of the wake.

### 5.2.3 Computation of the pressure forcing

We follow the DW method to compute the pressure forcing on each plate (Guo and Païdoussis, 2000b; Eloy et al., 2007). Each plate's displacement is decomposed into normal modes  $y^{(j)}(x, t) = \text{Re} [\zeta^{(j)}(x)e^{i\omega t}]$  with  $\omega$  a priori complex.  $\text{Re}(\omega)$  and  $-\text{Im}(\omega)$  are respectively the mode's frequency and growth rate. Unstable modes correspond to positive growth rate ( $\text{Im}(\omega) < 0$ ) and stable modes to negative growth rate ( $\text{Im}(\omega) > 0$ ). All quantities (pressure, potential) are also proportional to  $e^{i\omega t}$ , and in the following the time-dependence  $e^{i\omega t}$  will be implicit. The flow potential must satisfy the following system:

$$\nabla^2 \phi^{(j)} = \frac{\partial^2 \phi^{(j)}}{\partial x^2} + \frac{\partial^2 \phi^{(j)}}{\partial y^2} = 0, \quad 0 \leq j \leq Q \quad (5.7)$$

$$\nabla \phi^{(0)}|_{y \rightarrow -\infty} = \nabla \phi^{(Q)}|_{y \rightarrow \infty} = 0 \quad (5.8)$$

$$\frac{\partial \phi^{(j-1)}}{\partial y}(x, y = (j-1)d) = \frac{\partial \phi^{(j)}}{\partial y}(x, y = (j-1)d) = i\omega \zeta^{(j)} + \frac{d\zeta^{(j)}}{dx}, \quad \text{for } 0 \leq x \leq 1 \quad (5.9)$$

$$[p]^{(j)}(x) = 0, \quad \text{for } x \leq 0 \text{ and } x \geq 1 \quad (5.10)$$

with the pressure jump obtained from Bernoulli's equation (5.6) as

$$[p]^{(j)}(x) = - \left( i\omega + \frac{d}{dx} \right) [\phi^{(j)}(x, (j-1)d) - \phi^{(j-1)}(x, (j-1)d)]. \quad (5.11)$$

Equation (5.8) prescribes the correct decay of the flow perturbation: far from the plates in domain (0) and (Q), the velocity is dominated by the imposed unit parallel flow and the perturbation velocity becomes negligible. (5.9) enforces the slip boundary condition on each plate: on each side of the plate, the normal velocity of the flow must be equal to the plate's normal velocity. (5.10) is the regularity condition introduced by the wake downstream of the plates and the fictitious upstream wake: from (5.11), we see that it is equivalent to the advection by the mean flow of a discontinuity in the flow potential, or equivalently of a vorticity distribution on the horizontal axis (Eloy et al., 2007).

Using the Fourier transform in  $x$ , we look for solutions of the form

$$\phi^{(j)}(x, y) = \int_{-\infty}^{\infty} \tilde{\phi}^{(j)}(k, y) e^{ikx} dk, \quad (5.12)$$

and the function  $\tilde{\phi}^{(j)}(k, y)$  must satisfy from (5.7)

$$\frac{\partial^2 \tilde{\phi}^{(j)}}{\partial y^2} - k^2 \tilde{\phi}^{(j)} = 0, \quad (5.13)$$

whose general solution can be written

$$\tilde{\phi}^{(j)}(k, y) = A^{(j)}(k) e^{-|k|y} + B^{(j)}(k) e^{|k|y}. \quad (5.14)$$

From (5.9), we obtain:

$$B^{(j)}(k) - A^{(j)}(k) e^{-2|k|(j-1)d} = B^{(j-1)}(k) - A^{(j-1)}(k) e^{-2|k|(j-1)d}, \text{ for } 1 \leq j \leq Q. \quad (5.15)$$

The pressure difference at  $y = (j-1)d$  is then computed from (5.11) and (5.15) as

$$[p]^{(j)}(x) = -2i \int_{-\infty}^{\infty} (\omega + k) [A^{(j)}(k) - A^{(j-1)}(k)] e^{-|k|(j-1)d} e^{ikx} dk \quad (5.16)$$

$$= -2i \int_{-\infty}^{\infty} (\omega + k) [B^{(j)}(k) - B^{(j-1)}(k)] e^{|k|(j-1)d} e^{ikx} dk. \quad (5.17)$$

Differentiating (5.16)–(5.17) with respect to  $x$  and using the inverse Fourier transform and (5.10), we obtain

$$A^{(j)}(k) - A^{(j-1)}(k) = \frac{e^{|k|(j-1)d}}{4\pi k(\omega + k)} \int_0^1 [p]^{(j)}(\xi) e^{-ik\xi} d\xi \quad (5.18)$$

$$B^{(j)}(k) - B^{(j-1)}(k) = \frac{e^{-|k|(j-1)d}}{4\pi k(\omega + k)} \int_0^1 [p]^{(j)}(\xi) e^{-ik\xi} d\xi, \quad (5.19)$$

where prime quantities denote a derivative with respect to  $x$  ( $[p]^{(j)}$  is therefore the horizontal gradient of the pressure jump on plate  $j$ ). Using (5.8),  $A^{(0)} = B^{(Q)} = 0$  and therefore

$$A^{(j)}(k) = \frac{1}{4\pi k(\omega + k)} \sum_{l=1}^j e^{|k|(l-1)d} \int_0^1 [p]^{(l)}(\xi) e^{-ik\xi} d\xi \quad (5.20)$$

$$B^{(j)}(k) = \frac{1}{4\pi k(\omega + k)} \sum_{l=j+1}^Q e^{-|k|(l-1)d} \int_0^1 [p]^{(l)}(\xi) e^{-ik\xi} d\xi. \quad (5.21)$$

Finally, applying the operator  $(i\omega + d/dx)$  to (5.9), and using (5.14) and (5.20)–(5.21),

$$\begin{aligned} \left(i\omega + \frac{d}{dx}\right)^2 \zeta^{(j)}(x) &= i \int_{-\infty}^{\infty} |k|(\omega + k) (B^{(j)} e^{|k|(j-1)d} - A^{(j)} e^{-|k|(j-1)d}) e^{ikx} dk \\ &= -\frac{i}{4\pi} \int_{-\infty}^{\infty} \operatorname{sgn}(k) \sum_{l=1}^Q e^{-|k|(j-l)d} \int_0^1 [p]^{(l)}(\xi) e^{ik(x-\xi)} d\xi dk. \\ &= \frac{1}{2\pi} \sum_{l=1}^Q \int_0^1 K_{j,l}(x - \xi) [p]^{(l)}(\xi) d\xi \end{aligned} \quad (5.22)$$

with

$$K_{j,l}(u) = -\frac{i}{2} \int_{-\infty}^{\infty} \operatorname{sgn}(k) e^{-|k|(j-l)d} e^{iku} dk. \quad (5.23)$$

Using the following pair of Fourier transforms

$$-\frac{i}{2} \operatorname{sgn}(k) \longleftrightarrow \frac{1}{u}, \quad e^{-|k|\alpha} \longleftrightarrow \frac{2\alpha}{\alpha^2 + u^2}, \quad (5.24)$$

we obtain

$$K_{j,l}(u) = \frac{u}{u^2 + (j-l)^2 d^2} \quad \text{for } 1 \leq \{j, l\} \leq Q. \quad (5.25)$$

We therefore have to solve the following system of integral equations for the pressure gradients along each plate  $[p]^{(j)}$ :

$$\begin{aligned} -\omega^2 \zeta^{(j)} + 2i\omega \frac{d\zeta^{(j)}}{dx} + \frac{d^2 \zeta^{(j)}}{dx^2} = & \frac{1}{2\pi} \int_0^1 \frac{[p]^{(j)}(\xi) d\xi}{x - \xi} \\ & + \frac{1}{2\pi} \sum_{l \neq j} \int_0^1 \frac{x - \xi}{(x - \xi)^2 + (j - l)^2 d^2} [p]^{(l)}(\xi) d\xi, \end{aligned} \quad (5.26)$$

for  $1 \leq j \leq Q$ , with the additional constraints that  $[p]^{(j)} = 0$  at  $x = \{0, 1\}$  so that  $\int_0^1 [p]^{(j)} dx = 0$ . In (5.26), we have purposely isolated the term  $j = l$  which gives a Cauchy-type singular kernel. The first integral is understood as the Cauchy principal value. The linearity and form of (5.26) suggests to look for a solution of this system of integral equations in the following form (see for example Eloy et al., 2007):

$$[p]^{(j)}(x) = [p^{(K)}]^{(j)}(x) + 2i\omega [p^{(G)}]^{(j)}(x) - \omega^2 [p^{(M)}]^{(j)}(x), \quad (5.27)$$

with  $0 \leq x \leq 1$  and  $1 \leq j \leq Q$ . The pressure forcings  $[p^{(K)}]^{(j)}$ ,  $[p^{(G)}]^{(j)}$  and  $[p^{(M)}]^{(j)}$  are solutions of:

$$\begin{aligned} \frac{1}{2\pi} \int_0^1 \frac{[p^{(K)}]^{(j)}(\xi) d\xi}{x - \xi} + \frac{1}{2\pi} \sum_{l \neq j} \int_0^1 \frac{x - \xi}{(x - \xi)^2 + (j - l)^2 d^2} [p^{(K)}]^{(l)}(\xi) d\xi = & \frac{d^2 \zeta^{(j)}}{dx^2} \\ \text{with } \int_0^1 [p^{(K)}]^{(j)} dx = & 0, \end{aligned} \quad (5.28)$$

$$\begin{aligned} \frac{1}{2\pi} \int_0^1 \frac{[p^{(G)}]^{(j)}(\xi) d\xi}{x - \xi} + \frac{1}{2\pi} \sum_{l \neq j} \int_0^1 \frac{x - \xi}{(x - \xi)^2 + (j - l)^2 d^2} [p^{(G)}]^{(l)}(\xi) d\xi = & \frac{d\zeta^{(j)}}{dx} \\ \text{with } \int_0^1 [p^{(G)}]^{(j)} dx = & 0, \end{aligned} \quad (5.29)$$

$$\begin{aligned} \frac{1}{2\pi} \int_0^1 \frac{[p^{(M)}]^{(j)}(\xi) d\xi}{x - \xi} + \frac{1}{2\pi} \sum_{l \neq j} \int_0^1 \frac{x - \xi}{(x - \xi)^2 + (j - l)^2 d^2} [p^{(M)}]^{(l)}(\xi) d\xi = & \zeta^{(j)} \\ \text{with } \int_0^1 [p^{(M)}]^{(j)} dx = & 0. \end{aligned} \quad (5.30)$$

In (5.27)–(5.30), the pressure contributions with superscripts  $K$ ,  $G$  and  $M$  correspond respectively to added rigidity, gyroscopic and added inertia effects (Paidoussis, 2004).

### 5.2.4 Galerkin decomposition

The stability problem is then investigated using the Galerkin method. The displacement of each plate is decomposed onto the  $S$  first normal modes of the clamped-free beam in vacuum

$$\zeta^{(j)}(x) = \sum_{n=1}^S \alpha_n^{(j)} \psi_n(x), \quad (5.31)$$

$$\psi_n(x) = \cosh(\lambda_n x) - \cos(\lambda_n x) + \frac{\sin(\lambda_n) - \sinh(\lambda_n)}{\cos(\lambda_n) + \cosh(\lambda_n)} [\sinh(\lambda_n x) - \sin(\lambda_n x)],$$

and  $\lambda_n$  are the successive positive roots of

$$1 + \cos \lambda_n \cosh \lambda_n = 0. \quad (5.32)$$

These modes are solutions of the following problem:

$$\frac{d^4 \psi_n}{dx^4} = \lambda_n^4 \psi_n, \quad \psi_n(0) = \psi_n'(0) = \psi_n''(1) = \psi_n'''(1) = 0. \quad (5.33)$$

From this basis for one plate, we can easily build the basis for the  $Q$ -plate problem by considering the modes  $\Psi_m$  ( $1 \leq m \leq Q \times S$ ) defined as follow: mode  $(i-1)S + q$  (with  $1 \leq q \leq S$  and  $1 \leq i \leq Q$ ) corresponds to a displacement equal to  $\psi_q$  for plate  $i$ , all the other plates being held fixed. (In other words, if  $\boldsymbol{\psi}$  is the matrix of the value of the modes (5.31) at a set of points  $\mathbf{x}$ , the basis  $\boldsymbol{\Psi}$  for the  $Q$ -plate problem is block-diagonal with  $Q$  diagonal blocks equal to  $\boldsymbol{\psi}$ ).

From (5.27), for each mode  $\Psi_m$ , we obtain the pressure gradient  $P'_m$  as the following superposition:

$$P'_m = P_m^{(K)} + 2i\omega P_m^{(G)} - \omega^2 P_m^{(M)}, \quad (5.34)$$

with  $P_m^{(K)} = \left[ [p^{(K)}]_m^{(1)}, [p^{(K)}]_m^{(2)}, \dots, [p^{(K)}]_m^{(Q)} \right]^T$  and from (5.28)–(5.30),

$$\begin{aligned} \frac{1}{2\pi} \int_0^1 \frac{[p^{(K)}]_m^{(j)}(\xi) d\xi}{x - \xi} + \frac{1}{2\pi} \sum_{l \neq j} \int_0^1 \frac{x - \xi}{(x - \xi)^2 + (j - l)^2 d^2} [p^{(K)}]_m^{(l)}(\xi) d\xi &= \frac{d^2 \Psi_m^{(j)}}{dx^2}, \\ \int_0^1 [p^{(K)}]_m^{(j)}(x) dx &= 0, \end{aligned} \quad (5.35)$$

with  $\Psi_{(i-1)S+q}^{(j)}(x) = \delta_{ij}\psi_q(x)$ .  $P_m^{(G)}$  and  $P_m^{(M)}$  are obtained in the same way from (5.28)–(5.30), and the different pressure fields are then recovered by integration from the leading edge.

Equation (5.3) becomes for the  $Q$  plates (noting that most of the coefficients of each  $\Psi_m$  are equal to zero):

$$\sum_{m=1}^{Q \times S} \alpha_m \left[ -\omega^2 \Psi_m + \frac{1}{U^{*2}} \frac{d^4 \Psi_m}{dx^4} + M^* (-\omega^2 P_m^{(M)} + 2i\omega P_m^{(G)} + P_m^{(K)}) \right] = 0. \quad (5.36)$$

We define the scalar product  $\langle \cdot \rangle$  of two functions  $F = [f^{(1)}(x), \dots, f^{(Q)}(x)]^T$  and  $G = [g^{(1)}(x), \dots, g^{(Q)}(x)]^T$  as

$$\langle F, G \rangle = \sum_{j=1}^Q \int_0^1 f^{(j)}(x) g^{(j)}(x) dx. \quad (5.37)$$

Taking the scalar product of (5.36) with  $\Psi_n$ , we obtain a non-linear eigenvalue problem for  $(\boldsymbol{\alpha}, \omega)$ :

$$\left[ -\omega^2 (\mathbf{M} + M^* \mathbf{F}^{(M)}) + 2i\omega M^* \mathbf{F}^{(G)} + \frac{1}{U^{*2}} \mathbf{K} + M^* \mathbf{F}^{(K)} \right] \cdot \boldsymbol{\alpha} = 0 \quad (5.38)$$

where

$$\begin{aligned} M_{mn} &= \langle \Psi_m, \Psi_n \rangle, & K_{mn} &= \left\langle \frac{d^4 \Psi_m}{dx^4}, \Psi_n \right\rangle \\ F_{mn}^{(M)} &= \langle P_m^{(M)}, \Psi_n \rangle, & F_{mn}^{(G)} &= \langle P_m^{(G)}, \Psi_n \rangle, & F_{mn}^{(K)} &= \langle P_m^{(K)}, \Psi_n \rangle. \end{aligned} \quad (5.39)$$

Because  $\Psi_{(i-1)S+q}^{(j)} = \delta_{ij}\psi_p(x)$ , and the natural modes of the clamped-free beam are orthogonal and satisfy (5.33),  $\mathbf{M}$  is the identity matrix and  $\mathbf{K}$  is diagonal with

$$K_{(i-1)S+q} = \lambda_q^4 \quad \text{for } 1 \leq i \leq Q \text{ and } 1 \leq q \leq S, \quad (5.40)$$

and  $\lambda_q$  defined in (5.32).

## 5.2.5 Numerical solution

The main task consists in determining the matrices  $\mathbf{F}^{(M)}$ ,  $\mathbf{F}^{(G)}$  and  $\mathbf{F}^{(K)}$ . The results presented thereafter were obtained using  $S = 24$  modes for each

plate. A large enough number of Galerkin modes must be used to properly resolve the structure, growth rate and frequency of the physical modes (see for example Lemaitre et al., 2005), and tests with  $S = 48$  and  $S = 96$  were performed to ensure a proper convergence. Equation (5.38) has  $N_{tot} = 2Q \times S$  eigenmodes and the modes with largest frequency arise from the Galerkin decomposition and are not physical. We therefore chose to retain only the  $N_{tot}/4$  modes with smallest frequency in the remainder of the paper ( $12Q$  modes for  $S = 24$ ) to ensure we are studying only physical modes. This choice might lead us to discard some physical modes, but such discarded modes would have a very high frequency and short wavelength. Therefore, we expect these modes to have a negligible effect in the analysis of the real problem, as flow viscosity and material damping (both neglected in the present potential flow approach) would lead to a rapid dissipation of the energy in those modes.

Each function  $\psi_n(x)$  is evaluated on  $N_p = 200$  Gauss-Chebyshev points, and expanded using the first  $N_p$  Chebyshev polynomials of the first kind. Using this discretization is particularly well-suited for the solution of the coupled singular integral equations (5.28)–(5.30). The procedure for solving (5.28)–(5.30) is detailed in Appendix B. Once the different  $[p^{(K)}]^{(j)}$ ,  $[p^{(G)}]^{(j)}$  and  $[p^{(M)}]^{(j)}$  have been obtained, the matrix coefficients are computed using (5.37) and a Gauss–Chebyshev quadrature (Pozrikidis, 1998).

Once the matrices  $\mathbf{F}^{(M)}$ ,  $\mathbf{F}^{(G)}$  and  $\mathbf{F}^{(K)}$  have been obtained for a given value of  $d$ , the non-linear eigenvalue problem (5.38) is solved for given values of  $M^*$  and  $U^*$ .

We first note that, in (5.38),  $\omega$  always appears as powers of  $i\omega$  and all matrices are real. Therefore, if  $\omega$  is a solution,  $-\bar{\omega}$  is as well, with the same mode structure characteristics (the eigenfunctions are conjugate pairs). This result is a direct consequence of the choice made for the modal decomposition:  $y^{(j)}(x, t) = \text{Re} [\zeta^{(j)}(x)e^{i\omega t}]$ . The eigenvalues are therefore of two kinds: purely imaginary and pairs of eigenvalues with same imaginary parts but opposite real

parts. Because of this structure, in the following, we will only discuss the eigenvalue with positive real part, keeping in mind that when this real part is strictly positive, an associated eigenvalue also exists with opposite real part.

In the following, we study successively the stability properties of  $Q = 2$ ,  $Q = 3$  and  $Q \gg 1$  parallel elastic plates. In several places, we will consider the most unstable mode to determine for example the dominant mode's nature. We must point out here that this mode is dominant in the linear regime. Although several numerical and experimental studies on flexible flags have reported a good agreement between the structure of the observed dominant mode and the prediction of linear stability analysis (e.g. Eloy et al., 2008; Michelin et al., 2008), in the fully-developed regime, non-linear phenomena such as mode competition could modify the nature or properties of the dominant mode (e.g. frequency).

### 5.3 Stability of two coupled plates

In this section, we focus on the case of two identical flexible plates placed at a relative distance  $d$  from each other. The method outlined in the previous section is used setting  $Q = 2$ .

#### 5.3.1 Influence of $d$ on the stability of the flat state of rest

One question of interest when approaching two flexible plates to each other is whether and how the presence of the other plate will influence the stability threshold of the state of rest (flat and parallel to the imposed flow). The critical stability curve is plotted on Figure 5.4 for various values of the relative distance between the plates' leading edges. Below the critical curve, the state of rest is a stable equilibrium; above it, this state of rest is unstable and flapping can develop.

As a general result, we observe that the hydrodynamic coupling between the plates tends to destabilize the state of rest, as the stable range of parameter

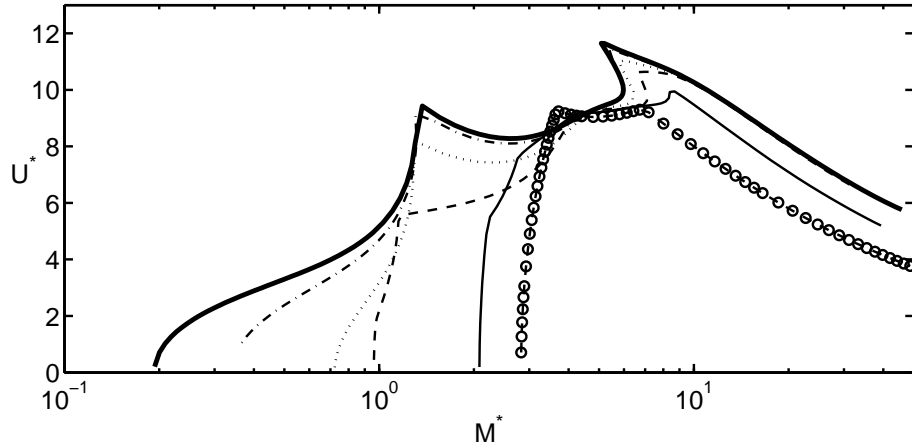


**Figure 5.4:** Critical stability curve of the state of rest of two plates in the  $(M^*, U^*)$ -plane for  $d = 0.1$  (circle),  $d = 0.2$  (thin solid),  $d = 0.5$  (dashed),  $d = 1$  (dotted) and  $d = 3$  (dash-dotted). The thick solid line is the stability curve for one flag only using the same approach (Eloy et al., 2007) and is equivalent to  $d = \infty$ .

values  $(M^*, U^*)$  shrinks with decreasing  $d$ . We observe that this reduction of the stability threshold  $U_c(M^*, d)$  with  $d$  (or the minimum  $U^*$  above which the state of rest becomes unstable) is not uniform with respect to  $M^*$ . Heavy flags ( $M^* \leq 1$ ) are destabilized for distances between the plates as large as three times their lengths, while the stability of light plates ( $M^* \geq 5$ ) is not affected until  $d < 0.5$ .

This is confirmed by looking at the growth rate of the most unstable mode, plotted on Figure 5.5(a) for several values of the relative distance between the plates. Two effects are evident from this picture. As expected for a particular distance  $d$ , the growth rate increases above the critical stability curve for increasing  $U^*$ : increasing  $U^*$  corresponds to an increasing forcing flow or a relatively smaller rigidity of the plates. More kinetic energy is then transferred from the outside flow to the plates' motion.

For small  $d$ , the dominant mode's stability properties are modified the most for small  $M^*$ : in that case, a significant increase of the dominant mode's growth rate is observed for decreasing  $d$ . The comparison of the different pictures

in Figure 5.5(a) also shows the evolution with  $d$  of the location of branches with reduced instability (light colors) in the  $(M^*, U^*)$ -plane, information that is not available when only the critical stability curve is considered. These regions are the most susceptible to become stable if a small amount of dissipation is added to the system.

This difference of behavior between small  $M^*$  and large  $M^*$  is illustrated on Figure 5.6 where the dominant mode characteristics are studied in the  $(U^*, d)$ -plane. For  $M^* = 2$ , the dominant mode stability, nature, growth rate and frequency depend strongly on  $d$ , while for  $M^* = 4$ ,  $d$  has a much weaker influence and the frequency and growth rate variations are due to changes in the dominant mode rather than a modification of a particular mode's properties with  $d$ .

One interpretation of the preferential destabilization of flags with low  $M^*$  lies in the mode structure associated with each branch on the stability curves in Figures 5.3 and 5.4. The most unstable branch at low  $M^*$  corresponds to modes with longer wavelengths than the subsequent branches. Modes with shorter wavelengths are expected to be less influenced by the presence of the second plate as the relevant aspect ratio is  $\lambda/D$  rather than  $L/D$  for this particular mode, with  $\lambda$  the wavelength of the mode.

### 5.3.2 In-phase and out-of-phase modes

For two coupled plates, eigenmodes can be of two natures: in-phase (the two plates having the same motion) and out-of-phase (the two plates having symmetric motions with respect to the horizontal axis) as illustrated on Figures 5.1 and 5.7. The nature of the mode is determined by computing the correlation between the spatial structure of the mode component along each plate. For a particular mode  $\omega$ , each plate's displacement can be defined as  $y^{(j)}(x, t) = \text{Re}[\zeta^{(j)}(x)e^{i\omega t}]$  with the same complex frequency  $\omega$ . The correlation coefficient for the motion of plates  $m$  and  $n$  is defined as the average value in  $x$  of the time correlation of these plates'

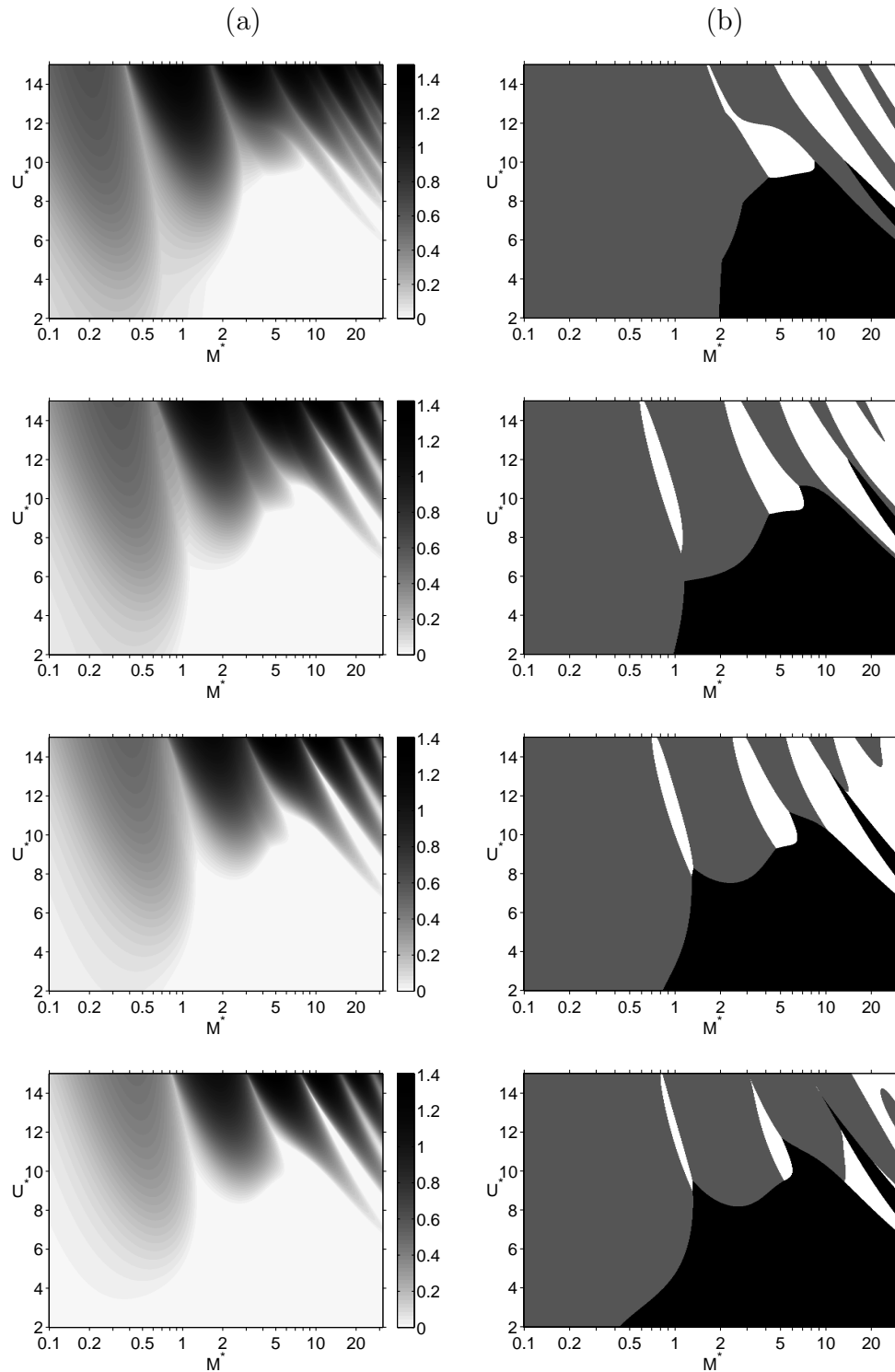


**Figure 5.5:** (a) Growth rate and (b) nature of the most unstable mode plotted in the  $(M^*, U^*)$ -plane for (from top to bottom)  $d = 0.2$ ,  $d = 0.5$ ,  $d = 1$  and  $d = 3$ . On the right column, the stability region of the state of rest is shown in black, while grey (resp. white) regions correspond to an out-of-phase (resp. in-phase) dominant mode.

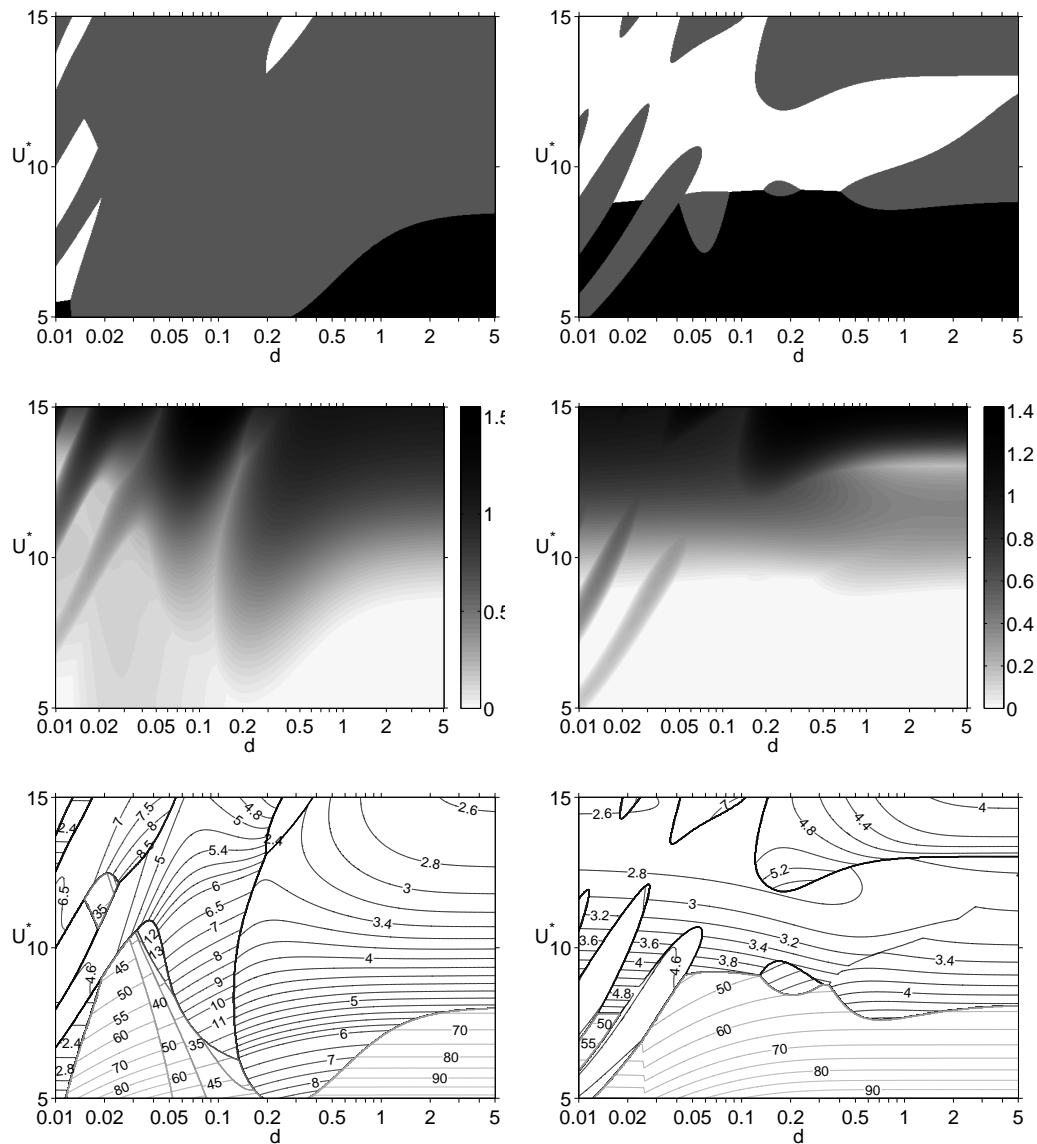


**Figure 5.6:** Evolution of the dominant mode properties in the  $(d, U^*)$ -plane for  $M^* = 2$  (left) and  $M^* = 4$  (right). (Top) Regime observed (with the same color code as in Figure 5.5). (Center) Growth rate of the most unstable mode (stable regions are indicated with a zero growth rate). (Bottom) Frequency of the dominant mode.

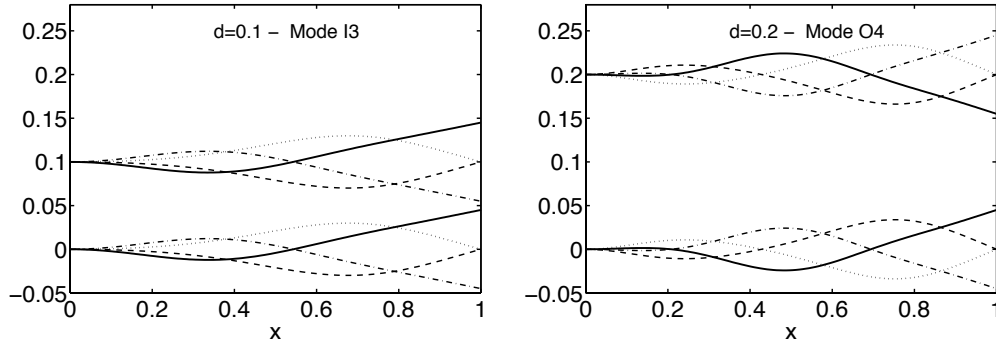


**Figure 5.7:** Dominant mode for  $M^* = 4$  and  $U^* = 13$  for (left)  $d = 0.1$  and (right)  $d = 0.2$ . The position of each plate is plotted at  $t = t_0$  (solid),  $t = t_0 + T/4$  (dashed),  $t = t_0 + T/2$  (dash-dotted) and  $t = t_0 + 3T/4$  (dotted), with  $T$  the pseudo-period of the mode ( $2\pi/\text{Re}(\omega)$ ). The same arbitrary amplitude of vertical motion was chosen for both cases.

displacement at  $x$ :

$$r_{mn} = \int_0^1 \frac{\text{Re} \left[ \zeta^{(m)}(x) \overline{\zeta^{(n)}(x)} \right]}{|\zeta^{(m)}(x) \zeta^{(n)}(x)|} dx \quad (5.41)$$

where the integrand is just the relative phase between  $\zeta^{(m)}(x)$  and  $\zeta^{(n)}(x)$ . This definition remains valid for the case of multiple plates. Here there are only two plates and only one correlation  $r = r_{12}$ . In practice, within each mode of the two-plate system, the motion of the plates were found either equal or opposite and a symmetry argument for this is given in section 5.5. Therefore, the correlation coefficient  $r$  is equal to  $\pm 1$ . A mode with  $r = 1$  (resp.  $r = -1$ ) is called thereafter an *in-phase* (resp. *out-of-phase*) mode. Figure 5.5(b) shows for given values of  $d$ , the nature of the most unstable mode in the  $(M^*, U^*)$ -plane. Alternatively, Figure 5.6 shows the evolution of the nature of the dominant mode in the  $(d, U^*)$ -plane for given  $M^*$ , thereby giving some insight on the influence of  $d$ .

In the following, modes will be referenced by their nature ( $I$  for in-phase modes and  $O$  for out-of-phase modes) and numbered by increasing frequencies at large  $d$ , to correspond for convenience to the numbering of the one-plate case (it is therefore possible for a mode 2 to have a higher frequency than a mode 3 at shorter distances).

These maps show that for increasing  $d$ , the domain of stability of the flat state of rest increases as observed in the previous section. From Figures 5.5 and 5.6, we also observe that for given values of  $M^*$  and  $U^*$ , it is possible to observe an in-phase mode at small distances  $d$  and a transition to an out-of-phase regime for increasing plate separation (see for example the case  $M^* = 4$  and  $U^* = 13$  on Figure 5.6 and in more details on Figure 5.8). This transition from in-phase to out-of-phase modes with increasing separation was observed experimentally (Zhang et al., 2000; Jia et al., 2007).

While it is clear from Figure 5.5(b) that the in-phase flapping modes are more often dominant at small distances than at larger distances, this transition is not always observed: in-phase flapping can be observed for large  $d$  (up to five times the plate's length for  $M^* = 4$  and  $U^* = 12.5$  as seen on Figure 5.6) and out-of-phase flapping can be observed for all values of  $d$  (for small inertia ratio  $M^*$ , the dominant mode is always out-of-phase). This is consistent with the soap-film experiments reported in Jia et al. (2007), which observed an out-of-phase mode at small and large distances for the shortest filament length (corresponding to smaller  $M^*$  and  $U^*$ , if all other properties are kept constant). It is also consistent with the results of Tang and Païdoussis (2009), who observed that the velocity threshold of the fluttering instability was always lower for out-of-phase modes than for in-phase modes in their study of plates with  $M^* = 0.2$ .

### 5.3.3 Influence of $d$ on the mode properties

Figures 5.8 and 5.9 show the evolution with  $d$  of the frequency  $\text{Re}(\omega)$  and growthrate  $\text{Im}(-\omega)$  of the lowest frequency in-phase and out-of-phase modes for two different sets of values of  $(M^*, U^*)$ . The branches on each of these plots correspond to continuous variations of the eigenvalue  $\omega$ . Note also that the nature of the mode (in-phase/out-of-phase) remains unchanged on a particular branch for all  $d$ -values (the correlation coefficient for each branch remains very close to either 1 or  $-1$ ).

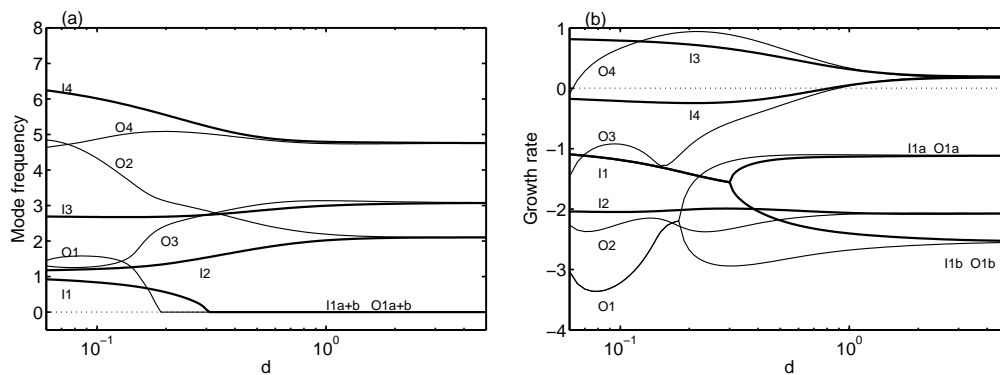


**Figure 5.8:**  $M^* = 4$  and  $U^* = 13$ . Variations of (a) the frequency and (b) the growth rate of the four in-phase (thick lines) and out-of-phase (thin lines) least stable modes. The modes are numbered by increasing frequency in the limit  $d \rightarrow \infty$ .

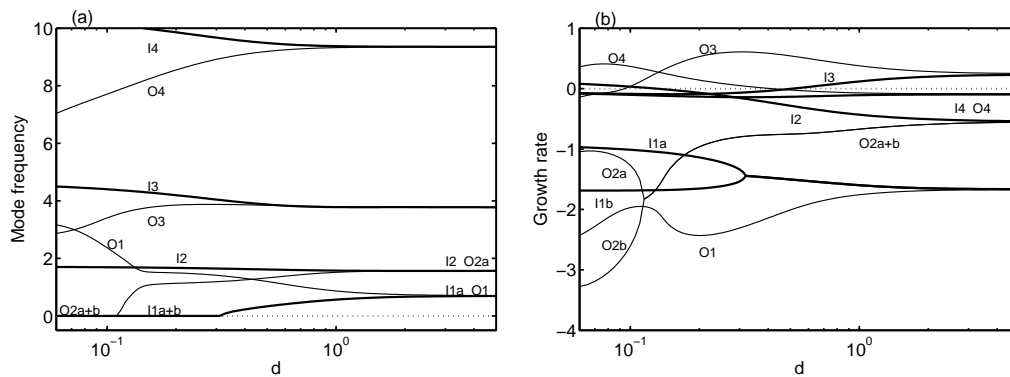


**Figure 5.9:** Same as figure 5.8 for  $M^* = 2$  and  $U^* = 10$ .

The structure of the mode (e.g. number of necks) can however vary with  $d$ , although we note that the most unstable modes preserve their general structure throughout the  $d$ -domain (Figure 5.10). Other more damped modes can however experience a strong modification of their structure as can be seen for mode O1b for example on Figure 5.10. The existence of a zero in the envelope corresponds to a standing wave mode ( $\text{Re}(\omega) = 0$ ).

At large distances, we observe the pairing of in-phase and out-of-phase branches. Within each pair, the mode frequencies, growth rates and mode structures become identical and approach asymptotically the mode characteristics obtained in the case of a single plate (Figures 5.8 and 5.10). Within each pair, the two modes differ however by the values of the correlation coefficient  $r$  (or the phase difference between the plates' motion) which are opposite.

We showed that the variations of the modes' growth rate with  $d$ ,  $M^*$  and  $U^*$  can induce a sudden change of the dominant mode nature as one parameter is varied (corresponding to the different domain boundaries on Figures 5.5(b) and 5.6). If the most linearly unstable mode determines the properties of the observed flapping in experiments and numerical simulations, then by varying one of the parameters (by either changing the separation  $D$  or the flow velocity  $U_\infty$  for example), one will experience a sudden change in the observed properties (for example, the flapping mode shape or its frequency). For  $M^* = 4$  and  $U^* = 13$ , the dominant mode is an in-phase flapping at short distances ( $d < 0.15$ ) and an out-of-phase flapping at larger distances (Figure 5.8). At the transition, the structure of the dominant mode (and therefore its characteristic wavelength) is also modified from a 2-neck mode (*I3*) to a 3-neck mode (*O4*) (see Figure 5.7), and a frequency jump is observed from  $\omega = 2.68$  (mode *I3*) to  $\omega = 4.96$  (mode *I4*). This frequency switch was also reported in previous experimental and numerical studies (Zhang et al., 2000; Farnell et al., 2004; Jia et al., 2007).

The frequency jump can be observed even when a transition occurs between two modes of the same nature. Figure 5.9 illustrates this with a case where

an out-of-phase mode is always dominant for  $M^* = 2$  and  $U^* = 10$ . Mode O4 is dominant for small distances  $d$ , while mode O3 is dominant at larger distances. The mode switch at  $d \sim 0.13$  leads to a negative dominant frequency switch from  $\omega = 8.1$  to  $\omega = 3.7$ .

This frequency jump and its variability with the parameter values are clearly visible on Figure 5.6. The frequency plots show some large variations of the dominant frequency with  $M^*$  and  $U^*$  for given  $d$ . Large frequency values can be achieved at low  $U^*$  (for large value of the plates' rigidity). We must point out that these frequencies occur mostly in the stability region where all modes have negative growth rates. In some situations, large dominant frequencies can also occur for unstable configurations but at very small separation distance (typically less than 5% of the plates' length as seen for  $M^* = 2$  on Figure 5.6). In the presence of a small amount of material damping or flow viscosity (neglected here), we expect these high-frequency modes to be the most affected.

## 5.4 Stability of three coupled plates

In the case of three evenly-spaced identical plates, three different types of modes are obtained that correspond to those observed experimentally (see Figure 5.1):

- an in-phase mode (I) where all three plates flap in phase. The correlation coefficients as defined in (5.41) satisfy  $r_{12} = r_{13} = r_{23} = 1$  and the outer plates have the same motion,
- an out-of phase mode (O) where the outer plates flap in phase with the same amplitude and the middle plate flaps with a phase equal to  $\pi$  with respect to the other plates ( $r_{12} = r_{23} = -1$  and  $r_{13} = 1$ ),
- a symmetric mode (S) where the outer plates have opposite vertical displacements and the middle plate remains still:  $r_{13} = -1$  and  $\zeta^{(2)}(x) = 0$ .

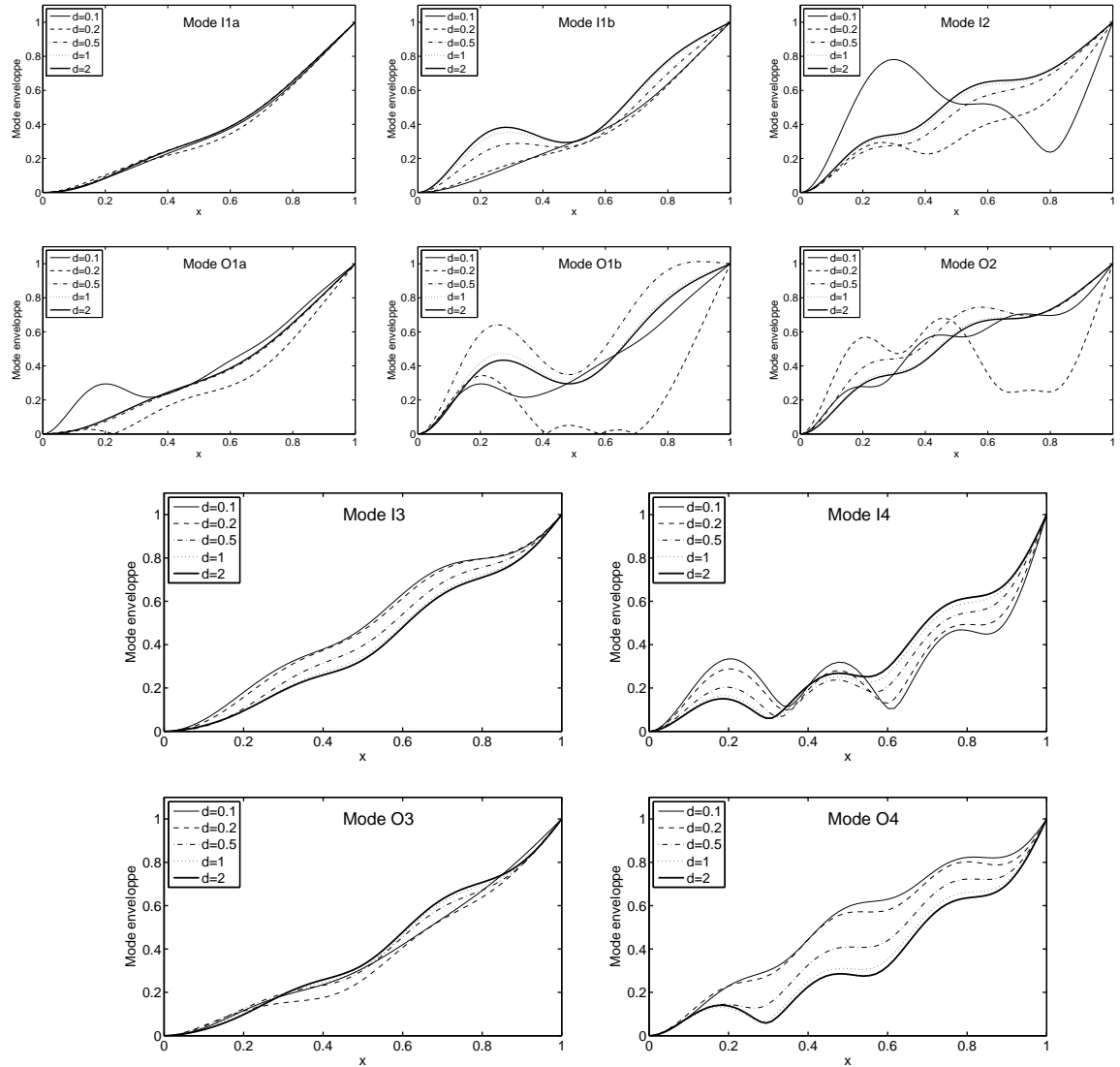


**Figure 5.10:** Evolution with  $d$  of the envelope of the least stable in-phase and out-of-phase modes for  $M^* = 4$  and  $U^* = 13$ . The indexing of the modes correspond to figure 5.8. The envelope is computed as the maximum vertical deflection achieved for  $0 \leq x \leq 1$ , for one of the two flags after normalizing the mode amplitude so that the amplitude at the trailing edge is always unity.

A symmetry argument for the existence of mode S will be given in section 5.5. The same symmetry argument will also prove that plates 1 and 3 always have equal or opposite motions, therefore their relative motion amplitude is equal to 1. However, in modes I and O, the motion of the center plate is in general not of the same amplitude as the two others' (although it was observed that it had the same  $x$  dependence leading to a correlation coefficient of  $\pm 1$ ).

For a given value of  $M^*$ , Figure 5.11 shows the evolution of the mode properties in the  $(d, U^*)$ -plane. We observe that at short distances and for light plates (large  $M^*$ ), the dominant mode structure is highly-sensitive to the problem parameters, with the presence of finger-shape regions of dominance of the O and S modes. At large distances the out-of-phase mode O prevails as for two plates. However for large  $d$ , the modes group in triplets. Within each triplet, one finds a mode of each kind (I, O and S) with frequency, growth rate and envelope asymptotically equal to the values for one plate only (Figure 5.12). For the particular choice  $M^* = 3$  and  $U^* = 13$ , we observe that for increasing  $d$ , the dominant mode takes alternatively each of the three possible natures (Figure 5.12). As for two plates, a switch in the dominant mode can lead to a sudden change of all the following: mode nature (I,O,S), mode structure and frequency.

## 5.5 Results for larger $Q$

### 5.5.1 Symmetry argument

In the previous sections, we have observed that all the modes are always symmetric or anti-symmetric in structure with respect to the axis of symmetry (between the two plates for  $Q = 2$  or on the middle plate for  $Q = 3$ ). We attempt here to provide a physical argument for this observation. A mathematical proof involving the structure of the matrices in (5.38) is presented in Appendix C.

The orientation of the horizontal axis is physically determined by the forcing flow. The orientation of the vertical axis is however purely arbitrary. For

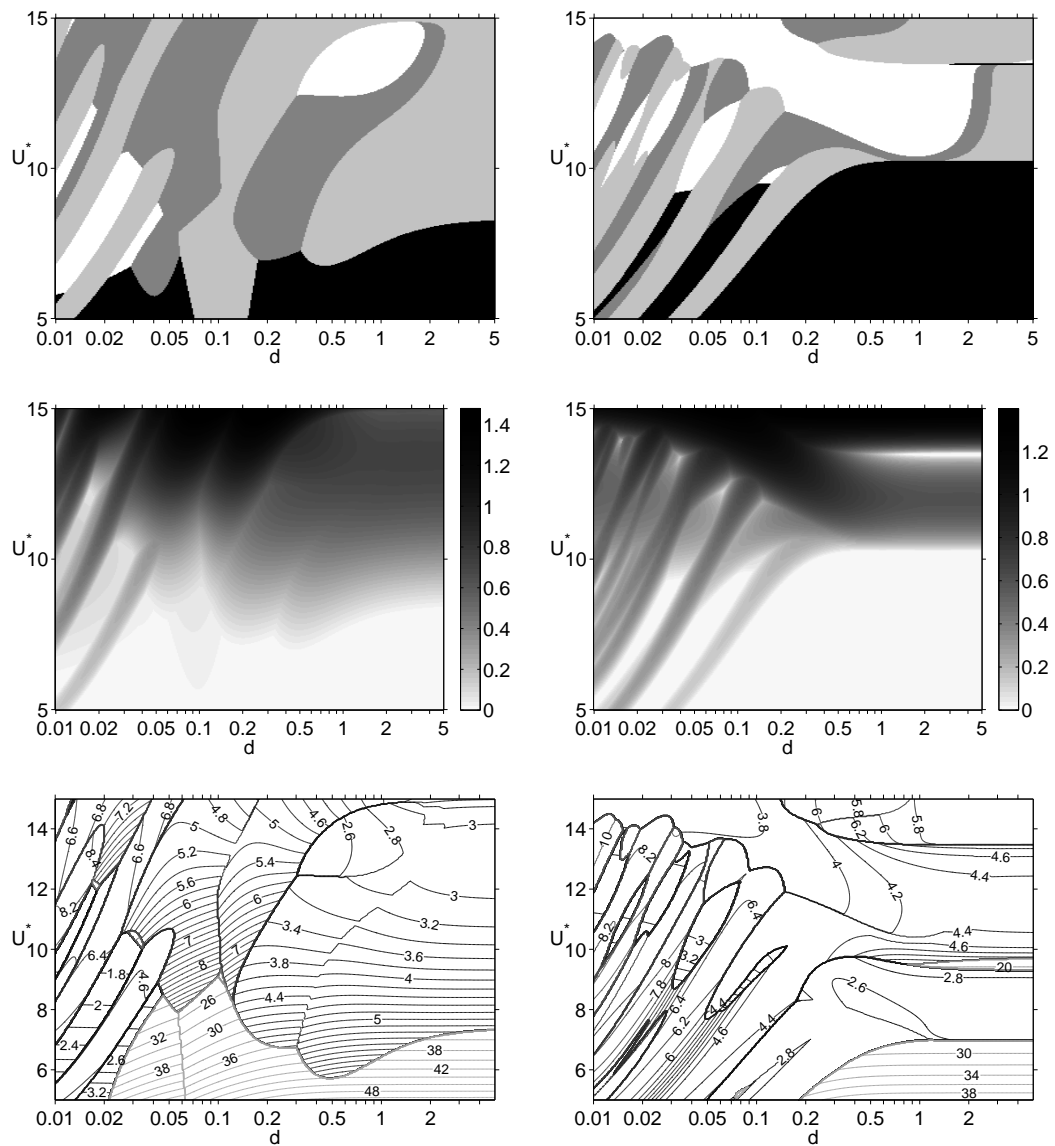


**Figure 5.11:** Evolution of the dominant mode properties for three plates with  $M^* = 3$  (left) and  $M^* = 10$  (right). (Top) The nature of the dominant mode is given in the  $(d, U^*)$ -plane: stability region (black), symmetric mode  $S$  (dark gray), out-of-phase mode  $O$  (light gray) and in-phase mode  $I$  (white). (Center) The maximum growth rate is plotted in the  $(d, U^*)$ -plane. Stability regions correspond to a zero growth rate for clarity. (Bottom) Contours of the dominant mode's frequency in the  $(d, U^*)$ -plane.

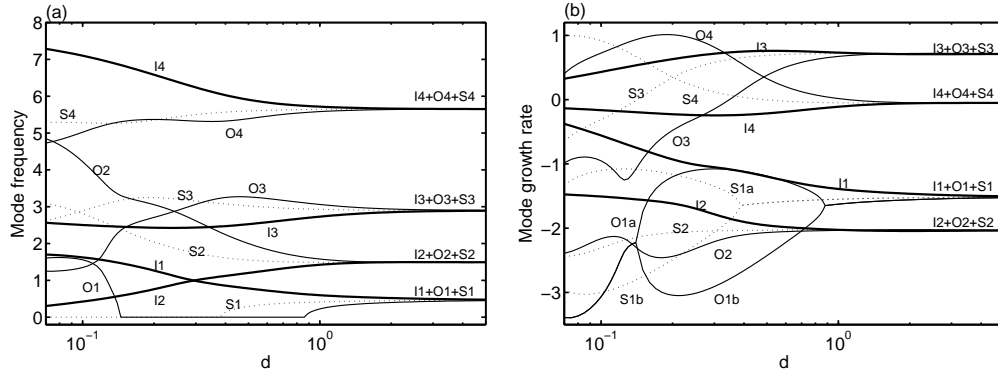


**Figure 5.12:** Evolution of the frequency (left) and growth rate (right) of the first four in-phase, out-of phase and symmetric modes for three plates with  $M^* = 3$  and  $U^* = 13$ . The branches corresponding to in-phase, out-of-phase and symmetric modes are plotted respectively with thick solid lines, thin solid lines and dotted lines.

a particular mode, define  $\zeta^{(j)}(x)$  the displacement of the plate clamped at  $y = (j - 1)d$ . Defining a new  $y$ -coordinate  $y'$  as  $y' = (Q - 1)d - y$  and a new indexing of the plates  $j' = Q + 1 - j$  will leave the problem absolutely unchanged. In this new situation, the displacement of the plate sitting at  $y' = (j - 1)d$  in a particular mode will be  $-\zeta^{(Q+1-j)}(x)$ . However, the physical problem is unchanged and the mode itself cannot have been modified, therefore there must exist a constant  $\lambda$  such that

$$\zeta^{(j)}(x) = -\lambda \zeta^{(Q+1-j)}(x) \text{ for all } 1 \leq j \leq Q. \quad (5.42)$$

Considering the previous equality for any pair  $j = i$  and  $j = Q + 1 - i$  ( $1 \leq i \leq Q$ ), we see that  $\lambda = \pm 1$ . In a particular mode, the displacements of plates  $j$  and  $Q + 1 - j$  must therefore be equal or opposite.

The correlation coefficient of the two plates as defined in (5.41) must be equal to  $\pm 1$ . Therefore, *the motion of the  $Q$  plates must be symmetric or anti-symmetric with respect to the plane located between plates  $Q/2$  and  $Q/2 + 1$  (resp. on plate  $(Q + 1)/2$ ) for even  $Q$  (resp. odd  $Q$ ).*

One consequence of this results is that for odd values of  $Q$ , symmetric modes correspond to a center plate at rest, as was observed for the case of three

plates in section 5.4.

### 5.5.2 The limit $Q \rightarrow \infty$

We now consider the limit case of a large number of plates  $Q$ . This geometry is particularly relevant in the study of plate assemblies as found in cooling systems or in some nuclear reactors (Miller, 1960; Kim and Davis, 1995; Guo and Païdoussis, 2000a). Since the problem is invariant by a translation of  $d$  along the vertical axis, we look for solutions of (5.7)–(5.10) in which the displacement  $\zeta^{(n)}$  and pressure perturbation  $[p]^{(n)}$  of plate  $n$  ( $-\infty < n < \infty$ ) are of the form

$$\zeta^{(n)}(x) = \zeta^{(0)}(x)e^{in\varphi}, \quad [p]^{(n)}(x) = [p]^{(0)}(x)e^{in\varphi} \quad (5.43)$$

with the phase  $\varphi$  being arbitrary between 0 and  $2\pi$ . From (5.26), we obtain  $[p]^{(0)}$  from  $\zeta^{(0)}$  as:

$$\frac{1}{2\pi} \int_0^1 K_\infty(x-\xi, \varphi) [p]^{(0)'}(\xi) d\xi = -\omega^2 \zeta^{(0)} + 2i\omega \frac{d\zeta^{(0)}}{dx} + \frac{d^2\zeta^{(0)}}{dx^2}, \quad \int_0^1 [p]^{(0)'}(\xi) d\xi = 0 \quad (5.44)$$

with the modified kernel  $K_\infty$  given by

$$K_\infty(u, \varphi) = \frac{1}{u} + 2 \sum_{n=1}^{\infty} \frac{u \cos n\varphi}{u^2 + n^2 d^2}. \quad (5.45)$$

We note here that  $K_\infty$  is an even function of  $\varphi$  (as expected since the problem is invariant by reversing the labeling order of the plates). In the following, we therefore restrict our study to  $0 \leq \varphi \leq \pi$ . Using Fourier series, we can determine  $K_\infty$  explicitly as

$$K_\infty(u, \varphi) = \frac{\pi \cosh \left[ \frac{u}{d} (\pi - \varphi) \right]}{d \sinh \left( \frac{\pi u}{d} \right)}, \quad \text{for } 0 \leq \varphi \leq \pi. \quad (5.46)$$

The case  $\varphi = 0$  will correspond to a purely in-phase mode (all the plates will have the same motion) and the case  $\varphi = \pi$  corresponds to the purely out-of-phase mode (any two consecutive plates have opposite vertical displacements). Guo and Païdoussis (2000a) studied the latter mode exclusively by assuming the symmetry

property to simplify the potential flow problem. They also used a different geometry with free boundary conditions applied at the leading and trailing edges, the side edges of the plate being clamped to a rigid wall. Here, we do not assume a priori a particular phase difference  $\varphi$  but instead consider all possible values of  $\varphi$  to determine the most unstable mode and its nature.

### Stability threshold at large $Q$

For a given  $\varphi$ , we can use the same approach as in section 5.2 and decompose  $\zeta^{(0)}$  over the first  $S$  fundamental modes of the clamped-free beam. For each mode  $\zeta_m^{(0)}$ , we then obtain from (5.44) and (5.27) the pressure gradients  $[p^{(M)}]_m^{(0)}$ ,  $[p^{(G)}]_m^{(0)}$  and  $[p^{(K)}]_m^{(0)}$ . For each value of  $\varphi$ , we compute the critical stability curve in the  $(M^*, U^*)$  plane of the modes with a phase difference  $\varphi$  between successive plates, and obtain the absolute stability curve by taking the intersection of the stability domains. The results are shown on Figure 5.13 for two values of the relative distance of the plates  $d = 0.2$  and  $d = 0.5$ , and compared to the results obtained using the method of section 5.2 with an increasing number of plates. We observe that the results obtained for increasing values of  $Q$  converge well to this limit boundary as  $Q \rightarrow \infty$ . We also observe that the stability curve converges rather fast toward this limit for both values of  $d$ . Most of the limit stability curve is obtained with a very good approximation for  $Q \geq 5$ .

### Properties of the dominant mode in the $Q \rightarrow \infty$ limit

Using the same method, we can compute the frequency and growth rate of the modes with a phase difference equal to  $\varphi$ . For a given value of  $M^*$ ,  $U^*$  and  $d$ , we search over all the possible values of  $\varphi$  for the most unstable mode. Figure 5.14 shows the phase difference between two plates corresponding to the most unstable mode, as well as this mode's frequency and growth rate. While the out-of-phase mode ( $\varphi = \pi$ ) tends to dominate for lower values of  $M^*$  and larger values of  $d$ , it is not necessarily the case. In particular, for large values of  $M^*$  or small values of  $d$ ,

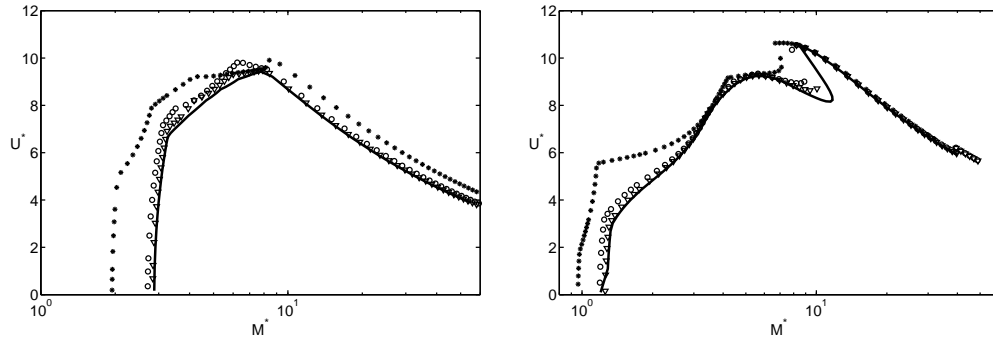


**Figure 5.13:** Evolution of the critical stability curve in the  $(M^*, U^*)$ -plane for  $d = 0.2$  (left) and  $d = 0.5$  (right), and an increasing number of plates:  $Q = 2$  (stars),  $Q = 5$  (circles) and  $Q = 10$  (triangles). The limit  $Q \rightarrow \infty$  described in section 5.5.2 is plotted as a thick black line.

the in-phase mode can be dominant. We also note that the transition from  $\varphi = 0$  to  $\varphi = \pi$  in the dominant mode is not necessarily discontinuous but that dominant modes with any value of  $\varphi$  can be found for a particular value of  $M^*$ ,  $U^*$  or  $d$ . This seems to contradict the assumption of Guo and Païdoussis (2000a) that the out-of-phase mode is dominant in the linear regime. We must however point out that Guo and Païdoussis (2000a) considered free-free boundary conditions, while the present work considers clamped-free plates. The change in boundary conditions is expected to have a significant impact on the position of the critical stability curve in the  $(M^*, U^*)$ -plane (Guo and Païdoussis, 2000b).

We noted previously that the convergence of the stability curve with increasing  $Q$  is a rather fast but inhomogeneous process,: some parts of the curve are obtained with a very good approximation for  $Q$  as low as 4 or 5, while others require a larger number of plates (Figure 5.13). From the top panel of Figure 5.14, we observe that the zones of fast convergence correspond to regions of the parameter space where the purely out-of-phase mode is dominant ( $\varphi = \pi$ ), while the slowest converging regions correspond to smaller values of  $\varphi$ . Physically, a mode with a phase difference  $\varphi$  between two successive plates can be seen as a wave traveling along the vertical axis with a wave-length equal to  $2\pi d/\varphi$  and the

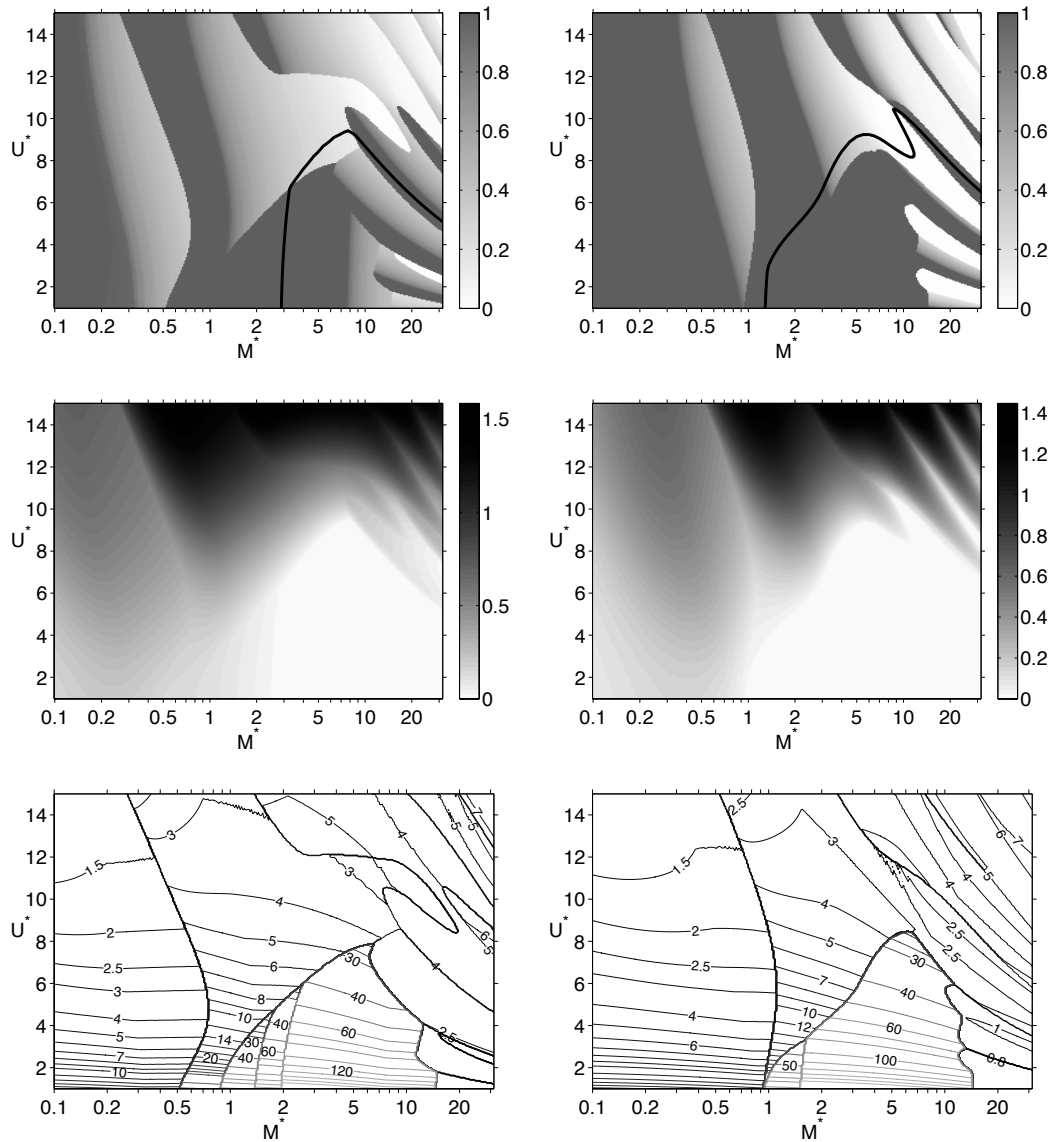


**Figure 5.14:** Evolution in the  $(M^*, U^*)$ -plane of the dominant mode properties for an infinite number of equally-spaced plates positioned at a distance  $d = 0.2$  (left) and  $d = 0.5$  (right) from each other. (Top) Relative phase  $\varphi$  between two consecutive plates (normalized by  $\pi$ ).  $\varphi/\pi = 1$  correspond to the purely out-of-phase mode where one plate's motion is opposite to its two neighbors'.  $\varphi/\pi = 0$  corresponds to the in-phase mode where all plates flap in phase. For reference, the stability curve of Figure 5.13 is also plotted (thick black line). (Center) Growth rate of the dominant mode. (Bottom) Frequency of the dominant mode.

number of plates necessary to describe that mode is of the order of  $2\pi/\varphi$ . For  $\varphi \sim \pi$ , the instability is well described by the motion of a plate coupled to its two nearest neighbors, while for small  $\varphi$ , a large number of plates is necessary to describe the structure of the mode accurately. The stability and properties of local modes (those described by a small number of plates) are less influenced by the total number of plates in the system.

## 5.6 Conclusions

Using the double-wake approach, we have performed the linear stability analysis of an array of  $Q$  parallel and identical flexible plates clamped at their leading edge in a horizontal flow. The behavior of two and three plates was discussed in more details, as well as the limit of an infinite number of plates.

This method allows one to reproduce important properties of the coupled motion of two plates observed in numerical and experimental studies. For a finite relative distance  $d$  between the plates, two types of modes are observed, corresponding to in-phase or out-of-phase motions of the plates. The linear stability framework allows one to obtain a map of the dominant modes in the  $(M^*, U^*, d)$ -space, and we observed that, while it is possible to observe a transition from in-phase to out-of-phase for increasing  $d$  and a particular choice of  $(M^*, U^*)$ , in some situations, the in-phase or the out-of-phase modes are dominant for all  $d$ , consistent with some recent experiments (Jia et al., 2007). In general, the presence of a second plate was shown to destabilize the straight rest position. The destabilizing effect was observed to be most significant for heavy or short flags (small  $M^*$ ). This preferential destabilization for small  $M^*$  was also observed in Guo and Paidoussis (2000b) for the stability of a single plate in a channel, linking this destabilization to confinement effects. Our analysis also shows that the dominant mode properties are strongly influenced by the fluid-solid inertia ratio  $M^*$ : the out-of-phase mode is linearly dominant for all values of  $d$  for heavy plates (small  $M^*$ ) as ob-

served numerically by Tang and Paidoussis (2009), while the in-phase mode can be dominant for larger values of  $M^*$ .

In the case of  $Q = 3$  plates, three types of modes (symmetric, in-phase and out-of-phase) were observed, consistently with recent wind-tunnel experiments by Schouveiler and Eloy (2009). The case of an infinite number of plates was then discussed. The stability curve was obtained as well as the properties of the most unstable mode. The out-of-phase mode (with two consecutive plates having opposite displacements) was shown to be the most unstable for low  $M^*$  and larger values of  $d$ . However, modes with any value of the phase difference  $\varphi \in [0, \pi]$  were shown to exist for some parameter values. The phase difference of the most unstable mode (or equivalently the number of plates necessary to describe this mode) was observed to condition the convergence of the stability curve for increasing  $Q$ .

The advantage of the present approach over the one-dimensional approach developed in Jia et al. (2007) and Shelley et al. (2005) lies in its ability to take into account the finite length of the plate and the presence of a wake enforcing a trailing edge regularity condition. However, additional modelling work is needed to include a more accurate representation of the vortical wake. From the comparison between the present double-wake approach and the vortex sheet representation for one plate, we expect the former to behave relatively well for larger values of  $M^*$ . For shorter or heavier flags, the influence of the wake is expected to be more important and we anticipate some discrepancies.

This Chapter, in part, has been accepted for publication in the *Journal of Fluids and Structures*, “Linear stability analysis of coupled parallel flexible plates in an axial flow” by S. Michelin and S. G. Llewellyn Smith (Elsevier Science), doi: 10.1016/j.jfluidstructs.2009.06.002. The dissertation author was the primary investigator and author of this material.

# 6

## Propulsive efficiency of a heaving flexible wing

### 6.1 Introduction

Unlike terrestrial animals that can use solid friction and a fixed support, insects and fishes must generate from the surrounding fluid the lift and thrust forces necessary to their motion in their environment (Lighthill, 1960, 1969; Childress, 1981; Triantafyllou et al., 2000; Wang, 2005). Beyond the fundamental interest of understanding the mechanism of insect flight and fish swimming, recent research on propulsion in fluids has also been motivated by the development of micro-aviation vehicles (MAV) and of more efficient propulsion techniques based on biomimetics or biomorphism (Jones et al., 2004).

Insects use thin flapping wings to generate an unsteady flow around them to produce these forces. The flow is characterized by a relatively large Reynolds number  $Re = UL/\nu$  with  $U$  the typical wing velocity,  $L$  its characteristic chord and  $\nu$  the kinematic viscosity of the surrounding fluid: Typically,  $Re \sim 100$ – $5000$  (Wang, 2005); in that range, the forces on the wings are dominated by the pressure contribution and viscous effects are concentrated in thin boundary layers near the solid's boundary. These boundary layers separate during the unsteady wing motion and roll up into strong coherent vortices (Thomas et al., 2004) that carry momentum away from the insect, thereby generating the propulsive forces.

The flow around the insect is highly unsteady, and an ongoing research challenge resides in the ability to describe the forces on the flapping structure without solving explicitly for the details of the flow (Ellington, 1984; Dickinson et al., 1999; Wang et al., 2004; Pesavento and Wang, 2004; Berman and Wang, 2007).

An important physical insight into the generation of propulsive forces by flapping or deforming solids has been provided by the study of active motion and deformation. In such experimental (Anderson et al., 1998; Godoy-Diana et al., 2008), theoretical (Wu, 1961; Lighthill, 1960) and numerical studies (Wang, 2000a,b; Miao and Ho, 2006; Shukla and Eldredge, 2007), the position of the solid is prescribed and the influence of the swimming stroke on the propulsive performance is analyzed.

The recent development of experimental imaging techniques has however shown that most insect wings are not purely rigid and that their deformation is not entirely controlled by the animal: the wing can experience large passive deformations during the stroke period (Wootton, 1992) under the action of the outside flow and its internal bending rigidity, whose spanwise and chordwise distribution results from the venation pattern of the wing (Combes and Daniel, 2003a,b). The wing motion is generally generated by a forcing applied by the insect through a main axis whose rigidity is significantly higher than the rest of the wing structure (e.g. the leading edge of the wing). An important challenge now is to understand the impact of such passive deformation on the propulsive performance of a flapping structure. In particular, one may be interested in potential reductions of energy usage induced by the flexibility or in examining whether the values of the rigidity for these structures lie within an "optimal" range for which the flapping efficiency is the highest. The definition of optimality in this work in terms only of propulsive efficiency and performances is purposely restrictive: from a biological point of view many other factors must be taken into account to define the optimal structure of an insect wing, including but not limited to material resistance and maneuverability.

The purpose of the present study is to investigate numerically the effect

of flexibility on the propulsive characteristics of a flapping appendage. In the following, we will refer to this structure as a wing with the understanding that the model could also be applied to a fish fin if it is allowed to deform passively under the effect of the flow and of its bending rigidity. Solving for the coupled motion of a flexible solid and a fluid is computationally challenging and expensive, primarily because of the coupling occurring on a moving boundary whose position is a priori unknown and must be solved for as well. Popular techniques to overcome this difficulty are the use of coupled fluid and solid solvers using fitted grids (Connell and Yue, 2007) and immersed boundary methods (Zhu and Peskin, 2002, 2003). The use of low-order models for the flexible wing also simplifies the computation while still retaining important physical results on the reaction of the body to the fluid flow (Bergou et al., 2007; Toomey and Eldredge, 2008).

The model used here focuses on a simplified two-dimensional propulsion problem using a flexible wing of infinite span, actuated at its leading edge in a purely heaving motion and reacting passively to the flow forces and its internal elasticity. The present model does not aim to represent a particular flying or swimming pattern, but rather considers a one-degree-of-freedom forcing to focus on the influence of flexibility on the performance of the apparatus. In the limit of high  $Re$ , viscous forces are neglected and viscosity's influence on the flow is retained in our potential flow formulation by the irreversible shedding of vorticity from the trailing edge of the flapping structure. This takes the form of point vortices whose unsteady intensity is determined so as to satisfy the regularity condition at the solid's trailing edge (Michelin and Llewellyn Smith, 2009c; Michelin et al., 2008). We thereby generalize in this Chapter the fluid-solid model presented in Chapter 4 for the motion of a passively flapping flag.

A similar approach was recently proposed by Alben (2008c) for a pitching flexible elastic sheet using a vortex sheet representation of the wake. Optimal values of the solid's rigidity were discussed in the limit of negligible solid inertia (particularly relevant in the case of fish swimming) and of infinitesimally small dis-

placements of the solid. The present work builds on these results and considers the general case of non-linear deformations of the sheet with non-negligible inertia (as is the case for a flapping insect wing). The use of the unsteady point vortex model rather than the full vortex sheet description also allows for a simpler treatment. Similar resonance patterns are observed and we provide a theoretical argument for their origin and position. The relation between thrust or drag production and vortex wake structure is also investigated.

In section 6.2, the fluid-solid model is presented and the propulsive performance quantities of interest are defined. Section 6.3 discusses briefly the numerical methods used as well as the existence of a periodic regime. Section 6.4 then investigates the influence of the solid's rigidity on the propulsion forces and efficiency and relates them to the structure of the solid's wake. Peaks of thrust are observed for particular values of the rigidity and in section 6.5, we show that the occurrence of such peaks correspond to a resonance between the forcing frequency and the natural frequencies of the fluid-solid system. Finally, section 6.6 presents some general conclusions and discusses the limitations of the model.

## 6.2 Description of the model

### 6.2.1 Solid model

We consider the following two-dimensional model for the flapping structure (see Figure 6.1). The wing is represented by an elastic sheet of chord  $L$  and infinite span, clamped at its leading edge on an attachment pole of negligible thickness, that is actuated by the operator (e.g. the main body of the insect). The operator applies a purely vertical motion to the sheet's leading edge, whose orientation is constrained to be strictly horizontal. The position and orientation of the wing at the leading edge are then:

$$\zeta_0(t) = ih(t) = ih_0(1 - \cos \omega t) \quad \text{and} \quad \theta_0(t) = 0, \quad (6.1)$$

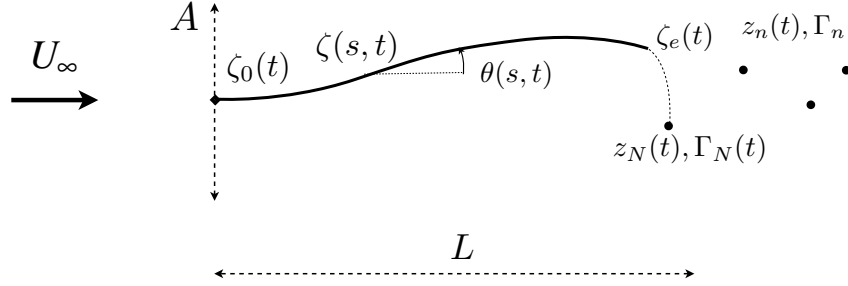


**Figure 6.1:** Heaving flexible wing in a steady axial flow. The heaving motion of amplitude  $A$  is imposed at the leading edge and vortices are shed from the trailing edge.

so that  $A = 2h_0$  and  $f = \omega/2\pi$  are respectively the amplitude and frequency of the flapping motion. To avoid confusion,  $\omega$  or its non-dimensional form will be referred to as the angular frequency in the following. The flapping wing has a chordwise flexural rigidity per unit length  $B$  and a mass per unit area  $\rho_s$ . Its thickness is negligible compared to  $L$ . The wing is placed in a uniform horizontal flow  $U_\infty$  of density  $\rho$ . The motion of the wing's leading edge is entirely prescribed by (6.1) but the rest of the wing has a purely passive motion in response to its internal elasticity, the leading-edge forcing and the pressure forces applied by the surrounding flow.

In the following,  $L$ ,  $U_\infty$  and  $\rho$  are used as reference quantities to non-dimensionalize the problem. The properties of the sheet are characterized by the mass ratio  $\mu$  and non-dimensional rigidity  $\eta$  defined as

$$\mu = \frac{\rho_s}{\rho L}, \quad \eta = \frac{B}{\rho U_\infty^2 L^3}, \quad (6.2)$$

and the leading-edge forcing is characterized by the non-dimensional forcing amplitude  $\varepsilon$  and frequency  $\bar{f}$

$$\varepsilon = \frac{h_0}{L} = \frac{A}{2L}, \quad \bar{f} = \frac{fL}{U_\infty}. \quad (6.3)$$

The forcing Strouhal number is defined in accordance with previous experimental studies (Anderson et al., 1998) as

$$St = \frac{fA}{U_\infty} = 2\varepsilon\bar{f}. \quad (6.4)$$

The motion of the wing is described using an inextensible Euler–Bernoulli beam representation (Michelin et al., 2008, and Chapter 4 of the present dissertation). We are interested in large displacements and deformation of the wing so all non-linear geometric terms must be included. The linear Euler–Bernoulli assumption remains valid if the curvature radius of the sheet is much larger than its thickness, which we assume here. The position and orientation of the wing are written respectively as  $\zeta(s, t)$  and  $\theta(s, t)$  with  $0 \leq s \leq 1$  the curvilinear coordinate along the wing. The conservation of momentum for each element of the wing and the inextensibility condition can be written as

$$\mu\ddot{\zeta} = [(T - i\eta\theta_{ss})e^{i\theta}]_s - i[p]^\pm e^{i\theta}, \quad \zeta_s = e^{i\theta}, \quad (6.5)$$

where  $[p]^\pm$  is the pressure difference between the top and bottom sides of the wing and  $T$  is the tension inside the wing that must be solved for at each time-step to enforce the inextensibility condition. The clamped-free boundary conditions are

$$\zeta(0, t) = \zeta_0(t) = i\varepsilon [1 - \cos(2\pi\bar{f}t)], \quad \theta(0, t) = 0, \quad (6.6)$$

$$\theta_s(1, t) = \theta_{ss}(1, t) = T(1, t) = 0. \quad (6.7)$$

Equations (6.5)–(6.7) can be rewritten as a system for  $\theta$  and  $T$  only (see Chapter 4 and Michelin et al., 2008):

$$T_{ss} - \theta_s^2 T = -[p]^\pm \theta_s - 2\eta\theta_s \theta_{sss} - \eta\theta_{ss}^2 - \mu\dot{\theta}^2, \quad (6.8)$$

$$\mu\ddot{\theta} = -[p]^\pm - \eta\theta_{ssss} + (T + \eta\theta_s^2)\theta_{ss} + 2T_s\theta_s, \quad (6.9)$$

$$\theta(0, t) = \theta_s(1, t) = \theta_{ss}(1, t) = T(1, t) = 0, \quad (6.10)$$

$$\mu\ddot{\zeta}_0 + \mu \int_0^1 \int_0^s e^{i\theta} (i\ddot{\theta} - \dot{\theta}^2) ds' ds = -T(0) + i\eta\theta_{ss}(0) - i \int_0^1 [p]^\pm e^{i\theta} ds. \quad (6.11)$$

## 6.2.2 Representation of the flow around the wing

The model of Chapter 4 for the flow over a deformable flag shedding vortices from its trailing edge is generalized here to the case of a flapping wing with imposed leading edge motion. The flow around the wing is taken to be potential. Point vortices are shed from the trailing edge  $\zeta_e = \zeta(1, t)$  with an unsteady intensity determined by the regularity condition on the flow field at  $\zeta_e$  (see section 2.4.1 and Michelin and Llewellyn Smith, 2009c). The shedding criterion of section 2.4.2 is used for the shedding of a new vortex. The equation of motion for these vortices is the Brown–Michael equation (see section 2.4.3):

$$\dot{z}_n + (z_n - \zeta_e) \frac{\dot{\Gamma}_n}{\Gamma_n} = \overline{\tilde{w}_n}, \quad (6.12)$$

where  $z_n$  and  $\Gamma_n$  respectively refer to the position and intensity of the point vortex.  $\tilde{w}_n$  is the desingularized velocity at the vortex position and the overbar denotes the complex conjugate. Equation (6.12) enforces the conservation of fluid momentum around the vortex and associated branch cut in an integral sense (see section 2.4.4 and Michelin and Llewellyn Smith, 2009c).

We neglect here the shedding of vorticity from the leading edge, as we focus mostly on situations where the angle of attack remains small at the leading edge (Alben, 2008c). Alternatively, our representation can also be seen as the limit case of a smoothed leading edge of very small curvature radius (as in an airfoil profile for example). Only one unsteady vortex is shed at a time (from the trailing edge). Noting  $N$  the number of vortices at a particular time, all vortex intensities  $\Gamma_n$  are therefore independent of time except for the last one  $\Gamma_N(t)$ .

The influence of the wing on the flow is represented using a bound vorticity distribution  $\kappa$  attached to the wing and the potential flow is obtained by superposition of the flow at infinity and the contribution of the bound and wake vorticity (see section 4.2.3). The normal flow continuity on the wing, the conservation of total circulation and the regularity condition lead to the following system

of equations for  $\kappa$  and  $\Gamma_N$ :

$$\frac{1}{2\pi} \int_0^1 \operatorname{Re} \left[ \frac{e^{i\theta(s)}}{\zeta(s_0) - \zeta(s)} \right] \kappa(s) ds = \operatorname{Im} \left[ e^{i\theta} \left( 1 + \frac{1}{2\pi i} \sum_{n=1}^N \frac{\Gamma_n}{\zeta - z_n} - \dot{\zeta} \right) \right], \quad (6.13)$$

$$\int_0^1 \kappa(s) ds + \sum_{n=1}^N \Gamma_n = 0, \quad (6.14)$$

$$\kappa(1, t) = 0. \quad (6.15)$$

From  $\kappa$ , the pressure jump  $[p]^\pm$  across the wing can be computed by integration of Bernoulli's theorem along the wing (see section 4.2.3 and equation (4.13)):

$$[p]^\pm(s_0) = \int_0^{s_0} \dot{\kappa}(s) ds + \kappa(s_0) w_p(s_0), \quad (6.16)$$

with  $w_p$  the principal value of the relative tangential velocity on the wing

$$w_p(s_0) = \operatorname{Re} \left[ e^{i\theta(s_0)} \left( \frac{1}{2\pi i} \int_0^1 \frac{\kappa(s) ds}{\zeta(s_0) - \zeta(s)} + U_\infty - \sum_{j=1}^N \frac{i\Gamma_j}{2\pi(\zeta(s_0) - z_j)} - \dot{\zeta}(s_0) \right) \right]. \quad (6.17)$$

### 6.2.3 Energy conservation

From (6.5), conservation of energy can be written for the wing

$$\frac{d}{dt} (E_k + E_p) = W_p + \mathcal{P}_{in}, \quad (6.18)$$

where

$$E_k = \frac{1}{2} \mu \int_0^1 |\dot{\zeta}|^2 ds, \quad (6.19)$$

$$E_p = \frac{1}{2} \eta \int_0^1 \theta_s^2 ds, \quad (6.20)$$

$$W_p = - \int_0^1 [p]^\pm \operatorname{Im} \left( \dot{\zeta} e^{-i\theta} \right) ds, \quad (6.21)$$

$$\mathcal{P}_{in} = - \operatorname{Re} \left[ \left( \dot{\zeta}(0) e^{-i\theta(0)} \right) (T(0) + i\eta \theta_{ss}(0)) \right] - \eta \dot{\theta}(0) \theta_s(0). \quad (6.22)$$

are respectively the kinetic and elastic potential energy of the wing, the rate of work of the pressure forces on the wing and the rate of work of the force and torque

applied by the attachment pole on the rest of the wing. In the particular case of a purely heaving motion considered here,  $\theta(0) = 0$  and  $\dot{\zeta}(0) = i\dot{h}$  is purely imaginary, so

$$\mathcal{P}_{in} = \eta\theta_{ss}(0)\dot{h}. \quad (6.23)$$

### 6.2.4 Propulsive performance

We are interested in the thrust generated by the flapping wing. The forces applied on the leading-edge attachment are:

- the elastic forces applied by the sheet on its attachment

$$[T(0) - i\eta\theta_{ss}(0)] e^{i\theta(0)}, \quad (6.24)$$

- the force applied by the operator (or animal) to prescribe the leading-edge motion  $F_{op} = F_{op}^x + iF_{op}^y$ ,
- the suction force created at the leading edge by the inverse-square root behavior of the pressure. This suction force is the limit of the suction force obtained on a smoothed contour when the curvature radius of the airfoil's leading edge tends to zero. This suction force is equal to (Saffman, 1992; Alben, 2008c; Gorelov, 2008)

$$F_s = -\frac{\pi e^{i\theta(0)}}{4} \left( \lim_{s \rightarrow 0} \left[ \sqrt{s(1-s)} \kappa(s) \right] \right)^2. \quad (6.25)$$

Neglecting the inertia of the attachment and defining the thrust (taken positive to the left) as  $\mathcal{T} = -F_{op}^x$ , the force balance along the horizontal direction together with (6.6)-(6.7) leads to

$$\mathcal{T} = \frac{\pi}{4} \left( \lim_{s \rightarrow 0} \left[ \sqrt{s(1-s)} \kappa(s) \right] \right)^2 - T(0). \quad (6.26)$$

The power input by the operator  $\mathcal{P}$  is

$$\mathcal{P} = \text{Re} \left( F_{op} \dot{\zeta}_0 \right) = F_{op}^y \dot{h}(t) = \eta\theta_{ss}(0, t)\dot{h}(t) = \mathcal{P}_{in}, \quad (6.27)$$

and is equal to the rate of work  $\mathcal{P}_{in}$  of the attachment pole on the wing. Note that this equality would not hold if the motion of the leading edge were a combination of both heaving and pitching, as the suction force  $F_s$  would have a non-zero rate of work in the vertical direction.

The useful power output is simply the rate of work  $\mathcal{T}U_\infty$  of the thrust force in the horizontal motion. In non-dimensional units, the flapping efficiency is then defined as the ratio of the average developed thrust to the average input power

$$r = \frac{\langle \mathcal{T} \rangle}{\langle \mathcal{P}^+ \rangle}, \quad (6.28)$$

where  $\langle . \rangle$  is the averaging operator

$$\langle g \rangle = \frac{1}{\tau} \int_0^\tau g(t) dt, \quad (6.29)$$

with  $\tau = 1/\bar{f}$  the non-dimensional period of the flapping motion and  $\mathcal{P}^+$  the positive part of  $\mathcal{P}$ . We assume here that the animal cannot store the energy extracted from the fluid during the possible fraction of the periodic motion where the input power is negative.

Finally, we define for convenience the following (non-dimensionalized) quantities:

- the trailing-edge peak-to-peak flapping amplitude  $\mathcal{D}$ ,
- the intensity of the wake  $\Gamma_w$ , defined as the mean value of the amplitude of the successive vortices (in absolute value),
- the induced velocity of the wake vortices  $\mathcal{V}$  defined as the horizontal velocity of the wake vortices relative to the imposed unit flow.  $\mathcal{V}$  is positive if the wake vortices move faster than the background flow, and negative otherwise.

### 6.3 Simulation of the initial value problem and convergence to a periodic state

Equations (6.8)–(6.12) and (6.13)–(6.16) are solved numerically expanding  $\theta(s, t)$  into a finite series of Chebyshev polynomials of the first kind and using a semi-implicit second-order time-stepping scheme. Taking advantage of the linear relation between  $[p]^\pm$  and  $\dot{\kappa}$ , added inertia terms can be isolated from the part of the pressure that can be explicitly computed at each time step, thereby avoiding the use of an iterative solver and greatly enhancing the computational efficiency (Michelin et al., 2008).

The system is started from rest. At  $t = 0$ , the horizontal flow is ramped up to its long time unit value and the motion of the leading edge (6.1) is imposed. After a transient regime of a few heaving periods, a permanent periodic regime is achieved for large enough values of the rigidity  $\eta$  (Figure 6.2a).

However, the harmonic heaving forcing can lead to highly unsteady behaviors if  $\eta$  becomes too small: below a certain critical value of the solid's rigidity  $\eta_m(\mu)$ , the purely passive elastic sheet (as in the flag problem) becomes unstable to fluttering modes and flapping can occur even in the absence of leading-edge forcing (Alben and Shelley, 2008; Michelin et al., 2008; Alben, 2008a) ( $\eta_m(\mu)$  was found to be equal to  $\eta_m = 2 \cdot 10^{-3}$  for  $\mu = 0.2$  and  $\eta_m = 4.8 \cdot 10^{-2}$  for  $\mu = 2$ , using the same point vortex model (Michelin et al., 2008)). In such cases, the spectrum of the trailing-edge motion can display several peaks, corresponding to the forcing frequency and to the frequency of the unstable modes (Figure 6.2b). The motion is of large enough amplitude for the regime to be non-linear and mode coupling is also expected. As  $\eta$  is reduced further, the periodicity is lost and the power spectrum is full; in such a case, determining averaged quantities is not possible anymore.

This explains the difficulty to observe a steady permanent regime when  $\eta$  is decreased below the critical value  $\eta_m$ . This difficulty was not present in the

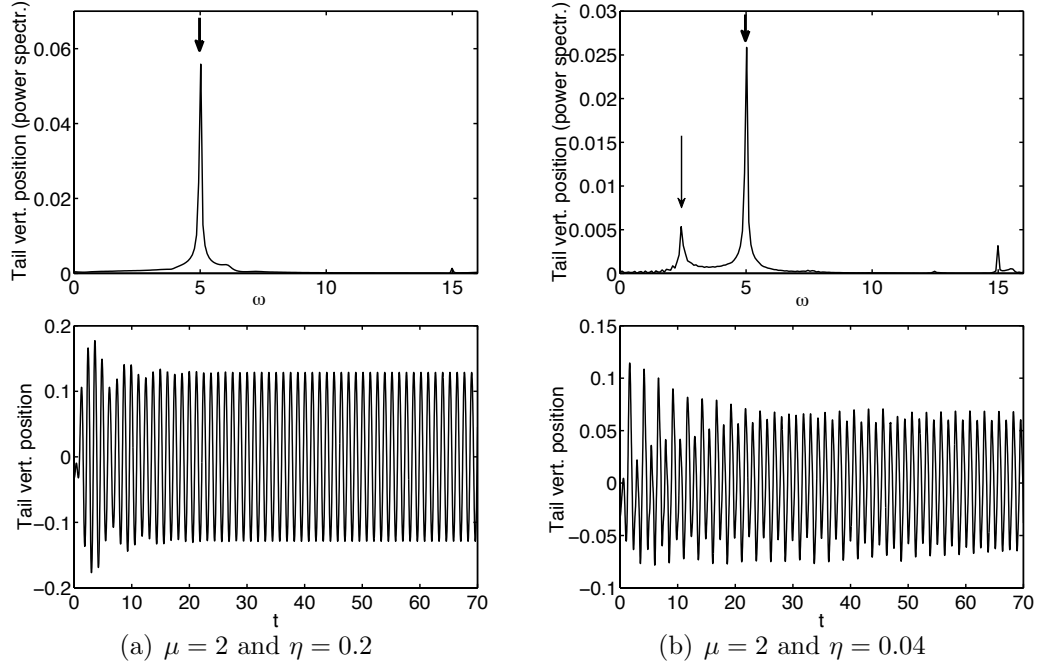


**Figure 6.2:** (Top) Frequency spectrum and (Bottom) time evolution of the trailing-edge absolute vertical displacement for  $\mu = 2$ ,  $\varepsilon = 0.05$  and  $\bar{f} = 5/2\pi$ . (Left)  $\eta = 0.2 > \eta_m(\mu = 2)$  lies in the stability region for the purely passive elastic sheet. The power spectrum displays only one peak (thick arrow) at an angular frequency of  $\omega_f = 2\pi\bar{f} = 5$ . (Right) The rigidity  $\eta$  is below its critical value  $\eta_m(\mu = 2) = 0.048$  and the elastic sheet is unstable to fluttering. The power spectrum displays two main peaks: one corresponding to the forcing frequency ( $\omega_f = 5$ , thick arrow) and one corresponding to the unstable fluttering mode ( $\omega_r \sim 2.3$ , thin arrow) that matches the flapping frequency observed in the purely passive case  $\varepsilon = 0$ . In both cases, small peaks can be seen for  $\omega \sim 3\omega_f = 15$ , corresponding to the third harmonic of the forced flapping. The fact that only odd harmonics appear in the tail motion was already previously observed in the case of a passive flag (Michelin et al., 2008).

linear study by Alben (2008c) as the inertia of the solid was neglected ( $\mu \rightarrow 0$ ). The inertia of the solid is essential to the development of fluttering instability and in the limit  $\mu \rightarrow 0$ , all the modes are linearly stable (Alben and Shelley, 2008; Alben, 2008a; Michelin et al., 2008). In the following, unless indicated otherwise, we consider range of parameter values for which a periodic state is achieved.

## 6.4 Wing flexibility and propulsive performance

We are interested in this section in the behavior of the propulsive performance (mean thrust, mean power input and efficiency) when the rigidity  $\eta$  of the wing is varied. Several values of the forcing frequency  $\bar{f}$ , forcing amplitude  $\varepsilon$  and mass ratio  $\mu$  were investigated.

### 6.4.1 Optimal flexibility for thrust generation and propulsion efficiency

For given mass ratio, forcing amplitude and frequency, the mean thrust, mean power input and propulsive efficiency were computed for each value of the rigidity  $\eta$ . As a general result, we observe that, starting from the case of a rigid wing ( $\eta \rightarrow \infty$ ), the mean thrust  $\langle \mathcal{T} \rangle$  and power input  $\langle \mathcal{P}^+ \rangle$  both increase when flexibility is introduced in the problem; however, the former increases faster and the resulting efficiency is an increasing function of flexibility (decreasing function of  $\eta$ ) for large values of  $\eta$  (Figure 6.3). When the solid's flexibility is further reduced,  $\langle \mathcal{T} \rangle$  and  $\langle \mathcal{P}^+ \rangle$  display successive peaks for the same values of  $\eta$ . The propulsive efficiency  $r$  displays in general one large peak (in general at a different value of the rigidity  $\eta$  than the thrust peaks) before dropping sharply to zero as the mean thrust vanishes (drag-thrust transition). The increase in the flapping efficiency and developed mean thrust for a flexible wing is significant compared to the case of a rigid wing: for  $\bar{f} = 5/2\pi$ , the peak value of the mean thrust can be greater than twice its value in the rigid case and the efficiency can increase from 27% to almost 60% (Figure 6.3b). Similar behavior is observed for  $\bar{f} = 1/\pi$  (Figure 6.3a).

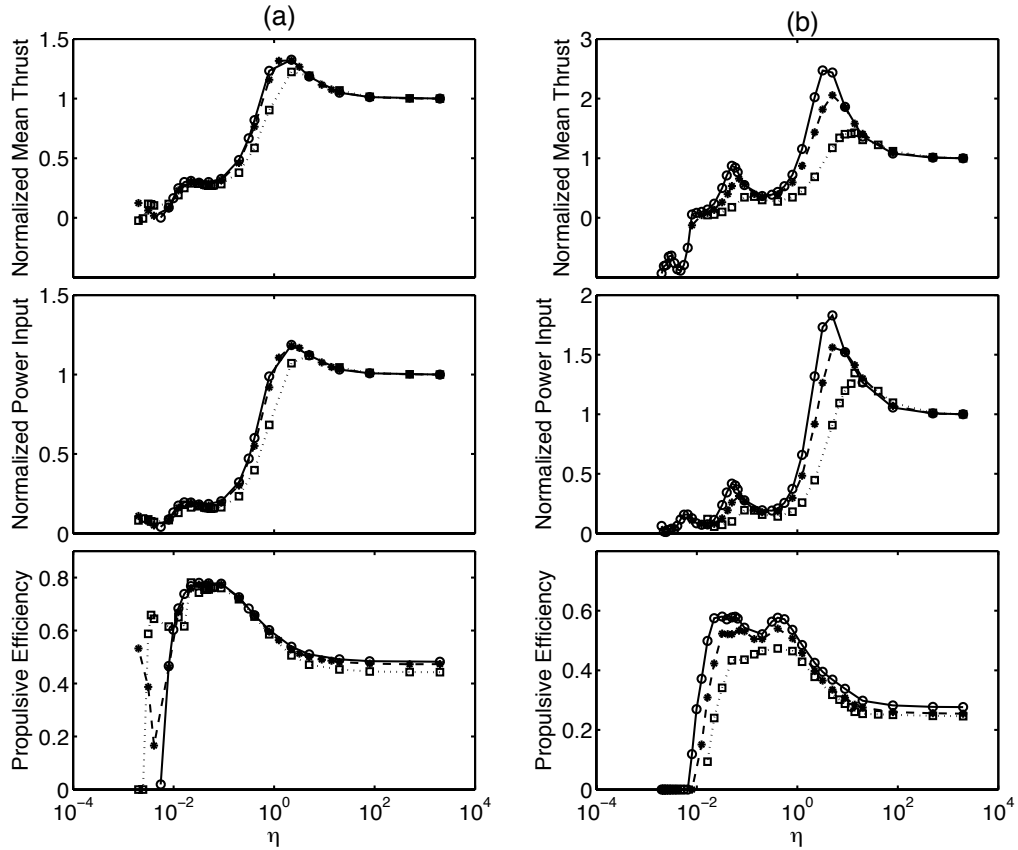


**Figure 6.3:** Evolution of the mean thrust  $\langle \mathcal{T} \rangle$  (top), power input (center) and propulsive efficiency (bottom) with the wing's rigidity  $\eta$ , for a flapping wing of mass ratio  $\mu = 0.2$ , flapping frequency (a)  $\bar{f} = 1/\pi$  and (b)  $\bar{f} = 5/2\pi$  and forcing amplitude  $\varepsilon = 0.1$  (solid-circle),  $\varepsilon = 0.2$  (dashed-star) and  $\varepsilon = 0.5$  (dotted-square). For comparison purposes, the mean power input and thrust have been normalized using the rigid-case value as  $\eta \rightarrow \infty$ .

Flexibility has therefore a significant impact on the performance of the propulsive apparatus considered here.

In Figure 6.3, we show the evolution of the propulsive properties for the values of  $\eta$  leading to a permanent periodic regime. In the higher frequency case ( $\bar{f} = 5/2\pi$ ), the drag-thrust transition was clearly observed while at lower frequency ( $\bar{f} = 1/\pi$ ), this transition is less well defined as unsteady phenomena start developing around the same value of the rigidity. Several factors lead to unsteadiness of the problem, including transitions in the wake behind the flapping

wing and development of the fluttering instability for low values of the rigidity (see section 6.3).

The behavior of  $\langle \mathcal{T} \rangle$ ,  $\langle \mathcal{P}^+ \rangle$  and  $r$  collapse rather well for leading-edge flapping amplitudes up to 50% of the wing's length and lower frequencies (Figure 6.3a). However, for higher frequencies, the influence of the forcing amplitude can be seen for values of  $\varepsilon$  as low as 0.1 (Figure 6.3b). As a general result, we observe that the propulsive efficiency and the normalized mean thrust and power input, decrease with  $\varepsilon$  when all other parameters are held fixed. The optimal values of  $\eta$  for maximal thrust or maximal efficiency are also observed to increase with  $\varepsilon$ .

We must emphasize here that the decrease of the achievable thrust and power input with the forcing amplitude  $\varepsilon$  are only relative to the rigid case: for higher forcing amplitudes, the absolute mean thrust and power input are larger in magnitude and, in the rigid limit, are observed to scale like  $\varepsilon^{5/2}$ .

## 6.4.2 Wake structure and thrust production

### Evolution of the wake structure with increasing flexibility

For given mass ratio, frequency and forcing amplitude  $\varepsilon$ , the variation of the flexibility of the wing induces important changes in the developed thrust and energy usage. As  $\eta$  is decreased from the rigid case ( $\eta \rightarrow \infty$ ), the wake behind the flapping wing also undergoes important modifications. Figure 6.4 shows the evolution of the flow pattern around the heaving wing for varying  $\eta$ . In the high-rigidity case (Figure 6.4a), the trailing-edge deflection is small. The wake vortices are arranged in a reverse Von Kármán vortex street, in which vortices with positive (resp. negative) intensity are positioned above (resp. below) the horizontal axis. This arrangement induces an acceleration of the fluid on the horizontal axis to the right and the vortices have a higher velocity than the imposed background flow (positive  $\mathcal{V}$ ). This jet carries momentum to the right which is consistent with the formation of a mean thrust on the wing. The formation of a reversed Von Kármán vortex street in thrust-producing propulsion schemes is well known and has been

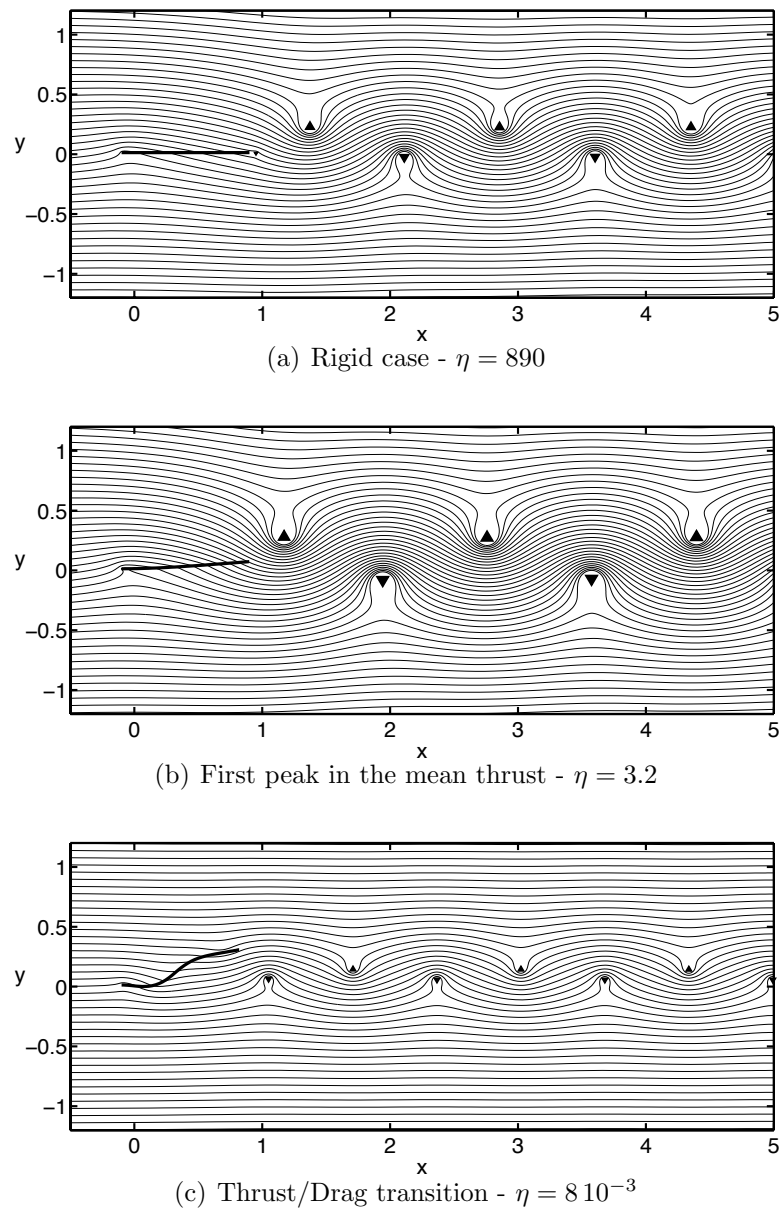


**Figure 6.4:** Streamlines of the flow over the flapping wing for  $\mu = 0.2$ ,  $\varepsilon = 0.1$  and  $\bar{f} = 5/2\pi$  and decreasing rigidity  $\eta$ . The positive (resp. negative) vortices are represented with upward- (resp. downward-) pointing triangles with sizes scaled to the intensity of the vortices. The streamlines are plotted for  $t = 20$  when the leading edge crosses the horizontal axis, and the leading-edge forcing for  $0 \leq t \leq 20$  was the same in all three cases.

observed in several experimental studies (Anderson et al., 1998; Godoy-Diana et al., 2008).

When  $\eta$  is decreased, the solid is more flexible and the trailing-edge flapping amplitude  $\mathcal{D}$  increases. As a result, the intensity of the wake vortices increases with decreasing rigidity and so does the thrust generated by the flapping motion. Figure 6.4(b) shows the streamlines and arrangement of the wake vortices for  $\eta = 3.2$ , which corresponds to the first peak in thrust production on Figure 6.3(b). The phase between the leading and trailing-edge displacements has also been modified compared to the rigid case. The increase in the vortex advection velocity can be seen as the distance between two successive vortices is slightly increased (the vortex shedding frequency is unchanged and equal to the forcing frequency).

For comparison, Figure 6.4(c) shows the flow pattern for the value of  $\eta$  corresponding to the thrust-drag transition. One observes immediately that the intensity of the wake vortices has decreased significantly and the width of the vortex street has almost vanished. In intermediate  $Re$  experiments, the formation of a classical Von-Kármán street is associated with drag on the generating solid body. It appears here that, even at the transition between thrust and drag production, the reversed Von Kármán pattern persists, although largely weakened. This result is consistent with the observation in recent experiments (Godoy-Diana et al., 2008) that the thrust-drag transition does not necessarily occur at the same time as the transition in the wake structure. A theoretical argument for this difference is also presented below. Furthermore, in purely inviscid simulations, the Von Kármán street in the drag-producing case is generally much weaker and instead the vortices tend to align along the axis (Alben and Shelley, 2008; Michelin et al., 2008).

### **Classical and reversed Von Kármán streets and thrust/drag production**

Here, we use theoretical results on vortex streets to understand the relationship between drag/thrust production and vortex wake structures. We focus on highly periodic cases where the structure of the reversed Von-Kármán or classical

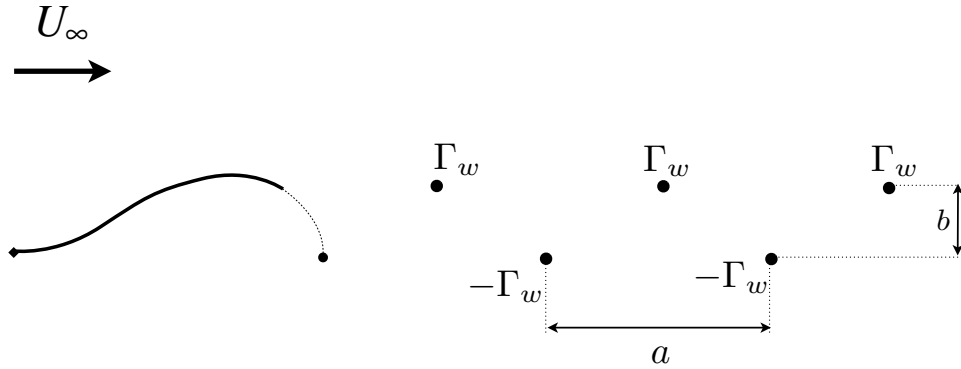


**Figure 6.5:** Characteristics of the reversed Von-Kármán street behind the flapping wing.  $\Gamma_w$  is the amplitude of the wake vortices,  $a$  the wavelength and  $b$  the width of the vortex street.

Von Kármán streets is easily identified.

For a given vortex wake intensity and vortex arrangement, the advection velocity of the vortices is the superposition of the incoming flow velocity (equal to 1 in non-dimensional units) and of the induced velocity  $\mathcal{V}$  of the vortex street, which is itself a direct function of the width of the vortex street (vertical distance between the two rows of opposite sign vortices), its intensity and its wavelength (horizontal distance between two successive vortices of identical sign). If the vortex street were infinite, its induced velocity  $\mathcal{V}$  would be (Lamb, 1932)

$$\mathcal{V} = \frac{\Gamma_w}{2a} \tanh\left(\frac{\pi b}{a}\right), \quad (6.30)$$

where  $\Gamma_w$  is the magnitude of the vortices,  $b$  the width of the vortex street and  $a$  its horizontal wavelength (see Figure 6.5). In (6.30), we chose the convention that  $b > 0$  (resp.  $b < 0$ ) for a reversed (resp. classical) Von-Kármán street in which positive vortices are located above (resp. below) the horizontal axis. If the shedding frequency (equal to the flapping frequency  $\bar{f}$ ) is fixed, then  $a = (1 + \mathcal{V})/\bar{f}$ . Measuring the width of the vortex street  $b$  and its intensity  $\Gamma_w$ , (6.30) leads to a non-linear equation for  $\mathcal{V}_L$ , the predicted value of the induced velocity, that can

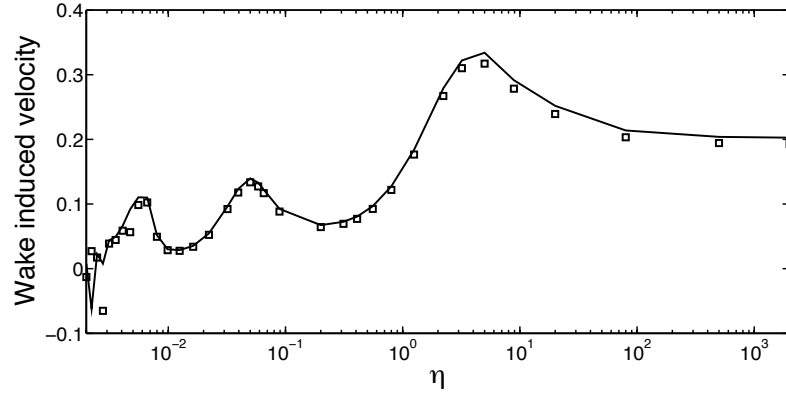


**Figure 6.6:** (Square) Induced wake vortices velocity  $\mathcal{V}$  behind the flapping wing for varying  $\eta$  and  $\mu = 0.2$ ,  $\varepsilon = 0.1$  and  $\bar{f} = 5/2\pi$ . The predicted value obtained for an infinite reversed Von-Kármán vortex street (Lamb, 1932) is plotted for comparison (solid line).

be solved numerically given  $b$  and  $\Gamma_w$

$$\mathcal{V}_L = \frac{\Gamma_w \bar{f}}{2(1 + \mathcal{V}_L)} \tanh\left(\frac{\pi b \bar{f}}{(1 + \mathcal{V}_L)}\right). \quad (6.31)$$

Figure 6.6 shows very good agreement between the measured value  $\mathcal{V}$  and the expected value  $\mathcal{V}_L$  for varying  $\eta$  (the other parameters taking the same values as in Figure 6.4), particularly above the thrust-drag transition at  $\eta = 8 \cdot 10^{-3}$  (Figure 6.6). This agreement shows that the induced velocity is mostly determined by the neighboring vortices, and the semi-infinite or infinite nature of the vortex street does not influence the induced velocity significantly.

The drag on a solid body placed in a uniform parallel flow and shedding vortices in the pattern of a staggered vortex street (regular or reversed Von-Kármán street) was computed by Von Kármán using the conservation of momentum around the solid body and part of its wake (Kochin et al., 1964; Saffman, 1992). The only important elements in the derivation are again the intensity  $\Gamma_w$ , wavelength  $a$  and width  $b$  of the vortex street. In particular, the motion (other than the main translation) and deformation of the body are irrelevant in Von Kármán's derivation. These results can easily be generalized to the case of a reversed Von-

Kármán street and in our notation, the predicted thrust  $\mathcal{T}_S$  is obtained as

$$\mathcal{T}_S = -\frac{\Gamma_w^2}{2\pi a} + \frac{\Gamma_w b}{a} (1 + 2\mathcal{V}), \quad \text{with } a = (1 + \mathcal{V})/\bar{f}. \quad (6.32)$$

This theoretical prediction compares very well to the results obtained for the thrust in our simulations (Figure 6.7). In particular, the transition between thrust and drag production is well reproduced. The agreement is lost at low values of  $\eta$ : For such low values of the rigidity, the highly regular structure of the wake is also lost as some natural modes of the passive elastic sheet become unstable to fluttering and the motion of the wing loses its strong periodicity, making the definition of  $a$ ,  $\Gamma_w$  and  $b$  difficult.

In (6.32), the thrust consists of two terms. The second term is positive in the case of a reversed Von Kármán street ( $b > 0$ ) and negative in the classical Von Kármán street (with  $b < 0$  and  $\mathcal{V} < 0$ , as long as  $\mathcal{V} > -1/2$ , which always occur in the weak Von Kármán streets observed here). The presence of the first term (which is always negative and therefore always leads to drag production) is responsible for the difference between the thrust/drag transition and the transition in the wake structure, observed in experimental or numerical studies (Godoy-Diana et al., 2008). As in the passive flapping flag case (Alben and Shelley, 2008; Michelin et al., 2008), it is possible to have net drag produced by a weak reversed Von Kármán street as the first term in (6.32) dominates the second one.

### 6.4.3 Resonance and optimal flexibility for thrust production

In Figure 6.3(b), we can observe successive peaks in the mean thrust created by the heaving wing, but also a peak in the mean drag (or negative thrust) below the drag-thrust transition that occurs around  $\eta \sim 8 \cdot 10^{-3}$ . Figure 6.8 shows the evolution of the mean thrust, flapping amplitude  $\mathcal{D}$ , wake intensity  $\Gamma_w$  and wake induced velocity  $\mathcal{V}$  for the same values of the parameters  $\mu$ ,  $\varepsilon$  and  $\bar{f}$  as in Figure 6.3.

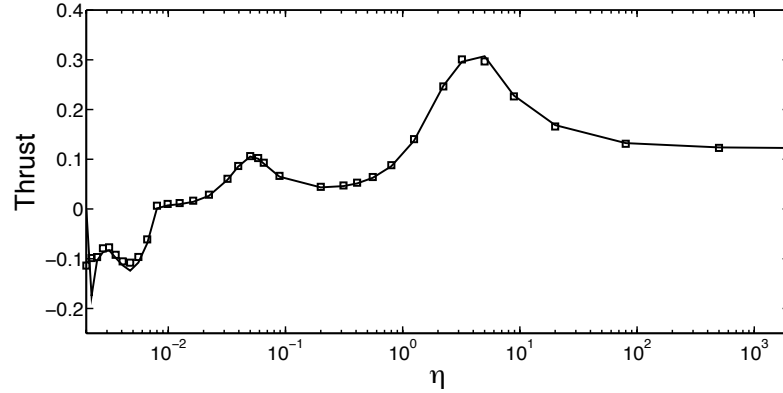


**Figure 6.7:** (Square) Mean thrust  $\langle T \rangle$  produced by the flapping wing for varying  $\eta$  and  $\mu = 0.2$ ,  $\varepsilon = 0.1$  and  $\bar{f} = 5/2\pi$ . The predicted value  $\mathcal{T}_S$  (6.32) based on impulse conservation (Kochin et al., 1964; Saffman, 1992) is also plotted for comparison (solid line).  $\mathcal{T}_S$  was computed from (6.32) using the values of the vortex street intensity, width and induced velocity obtained with our model.

We observe a very clear correlation between the occurrence of the maxima (in magnitude) for the mean thrust (or drag) and for the other quantities, which confirms the argument presented in the previous section: the mean thrust and drag peaks are created by an increase in the flapping motion at the trailing edge, where the vortex wake is formed. An increase in  $\mathcal{D}$  (with a constant flapping frequency) induces a higher relative velocity at the trailing edge, and therefore stronger shed vortices. While this increase in  $\Gamma_w$  with  $\mathcal{D}$  is physical, it is however not possible to find a simple scaling of  $\Gamma_w$  with  $\mathcal{D}$ , as other factors that depend on  $\eta$  must be taken into account (e.g. the orientation of the trailing edge relative to its velocity). The induced velocity on the vortex street  $\mathcal{V}$  is therefore also increased and the wake carries a larger fluid momentum downstream, thereby creating a greater thrust on the profile.

It is also interesting to notice that the maximum drag observed for  $\eta \sim 5 \cdot 10^{-3}$  is also associated with a maximum in  $\mathcal{D}$  and  $\Gamma_w$ . In that case, the large amplitude of motion at the trailing edge opposes the imposed flow and creates a net drag on the body.

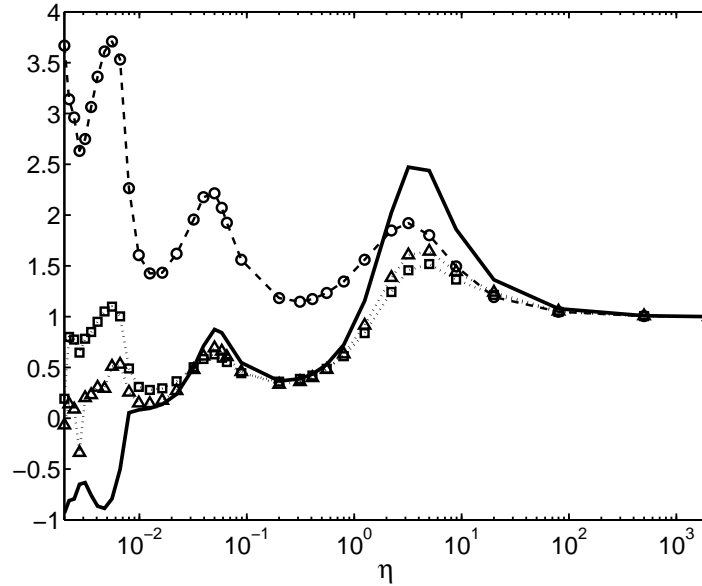


**Figure 6.8:** Evolution of the mean thrust  $\langle \mathcal{T} \rangle$  (solid), trailing-edge flapping amplitude  $\mathcal{D}$  (dashed-circle), vortex wake intensity  $\Gamma_w$  (dotted-square) and induced vortex velocity  $\mathcal{V}$  (dotted-triangle) with the wing's rigidity  $\eta$  for  $\mu = 0.2$ ,  $\varepsilon = 0.1$  and  $\bar{f} = 5/2\pi$ . All quantities have been normalized by their rigid-case value ( $\eta \rightarrow \infty$ ).

## 6.5 Influence of flexibility on the flapping amplitude and mode shape

### 6.5.1 Resonances between the forcing frequency and the natural frequencies of the system

In this section, we are interested in the origin of the maxima in the trailing-edge flapping amplitude  $\mathcal{D}$ . The successive peaks in  $\mathcal{D}$  as  $\eta$  is varied suggest a resonance phenomena. By varying the rigidity of the solid  $\eta$ , we also modify the natural frequencies of the system. For an elastic sheet in vacuum, these frequencies scale like  $\sqrt{B/\rho_s}$ . Looking for solutions of (6.8)–(6.11) in the linear limit with no fluid forcing, the fundamental angular frequencies  $\omega_{0n} = 2\pi f_n$  of a

clamped-free elastic sheet in vacuum are obtained in non-dimensional form as

$$\omega_{0n} = \lambda_n^2 \sqrt{\frac{\eta}{\mu}}, \quad \text{with } 1 + \cosh \lambda_n \cos \lambda_n = 0. \quad (6.33)$$

The ratio  $\sqrt{\mu/\eta}$  can be thought of as the non-dimensional time-scale associated with the frequency of the sheet's natural oscillations in vacuum, or alternatively as the outside flow velocity non-dimensionalized by the characteristic velocity associated with the sheet's properties.

### **Influence of $\mu$ and $\varepsilon$ on the position of the resonance peaks in $\mathcal{D}$**

However, the resonance peaks observed in Figure 6.8 do not correspond to a resonance with the natural frequency of the sheet in vacuum. If this were the case, then the resonances would be achieved for all values of the mass ratio  $\mu$  at the same values of  $\sqrt{\eta/\mu}$ . We observe on Figure 6.9 that such a coincidence does not occur: the position of the successive resonances is actually strongly influenced by the fluid-solid inertia ratio  $\mu$ . This difference makes sense physically, as the eigenfrequencies of the system are modified by the presence of the forcing horizontal flow, and such effects as added inertia are expected to be important. Instead, the natural frequencies of the system {wing + outside uniform flow} should be considered. A comparison with linear analysis predictions is proposed below.

Before comparing our results to the linear analysis, we study the influence of the forcing amplitude  $\varepsilon$  on the position of the resonances. We have noticed in section 6.4.1 that the normalized thrust and power input follow similar patterns for values of  $\varepsilon$  up to 0.2 to 0.5 depending on the value of  $\mu$ . In an attempt to determine the exact value of  $\eta$  leading to a resonance, we study how the resonance peaks in  $\mathcal{D}$  are modified as  $\varepsilon$  is varied between 0.01 and 0.5. Starting from small  $\varepsilon$ , one observes that the increase in  $\varepsilon$  induces a shift of the resonance peaks toward larger values of  $\eta$  and a smoothing of the resonance peaks (Figure 6.10). We also observe that the convergence toward the limit case of small  $\varepsilon$  is faster for the second and third resonance peaks than for the first one (labeling the peaks from the right as  $\eta$

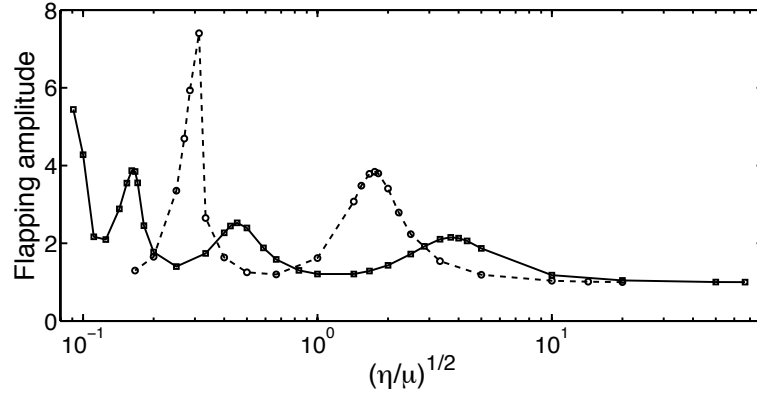


**Figure 6.9:** Evolution of the normalized trailing-edge flapping amplitude  $\mathcal{D}$  with  $\sqrt{\eta/\mu}$  for  $\varepsilon = 0.05$ ,  $\bar{f} = 5/2\pi$  and for  $\mu = 0.2$  (solid-squares) and  $\mu = 2$  (dashed-circle). The flapping amplitude was normalized using the asymptotic rigid case limit ( $\eta \rightarrow \infty$ ).

is decreased from the rigid case limit). This will be of importance when discussing the modification of the resonance position by non-linear effects.

### Absolute and relative trailing-edge flapping amplitude

We have previously defined  $\mathcal{D}$  as the peak-to-peak amplitude of the trailing-edge flapping motion in the laboratory frame (thereafter referred to as absolute flapping amplitude). In the following, we are also interested in the motion of the wing *in the frame moving with the leading edge*. In this frame, the peak-to-peak trailing-edge flapping amplitude is  $\mathcal{D}^*$  (thereafter referred to as relative flapping amplitude).  $\mathcal{D}$  and  $\mathcal{D}^*$  are not necessarily equal because of the phase difference between the motion of the leading and trailing edges (Figure 6.11). This delay is, in general, a decreasing function of the solid's rigidity. In the limit of a rigid wing  $\eta \rightarrow \infty$ , the trailing edge flaps in phase with the leading edge and with the same amplitude ( $\mathcal{D}^* = 0$  and  $\mathcal{D} = 2\varepsilon$ ). As  $\eta$  is decreased, a delay appears between the motion of the leading and trailing edges: the elasticity of the wing takes more time to carry along its length the signal imposed at the leading edge. As a result, the relative amplitude  $\mathcal{D}^*$  increases.

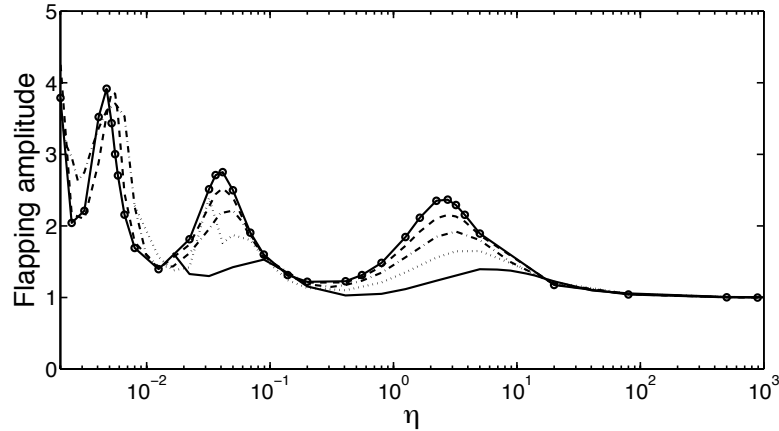


**Figure 6.10:** Influence of the forcing amplitude  $\varepsilon$  on the position of the resonances in the trailing-edge flapping amplitude for  $\mu = 0.2$  and  $\bar{f} = 5/2\pi$ . The results are plotted for  $\varepsilon = 0.01$  (solid-circles),  $\varepsilon = 0.05$  (dashed),  $\varepsilon = 0.1$  (dash-dotted),  $\varepsilon = 0.2$  (dotted) and  $\varepsilon = 0.5$  (solid). The trailing-edge flapping amplitude was normalized by its rigid-case value ( $\eta \rightarrow \infty$ ).

One of the main consequences of the apparition of such a delay is the non-coincidence of the first resonance peak (with largest  $\eta$ ) in the flapping amplitude, whether  $\mathcal{D}$  or  $\mathcal{D}^*$  is considered. The position of the subsequent peaks is not significantly affected (Figure 6.11a)

### Comparison with the natural frequencies of the system

In this section, we test the conjecture that the trailing-edge flapping amplitude peaks are due to a resonance with the natural frequencies of the {wing + imposed flow} system, by comparing the value of the rigidity  $\eta$  leading to a peak value for  $\mathcal{D}$  to the value of  $\eta$  for which the forcing frequency matches a natural frequency of the system. The position of the peaks in  $\mathcal{D}$  is measured in the limit of small forcing amplitude (typically  $\varepsilon = 0.01$ ). The natural frequencies of a purely passive wing clamped at its leading edge in a uniform flow are determined using the linear stability analysis method developed by Kornecki et al. (1976). A brief summary of this method is given in Appendix A. For given  $\mu$  and  $\eta$ , the eigenfrequencies of the system are computed. The lowest frequencies are also associated

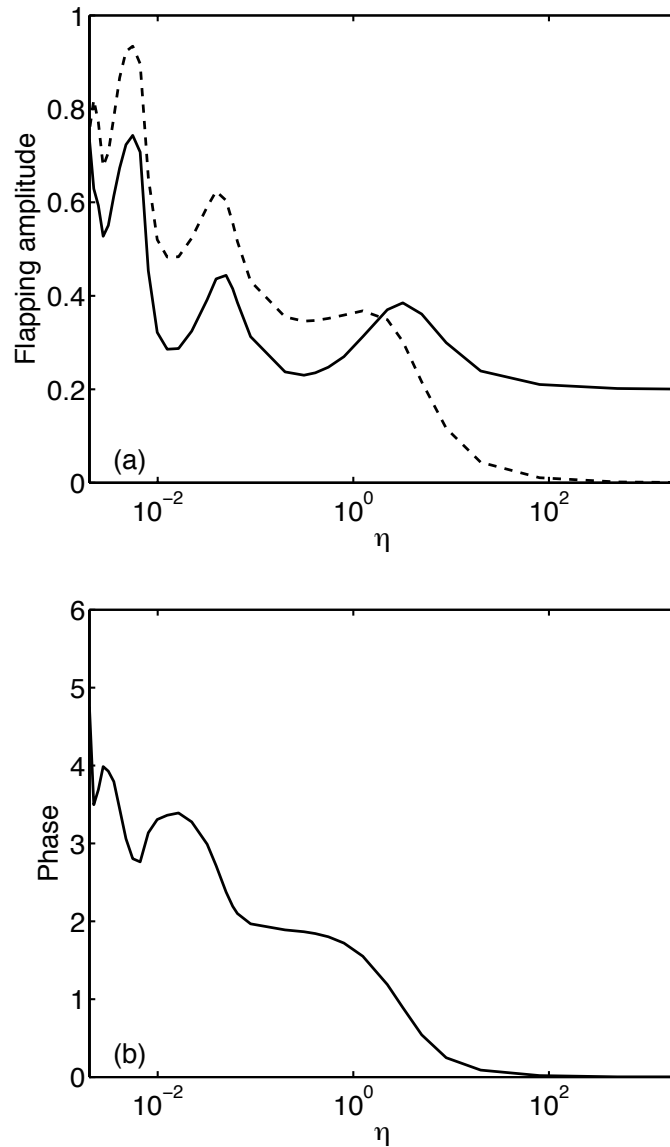


**Figure 6.11:** (a) Comparison between the absolute flapping amplitude  $\mathcal{D}$  and relative flapping amplitude  $\mathcal{D}^*$  at the trailing edge, for  $\mu = 0.2$ . (b) Phase difference between the leading-edge and trailing-edge motions.

with the modes of lowest order (those with the longest wavelength). Here, we are interested in the following equivalent problem: for a given  $\mu$  and  $\bar{f}$ , we want to find the values  $\eta$  for which a mode of the passive flexible wing in axial flow has the particular frequency  $\bar{f}$ , regardless of its growth rate.

Figure 6.12 shows the position in the  $(\eta, \bar{f})$ -plane of the first resonances observed in the trailing-edge flapping amplitude  $\mathcal{D}$  for small heaving amplitude  $\varepsilon$ , starting from the rigid case  $\eta \rightarrow \infty$ . Although  $\varepsilon$  is small,  $\mathcal{D}$  can be significant (greater than  $20\varepsilon$  at the resonance in the case of the heavier wing ( $\mu = 2$ ), thereby representing more than 20% of the wing's length). These results are compared to the natural frequencies of the system {wing + parallel flow} as predicted by the linear analysis. We observe very good agreement between the numerical results and the theoretical predictions. The position of the resonances in  $\mathcal{D}^*$  are also indicated. Resonances in  $\mathcal{D}^*$  and  $\mathcal{D}$  coincide except for the first resonance peak in the case of the smaller mass ratio  $\mu$ .

The linear analysis seems to underpredict slightly the values of  $\eta$  corresponding to the resonance for a given frequency  $\omega$ . This difference is consistent with the amplitude of discrepancy between the point vortex model and the linear stability analysis observed in the study of a purely passive elastic sheet or flag (Michelin et al., 2008). Two other factors can also explain the small discrepancy in the results:

- As we pointed out, the motion of the wing is not infinitesimally small here, even for  $\varepsilon = 0.01$ ; it is therefore possible that non-linear effects modify the exact position of the resonances. In the previous section, the effect of increasing  $\varepsilon$  was shown to shift the resonance peaks toward larger  $\eta$ , particularly for the first peak, and this could account for a significant part of the observed discrepancy.
- We are interested here in the amplitude of flapping in the laboratory frame. However, even for small  $\varepsilon$ , this amplitude differs from the relative flapping

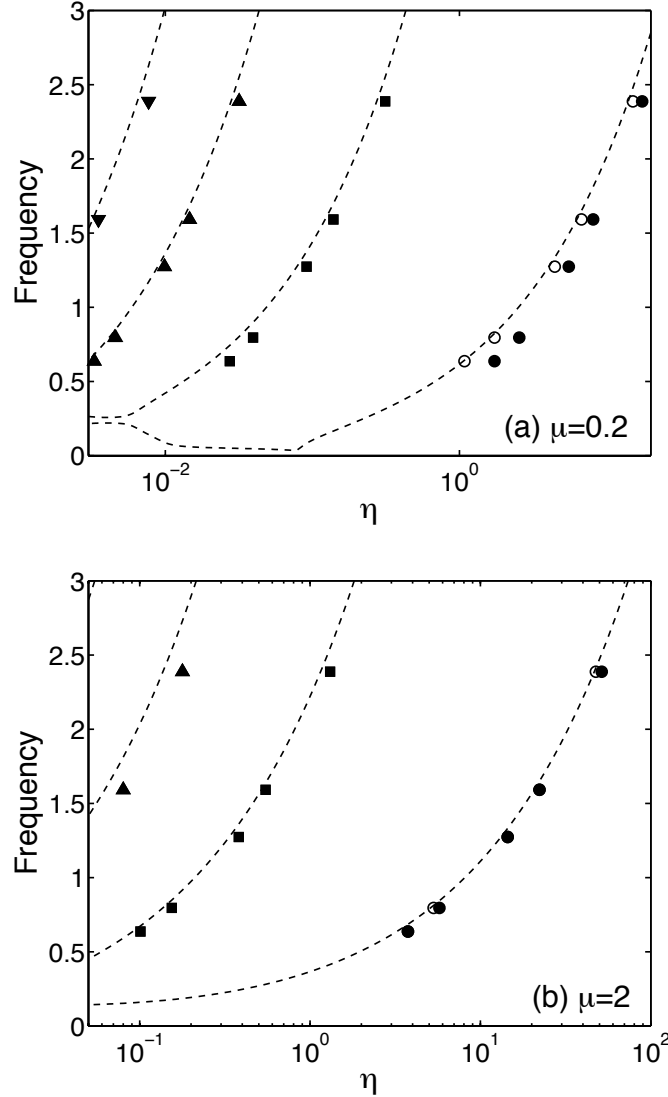


**Figure 6.12:** Position of the resonances for the trailing-edge flapping amplitude in the  $(\eta, \bar{f})$ -plane obtained using the present model (symbols) with  $\varepsilon = 0.01$  and (a)  $\mu = 0.2$  and (b)  $\mu = 2$ . The different symbols correspond to the nature of the mode: modes 1 have no neck in the flapping envelope (circles); modes 2 (squares), modes 3 (upward-pointing triangle) and modes 4 (downward-pointing triangles) have respectively 1, 2 and 3 necks in their motion envelope. The black symbols correspond to resonances in the absolute flapping amplitude  $\mathcal{D}$ . Open symbols correspond to resonances in the relative flapping amplitude  $\mathcal{D}^*$  when they differ from the resonances in  $\mathcal{D}$ . The position of the resonances is compared to the prediction of the linear analysis (dashed) for the natural frequency of the purely passive elastic sheet (or flag) in axial flow (see Appendix A).

amplitude defined in the frame moving with the leading edge (see Figure 6.11), because of the existence of a non-zero phase between the motion of the leading and trailing edges. We observed in Figure 6.11 that the resonance in relative amplitude occurs for smaller values of  $\eta$ , particularly for the first resonance (largest  $\eta$ ). In the linear analysis, both amplitudes (relative and absolute) are identical since the leading edge is held fixed. We see on Figure 6.12, that for  $\mu = 0.2$ , the agreement is improved for the position of the first resonance if  $\mathcal{D}^*$  is considered instead of  $\mathcal{D}$ .

Figure 6.12 also indicates the nature of the observed mode, in particular the number of necks in the envelope of the wing's motion. One observes that resonances located on a same branch of the linear analysis prediction share the same general structure, and the number of necks is consistent with that predicted by the linear analysis: for given  $\mu$  and  $\eta$ , the lowest frequency mode has the longest wavelength and no neck in its envelope. The next lowest frequency corresponds to a mode with one neck, and so on for the successive frequencies. The evolution of the mode shape for varying  $\eta$  is studied in more detail in section 6.5.2.

### 6.5.2 Evolution of the flapping mode shape with the flexibility of the profile

To confirm that the maxima of flapping amplitude actually correspond to resonances between the forcing frequency and the natural frequency of the passive elastic sheet in a parallel flow, we consider the evolution of the mode shape with  $\eta$ . For comparison with the case of a purely passive elastic sheet, we define as the mode shape the envelope of the motion of the wing *in the frame moving with the leading edge*. Figure 6.13 shows the mode shape in permanent regime at the values of  $\eta$  leading to peak values of the absolute trailing-edge flapping amplitude and to the minima between two successive peaks. Note that on Figure 6.13, case *B* seems to correspond to a wider envelope than case *A*, although the absolute flapping amplitude is smaller for *B* than for *A*. This is the result of the change of

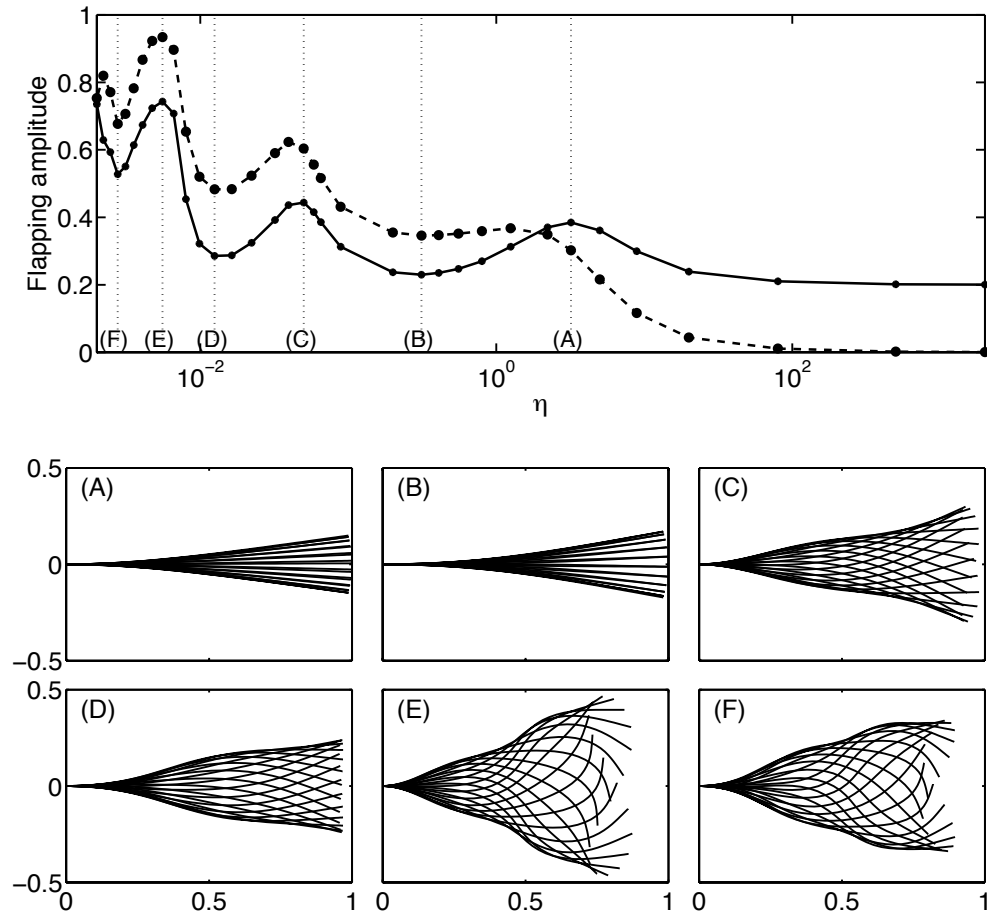


**Figure 6.13:** Evolution of the mode shape with  $\eta$  for  $\mu = 0.2$ ,  $\varepsilon = 0.1$  and  $\bar{f} = 5/2\pi$ . (Top) Trailing-edge flapping amplitude in the stationary frame  $\mathcal{D}$  (solid) and in the frame attached to the leading edge  $\mathcal{D}^*$  (dotted). Note that the value of  $\eta$  leading to a resonance in  $\mathcal{D}$  does not necessarily correspond to the value of  $\eta$  leading to a resonance in  $\mathcal{D}^*$ . (Bottom) Mode shape plotted for the value of  $\eta$  indicated on the top panel. The position of the wing in the frame moving with the leading edge is plotted every  $\Delta t = 0.06$ .

frame: if one considers the flapping amplitude in the moving frame, the position of the maxima differs from that of the peaks in absolute flapping amplitude (see Figure 6.11). Cases *A*, *C* and *E* correspond to the resonances while *B*, *D* and *F* correspond to local minima of the absolute flapping amplitude.

Comparing the mode shapes *C* and *E* with the envelope of the first two flapping modes observed for a passive flexible flag (Michelin et al., 2008), we observe that they are structurally similar, which is consistent with *C* and *E* corresponding to resonances between the flapping frequency and flapping modes 2 and 3 (one- and two-neck modes respectively). *A* corresponds to mode 1 of the passively flapping elastic sheet, which was not observed in the study of flapping flags (Michelin et al., 2008) as it is always stable (Eloy et al., 2007) and therefore does not lead to large-scale flapping.

## 6.6 Conclusions

Using a reduced-order model for the flow past a two-dimensional heaving flexible wing, we have investigated the influence of the wing's passive flexibility on its propulsive performance (mean thrust, flapping efficiency). Starting from the purely rigid case, we observed that flexibility allowed for a larger trailing-edge flapping amplitude, thereby generating a stronger wake and an increased mean thrust. The energy usage also increases with the introduction of flexibility, but more slowly than the mean thrust, resulting in a net increase in the flapping efficiency with reduced rigidity. This efficiency gain can be significant (up to twice the efficiency of the rigid case). While the mean thrust and power input display several peaks when the rigidity  $\eta$  is decreased from the purely rigid case, the flapping efficiency displays one wide peak before falling sharply as  $\eta$  nears the value leading to the thrust-drag transition. Below this threshold, the wing is too flexible to communicate momentum to the flow and instead starts creating a net drag on the leading-edge attachment.

The relationship between thrust production and wake structure was then investigated, taking advantage of the discrete representation of the wake. Analytical predictions for the induced vortex street velocity and mean thrust in terms of the vortex street strength and spatial arrangement were successfully compared to our simulation results.

The peaks in mean thrust were found to correspond to maximum values in the trailing-edge amplitude, and shown to be the result of the resonance between the forcing frequency of the heaving motion and the natural frequencies of the system. A quantitative comparison showed very good agreement between the optimal values of the solid's rigidity and the linear analysis predictions for the resonances position. The existence of these resonance phenomena was further confirmed by comparing the flapping mode shape to the mode shape observed for a freely flapping elastic sheet (e.g. the flag problem (Michelin et al., 2008)).

The natural frequencies of the system are strongly dependent on both the solid's flexibility and the ratio of fluid and solid inertia, and so are the optimal values of the solid's rigidity. For a slender neutrally buoyant fish fin, the inertia ratio  $\mu$  can generally be neglected (Alben, 2008c). However, in the case of an insect wing, the small thickness-to-chord ratio is balanced by the large difference in density for the fluid and solid, and our analysis shows that the mass ratio  $\mu$  plays an important role in defining the optimal value of the flexibility.

The model presented here used a potential flow representation and the shedding of point vortices to describe the highly-unsteady flow around the insect wing. Vortices were shed only from the trailing edge. This approximation is reasonable for small angle of attack (proportional to the Strouhal number  $St$  in the case of a purely heaving motion). Then, the vorticity shed at the leading edge is negligible or merges with the vorticity shed by separation of the boundary layers at the trailing edge (Anderson et al., 1998), leading to the shedding of two individual vortices every flapping period and so-called  $2S$  wakes (Williamson and Roshko, 1988). However, when the flapping amplitude and frequency are increased,

more complex wakes are expected as vorticity is shed from both the trailing and leading edges, inducing for example the formation of the so-called  $2P$  wake, where two vortex pairs are shed during each period. The representation of the leading-edge vortex falls however beyond the scope of inviscid methods such as the present point vortex model or a vortex sheet approach as the effect of viscosity cannot be neglected (Michelin and Llewellyn Smith, 2009a,c): the leading-edge vortex is expected to remain close to the body for a sufficiently long time to interact with the boundary layers. The use of point vortices also restricts this method to two-dimensional problems and therefore does not allow the study of such effects as wing-tip vortices that are expected to influence significantly the flight performance. The present study however does not aim at reproducing the exact flow around an insect wing but to present a test case where the effect of flexibility can be isolated from other factors such as leading-edge and wing-tip vortices.

Despite these limitations, the present method offers the advantage of a considerable reduction in computational cost for two-dimensional fluid-solid simulations. This is particularly attractive for situations where the cost of full numerical simulation is prohibitive and a large number of simulations are required (typically in the case of optimization problems).

The present work was purposely limited to a one-degree of freedom flapping pattern (pure heaving) in order to limit the number of free parameters and focus on the fundamental effect of solid flexibility on the flapping performance. In future work, more realistic flapping schemes should be considered to follow more closely the flapping pattern of an insect wing. In particular, a combination of heaving and pitching should be considered to determine the influence of the relative phase between heaving and pitching motions on the results presented in this work. The interaction between two flapping elastic sheets should also be investigated to understand the lift and thrust generation by insects with multiple pairs of flexible wings [e.g. dragonfly (Wang and Russell, 2007)] or the efficiency of fish schooling, and to complement recent experimental studies on multiple passive flexible fila-

ments (Zhang et al., 2000; Jia et al., 2007; Jia and Yin, 2008; Ristroph and Zhang, 2008).

Chapter 6, in part, has been published in *Physics of Fluids*, “Resonance and propulsive efficiency of a heaving flexible membrane” by S. Michelin and S. G. Llewellyn Smith, 2009, **21** (7), 071902, (American Institute of Physics), doi: 10.1063/1.3177356. The dissertation author was the primary investigator and author of this material.

# 7

## Conclusions

### 7.1 Using a point vortex model to study fluid-solid interactions

The present dissertation focuses on the development and application of a reduced-order model for two-dimensional high- $Re$  fluid-solid interactions, based on a representation of the flow around a flexible or rigid body using potential flow theory and the shedding of point vortices with unsteady intensity to represent the vortex wake shed from the solid's sharp corners. The purpose of such a simplified model is not to replace entirely the full numerical simulation of the interaction, but rather to provide an accurate physical insight in some class of problems at a low computational cost. This inviscid model is only valid for flows for which  $Re$  is sufficiently high for viscous forces to be small compared to the pressure forces but low enough for the flow to remain laminar in the vicinity of the solid.

Beyond the computational advantage, representing the flow using a discrete set of point vortices allows for an easier physical analysis of the wake of an object, particularly in terms of momentum transferred by the solid to the flow. In Chapter 3, the forces and torques applied on a general solid body were for example interpreted as the superposition of two contributions: an added inertia (present in any potential flow representation) and a transfer of momentum to the vortex wake. Taking advantage of this representation, we also proposed an argument for

the destabilization of a falling thin card by studying small perturbations of the broadside-on fall and its consequences in terms of horizontal momentum.

In Chapters 4 and 6, the arrangement of the vortex wake determined the net horizontal force on the flapping membrane. For example, the classical Von-Kármán street is associated with a net drag on the solid, while the reversed Von-Kármán street is generally associated with thrust production (although we pointed out in section 6.4.2 that the transitions between drag and thrust production and between the classical and reversed Von-Kármán vortex streets do not exactly coincide).

The point vortex model however introduces some strong limitations on the regimes considered. In particular, the flow must be two-dimensional and the generalization to three-dimensions in terms of vortex rings is very challenging. The model presented here relies heavily on the results and tools of potential flow theory, and is thereby fundamentally inviscid. Any adhoc correction such as a decay and spread of the vortices in time to account for viscous diffusion will cause a significant modification of the approach used. These two limitations are however not prohibitive provided (i) that the aspect ratio of the solid is large so that the flow can be considered locally as two-dimensional with a reasonable accuracy and (ii) that the vortices are advected away from the body fast enough that their viscous spreading is irrelevant in the forces applied on the solid (at leading order, their effect on the flow next to the solid will still be dominated by their point vortex equivalent). The time-scale associated with the residence time around the solid is  $L/U$  with  $U$  the velocity of the outside flow. The typical viscous length scale over such a time-scale is  $(\nu L/U)^{1/2}$  should be much smaller than the other characteristic length-scales of the problem (e.g. the size  $L$  of the solid).

The inviscid nature of the model however introduces another limitation that was discussed in detail in section 3.3.3: if a new vortex is started from the leading edge of the solid body under small angle-of-attack conditions, the equations

of the problem are not well-posed, representing the tendency of the outside flow to push the new vortex back onto the shedding solid. In the real physical problem, the leading-edge vortex will remain attached to the solid or at least sufficiently close to interact significantly with the boundary layers. This situation cannot be represented with an inviscid model. Higher-order representations of the flow can be considered within the inviscid potential framework, for example by considering the shedding of multiple vortices to account for the secondary shedding resulting from the interaction of the main vortex with the boundary layers, or the shedding of higher-order singularities such as dipoles along the body surface to represent the attached vorticity. Any such method however introduces some arbitrary parameter (time or location of shedding for example), in contrast with the point vortex approach, while still not addressing the issue of the viscous nature of the phenomenon.

We therefore did not attempt to modify the point vortex model in such a way, instead restricting carefully its applications to situations where the angle-of-attack is large enough for this problem not to appear (Chapter 3) or to situations where the angle-of-attack at the leading edge is small enough for the shedding from the leading edge to be neglected (Chapters 4 and 6). In the real physical problem, vorticity will be formed within the boundary layers close to the leading edge but will be advected along the solid down to the trailing edge where it will be merged with the vorticity shed by the flapping motion of the trailing edge.

Within these limitations, the point vortex representation of the solid's wake appears to be a powerful tool for analyzing fluid-solid interactions and physical effects such as flexibility in the solid or stability of a coupled fluid-solid problem. It introduces significant computational advantages in comparison with a full numerical simulation or even a vortex sheet description of the wake. The computational cost is reduced by several orders of magnitude compared to the former, and the point vortex approach is numerically simpler than the latter, in particular

because no smoothing kernel is necessary. This makes it attractive for problems where a large number of computations is necessary such as optimization for which full numerical simulation is prohibitively expensive and reduced-order models are preferred.

## 7.2 High- $Re$ fluid-solid interactions

Using the point vortex representation and linear stability analysis, this dissertation investigated several examples of strongly-coupled fluid-solid interactions: the fall of a paper card, the flapping of flags in the wind, the coupling of multiple parallel flapping elastic plates and the propulsive forces created by a flexible insect wing. The reduced-order model of the wake in terms of point vortices was used to study both the influence of the wake on the stability of the solid (particularly in the case of the broadside-on fall of a paper card) and the relation between propulsive forces and wake structure.

Through these examples, we pointed out the importance of vortex shedding in this particular regime of fluid-solid interactions. Although viscosity is small and its effect on fluid forces can be neglected in general compared to the pressure forces, vortex shedding resulting from the presence of even an infinitesimal amount of viscosity is an essential element to the understanding of such problems and should be included in a reduced-order model. Empirical models based only on optimized drag coefficients are not well-suited for such situations. This illustrates the fundamental difference between a purely inviscid representation and the point vortex (or the vortex sheet) representation. In the former, the flow is purely potential and the influence of viscosity is totally neglected. The latter neglects the influence of viscosity on the fluid forces but acknowledges the fundamental role of viscosity in the shedding of vorticity. When the geometry and motion of the solid are such that boundary layer separation and vortex shedding will occur, even for very small viscosity  $\nu$ , then the purely potential representation is not a good

model for the limit of a real flow when  $Re$  goes to infinity. Instead, inviscid vortex shedding models are more appropriate.

The interaction of the internal dynamics of a passively or actively flapping flexible membrane with an outside imposed flow was also investigated. This interaction is at the origin of the fluttering instability of a flag that is somewhat similar to the instability of a fluid-conveying pipe (Paidoussis, 1998) with clamped-free boundary conditions. Other boundary conditions, such as the case of a flexible plate clamped at both edges, are relevant in other applications like cooling systems (see for example Miller, 1960; Kim and Davis, 1995). Under such configurations, the plate or plate assembly can lose stability to flutter through a Hopf bifurcation (leading to two unstable modes with same frequency and traveling waves modes as in the case of the flapping flag) or by divergence through a pitchfork bifurcation (leading to two purely imaginary modes, one of them being unstable). The latter was not possible with clamped-free boundary conditions.

Several linear analysis methods have been presented in the literature and we emphasized in this dissertation some of their main differences, particularly in the treatment of the wake. The treatment as a vortex sheet as suggested by Kornecki et al. (1976) is the most physical but its application is limited. We were unable to generalize it to more complex geometries (e.g multiple plates or a single plate in a bounded domain) and other models must be considered.

Linear stability analysis provides an interesting insight into the stability of the system and the structure of the different modes. However, the exponential growth of unstable modes quickly leads to regimes where the flapping amplitude is not negligible compared to the plate's length and the use of a reduced-order model to solve the initial value problem is valuable to compare the linear stability analysis predictions to the non-linear observed regimes (particularly in terms of dominant mode structures).

In Chapter 6, we further investigated the effect of flexibility by looking at a simple model for propulsion using a passive flapping wing forced at its leading

edge. Compared to purely rigid profiles, we found on this simple case that the use of flexible structures can lead to significant improvements in both the produced forces and the flapping efficiency. Higher thrust or drag were identified as resonances between the forcing frequency and the fundamental frequencies of the system. This is particularly important for the understanding of biological locomotion techniques used by fishes and insects, whose fins and wings are fundamentally flexible, and for the design of more efficient propulsion systems. This study shows for a very simple case that optimal propulsion can be achieved by a proper tuning of the material properties to the flapping characteristics (e.g. frequency).

Several approximations were made in the study of a flapping wing including the two-dimensional nature of the flow and the absence of viscous dissipation or material damping. The latter can easily be introduced in the present model to investigate the effect of this energy dissipation on the coupled system: only the solid dynamics is modified and the point vortex approach for the fluid is still valid. The propulsion performance analysis of Chapter 6 is extended in Appendix D as an example to the case of a solid with material damping. Beyond the importance of considering material damping because of its presence in any biological system, the understanding of the influence of material damping on phenomena such as the spontaneous flapping of flexible plates is important in the design of energy harvesting systems. With the increasing need to design new systems to produce energy from renewable sources, harvesting energy from permanently available geophysical flows such as wind and currents is becoming more and more attractive. Preliminary designs of apparatus using passively oscillating or flapping structures have been recently proposed (see for example the energy harvesting eel described in Allen and Smits, 2001).

In such systems, the energy harvesting through the conversion of solid mechanical energy into electrical power, for example, introduces a damping in the motion of the structure, whose effect on the solid motion must be taken into ac-

count. The energy dissipated by material damping is also a measure of the energy available for conversion into electricity for example (a conversion efficiency should then also be introduced). If the amount of material damping introduced in the fluid-solid problem is very small, the motion of the solid body might not be significantly influenced (in particular the solid motion amplitude, and therefore its energy, might not be significantly reduced) compared to the non-dissipative case. However, in such a situation, only a small amount of mechanical energy is available for conversion. If material damping is very large, then the solid's motion might be too damped for the solid to actually extract a significant amount of energy from the fluid and once again the energy available for conversion will be small. A trade-off between these two effects is expected to define an optimal value for the solid material damping that maximizes the energy dissipation (or conversion).

# Appendix A

## Linear stability analysis of a cantilevered plate in axial flow

In Chapter 4, we presented the results obtained with the point vortex method on the stability of the flat state of rest of a clamped-free flexible flag in a parallel flow, and compared them with linear stability analysis. Chapter 6 used the same fluid-solid model to study resonance phenomena in the flapping amplitude and thrust production of a heaving flexible wing and compared the resonances' position with the linear stability analysis for the modes of a clamped-free flexible plate in axial flow.

The stability analysis framework used in both cases was first presented by Kornecki et al. (1976) and more recently used by Eloy et al. (2008). We only present here a brief description of this method for reference, which was mentioned as the vortex sheet (VS) method in Chapter 5. More details can be found in Kornecki et al. (1976) and Bisplinghoff et al. (1955).

The VS method differs from the double wake (DW) approach (used to study the linear stability analysis of  $Q$  flexible plates in Chapter 5) in its treatment of the vortical wake shed from the solid's trailing edge. In both frameworks, infinitesimal perturbations to the state of rest (where the plate is purely horizontal) are considered. In the DW method of Chapter 5, the presence of a vortex wake was taken into account by the continuity of the pressure across the horizontal axis

downstream from the plate: a free vortex sheet can not sustain any pressure jump. To be able to solve explicitly for the flow potential around the flexible plate, this method also requires a similar constraint *upstream* from the plate, thereby introducing a fictitious upstream wake.

The VS method presented here considers an explicit description of the wake in terms of a continuous vortex sheet advected, at leading order, by the imposed flow along the horizontal axis. In that regard, the VS method is more physical. However, it is more complicated than the DW method and is not generalizable as is to more complex geometries (e.g. multiple plates).

In the case of one plate only, VS and DW methods lead to qualitatively similar results regarding the stability domain of the flag state of rest, but they differ in the velocity threshold for instability in the limit of very heavy flags, for which dominant modes have the longest wavelength (see figure 5.3). In that case, the treatment of the wake has a significant impact on the result. For lighter plates (and shorter dominant wave lengths), the impact of the wake treatment method is reduced.

We are interested here in the linear stability of an infinitesimally thin flag (or plate) with flexural rigidity, initially straight in a uniform flow. All the physical quantities are non-dimensionalized using the length of the plate  $L$ , the flow velocity  $U_\infty$  and the fluid density  $\rho$ . The equation of motion for the flexible solid is obtained from (5.3)

$$\ddot{y} = -\frac{1}{U^{*2}} y'''' - M^* [p]^\pm \quad (\text{A.1})$$

with  $M^*$  and  $U^*$  defined in (4.5).  $[p]^\pm = p^+ - p^-$  is the pressure difference between the top and bottom side of the flag.  $y(x, t)$  is the vertical position of the point on the flag located at  $(x, 0)$  in the rest position. As in Chapter 5,  $|y| \ll 1$  and we neglect the horizontal displacement of the plate, which is of higher order. A dotted variable denotes differentiation in time, and a primed variable denotes differentiation in  $x$ .

The clamped-free boundary conditions on the plate's displacement are

$$y(0) = y'(0) = 0, \quad y''(1) = y'''(1) = 0. \quad (\text{A.2})$$

To compute the pressure jump, potential flow theory is used. The presence of the plate is represented by a distribution of bound vorticity  $\kappa(x, t)$  with  $0 \leq x \leq 1$  as in Chapter 4. The wake is represented as a continuous vortex sheet  $\gamma(x, t)$  for  $x \geq 1$ . The flow velocity is obtained by superposition of the outside flow  $U_\infty = 1$  and the effect of the attached and free vortex sheets:

$$w(z) = 1 + \frac{1}{2\pi i} \left[ \int_0^1 \frac{\kappa ds}{z-s} + \int_1^\infty \frac{\gamma d\xi}{z-\xi} \right]. \quad (\text{A.3})$$

The continuity of normal flow at the solid's boundary prescribes  $\text{Im}[w] = -v = -\dot{y} - y'$ , and  $\kappa(x, t)$  is the solution of the singular integral equation

$$\frac{1}{2\pi} \int_0^1 \frac{\kappa(s) ds}{s_0 - s} = v(s_0) - \frac{1}{2\pi} \int_1^\infty \frac{\gamma(\xi) d\xi}{s_0 - \xi}, \quad \int_0^1 \kappa(s) ds + \int_1^\infty \gamma(\xi) d\xi = 0 \quad (\text{A.4})$$

with no net circulation at infinity. This can be solved exactly (see for example Tuck, 1980):

$$\kappa(x) = \frac{1}{\pi \sqrt{x(1-x)}} \int_1^\infty \frac{\sqrt{\xi(\xi-1)} \gamma(\xi) d\xi}{x-\xi} - \frac{2}{\pi \sqrt{x(1-x)}} \int_0^1 \frac{\sqrt{s(1-s)} v(s) ds}{x-s}. \quad (\text{A.5})$$

The regularity condition imposes that  $\kappa(1) = 0$ , therefore:

$$\int_1^\infty \sqrt{\frac{\xi}{\xi-1}} \gamma(\xi) d\xi + 2 \int_0^1 \sqrt{\frac{s}{1-s}} v(s) ds = 0. \quad (\text{A.6})$$

At leading order, the pressure jump is obtained from (4.13) as:

$$[p]^\pm = \int_0^x \kappa dx' + \kappa(x). \quad (\text{A.7})$$

The free vortex sheet is advected by the mean flow, therefore  $\dot{\gamma} = -\gamma'$ . Then,

$$\begin{aligned}
[p]^\pm(x) &= -\frac{2}{\pi} \int_0^1 \dot{v}(s_0) \sqrt{s_0(1-s_0)} \left( \int_0^x \frac{ds}{\sqrt{s(1-s)}(s-s_0)} \right) ds_0 \\
&\quad - \frac{1}{\pi} \int_1^\infty \gamma'(\xi) \sqrt{\xi(\xi-1)} \left( \int_0^x \frac{ds}{(s-\xi)\sqrt{s(1-s)}} \right) d\xi \\
&\quad + \frac{1}{\pi\sqrt{x(1-x)}} \int_1^\infty \frac{\sqrt{\xi(\xi-1)}\gamma(\xi)d\xi}{x-\xi} \\
&\quad - \frac{2}{\pi\sqrt{x(1-x)}} \int_0^1 \frac{\sqrt{s(1-s)}v(s)ds}{x-s},
\end{aligned} \tag{A.8}$$

which can be simplified into

$$\begin{aligned}
[p]^\pm(x) &= \frac{2}{\pi} \int_0^1 \dot{v}(s_0) \log \left| \frac{\sqrt{\frac{x}{1-x}} + \sqrt{\frac{s_0}{1-s_0}}}{\sqrt{\frac{x}{1-x}} - \sqrt{\frac{s_0}{1-s_0}}} \right| ds_0 \\
&\quad + \frac{2}{\pi} \int_1^\infty \gamma'(\xi) \tan^{-1} \left( \sqrt{\frac{x(\xi-1)}{\xi(1-x)}} \right) d\xi \\
&\quad + \frac{1}{\pi\sqrt{x(1-x)}} \int_1^\infty \frac{\sqrt{\xi(\xi-1)}\gamma(\xi)d\xi}{x-\xi} \\
&\quad - \frac{2}{\pi\sqrt{x(1-x)}} \int_0^1 \frac{\sqrt{s(1-s)}v(s)ds}{x-s}.
\end{aligned} \tag{A.9}$$

Integrating by part and rearranging, we obtain

$$\begin{aligned}
[p]^\pm(x) &= \frac{2}{\pi} \int_0^1 \dot{v}(s_0) \log \left| \frac{\sqrt{\frac{x}{1-x}} + \sqrt{\frac{s_0}{1-s_0}}}{\sqrt{\frac{x}{1-x}} - \sqrt{\frac{s_0}{1-s_0}}} \right| ds_0 \\
&\quad - \frac{2}{\pi\sqrt{x(1-x)}} \int_0^1 \frac{\sqrt{s(1-s)}v(s)ds}{x-s} \\
&\quad - \left( \frac{1}{\pi} \int_1^\infty \gamma(\xi) \sqrt{\frac{\xi}{\xi-1}} d\xi \right) \left[ \frac{2x-1}{\sqrt{x(1-x)}} + \sqrt{\frac{1-x}{x}} \underbrace{\frac{\int_1^\infty \frac{\gamma(2\xi-1)d\xi}{\sqrt{\xi(\xi-1)}}}{\int_1^\infty \gamma \sqrt{\frac{\xi}{\xi-1}} d\xi}}_C \right].
\end{aligned} \tag{A.10}$$

We consider solutions of the problem of the form  $y(x, t) = h(x)e^{i\omega t}$ ; then  $\gamma(\xi, t) = \gamma_0 e^{i\omega(t-\xi)}$  and the function  $C$  in (A.10) depends only on  $\omega$  and can be expressed in

terms of Hankel's function of the second kind (Abramowitz and Stegun, 1964)

$$C(\omega) = \frac{\int_0^\infty \cosh u e^{-i\omega\left(\frac{1+\cosh u}{2}\right)} du}{\int_0^\infty \left(\frac{1+\cosh u}{2}\right) e^{-i\omega\left(\frac{1+\cosh u}{2}\right)} du} = \frac{2H_1^{(2)}\left(\frac{\omega}{2}\right)}{H_1^{(2)}\left(\frac{\omega}{2}\right) + iH_0^{(2)}\left(\frac{\omega}{2}\right)}. \quad (\text{A.11})$$

$C$  is also known as the Theodorsen function (Theodorsen, 1935) and satisfies the following properties:

$$\lim_{\omega \rightarrow 0} C(\omega) = 2, \quad \lim_{\omega \rightarrow \infty} C(\omega) = 1. \quad (\text{A.12})$$

Finally using (A.6),

$$\begin{aligned} -\omega^2 h + \frac{1}{U^*2} h'''' &= -\frac{2i\omega M^*}{\pi} \int_0^1 \log \left| \frac{\sqrt{\frac{x}{1-x}} + \sqrt{\frac{\xi}{1-\xi}}}{\sqrt{\frac{x}{1-x}} - \sqrt{\frac{\xi}{1-\xi}}} \right| (i\omega h + h') d\xi \\ &+ \frac{2M^*}{\pi\sqrt{x(1-x)}} \int_0^1 \frac{\sqrt{\xi(1-\xi)}}{x-\xi} (i\omega h + h') d\xi \\ &- \frac{2M^*}{\pi} \int_0^1 \sqrt{\frac{\xi}{1-\xi}} (i\omega h + h') d\xi \left[ \frac{2x-1}{\sqrt{x(1-x)}} + \sqrt{\frac{1-x}{x}} C(\omega) \right]. \end{aligned} \quad (\text{A.13})$$

Kornecki et al. (1976) uses a slightly different method inspired by Theodorsen theory to derive the same result (see for example Bisplinghoff et al., 1955).

As in Chapter 5, the eigenvalue problem (A.13) in  $\omega$  is solved using the Galerkin method and the natural modes  $\psi_n$  of the clamped-free beam in vacuum satisfying

$$\psi_n'''' = \lambda_n^4 \psi_n \quad \text{with } 1 + \cos \lambda_n \cosh \lambda_n = 0, \quad (\text{A.14})$$

and the boundary conditions (A.2). This set of orthogonal functions is defined as

$$\psi_n = \cosh \lambda_n x - \cos \lambda_n x + \frac{\sin \lambda_n - \sinh \lambda_n}{\cos \lambda_n + \cosh \lambda_n} (\sinh \lambda_n x - \sin \lambda_n x). \quad (\text{A.15})$$

The function  $h(x)$  in (A.13) is expanded on a finite number  $S$  of these modes

$$h(x) = \sum_{n=1}^S \alpha_n \psi_n(x) \quad (\text{A.16})$$

and the resulting equation is then projected on these same modes. The eigenvalue problem (A.13) is then of the form

$$\mathbf{A} \cdot \boldsymbol{\alpha} = 0, \quad \text{with} \quad (\text{A.17})$$

$$\mathbf{A} = -\omega^2 \mathbf{I} + \frac{1}{U^{*2}} \mathbf{K} + M^* [\mathbf{M}^{(0)} + i\omega \mathbf{M}^{(1)} - \omega^2 \mathbf{M}^{(2)} + C(\omega) (\mathbf{M}^{C1} + i\omega \mathbf{M}^{C2})]$$

with the coefficient of the different matrices defined as:

$$\begin{aligned} K_{ij} &= \lambda_j^4 \delta_{ij}, & M_{ij}^{(K)} &= \mathcal{F}_1(\psi^{(i)}, \psi_x^{(j)}) + \mathcal{F}_2(\psi^{(i)}, \psi_x^{(j)}), \\ M_{ij}^{(G)} &= \mathcal{F}_1(\psi^{(i)}, \psi^{(j)}) + \mathcal{F}_2(\psi^{(i)}, \psi^{(j)}) + \mathcal{F}_3(\psi^{(i)}, \psi_x^{(j)}), \\ M_{ij}^{(M)} &= \mathcal{F}_3(\psi^{(i)}, \psi^{(j)}), & M_{ij}^{C1} &= \mathcal{F}_4(\psi^{(i)}, \psi_x^{(j)}), & M_{ij}^{C2} &= \mathcal{F}_4(\psi^{(i)}, \psi^{(j)}), \end{aligned}$$

with the functionals  $\mathcal{F}_k$  ( $1 \leq k \leq 4$ ) defined as

$$\begin{aligned} \mathcal{F}_1(f, g) &= -\frac{2}{\pi} \int_0^1 \frac{f(x)}{\sqrt{x(1-x)}} \left[ \int_0^1 \frac{\sqrt{\xi(1-\xi)}}{x-\xi} g(\xi) d\xi \right] dx \\ \mathcal{F}_2(f, g) &= \frac{2}{\pi} \left[ \int_0^1 \frac{(2x-1)f(x)}{\sqrt{x(1-x)}} dx \right] \left[ \int_0^1 \sqrt{\frac{x}{1-x}} g(x) dx \right], \\ \mathcal{F}_3(f, g) &= \frac{2}{\pi} \int_0^1 f(x) \left[ \int_0^1 g(\xi) \log \left| \frac{\sqrt{\frac{x}{1-x}} + \sqrt{\frac{\xi}{1-\xi}}}{\sqrt{\frac{x}{1-x}} - \sqrt{\frac{\xi}{1-\xi}}} \right| d\xi \right] dx, \\ \mathcal{F}_4(f, g) &= \frac{2}{\pi} \left[ \int_0^1 f(x) \sqrt{\frac{1-x}{x}} dx \right] \left[ \int_0^1 \sqrt{\frac{x}{1-x}} g(x) dx \right]. \end{aligned}$$

This non-linear eigenvalue problem must be solved for numerically. For a given number of normal modes, the different matrices involved in (A.17) can be computed numerically. Four of these integrals require a particular treatment because of their singular logarithmic or Cauchy-type kernel. More precisely, given two functions  $f$  and  $g$  continuously differentiable on  $[0, 1]$ , we are interested in the two following integrals:

$$I_1(f, g) = \int_0^1 f(x) \int_0^1 g(\xi) \log \left| \frac{\sqrt{\frac{x}{1-x}} + \sqrt{\frac{\xi}{1-\xi}}}{\sqrt{\frac{x}{1-x}} - \sqrt{\frac{\xi}{1-\xi}}} \right| d\xi dx, \quad (\text{A.18})$$

$$I_2(f, g) = \int_0^1 \frac{f(x)}{\sqrt{x(1-x)}} \left[ \int_0^1 \frac{\sqrt{\xi(1-\xi)}}{x-\xi} g(\xi) d\xi \right] dx. \quad (\text{A.19})$$

Isolating the logarithmic singularity at  $x = \xi$  in (A.18),  $I_1$  becomes

$$I_1(f, g) = \int_0^1 f(x)g(x) \int_0^1 \log \left| \frac{\sqrt{\frac{x}{1-x}} + \sqrt{\frac{\xi}{1-\xi}}}{\sqrt{\frac{x}{1-x}} - \sqrt{\frac{\xi}{1-\xi}}} \right| d\xi dx \quad (\text{A.20})$$

$$+ \int_0^1 f(x) \int_0^1 (g(\xi) - g(x)) \log \left| \frac{\sqrt{\frac{x}{1-x}} + \sqrt{\frac{\xi}{1-\xi}}}{\sqrt{\frac{x}{1-x}} - \sqrt{\frac{\xi}{1-\xi}}} \right| d\xi dx.$$

Integrating by part the  $\xi$ -integral in the first term,  $I_1$  simplifies into

$$I_1(f, g) = \int_0^1 \int_0^1 f(x) [g(\xi) - g(x)] \log \left| \frac{\sqrt{\frac{x}{1-x}} + \sqrt{\frac{\xi}{1-\xi}}}{\sqrt{\frac{x}{1-x}} - \sqrt{\frac{\xi}{1-\xi}}} \right| d\xi dx$$

$$+ \pi \int_0^1 f(x)g(x) \sqrt{x(1-x)} dx. \quad (\text{A.21})$$

The second integral is now regular at  $x = \xi$  (the integrand vanishes there).

In the same way for  $I_2(f, g)$ ,

$$I_2(f, g) = \int_0^1 f(x)g(x) \log \left[ \frac{x}{1-x} \right] dx \quad (\text{A.22})$$

$$+ \int_0^1 \frac{f(x)}{\sqrt{x(1-x)}} \left[ \int_0^1 \frac{\sqrt{\xi(1-\xi)}g(\xi) - \sqrt{x(1-x)}g(x)}{x-\xi} d\xi \right] dx.$$

Using the changes of variable  $x = (1 - \cos \theta)/2$  and  $\xi = (1 - \cos \psi)/2$  in the second integral, and noting for simplicity  $f(\theta) = f(x(\theta))$  and  $g(\psi) = g(\xi(\psi))$ , we obtain

$$I_2(f, g) = \int_0^1 [f(x)g(x) - f(0)g(0) + f(1)g(1) - f(1-x)g(1-x)] \log x dx$$

$$+ f(1)g(1) - f(0)g(0) + \frac{1}{2} \int_0^\pi f(\theta) \left[ \int_0^\pi \frac{\sin^2 \psi g(\psi) - \sin \psi \sin \theta g(\theta)}{\cos \psi - \cos \theta} d\psi \right] d\theta \quad (\text{A.23})$$

The integrand in both terms are now regular. In particular, for the second term, at  $x \sim \xi$ ,

$$\frac{\sin^2 \psi g(\psi) - \sin \psi \sin \theta g(\theta)}{\cos \psi - \cos \theta} \sim -\cos \theta g(x(\theta)) - \frac{\sin^2 \theta}{2} g'(x(\theta)). \quad (\text{A.24})$$

The integrals involved in (A.21) and (A.23) all have regular integrands and can be computed numerically using any standard routine (such as Matlab's `quad` and `dblquad`).

Once all the matrices involved in (A.17) have been precomputed, for given values of  $M^*$  and  $U^*$ , the eigenvalue problem (A.17) can be solved iteratively. An initial guess is obtained by replacing  $C(\omega)$  by its value at infinity and using the `polyeig` Matlab routine to solve for the generalized eigenvalue problem. The eigenvalue problem is then solved iteratively using a Newton–Kantorovitch method (Boyd, 2001). Given a guess  $\omega^{(j)}$  and  $\boldsymbol{\alpha}^{(j)}$  for eigenvalue and corresponding eigenvector, and assuming that  $\omega^{(j+1)}$  and  $\boldsymbol{\alpha}^{(j+1)}$  are solutions of (A.17), we obtain by linearization

$$\begin{aligned} 0 &= \mathbf{A}(\omega^{(j+1)}) \cdot \boldsymbol{\alpha}^{(j+1)} \\ &= \mathbf{A}(\omega^{(j)}) \cdot \boldsymbol{\alpha}^{(j)} + \frac{\partial \mathbf{A}}{\partial \omega}(\omega^{(j)}) \cdot \boldsymbol{\alpha}^{(j)} (\omega^{(j+1)} - \omega^{(j)}) + \mathbf{A}(\omega^{(j+1)}) \cdot (\boldsymbol{\alpha}^{(j+1)} - \boldsymbol{\alpha}^{(j)}) \end{aligned} \quad (\text{A.25})$$

which can be reformulated as

$$\begin{bmatrix} \frac{\partial \mathbf{A}}{\partial \omega}(\omega^{(j)}) \cdot \boldsymbol{\alpha}^{(j)} & \mathbf{A}(\omega^{(j+1)}) \end{bmatrix} \cdot \begin{pmatrix} \omega^{(j+1)} - \omega^{(j)} \\ \boldsymbol{\alpha}^{(j+1)} - \boldsymbol{\alpha}^{(j)} \end{pmatrix} = -\mathbf{A}(\omega^{(j)}) \cdot \boldsymbol{\alpha}^{(j)}. \quad (\text{A.26})$$

The previous problem is overdetermined since for any  $\lambda$ ,  $\lambda \boldsymbol{\alpha}$  is an eigenvector if  $\boldsymbol{\alpha}$  is an eigenvector. This is overcome for example either by considering that  $\Delta \boldsymbol{\alpha}$  must be orthogonal to  $\boldsymbol{\alpha}$  or that  $\alpha_q^{(j)} = \alpha_q^{(j+1)}$  for a given  $q$ , introducing an additional constraints to make the system invertible. To avoid numerical problems introduced by  $|\boldsymbol{\alpha}|$  being too small, at the end of each iteration  $\boldsymbol{\alpha}$  is rescaled to be of unit norm.

Using the previously outlined method, one can compute for given  $M^*$  and  $U^*$ , the  $2S$  eigenvalues of (A.17). Not all of the eigenvalues are physical, in particular the eigenvalues with the largest frequencies are purely numerical. In the flag problem, we are most interested in the lowest frequencies modes (that are also associated with the least stable modes). The critical curve for the stability of one flag (figure A.1) is obtained by finding the particular values of  $M^*$  and  $U^*$  for which one of the physical modes becomes unstable. The different branches on the

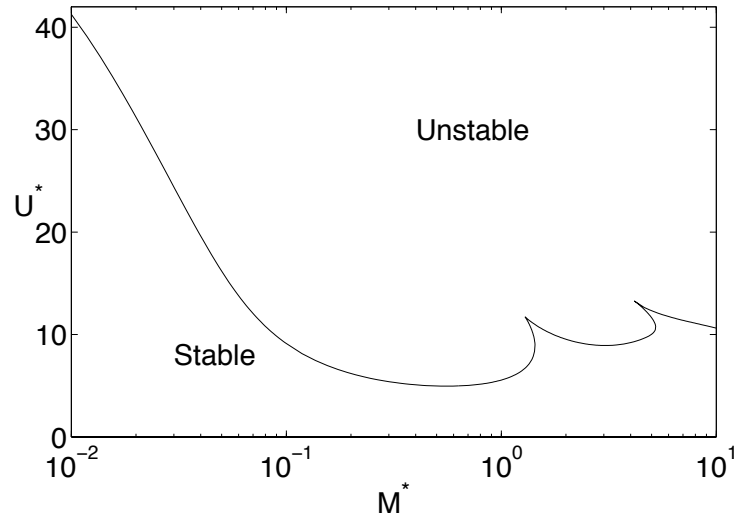


**Figure A.1:** Critical stability curve obtained with the VS linear stability analysis method for a single flexible plate clamped at its leading edge and placed in a uniform axial flow.

critical curve correspond to different modes becoming unstable: at low  $M^*$ , the first unstable mode is a mode 2 (one neck). The second branch correspond to a mode 3 (two necks), and so on (Eloy et al., 2008). Mode 1 is always stable for the clamped-free boundary conditions.

Looking back at the derivation of (A.13) and (A.17), we observe that the key element leading to the result is the possibility to factor out the influence of the mode frequency in the circulatory pressure into the Theodorsen function  $C(\omega)$ . Such a factorization is possible because we are able to solve explicitly for  $\kappa$  in (A.4). In the case of two plates or more, this integral equation must be solved for numerically (see for example appendix B) ruling out the possibility to obtain an equivalent of the Theodorsen function.

# Appendix B

## Numerical solution of Cauchy-type singular integral equations

In Chapters 4 and 5 of this dissertation, we have been confronted to the problem of solving a system of integral equations of the form

$$\int_0^1 \left[ \frac{\delta_{pq}}{2\pi(x-x')} + K_{pq}(x, x') \right] \kappa_q(x') dx' = f_p(x), \quad \int_0^1 \kappa_p(x') dx' = \gamma_p \quad (\text{B.1})$$

with  $1 \leq p, q \leq Q$ , where all  $K_{pq}(x, x')$  and  $f_p(x)$  are regular for  $0 \leq x, x' \leq 1$ ,  $\gamma_p$  are given constants and  $K_{pq} = K_{qp}$ . We present here the method used to solve (B.1) numerically using Chebyshev expansions. For clarity, we only present the case  $Q = 2$ , the method being easily generalized to  $Q \geq 2$ .

We are interested here in the numerical solution of a system of integral equations for  $\kappa_1(x)$  and  $\kappa_2(x)$  of the form

$$\int_0^1 K_s(x, x') \kappa_1(x') dx' + \frac{1}{2\pi} \int_0^1 \frac{\kappa_1(x') dx'}{x-x'} + \int_0^1 K_a(x, x') \kappa_2(x') dx' = f_1(x) \quad (\text{B.2})$$

$$\int_0^1 K_a(x, x') \kappa_1(x') dx' + \frac{1}{2\pi} \int_0^1 \frac{\kappa_2(x') dx'}{x-x'} + \int_0^1 K_s(x, x') \kappa_2(x') dx' = f_2(x) \quad (\text{B.3})$$

$$\int_0^1 \kappa_1(x') dx' = \gamma_1, \quad \int_0^1 \kappa_2(x') dx' = \gamma_2. \quad (\text{B.4})$$

where the kernels  $K_s(x, x')$  and  $K_a(x, x')$  are regular for  $0 \leq x, x' \leq 1$ . Equations (B.4) are necessary for the system to be well-posed because of the Cauchy nature

of the kernels involved in the integral equation (Tuck, 1980).

Following Tuck (1980), both integral equations are then integrated in  $x$

$$\int_0^1 L_s(x, x') \kappa_1(x') dx' + \frac{1}{2\pi} \int_0^1 \kappa_1(x') \log |x - x'| dx' + \int_0^1 L_a(x, x') \kappa_2(x') dx' = g_1(x) + \beta_1 \quad (\text{B.5})$$

$$\int_0^1 L_a(x, x') \kappa_1(x') dx' + \frac{1}{2\pi} \int_0^1 \kappa_2(x') \log |x - x'| dx' + \int_0^1 L_s(x, x') \kappa_2(x') dx' = g_2(x) + \beta_2 \quad (\text{B.6})$$

where  $K_s(x, x') = \partial L_s / \partial x$ ,  $K_a(x, x') = \partial L_a / \partial x$  and  $f_j(x) = g'_j(x)$ , and  $\beta_j$  are unknown constants. Because of the logarithmic kernel, we expect  $\kappa_j$  to have inverse square-root singularities at both ends of the interval of integration. We therefore define the regularized functions  $\tilde{\kappa}_j(x) = \kappa_j(x) \sqrt{x(1-x)}$ .

Take  $N_p$  Gauss-Chebyshev points defined as

$$x_p = \frac{1 - \cos \theta_p}{2}, \quad \theta_p = \cos \left( \frac{(p - \frac{1}{2}) \pi}{N_p} \right), \quad 1 \leq p \leq N_p. \quad (\text{B.7})$$

We note  $\tilde{\kappa}_j$  the vector of the values of  $\tilde{\kappa}_j(x_p)$ . Using the change of variables  $x' = (1 - \cos \theta')/2$  in (B.5)–(B.6) leads to

$$\int_0^\pi L_s(x, \theta') \tilde{\kappa}_1(\theta') d\theta' + \frac{1}{2\pi} \int_0^\pi \tilde{\kappa}_1(\theta') \log |2x - (1 - \cos \theta')| d\theta' + \int_0^\pi L_a(x, \theta') \tilde{\kappa}_2(\theta') d\theta' = g_1(x) + \tilde{\beta}_1 \quad (\text{B.8})$$

$$\int_0^\pi L_a(x, \theta') \tilde{\kappa}_1(\theta') d\theta' + \frac{1}{2\pi} \int_0^\pi \tilde{\kappa}_2(\theta') \log |2x - (1 - \cos \theta')| d\theta' + \int_0^\pi L_s(x, \theta') \tilde{\kappa}_2(\theta') d\theta' = g_2(x) + \tilde{\beta}_2 \quad (\text{B.9})$$

where for convenience of notation we understand  $\tilde{\kappa}(\theta')$  to mean  $\tilde{\kappa}(x(\theta'))$ .  $\tilde{\beta}_j$  are modified constants. The previous system is then evaluated at  $x = x_p$  and the different integrals in  $\theta'$  are divided in  $N_p$  intervals of equal length centered on  $\theta_p$ .

For example, for the regular kernel  $L_s$ ,

$$\begin{aligned} \int_0^\pi L_s(x_p, \theta') \tilde{\kappa}_j(\theta') d\theta' &= \sum_{n=1}^{N_p} \int_{\theta_n^c}^{\theta_{n+1}^c} L_s(x_p, \theta') \tilde{\kappa}_j(\theta') d\theta' \\ &\sim \sum_{n=1}^{N_p} \tilde{\kappa}_j(\theta_n) \int_{\theta_n^c}^{\theta_{n+1}^c} L_s(x_p, \theta') d\theta' \end{aligned}$$

with  $\theta_n^c = (n-1)\pi/N_p$  for  $1 \leq n \leq N_p + 1$ , and therefore  $\theta_p = (\theta_p^c + \theta_{p+1}^c)/2$ .

The evaluation of the integral involving the logarithmic kernel is more subtle. The integral can still be split over the  $N_p$  equal intervals, and evaluated as previously for  $n \neq p$ . We evaluate separately the case  $n = p$ . Using the definition of  $x_p$  in terms of  $\theta_p$ :

$$\int_{\theta_p^c}^{\theta_{p+1}^c} \tilde{\kappa}_j(\theta') \log |2x_p - (1 - \cos \theta')| d\theta' = \int_{\theta_p^c}^{\theta_{p+1}^c} \tilde{\kappa}_j(\theta') \log |\cos \theta' - \cos \theta_p| d\theta'. \quad (\text{B.10})$$

On this interval,  $|\theta' - \theta_p| \leq \Delta\theta/2$  with  $\Delta\theta = \pi/N_p$ . Assuming this interval is small, we can expand  $\tilde{\kappa}_j(\theta')$  and  $\cos \theta' - \cos \theta_p$  about  $\theta_p$ . Keeping only the dominant terms in  $\Delta\theta$ , we obtain

$$\int_{\theta_p^c}^{\theta_{p+1}^c} \tilde{\kappa}_j(\theta') \log |2x_p - (1 - \cos \theta')| d\theta' \sim \tilde{\kappa}_j(\theta_p) \Delta\theta \left( \log \left| \frac{\sin \theta_p \Delta\theta}{2} \right| - 1 \right). \quad (\text{B.11})$$

Using these results, (B.5)–(B.6) is approximated as

$$\mathbf{C} \cdot \begin{pmatrix} \tilde{\kappa}_1 \\ \tilde{\kappa}_2 \end{pmatrix} = \begin{pmatrix} \mathbf{C}^{(1)} & \mathbf{C}^{(2)} \\ \mathbf{C}^{(2)} & \mathbf{C}^{(1)} \end{pmatrix} \cdot \begin{pmatrix} \tilde{\kappa}_1 \\ \tilde{\kappa}_2 \end{pmatrix} = \begin{pmatrix} \mathbf{g}_1 \\ \mathbf{g}_2 \end{pmatrix} + \tilde{\beta}_1 \begin{pmatrix} \mathbf{1} \\ \mathbf{0} \end{pmatrix} + \tilde{\beta}_2 \begin{pmatrix} \mathbf{0} \\ \mathbf{1} \end{pmatrix} \quad (\text{B.12})$$

with  $\mathbf{1}$  and  $\mathbf{0}$  the column vectors of  $N_p$  elements all equal respectively to 1 and 0.

The influence coefficients matrices  $\mathbf{C}^{(1)}$  and  $\mathbf{C}^{(2)}$  have coefficients

$$C_{mn}^{(1)} = \frac{1}{2\pi} \int_{\theta_n^c}^{\theta_{n+1}^c} \log |2x_m - 1 + \cos \theta'| dx' + \int_{\theta_n^c}^{\theta_{n+1}^c} L_s(x_m, \theta') d\theta', \quad (\text{B.13})$$

$$C_{mn}^{(2)} = \int_{\theta_n^c}^{\theta_{n+1}^c} L_a(x_m, \theta') d\theta'. \quad (\text{B.14})$$

All the contributions to  $\mathbf{C}^{(1)}$  and  $\mathbf{C}^{(2)}$  of the regular kernels and the non-diagonal contributions to  $\mathbf{C}^{(1)}$  of the logarithmic kernel are computed using the trapezoidal

rule. Diagonal terms of the contribution to  $\mathbf{C}^{(1)}$  of the logarithmic kernel are obtained using (B.11). The integration in  $x$  to obtain  $L_s$ ,  $L_a$  and  $g_j$  is performed using Gauss–Chebyshev quadrature (Pozrikidis, 1998).

The matrix  $\mathbf{C}$  is non-singular and can be inverted:

$$\begin{pmatrix} \tilde{\kappa}_1 \\ \tilde{\kappa}_2 \end{pmatrix} = \mathbf{C}^{-1} \cdot \left[ \begin{pmatrix} \mathbf{g}_1 \\ \mathbf{g}_2 \end{pmatrix} + \tilde{\beta}_1 \begin{pmatrix} \mathbf{1} \\ \mathbf{0} \end{pmatrix} + \tilde{\beta}_2 \begin{pmatrix} \mathbf{0} \\ \mathbf{1} \end{pmatrix} \right] \quad (\text{B.15})$$

and the constants  $\tilde{\beta}_1$  and  $\tilde{\beta}_2$  are obtained by enforcing  $\int_0^\pi \tilde{\kappa}_j(\theta') d\theta' = \gamma_j$ . The approach is easily transposed to the case of  $Q$  functions  $\kappa_j$  as in (5.26).

# Appendix C

## Symmetry of the coupled modes of $Q$ flexible plates

We provide here a more rigorous mathematical argument for the symmetry or anti-symmetry of all the linear flapping modes of  $Q$  parallel flexible plates with respect to the middle plane, understood as the plane  $y = (Q - 1)d/2$  (see Chapter 5). For  $Q$  flexible plates, the problem is doubly symmetric in the following sense: the effect of an arbitrary displacement, velocity or acceleration of plate  $i$  on the pressure jump on plate  $j$  is exactly equal to the effect of *the same* arbitrary displacement, velocity or acceleration of plate  $j$  on the pressure jump on plate  $i$ , and is also equal to the effect of *the same* displacement, velocity or acceleration of plate  $Q + 1 - i$  on the pressure forcing on plate  $Q + 1 - j$ . Mathematically, this is expressed by the symmetry and structure of the operator acting on the vector  $([p]^{(1)}, [p]^{(2)}, \dots, [p]^{(Q)})$  in equation (5.26). If we rewrite equation (5.26) as

$$\mathcal{P} \cdot \begin{pmatrix} [p]^{(1)} \\ \vdots \\ [p]^{(Q)} \end{pmatrix} = \dots \quad \text{with } \mathcal{P}_{ij}(f)(x) = \frac{1}{2\pi} \int_0^1 \frac{(x - \xi)f(\xi)d\xi}{(x - \xi)^2 + (i - j)^2d^2} \quad (\text{C.1})$$

then the operator matrix  $\mathcal{P}$  is such that  $\mathcal{P}_{ij}$  only depends on  $|i - j|$ . Then one can prove easily that its inverse  $\mathcal{R}$  satisfies

$$\mathcal{R}_{ij} = \mathcal{R}_{Q-i, Q-j}. \quad (\text{C.2})$$

A close look at the definition of the five different matrices defined in (5.38) will show that they satisfy the same symmetry *by block*, and we explain here what we mean by that. Let  $\mathbf{B}$  be the matrix in bracket in (5.38), and define the block matrices  $\tilde{\mathbf{B}}^{(ij)}$  with  $1 \leq \{i, j\} \leq Q$  such that  $B_{(i-1)S+q, (j-1)S+s} = \tilde{B}_{qs}^{(ij)}$  for  $1 \leq \{q, s\} \leq S$  then

$$\tilde{\mathbf{B}}^{(ij)} = \tilde{\mathbf{B}}^{(Q+1-j, Q+1-i)}. \quad (\text{C.3})$$

Decomposing in the same way the eigenvector  $\boldsymbol{\alpha}$  in blocks  $\tilde{\boldsymbol{\alpha}}$ :  $\alpha_{(r-1)Q+s} = \tilde{\alpha}_s^{(r)}$ , (5.38) becomes

$$\sum_{j=1}^Q \sum_{s=1}^S \tilde{B}_{qs}^{(ij)} \tilde{\alpha}_s^{(j)} = 0, \quad (\text{C.4})$$

for  $1 \leq i \leq Q$  and  $1 \leq q \leq S$ . But, through (C.3) we also have:

$$\sum_{j=1}^Q \sum_{s=1}^S \tilde{B}_{qs}^{(ij)} \tilde{\alpha}_s^{(Q+1-j)} = \sum_{r'=1}^Q \sum_{s=1}^S \tilde{B}_{qs}^{(i, Q+1-j')} \tilde{\alpha}_s^{(j')} = \sum_{j'=1}^Q \sum_{s=1}^S \tilde{B}_{qs}^{(Q+1-i, j')} \tilde{\alpha}_s^{(j')} = 0, \quad (\text{C.5})$$

for  $1 \leq i \leq Q$  and  $1 \leq q \leq S$ . The vector  $\boldsymbol{\beta}$  defined as  $\beta_{(j-1)S+s} = \tilde{\alpha}_s^{(Q+1-j)}$  is also an eigenvector of  $\mathbf{B}$ . It is therefore proportional to  $\boldsymbol{\alpha}$  and

$$\tilde{\alpha}_s^{(j)} = \lambda \tilde{\alpha}_s^{(Q+1-j)}, \quad \text{for } 1 \leq j \leq Q \text{ and } 1 \leq s \leq S. \quad (\text{C.6})$$

Applying this relationship twice, we find immediately that  $\lambda^2 = 1$  and  $\lambda = \pm 1$ .  $\boldsymbol{\alpha}$  gives the decomposition of the eigenmode along the basis built from the free modes. This symmetry property therefore immediately transfers to the displacement of the plates in a particular mode  $\zeta_m^{(j)}(x)$  with  $1 \leq j \leq Q$  and  $1 \leq m \leq Q \times S$ :

$$\zeta_m^{(j)}(x) = \pm \zeta_m^{(Q+1-j)}(x). \quad (\text{C.7})$$

# Appendix D

## Effect of material damping on the performance of a flexible flapping wing

The study of Chapter 6 on the propulsive efficiency of a flexible heaving wing considered a non-dissipative solid model for the wing. Although very little data are available on the visco-elastic damping coefficients of typical fish fins or insect wings (Cheng et al., 1998), it is expected that all such structures present some amount of material damping that opposes the deformation of the solid. We briefly address the issue of its effect on the flapping properties here.

### D.1 Modification of the solid's equations

The flow representation remains unchanged compared to Chapters 4 and 6. The beam model of section 4.2.1 is modified to include an additional dissipative torque in the form of a Kelvin–Voigt model (Snowdon, 1968). With  $0 \leq s_0 \leq 1$ , the visco-elastic torque applied by the right section of the wing  $s_0 \leq s \leq 1$  on the left section  $0 \leq s \leq s_0$  is now given by

$$M(s_0) = \eta \left( \theta_s + \sigma \dot{\theta}_s \right), \quad (\text{D.1})$$

where  $\sigma = DU_\infty/BL$  is a new non-dimensional parameter:  $B$  is the flexural rigidity of the wing and  $D$  is the visco-elastic damping coefficient. As in section 4.2.1, the

equation of motion for the beam can be derived:

$$\mu\ddot{\zeta} = \left[ e^{i\theta} \left( T - i\eta(\theta_{ss} + \sigma\dot{\theta}_{ss}) \right) \right]_s - ie^{i\theta}[p]^\pm, \quad \zeta_s = e^{i\theta}. \quad (\text{D.2})$$

The energy equation (6.18) becomes

$$\frac{d}{dt}(E_k + E_p) = W_p + \mathcal{P}_{in}^* - W_{loss}, \quad (\text{D.3})$$

with  $W_{loss}$  the loss of mechanical energy due to material damping

$$W_{loss} = \eta\sigma \int_0^1 \dot{\theta}_s^2 ds > 0. \quad (\text{D.4})$$

$E_k$ ,  $E_p$  and  $W_p$  are defined in section 6.2.3 and  $\mathcal{P}_{in}^*$  is the modified power input:

$$\begin{aligned} \mathcal{P}_{in}^* &= -\text{Re} \left[ \left( \dot{\zeta}(0)e^{-i\theta(0)} \right) \left( T(0) + i\eta\theta_{ss}(0) + i\eta\sigma\dot{\theta}_{ss}(0) \right) \right] - \eta\dot{\theta}(0) \left( \theta_s(0) + \sigma\dot{\theta}_s(0) \right) \\ &= \eta\dot{h} \left( \theta_{ss}(0) + \sigma\dot{\theta}_{ss}(0) \right). \end{aligned} \quad (\text{D.5})$$

## D.2 Propulsive performance of a heaving visco-elastic wing

Using this model, we study the influence of material damping on the flapping properties and performance of the heaving wing. Two main effects are observed: the resonances still exist in the presence of material damping but the resonance peaks are in general less sharp (see Figures D.1a and c), and the overall efficiency of the propulsive system is reduced (see Figure D.1b). For a large enough value of  $\sigma$ , the peaks in the thrust production and flapping amplitude are smoothed out and the flapping efficiency gain associated with the use of a flexible profile disappears. We also note a slight delay in the thrust/drag transition due to the presence of material damping.

To analyze the qualitative effect of the damping ratio  $\sigma$  on the position of the resonances, we consider the linear limit of a clamped-free beam in vacuum. In the linear limit, the natural frequencies of the system are modified from (6.33) into

$$\tilde{\omega}_{0,n}(\sigma) = \lambda_n^2 \sqrt{\frac{\eta}{\mu}} \left( 1 - \frac{\sigma^2 \eta \lambda_n^4}{4\mu} \right)^{1/2} + \frac{i\eta \lambda_n^4 \sigma}{2\mu}. \quad (\text{D.6})$$

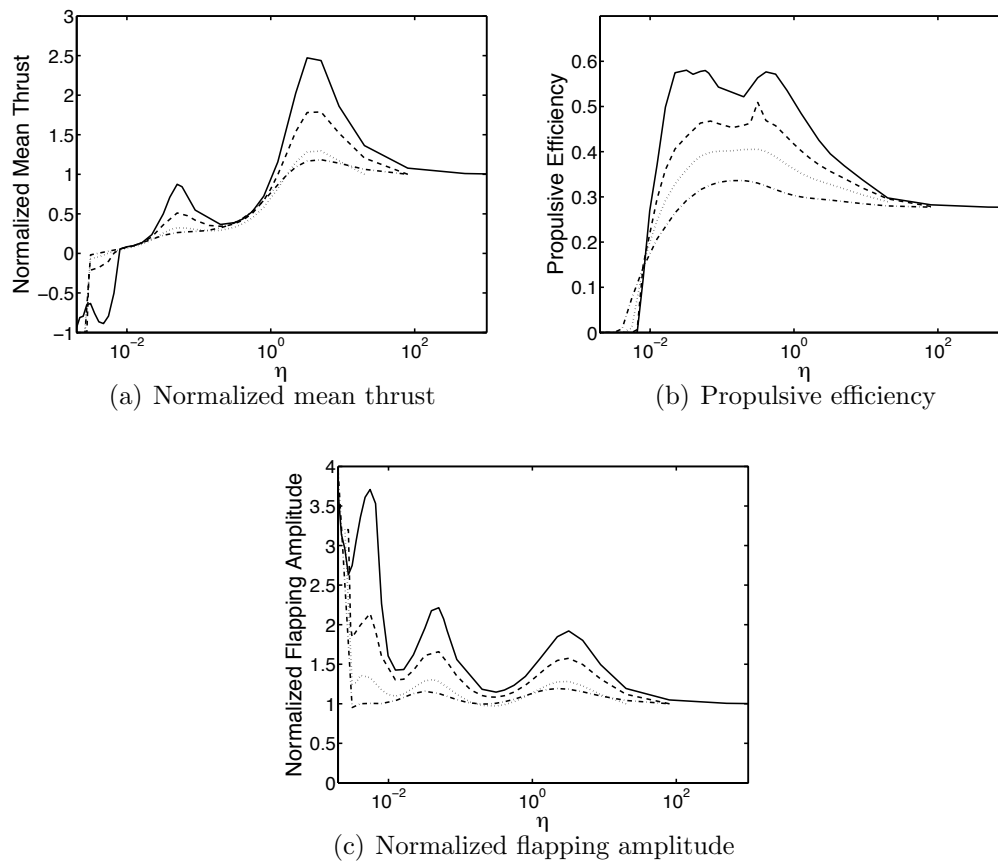


**Figure D.1:** Evolution of the (a) mean thrust, (b) flapping efficiency and (c) trailing edge absolute flapping amplitude with wing rigidity for  $\mu = 0.2$  and  $\epsilon = 0.1$ , and increasing values of the material damping coefficient:  $\sigma = 0$  (solid),  $\sigma = 0.05$  (dashed),  $\sigma = 0.1$  (dotted) and  $\sigma = 0.2$  (dash-dotted). As in previous figures, the mean thrust and flapping amplitude have been normalized by their rigid-case value.

For small  $\eta$ , these modes are damped with a damping rate that is a linear function of  $\sigma$ . The modification in the natural frequencies is however quadratic in  $\sigma$  at leading order and tends to reduce the natural frequency of the system. Although we expect the presence of the fluid to modify the quantitative analysis, these results are consistent with the observations on Figures D.1(a) and (c) that the position of resonance peaks is only weakly influenced by  $\sigma$ . When  $\sigma$  gets larger than a critical value  $\sigma_c = (4\mu/\eta\lambda_n^4)^{1/2}$ , the natural frequencies are purely imaginary (with positive imaginary part), and the natural modes are purely damped standing waves, that cannot resonate with the forcing frequency. Although (D.6) does not include any effect from the fluid, this qualitative behavior is consistent with the disappearance of the resonance peaks for overly large values of  $\sigma$ .

# References

- Abramowitz, M., and Stegun, I. A., 1964: *Handbook of Mathematical Functions with Formulas, Graphs, and Mathematical Tables*. Dover, New York.
- Alben, S., 2008a: The flapping-flag instability as a non-linear eigenvalue problem. *Phys. Fluids*, **20**, 104106.
- Alben, S., 2008b: An implicit method for coupled flow-body dynamics. *J. Comp. Phys.*, **227**, 4912–4933.
- Alben, S., 2008c: Optimal flexibility of a flapping appendage in an inviscid fluid. *J. Fluid Mech.*, **614**, 355–380.
- Alben, S., 2009: Simulating the dynamics of flexible bodies and vortex sheets. *J. Comp. Phys.*, **228**, 2587–2603.
- Alben, S., and Shelley, M., 2005: Coherent locomotion as an attracting state for a free flapping body. *Proc. Nat. Acad. Sci.*, **102**, 11163–11166.
- Alben, S., Shelley, M., and Zhang, J., 2002: Drag reduction through self-similar bending of a flexible body. *Nature*, 479–481.
- Alben, S., Shelley, M., and Zhang, J., 2004: How flexibility induces streamlining in a two-dimensional flow. *Phys. Fluids*, **16**, 1694–1713.
- Alben, S., and Shelley, M. J., 2008: Flapping states of a flag in an inviscid fluid: bistability and the transition to chaos. *Phys. Rev. Lett.*, **100**, 074301.
- Allen, J. J., and Smits, A. J., 2001: Energy harvesting eel. *J. Fluids Struct.*, **15**, 629–640.
- Andersen, A., Pesavento, U., and Wang, Z. J., 2005a: Analysis of transitions between fluttering, tumbling and steady descent of falling cards. *J. Fluid Mech.*, **541**, 91–104.
- Andersen, A., Pesavento, U., and Wang, Z. J., 2005b: Unsteady aerodynamics of fluttering and tumbling plates. *J. Fluid Mech.*, **541**, 65–90.

- Anderson, J. M., Streitlien, K., Barrett, D. S., and Triantafyllou, M. S., 1998: Oscillating foils of high propulsive efficiency. *J. Fluid Mech.*, **360**, 41–72.
- Angot, P., Bruneau, C.-H., and Fabrie, P., 1999: A penalization method to take into account obstacles in incompressible viscous flows. *Numer. Math.*, **81**, 497–520.
- Argentina, M., and Mahadevan, L., 2005: Fluid-flow-induced flutter of a flag. *Proc. Nat. Acad. Sci.*, **102**, 1829–1834.
- Balint, T. S., and Lucey, A. D., 2005: Instability of a cantilevered flexible plate in viscous channel flow. *J. Fluids Struct.*, **20**, 893–912.
- Barnett, T. P., 1983: Interaction of the Monsoon and Pacific trade wind system at interannual time scales. Part I: The equatorial zone. *Mon. Weath. Rev.*, **111**, 756–773.
- Beal, D. N., Hover, F. S., Triantafyllou, M. S., Liao, J. C., and Lauder, G. V., 2006: Passive propulsion in vortex wakes. *J. Fluid Mech.*, **549**, 385–402.
- Belmonte, A., Eisenberg, H., and Moses, E., 1998: From flutter to tumble: inertial drag and Froude similarity in falling paper. *Phys. Rev. Lett.*, **81**, 345–348.
- Belmonte, A., and Moses, E., 1999: Flutter and tumble in fluids. *Phys. World*, **12**, 21–25.
- Bergou, A., Xu, S., and Wang, Z. J., 2007: Passive wing pitch reversal in insect flight. *J. Fluid Mech.*, **591**, 321–337.
- Berman, G., and Wang, Z. J., 2007: Energy-minimizing kinematics in hovering insect flight. *J. Fluid Mech.*, **582**, 153–168.
- Bisplinghoff, R. L., Ashley, H., and Halfman, R. L., 1955: *Aeroelasticity*. Addison–Wesley.
- Borisov, A. V., Kozlov, V. V., and Mamaev, I. S., 2007a: Asymptotic stability and associated problems of dynamics of falling rigid body. *Reg. Chaotic Dyn.*, **12**, 531–565.
- Borisov, A. V., Mamaev, I. S., and Ramodanov, S. M., 2007b: Dynamic interaction of point vortices and a two-dimensional cylinder. *J. Math. Phys.*, **48**, 065403.
- Boyd, J. P., 2001: *Chebyshev and Fourier Spectral Methods*. Dover, New York, 2nd edition.
- Brown, C. E., and Michael, W. H., 1954: Effect of leading edge separation on the lift of a delta wing. *J. Aero. Sci.*, **21**, 690–694 & 706.

- Cheng, H. K., 1954: Remarks on non linear lift and vortex separation. *J. Aero. Sci.*, **19**, 212–214.
- Cheng, J.-Y., Pedley, T. J., and Altringham, J. D., 1998: A continuous dynamic beam model for swimming fish. *Phil. Trans. R. Soc. Lond. B*, **353**, 981–997.
- Childress, S., 1981: *Mechanics of Swimming and Flying*. Cambridge University Press, Cambridge.
- Childress, S., Vandenberghe, N., and Zhang, J., 2006: Hovering of a passive body in an oscillating airflow. *Phys. Fluids*, **18**, 117103.
- Clements, R. R., 1973: An inviscid model of two-dimensional vortex shedding. *J. Fluid Mech.*, **57**, 321–336.
- Combes, S. A., and Daniel, T. L., 2003a: Flexural stiffness in insect wings I. Scaling and the influence of wing venation. *J. Exp. Biol.*, **206**, 2979–2987.
- Combes, S. A., and Daniel, T. L., 2003b: Flexural stiffness in insect wings II. Spatial distribution and dynamic wing bending. *J. Exp. Biol.*, **206**, 2989–2997.
- Connell, B. S. H., 2006: *Numerical investigation of the flow-body interaction of thin flexible foils and ambient flow*. Ph.D. thesis, Massachusetts Institute of Technology.
- Connell, B. S. H., and Yue, D. K. P., 2007: Flapping dynamics of a flag in uniform stream. *J. Fluid Mech.*, **581**, 33–67.
- Cortelezzi, L., 1993: *A theoretical and computational study on active wake control*. Ph.D. thesis, California Institute of Technology.
- Cortelezzi, L., 1995: On the unsteady separated flow past a semi-infinite plate. exact solution of the Brown and Michael model, scaling and universality. *Phys. Fluids*, **7**, 526–529.
- Cortelezzi, L., 1996: Nonlinear feedback control of the wake past a plate with a suction point on the downstream wall. *J. Fluid Mech.*, **327**, 303–324.
- Cortelezzi, L., Chen, Y. C., and Chang, H. L., 1997: Nonlinear feedback control of the wake past a plate: from a low-order model to a higher-order model. *Phys. Fluids*, **9**, 2009–2022.
- Cortelezzi, L., and Leonard, A., 1993: Point vortex model of the unsteady separated flow past a semi-infinite plate with transverse motion. *Fluid Dyn. Res.*, **11**, 263–295.
- Crowdy, D. G., Surana, A., and Yick, K.-Y., 2007: The irrotational motion generated by two planar stirrers in inviscid fluid. *Phys. Fluids*, **19**, 018103.

- Datta, S. K., and Gottenberg, W. G., 1975: Instability of an elastic strip hanging in an airstream. *J. Appl. Mech.*, **42**, 195–198.
- de Langre, E., 2001: *Fluides et Solides*. Editions de l’Ecole Polytechnique, Palaiseau.
- de Langre, E., 2008: Effects of wind on plants. *Ann. Rev. Fluid Mech.*, **40**, 141–168.
- Dickinson, M., Lehmann, F. O., and Sane, S. P., 1999: Wing rotation and the aerodynamic basis of insect flight. *Science*, **284**, 1954–1960.
- Edwards, R. H., 1954: Leading-edge separation from delta wings. *J. Aero. Sci.*, **21**, 134–135.
- Eldredge, J. D., and Pisani, D., 2008: Passive locomotion of a simple articulated fish-like system in the wake of an obstacle. *J. Fluid Mech.*, **607**, 279–288.
- Ellington, C. P., 1984: The aerodynamics of hovering insect flight. *Phil. Trans. R. Soc. London B*, **305**, 1–181.
- Eloy, C., Lagrange, R., Souilliez, C., and Schouveiler, L., 2008: Aeroelastic instability of a flexible plate in a uniform flow. *J. Fluid Mech.*, **611**, 97–106.
- Eloy, C., Souilliez, C., and Schouveiler, L., 2007: Flutter of a rectangular plate. *J. Fluids Struct.*, **23**, 904–919.
- Farnell, D. J. J., David, T., and Barton, D. C., 2004: Coupled states of flapping flags. *J. Fluids Struct.*, **19**, 29–36.
- Fernandes, P. C., Ern, P., Risso, F., and Magnaudet, J., 2005: On the zigzag dynamics of freely moving axisymmetric bodies. *Phys. Fluids*, **17**, 098107.
- Fernandes, P. C., Risso, F., Ern, P., and Magnaudet, J., 2007: Oscillatory motion and wake instability of freely rising axisymmetric bodies. *J. Fluid Mech.*, **573**, 479–502.
- Field, S. B., Klaus, M., Moore, M. G., and Nori, F., 1997: Chaotic dynamics of falling disks. *Nature*, **388**, 252–254.
- Godoy-Diana, R., Aider, J. L., and Wesfreid, J. E., 2008: Transitions in the wake of a flapping foil. *Phys. Rev. E*, **77**, 016308.
- Gorelov, D. N., 2008: Calculation of pressure on an airfoil contour in an unsteady separated flow. *J. Appl. Mech. Tech. Phys.*, **49**, 437–441.
- Graham, J. M. R., 1977: Vortex shedding from sharp edges. *Imperial College Aero. Rep.*, **77-06**.

- Graham, J. M. R., 1980: The forces on sharp-edged cylinders in oscillatory flow at low Keulegan-Carpenter numbers. *J. Fluid Mech.*, **97**, 331–346.
- Guo, C. Q., and Païdoussis, M. P., 2000a: Analysis of hydroelastic instabilities of rectangular parallel-plate assemblies. *ASME J. Press. Vess. Technol.*, **122**, 502–508.
- Guo, C. Q., and Païdoussis, M. P., 2000b: Stability of rectangular plates with free side-edges in two-dimensional inviscid channel flow. *J. Appl. Mech.*, **67**, 171–176.
- Harder, D. L., Speck, O., Hurd, C. L., and Speck, T., 2004: Reconfiguration as a prerequisite for survival in highly unstable flow-dominated habitats. *J. Plant Growth Regul.*, **23**, 98–107.
- Howe, M. S., 1996: Emendation of the Brown and Michael equation, with application to sound generation by a vortex motion near a half-plane. *J. Fluid Mech.*, **329**, 89–101.
- Huang, J. Y., 2001: Moving coordinates methods and applications to the oscillations of a falling slender body. In *Moving Boundaries VI: computational modelling of free and moving boundary problems*, editors B. Šarler, and C. A. Brebbia, 73–82. WIT Press, Southampton.
- Huang, L., 1995: Flutter of cantilevered plates in axial flow. *J. Fluids Struct.*, **9**, 127–147.
- Huang, W.-X., Shin, S. J., and Sung, H. J., 2007: Simulation of flexible filaments in uniform flow by the immersed boundary method. *J. Comp. Phys.*, **226**, 2206–2228.
- Jia, L.-B., Li, F., Yin, X.-Z., and Yin, X.-Y., 2007: Coupling modes between two flapping filaments. *J. Fluid Mech.*, **581**, 199–220.
- Jia, L.-B., and Yin, X.-Z., 2008: Passive oscillations of two tandem flexible filaments in a flowing soap film. *Phys. Rev. Lett.*, **100**, 228104.
- Jones, K. D., Bradshaw, C. J., Papadopoulos, J., and Platzler, M. F., 2004: Improved performance and control of flapping-wing propelled micro-air vehicles. AIAA Paper 2004-0399.
- Jones, M. A., 2003: The separated flow of an inviscid fluid around a moving plate. *J. Fluid Mech.*, **496**, 405–441.
- Jones, M. A., and Shelley, M. J., 2005: Falling cards. *J. Fluid Mech.*, **540**, 393–425.
- Kanso, E., and Oskouei, B. G., 2008: Stability of a coupled body–vortex system. *J. Fluid Mech.*, **600**, 77–94.

- Keller, J. B., 1998: Vortex sheets as vortices in two-dimensional flow around a body. Unpublished manuscript.
- Kim, G., and Davis, D. C., 1995: Hydrodynamic instabilities in flat-plate-type fuel assemblies. *Nuc. Eng. Des.*, **158**, 1–17.
- Kochin, N. E., Kibel, I. A., and Roze, N. V., 1964: *Theoretical Hydromechanics*. Interscience Publishers, New York.
- Kolomenskiy, D., Moffatt, K., Farge, M., and Schneider, K., 2008: Vorticity generation during the clap-fling-sweep of some hovering insects. Submitted to *Theor. Comp. Fluid Dyn.*
- Kolomenskiy, D., and Schneider, K., 2008: Numerical simulations of falling leaves using a pseudo-spectral method with volume penalization. Submitted to *Theor. Comp. Fluid Dyn.*
- Kornecki, A., Dowell, E. H., and O'Brien, J., 1976: On the aeroelastic instability of two-dimensional panels in uniform incompressible flow. *J. Sound Vib.*, **47**, 163–178.
- Kozlov, V. V., 1989: Heavy rigid body falling in an ideal fluid. *Mech. Solids*, **24**, 9–17.
- Kozlov, V. V., 1990: On the problem of a heavy rigid body falling in a resisting medium. *Vestnik Moskov. Univ. Ser. I Mat. Meekh.*, **1**, 79–86.
- Krasny, R., 1986a: Desingularisation of periodic vortex sheet roll-up. *J. Comp. Phys.*, **65**, 292–313.
- Krasny, R., 1986b: A study of singularity formation in a vortex sheet by the point-vortex approximation. *J. Fluid Mech.*, **167**, 65–93.
- Lamb, H., 1932: *Hydrodynamics*. Dover, New York, 6th edition.
- Lasheras, J. C., 2007: The biomechanics of arterial aneurysms. *Ann. Rev. Fluid Mech.*, **39**, 293–319.
- Lemaitre, C., Hémon, P., and de Langre, E., 2005: Instability of a long ribbon hanging in axial air flow. *J. Fluids Struct.*, **20**, 913–925.
- Liao, J. C., Beal, D. N., Lauder, G. V., and Triantafyllou, M. S., 2003a: Fish exploiting vortices decrease muscle activity. *Science*, **302**, 1566–1569.
- Liao, J. C., Beal, D. N., Lauder, G. V., and Triantafyllou, M. S., 2003b: The Kármán gait: novel body kinematics of rainbow trout swimming in a vortex street. *J. Exp. Biol.*, **206**, 1059–1073.

- Lighthill, M. J., 1960: Note on the swimming of slender fish. *J. Fluid Mech.*, **9**, 305–317.
- Lighthill, M. J., 1969: Hydromechanics of aquatic animal propulsion. *Ann. Rev. Fluid Mech.*, **1**, 413–446.
- Lin, C. C., 1941: On the motion of vortices in two dimensions. *Proc. Natl. Acad. Sci.*, **27**, 570–575.
- Llewellyn Smith, S. G., Michelin, S., and Crowdy, D. G., 2008: The dipolar field of rotating bodies in two dimensions. *J. Fluid Mech.*, **607**, 109–118.
- Lucey, A. D., and Carpenter, P. W., 1993: The hydroelastic stability of three-dimensional disturbances of a finite compliant wall. *J. Sound Vib.*, **165**, 527–552.
- Mahadevan, L., 1996: Tumbling of a falling card. *C. R. Acad. Sci. Ser. IIb*, **323**, 729–736.
- Mahadevan, L., Aref, H., and Jones, S. W., 1995: Comment on ‘behavior of a falling paper’ (with reply). *Phys. Rev. Lett.*, **75**, 1420.
- Mahadevan, L., Ryu, W. S., and Samuel, A. D. T., 1999: Tumbling cards. *Phys. Fluids Lett.*, **11**, 1–3.
- Mason, R., 2003: *Fluid locomotion and trajectory planning for shape-changing robots*. Ph.D. thesis, California Institute of Technology.
- Maxwell, J. C., 1854: On a particular case of the descent of a heavy body in a resisting medium. *Camb. Dublin Math. J.*, **9**, 145–148.
- Miao, J.-M., and Ho, M.-H., 2006: Effect of flexure on aerodynamic propulsive efficiency of flapping flexible airfoil. *J. Fluids Struct.*, **22**, 401–419.
- Michelin, S., and Llewellyn Smith, S. G., 2009a: Falling cards and flapping flags: understanding fluid-solid interactions using an unsteady point vortex model. *Theor. Comp. Fluid Dyn.* doi:10.1007/s00162-009-0117-6. (in press).
- Michelin, S., and Llewellyn Smith, S. G., 2009b: Linear stability analysis of coupled parallel flexible plates in an axial flow. Submitted to *J. Fluids Struct.*
- Michelin, S., and Llewellyn Smith, S. G., 2009c: An unsteady point vortex method for coupled fluid-solid problems. *Theor. Comp. Fluid Dyn.*, **23**, 127–153.
- Michelin, S., Llewellyn Smith, S. G., and Glover, B. J., 2008: Vortex shedding model of a flapping flag. *J. Fluid Mech.*, **617**, 1–10.

- Miller, D. R., 1960: Critical flow velocities for collapse of reactor parallel-plate fuel assemblies. *Trans. ASME, J. Eng. Power*, **82**, 83–95.
- Milne-Thomson, L. M., 1968: *Theoretical Hydrodynamics*. Macmillan Press.
- Mittal, R., and Iaccarino, G., 2005: Immersed boundary methods. *Ann. Rev. Fluid Mech.*, **37**, 239–261.
- Mittal, R., Seshadri, V., and Udaykumar, H. S., 2004: Flutter, tumble and vortex induced autorotation. *Theoret. Comput. Fluid Dyn.*, **17**, 165–170.
- Nehari, Z., 1952: *Conformal Mapping*. McGraham–Hill, New York.
- Newman, J. N., 1977: *Marine Hydrodynamics*. MIT Press, Cambridge, MA.
- Paidoussis, M. P., 1998: *Fluid-Structure Interactions, Slender Structures and Axial Flows*, volume 1. Academic Press, London.
- Paidoussis, M. P., 2004: *Fluid-Structure Interactions, Slender Structures and Axial Flows*, volume 2. Academic Press, London.
- Pesavento, U., and Wang, Z. J., 2004: Falling paper: Navier–Stokes solutions, model of fluid forces, and center of mass elevation. *Phys. Rev. Lett.*, **93**, 144501.
- Peskin, C. S., 1972: Flow patterns around heart valves: a numerical method. *J. Comp. Phys.*, **10**, 252–271.
- Peskin, C. S., 1977: Numerical analysis of blood flow in the heart. *J. Comp. Phys.*, **25**, 220–252.
- Pozrikidis, C., 1998: *Numerical Computation in Science and Engineering*. Oxford Univ. Press.
- Pullin, D. I., 1978: The large-scale structure of unsteady self-similar rolled-up vortex sheets. *J. Fluid Mech.*, **88**, 401–430.
- Ramodanov, S. M., 2000: Motion of a circular cylinder and a vortex in an ideal fluid. *Reg. Chaotic Dyn.*, **6**, 33–38.
- Rayleigh, L., 1878: On the instability of jets. *Proc. Lond. Math. Soc.*, **10**, 4–13.
- Ristroph, L., and Zhang, J., 2008: Anomalous hydrodynamic drafting of interacting flapping flags. *Phys. Rev. Lett.*, **101**, 194502.
- Rott, N., 1956: Diffraction of a weak shock with vortex generation. *J. Fluid Mech.*, **1**, 111–128.
- Saffman, P. G., 1992: *Vortex Dynamics*. Cambridge University Press.

- Schouveiler, L., and Eloy, C., 2009: Coupled flutter of parallel plates. Submitted to *Phys. Fluids*.
- Sedov, L. I., 1965: *Two-Dimensional Problems in Hydrodynamics and Aerodynamics*. Interscience Publishers.
- Shashikanth, B. N., 2005: Poisson brackets for the dynamically interacting system of a 2D rigid cylinder and N point vortices: the case of arbitrary smooth cylinder shapes. *Reg. Chaotic Dyn.*, **10**, 1–14.
- Shashikanth, B. N., Marsden, J. E., Burdick, J. W., and Kelly, S. D., 2002: The hamiltonian structure of a 2D rigid circular cylinder interacting dynamically with N point vortices. *Phys. Fluids*, **14**, 1214–1227.
- Shayo, L. K., 1980: The stability of cantilever panels in uniform incompressible flows. *J. Sound Vib.*, **68**, 341–350.
- Shelley, M., Vandenberghe, N., and Zhang, J., 2005: Heavy flags undergo spontaneous oscillations in flowing water. *Phys. Rev. Lett.*, **94**, 094302.
- Shukla, R. K., and Eldredge, J. D., 2007: An inviscid model for vortex shedding from a deforming body. *Theor. Comput. Fluid Dyn.*, **21**, 343–368.
- Smith, E. H., 1971: Autorotating wings: an experimental investigation. *J. Fluid Mech.*, **50**, 513–534.
- Smith, J. H. B., 1968: Improved calculations of leading edge separation from slender delta wings. *Proc. R. Soc. A*, **306**, 67–90.
- Snowdon, J. C., 1968: *Vibration and Shock in Damped Mechanical Systems*. Wiley, New York.
- Tanabe, Y., and Kaneko, K., 1994: Behavior of a falling paper. *Phys. Rev. Lett.*, **73**, 1372–1375.
- Tanabe, Y., and Kaneko, K., 1995: Tanabe and Kaneko reply. *Phys. Rev. Lett.*, **75**, 1421.
- Tang, L., and Paidoussis, M. P., 2009: The coupled dynamics of two cantilevered flexible plates in axial flow. *J. Sound Vib.*, **323**, 214–231.
- Theodorsen, T., 1935: General theory of aerodynamic instability and the mechanism of flutter. NACA Report 496.
- Thomas, A. L. R., Taylor, G. K., Srygley, R. B., Nudds, R. L., and Bomphrey, R. J., 2004: Dragonfly flight: free-flight and tethered flow visualizations reveal a diverse array of unsteady lift-generating mechanisms, controlled primarily via angle of attack. *J. Exp. Biol.*, **207**, 4299–4323.

- Toomey, J., and Eldredge, J. D., 2008: Numerical and experimental study of the fluid dynamics of a flapping wing with low-order flexibility. *Phys. Fluids*, **20**, 073603.
- Triantafyllou, G. S., 1992: Physical condition for absolute instability in inviscid hydroelastic coupling. *Phys. Fluids A*, **4**, 544–552.
- Triantafyllou, M. S., Triantafyllou, G. S., and Yue, D. K. P., 2000: Hydrodynamics of fishlike swimming. *Annu. Rev. Fluid Mech.*, **32**, 33–53.
- Tuck, E. O., 1980: Application and solution of Cauchy singular integral equations. In *The Application and Numerical Solution of Integral Equations*, 21–50. Alphen aan den Rijn: Sijthoff and Noordhoff.
- Vandenbergh, N., Childress, S., and Zhang, J., 2006: On unidirectional flight of a free flapping wing. *Phys. Fluids*, **18**, 014102.
- Vandenbergh, N., Zhang, J., and Childress, S., 2004: Symmetry breaking leads to forward flapping flight. *J. Fluid Mech.*, **506**, 147–155.
- Vogel, S., 1989: Drag and reconfiguration of broad leaves in high winds. *J. Exp. Bot.*, **40**, 941–948.
- Wallace, J. M., and Dickinson, R. E., 1972: Empirical orthogonal representation of time series in the frequency domain. Part I: Theoretical considerations. *J. Appl. Met.*, **11**, 887–892.
- Wang, Z. J., 2000a: Two dimensional mechanism for insect hovering. *Phys. Rev. Lett.*, **85**, 2216–2219.
- Wang, Z. J., 2000b: Vortex shedding and frequency selection in flapping flight. *Phys. Rev. Lett.*, **410**, 323–341.
- Wang, Z. J., 2005: Dissecting insect flight. *Annu. Rev. Fluid Mech.*, **37**, 183–210.
- Wang, Z. J., Birch, J. M., and Dickinson, M. H., 2004: Unsteady forces and flows in low Reynolds number hovering flight: two-dimensional computations vs robotic wing experiments. *J. Exp. Biol.*, **207**, 449–460.
- Wang, Z. J., and Russell, D., 2007: Effect of forewing and hindwing interactions on aerodynamic forces and power in hovering dragonfly flight. *Phys. Rev. Lett.*, **99**, 148101.
- Watanabe, Y., Isogai, K., Suzuki, S., and Sugihara, M., 2002a: A theoretical study of paper flutter. *J. Fluids Struct.*, **16**, 543–560.

- Watanabe, Y., Suzuki, S., Sueoka, Y., and Kunimaru, H., 1991: The flutter mechanism of sheet. In *Proceedings of the First International Conference on Web Handling*, 246–256. Oklahoma State University, Stillwater.
- Watanabe, Y., Suzuki, S., Sugihara, M., and Sueoka, Y., 2002b: An experimental study of paper flutter. *J. Fluids Struct.*, **16**, 529–542.
- Williamson, C. H. K., and Roshko, A., 1988: Vortex formation in the wake of an oscillating cylinder. *J. Fluids Struct.*, **2**, 355–381.
- Willmarth, W. W., Hawk, N. E., and Harvey, R. L., 1964: Steady and unsteady motions and wakes of freely falling disks. *Phys. Fluids*, **7**, 197–208.
- Wooton, R. J., 1992: Functional morphology of insect wings. *Ann. Rev. Entomol.*, **37**, 113–140.
- Wu, T. Y., 1961: Swimming of a waving plate. *J. Fluid Mech.*, **10**, 321–344.
- Xiong, H., and Kelly, S. D., 2008: Self-propulsion of a deformable joukowski foil in a perfect fluid with vortex shedding. Submitted to *J. Nonlinear Sci.*
- Yadykin, Y., Tenetov, V., and Levin, D., 2001: The flow-induced vibration of a flexible strip hanging vertically in a parallel flow. Part 1: Temporal aeroelastic instability. *J. Fluids Struct.*, **15**, 1167–1185.
- Zhang, J., Childress, S., Libchaber, A., and Shelley, M., 2000: Flexible filaments in a flowing soap film as a model for one-dimensional flags in a two-dimensional wind. *Nature*, **408**, 835–839.
- Zhu, L., and Peskin, C., 2002: Simulation of flapping flexible filament in a flowing soap film by the immersed boundary method. *J. Comput. Phys.*, **179**, 452–468.
- Zhu, L., and Peskin, C., 2003: Interaction of two flapping filaments in a flowing soap film. *Phys. Fluids*, **15**, 1954–1960.